22/12/2023

PhD title

Exploiting High-Index Dielectric Structures on Optical Fibres to Achieve High-Spatial Resolution via Photonic Nanojets

By

Wasem Khalaf Aljuaid

Submitted to the Programme: PhD Physics (FT) (Experimental)

School of Mathematics, Statistics and Physics

Newcastle University

NE1 7RU

Newcastle upon Tyne

United Kingdom

Main supervisor: Dr Victor Pacheco-Peña

Co-supervisor: Prof. Noel Healy

Submitted on December 2023

Declaration

The work presented in this thesis is completely original and has not been plagiarized or copied from any other sources. Every effort has been made to ensure that all sources and references used in this research are properly cited and attributed. I confirm that this thesis follows all the guidelines, regulations, and policies established by the School of Mathematics, Statistics, and Physics at Newcastle University. The main contribution of this work revolves around the successful achievement of photonic nanojets (PNJs) with a high-resolution spatial focusing of electromagnetic waves, particularly on top of an optical fibre.

December 2023

Wasem Khalaf Aljuaid

Abstract

In this thesis, we propose a mechanism for achieving high-resolution spatial focusing of electromagnetic waves at telecommunication wavelengths ($\lambda_0 = 1.55$ μm) using high-refractive index dielectrics. Our approach involves the production of photonic nanojets (PNJs) with a high intensity and spatial resolution. We use cylindrical and spherical dielectrics with radii ranging from $R = 0.15\lambda_0$ to $1.55\lambda_0$, placed at the end of an optical fibre to achieve PNJ focusing. We evaluate the response of the device in 2D and 3D configurations using cylindrical and spherical dielectrics, respectively. By truncating the output profile of the dielectric, we are able to shift the PNJs towards the output surface of the high-index dielectric, resulting in a high transversal resolution. The Full-Width at Half-Maximum (*FWHM*) achieved is $FWHM = 0.28\lambda_0$ (2D truncated dielectric), and $FWHMy = 0.17\lambda_0$ and $FWHMx = 0.21\lambda_0$ (3D truncated dielectric). We also explore the potential of a specific structure for applications requiring high spatial resolution working at $\lambda_0 = 2$ μm. Specifically, we report preliminary results from an experiment involving a full and truncated Germanium (Ge) sphere surrounded by cladding material, placed on top of the core of an optical fibre. Our findings demonstrate that this structure is able to generate PNJs with a high transversal resolution at the output surface of the truncated dielectric sphere, measuring $FWHMy = 0.13\lambda_0$ and $FWHMx = 0.16\lambda_0$. Interestingly, we also observe the PNJs beyond the output surface of the truncated dielectric sphere (outside) at a distance of $0.1\lambda_0$, with a resolution of $FWHMy = 0.43\lambda_0$ and $FWHMx = 0.41\lambda_0$. Our proposed structure consisting of an optical fibre and a truncated high index dielectric may have applications in sensing and imaging systems that require near-field high spatial resolution.

Acknowledgement

I am grateful to my dedicated advisors, Dr. Victor Pacheco Peña and Prof. Noel Healy, for their guidance, support, and valuable feedback throughout my research journey. I would also like to acknowledge Christian Johnson-Richards's (postdoctoral) contributions to the collaborative efforts in the photonic lab, particularly sections 4.2.4 and 4.2.6. Additionally, I am thankful to Luke Stocks (postgraduate research) for allowing me to use his furnace and gas pressure equipment in the photonic lab and for his collaboration on the utilization of the CO_2 laser in section 4.2.5. Dr. Toby Hallam, Dr. Jonathan Mar, and Dr. Clive Emary, members of my thesis committee, deserve thanks for their helpful advice and support. Financial support from the Islamic University of Madinah is gratefully acknowledged. I would like to thank the School of Mathematics, Statistics, and Physics at Newcastle University for providing the necessary resources, such as libraries, labs, and infrastructure, which were important in the successful completion of my research. On a personal note, I would like to thank my wife and children for providing support during my time in Newcastle. I am deeply grateful to my parents and siblings in the Kingdom of Saudi Arabia for their continued assistance throughout my research journey. Lastly, I would like to thank our group of the Metamaterials and Plasmonics Lab for their assistance and valuable counsel during my thesis research.

Table of Content

Content

List of Figures

Appendix:

List of Tables

Chapter 1 : Introduction

In this chapter, we investigate the fundamentals of photonics and its different applications. We begin by discussing the significance of the electromagnetic spectrum, which classified in term of the wavelengths ranging from one kilometre to one nanometer in a different field. Furthermore, we emphasise the significant role of photonics in technology, where the manipulation of photons through transmission, emission, and sensing is the main factor behind technology. The exploration of a particular photonics application known as photonic nanojets (PNJs) is the primary focus of this dissertation. We emphasise the significance of the infrared spectrum and its applications, such as near-infrared spectroscopy for imaging and sensing and optical fibre communications. Moreover, we discuss the concept into the realm of waveguides, particularly dielectric waveguides and optical fibres, which enable the guided transmission of electromagnetic waves. Additionally, the dispersion properties of dielectrics and optical fibres are discussed focusing on the behaviour of electromagnetic wave inside these structures. Furthermore, we investigate the field of optical microscopy using simple and compound microscope systems with a focus on achieving higher magnification levels. Finally, we address the diffraction limit of electromagnetic waves and its impact on the spatial resolution of imaging systems. To overcome this limitation, we discuss devices with high spatial resolution, such as superlenses and PNJs. We emphasise the importance of PNJs in imaging and sensing applications, particularly their ability to detect subwavelength particles. This chapter introduces photonics and provides a platform for the study of PNJs and their great potential.

1.1 An introduction to photonics

This section will discuss three topics briefly: the electromagnetic spectrum, the technological revolution utilizing photonics, and the significance of the infrared spectrum. We will investigate these topics to understand their implications and effects.

1.1.1 Electromagnetic spectrum

Controlling wave-matter interactions is being explored in many research fields for an optical wavelength [1]. In this realm, as shown in Fig. 1.1 the electromagnetic spectrum can be classified in term of the wavelengths ranging from one kilometre to one nanometre [2]. Beginning with wavelengths that are larger than one metre in length (frequencies below 0.3 GHz) such as amplitude modulation (AM), radio, television, and frequency modulation (FM)

waves. This spectrum of electromagnetic waves is commonly referred to as the global communication system because it is utilised to transmit high-quality video and audio over large distances utilising electronic devices [3]. Next is the microwave range, whose wavelength ranges from 3 mm to 1 m (frequencies from 0.3 to 100 GHz). This radiation is commonly employed in communication systems such as radar systems, space-vehicle communications, mobile phones, and Wi Fi [4,5].

Millimetre waves have a wavelength between 1 and 10 mm (frequencies from 30 to 300 GHz) and are situated between microwaves and terahertz waves on the electromagnetic spectrum; millimetre waves are used in some applications such as fifth generation communication (5G) [6,7]. Following the millimetre wave spectrum is the terahertz range, which begins at 30 μm and ends at 3 mm (frequencies from 0.1 to 10 THz) [8]. Terahertz wave transmission has generally been conducted as freespace beams travelling through air to avoid significant absorption in the spectrum of THz-range media [9]. Some applications of Terahertz gap range are for DNA signature and gene diagnosis since it is non-ionizing radiation for human living tissue [10].

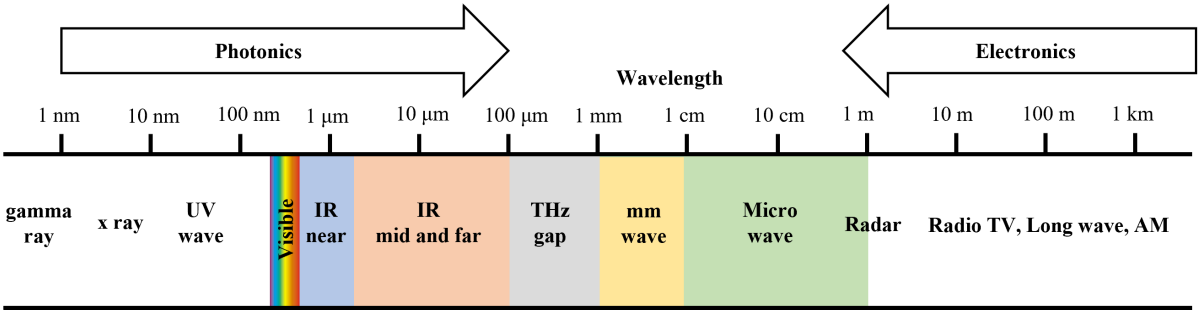

Figure 1.1: The electromagnetic spectrum of wavelength from 1 kilometre to 1 nanometre.

After the terahertz range is the infrared (IR) range, which ranges from the edge of the red colour 750 nm to 0.1 mm (frequencies from 3 to 400 THz) [11]. This spectral range can be separated into three sections according to the ISO 20473 standard for the sub-division of the IR classification: far (FIR), medium (MIR), and near (NIR) infrared. The first portion, FIR, is approximately 50 μm to 0.1 mm in wavelength (frequencies from 3 to 6 THz). FIR transports energy solely in the form of thermal energy, which thermoreceptors on human skin sense as radiant heat [11]. In addition to being absorbed by the human body, FIR is also emitted by the body as black body radiation, thus thermal infrared imaging refers to FIR [11,12]. The second portion, MIR, is wavelengths range from 3 to 50 μm (frequencies from 6 to 100 THz). MIR spectra are also used for thermal infrared imaging and often have more absorbance than FIR spectra, making them appropriate for a variety of photonic sensors [12,13]. The third component

is NIR, which consists of wavelengths between 780 nm and 3 μm (frequencies from 100 to 385 THz). NIR has shown considerable promise for a variety of applications in various domains, including optical communications, biological imaging, sensors, lasers, and solar energy conversion; nevertheless, imaging equipment in this range still need to be developed [14–19]. This thesis will concentrate on NIR, which is described in more detail in section 1.1.3.

The following range is visible radiation, the wavelengths range from 400 to 700 nm (frequencies from 428 to 750 THz) [3]. Visible light can be used, for instance, to create a high-power intracavity frequency-doubled 532 nm laser for the medical treatment of vascular diseases [20]. From 400 nm and below (frequencies from 750 THz and above), the wavelength ranges from ultraviolet radiation to x-ray to gamma radiation. One of the uses of short wavelengths, for example, is the study of the crystal structure by x-ray because the wavelengths of x-rays are comparable to the distances between atoms in solids [3]. As is well-known, as the wavelength becomes shorter, the frequency rises, resulting in an increase in photon energy; thus short wavelength is typically not employed in the study of living tissues, as it may cause damage to human living cell [19]. Depending on the interaction between the light and the matter, different wavelengths are used for various applications. In the following section, we will discuss how photonics, the interaction of light with a matter, influenced the evolution of technology.

1.1.2 Technology revolution using photonics

Photonics and electronics deal with fundamentally different types of particles. Typically, electrons carry out the transmission in an electronics circuit. In contrast, photons perform this role in a photonic circuit. Photonics is superior than electronics because the circuit containing photons oscillates at a substantially faster rate than the circuit surrounding electrons. Photonics is further along in its development [21].

Walter Brattain, John Bardeen, and William Shockley at Bell Laboratories created a method using photons for communication via the commonly known fibres, and coined the term photonics which is a combination of the words photons and electronics [22]. The method of using photons for communication began after the laser became commercially available, after its initial implementation in 1960 by Theodore Harold Maiman [21,22]. Laser is appropriate for long-distance communications because it produces coherent light, where the light waves are perfectly aligned and maintain their phase relationship over long distances. This coherence enables the laser to propagate efficiently over long distances without significant spreading or attenuation [22–24]. Moreover, laser light photons are useful for many purposes other than

communication such as cutting or welding [25]. Lasers and optical fibres are just some of the many applications that fall under the umbrella of the photonics field [26,27].

Photonics applications encompass all technical applications across the whole optical spectrum, the great majority of photonics applications extend from NIR to visible waves [26,28,29]. The famous lecture of Richard P. Feynman in 1959 "*There's Plenty of Room at the Bottom*. ..." emphasises the significance of controlling a small object in a size of nanometre for modern technologies [30]. The term photonics in the most recent applications has been expanded to encompass nearly all processes that utilise photons in science by their detection, and their manipulation through transmission, emission, and sensing [26]. The manipulation of photons traveling in freespace or when interacting with matter is at the heart of photonics [1,31]. This thesis will explore one of the photonics applications used to create a high-intensity focal spot, called photonic nanojets (PNJs), by placing a dielectric at the end of an optical fibre. These PNJs can be utilized as imaging and sensing devices.

1.1.3 Importance of infrared spectrum

As previously mentioned in 1.1.1, the infrared spectrum extends from 780 nm to 0.1 mm, with frequencies ranging from 3 to 400 THz. Fredrick William Herschel discovered infrared in 1800. Fredrick noted that a thermometer temperature increased when it was passed across a longer wavelength than visible regain. Accordingly, Fredrick concluded that longer wavelengths mean higher temperatures and increased thermometer readings indicate the existence of invisible waves [19,32].

The range of the infrared spectrum is extensive, offering a wide range of applications based on the thermal properties of the radiation [11]. FIR and MIR wavelengths are particularly useful for applications that require the detection and measurement of thermal energy [12,33]. Thermal imaging cameras, for example, use these wavelengths to create images that highlight temperature differences in an object. While FIR and MIR wavelengths are useful for many applications, they are not always suitable for analysing small samples. This is because the radiation can generate heat in the samples, potentially damaging or altering them. In such cases, NIR can be used as an alternative. NIR has lower thermal energy than FIR and MIR, meaning that it produces less heat on the samples. This makes it ideal for evaluating small samples that are sensitive to heat such as biological tissues [18,19].

NIR is also commonly used in non-destructive analytical techniques such as near-infrared spectroscopy [34]. Near-infrared spectroscopy is a technique that uses NIR to measure the absorption, reflection, and scattering of light by a sample. By analysing the resulting spectrum,

it is possible to identify the chemical composition of the sample. This technique is useful in a variety of fields, including food quality control, medical diagnostics, and environmental monitoring [34].

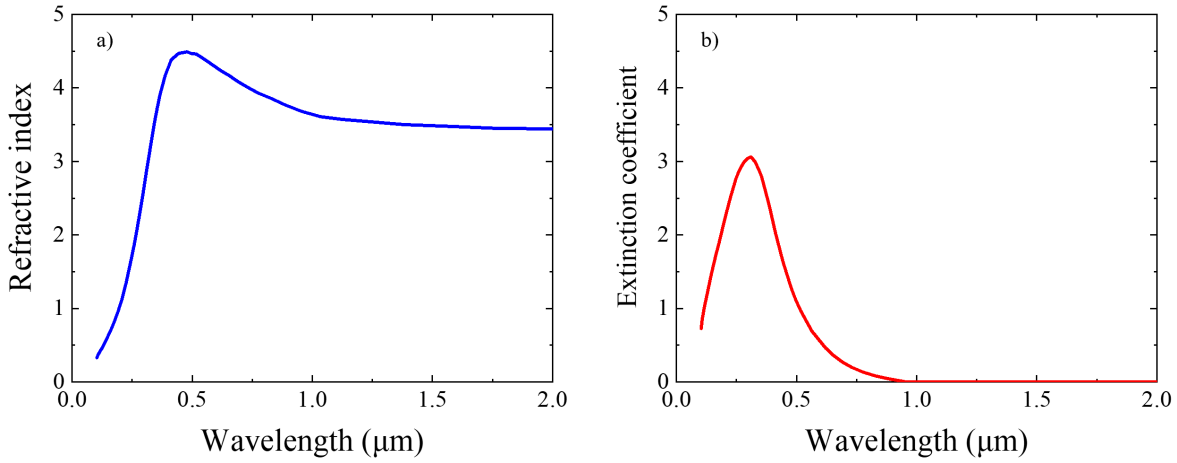

Figure 1.2: As a function of the various wavelengths, refractive index (a) and extinction coefficient (b) of silicon are illustrated [35].

Different materials react differently to electromagnetic waves and the property of NIR range is that it cannot penetrate metals but can travel through numerous crystalline substances such as fused silica and sapphire [32,36]. The most common uses of NIR in photonics are optical fibres and imaging systems [29,37,38]; these examples will be explored in more detail in section 1.2 below. One of the most important common materials that have helped improve technology which is a type of semiconductor is silicon [39]. The complex refractive index ñ of a material is given by the following equation [40]:

$$\tilde{n} = n + ik \tag{1.1}$$

The behaviour of silicon material, for example amorphous silicon, with respect to the real part of the refractive index n and the imaginary part of the extinction coefficient k in response to different wavelength is depicted in Fig. 1.2 [35]. The refractive index defines the degree to which a material bends or refracts light as it travels through it. The extinction coefficient describes the attenuation of electromagnetic wave energy during wave transmission through a medium [40]. In the NIR and at wavelengths even longer than this range, the extinction coefficient is at its lowest value with a slight change in the refractive index, silicon is therefore an ideal material for use in technical applications [41,42].

1.2 Applications of photonic devices

This section examines waveguides, focusing specifically on dielectrics and optical fibres. We begin by examining the dispersion of dielectric materials, followed by an analysis of the

modes present in optical fibres. Additionally, we investigate dispersion within optical fibres. Furthermore, optical microscopy is discussed.

1.2.1 Waveguides: dielectrics and optical fibres

Waveguides are structures that can guide waves in any direction; dielectric waveguides and optical fibres are examples of waveguides that use electromagnetic waves to transmit through them [21]. There are many different examples of dielectrics, such as lenses, prisms, plates, and films [2]. One of the factors that influence the dielectric and optical fibre is dispersion, which relates to the phenomenon in which the index of refraction of a medium varies with frequency [2,43].

1.2.1.1 Dispersion of dielectric

When an electromagnetic wave illuminates a dielectric, the electric dipoles of the dielectric medium become altered. These alterations within the dielectric are known as electric polarisation $\boldsymbol{P}$, and for the majority of materials, $\boldsymbol{P}$ is proportional with the electric field $\boldsymbol{E}$ [2]. Dielectric materials do not exhibit significant magnetic properties due to the way their electrons are arranged. As there are no unpaired electrons, these materials lack magnetic moments, which means that they are not magnetic and cannot align with an external magnetic field to produce magnetic dipoles [2,43]. The electric polarisation can be calculated by taking the electric field of the medium and subtracting the electric field of the vacuum which is given by [2]:

$$\boldsymbol{P} = \boldsymbol{E}\,(\epsilon - \epsilon_0) \tag{1.2}$$

where ϵ and ϵ_0 are the absolute permittivity in matter and vacuum respectively, that measure the ability of a dielectric to response to the electric field.

The speed of an electromagnetic wave in a medium v is determined by the following formula and is lower than the speed of the wave in a vacuum c:

$$v = \frac{1}{\sqrt{\epsilon\mu}} \quad \text{and} \quad c = \frac{1}{\sqrt{\epsilon_0\mu_0}} \tag{1.3}$$

where μ and μ_0 are the absolute permeability in matter and vacuum respectively.

The absolute index of refraction n is given as the ratio of the speed of an electromagnetic wave in a vacuum to that of the wave when it is passing through matter:

$$n = \frac{c}{v} = \sqrt{\frac{\epsilon\mu}{\epsilon_0\mu_0}} \tag{1.4}$$

The term "dispersion" refers to the relationship between the frequency f and the refractive index n. When the permeability of the magnetic field is negligibly, the relationship between $\boldsymbol{P}$, $\boldsymbol{E}$, and n will lead to the dispersion equation of the dielectric [2]:

$$n^2 = \frac{\epsilon}{\epsilon_0} = 1 + \frac{Nq_e^2}{\epsilon_0 m_e}\left[\frac{1}{\omega_0^2 - \omega^2}\right] \tag{1.5}$$

where N donating electrons per unit volume. q_e and m_e are electron charge and mass respectively. ω is the angular frequency, defined as $\omega = 2\pi f = 2\pi c/\lambda$. ω_0 denotes the resonance frequency.

1.2.1.2 Optical fibre mode

After the invention of the laser, optical fibre became one of the most significant advances in photonics [22]. Optical fibres utilise the speed of light for long-distance data transmission within a fibre material and it is one of the earliest uses within the field of photonics [29]. Optical fibres can be manufactured in different shapes, whereas cylindrical is the most common [43–45].

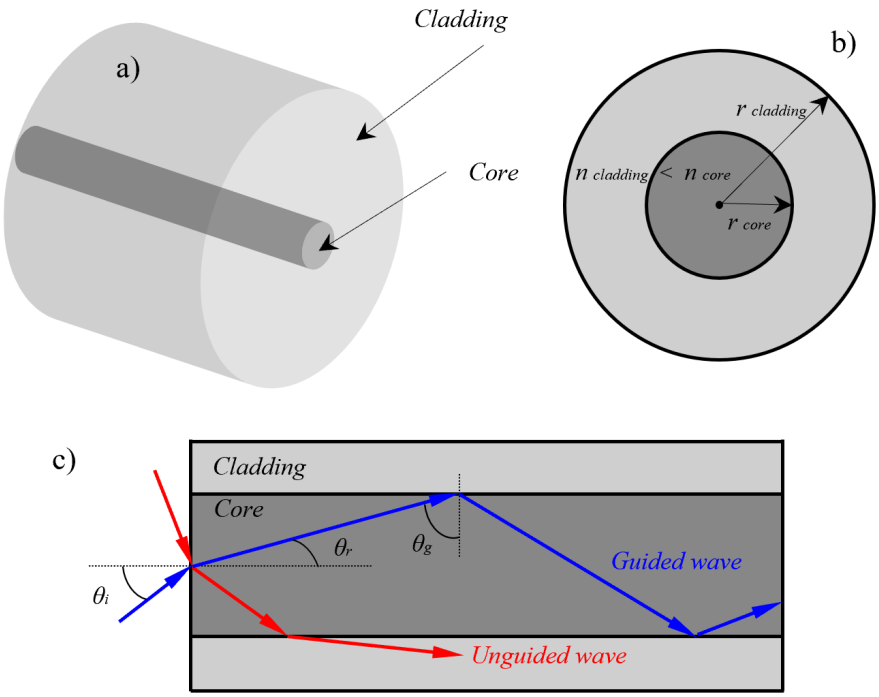

Figure 1.3 (a) The schematic of a cylinder optical fibre illustrates when the core cylinder is covered by cladding cylinder. (b) The parameters of the cylinder optical fibre of its refractive index and radius are shown. (c) The total internal reflection of light within the core of an optical fibre is displayed. The blue arrow indicates a guided wave within the core for which the incidence angle θ_g is greater than the critical angle θ_c. The red arrow represents an unguided wave with an incidence angle θ_g smaller than the critical angle θ_c.

The cylindrical fibre consists of two cylinders, a core and cladding. The core cylinder is surrounded by the cladding cylinder. This shape is illustrated in Fig. 1.3 a. The cladding

cylinder has a larger diameter than the core cylinder, although the core has a higher refractive index Fig. 1.3 b.

The idea behind optical fibres relies on the use of a process known as total internal reflection of light within the core [43]. When light is transmitted through the core of an optical fibre, it travels through the centre of the core and strikes the cylindrical edges of the core at different angles, depending on the refractive index of the core and cladding materials, as shown with blue arrow in Fig. 1.3 c. According to the Snell's law, when the angle of incident light θ_g is greater than the critical angle θ_c, light is completely reflected and stays contained within the core of an optical fibre. The critical angle θ_c is defined as the incidence angle that produces a refraction angle of 90 degrees.

Multi-mode fibre and single-mode fibre are two of the optical fibre types, as shown in Fig. 1.4 a,b. The wavelength λ, the core radius of the optical fibre, and the numerical aperture are the three pieces of information that must be known in order to calculate the number of modes contained in an optical fibre [43]. The V_{number} (normalized frequency) is a useful fibre parameter that can be used to indicate the number of modes at a given wavelength and cut-off (λ_c) conditions. λ_c is defined as the shortest wavelength that can form a single mode. V_{number} depends on these three variables as shown in the equation below [43]:

$$V_{number} = 2\pi \, NA_f \, \frac{r_{core}}{\lambda} \tag{1.6}$$

where NA_f is numerical aperture of the fibre, r_{core} is the radius of the core, and λ is the operator wavelength. The Eq. 1.6 will be employed in chapter 2 for Fig. 2.7 and in chapter 4 for Fig. 4.12 (a). The value of the NA_f represents the ability of the optical fibre to gather light and is given for an optical fibre by [2,43]:

$$NA_f = \sqrt{(n_{core})^2 - (n_{cladding})^2} \tag{1.7}$$

In chapter 2, the Eq. 1.7 will be used for the design of Fig. 2.7. When the value of V_{number} increases, the number of modes also increases [43]. When V_{number} falls below < 2.405, a single mode is created in an optical fibre. This shift from multi modes to a single mode is known as λ_c (cut-off). When the wavelength is reduced below λ_c, several modes are formed according to the formula below [46]:

$$\lambda_c = 2\pi \, NA_f \, \frac{r_{core}}{V_c} \tag{1.8}$$

where V_c is the cut-off number (V_c = 2.405). The Eq. 1.8 will be applied in chapter 2 for Fig. 2.7 and Fig. 2.10, as well as in chapter 4 for Fig. 4.1.

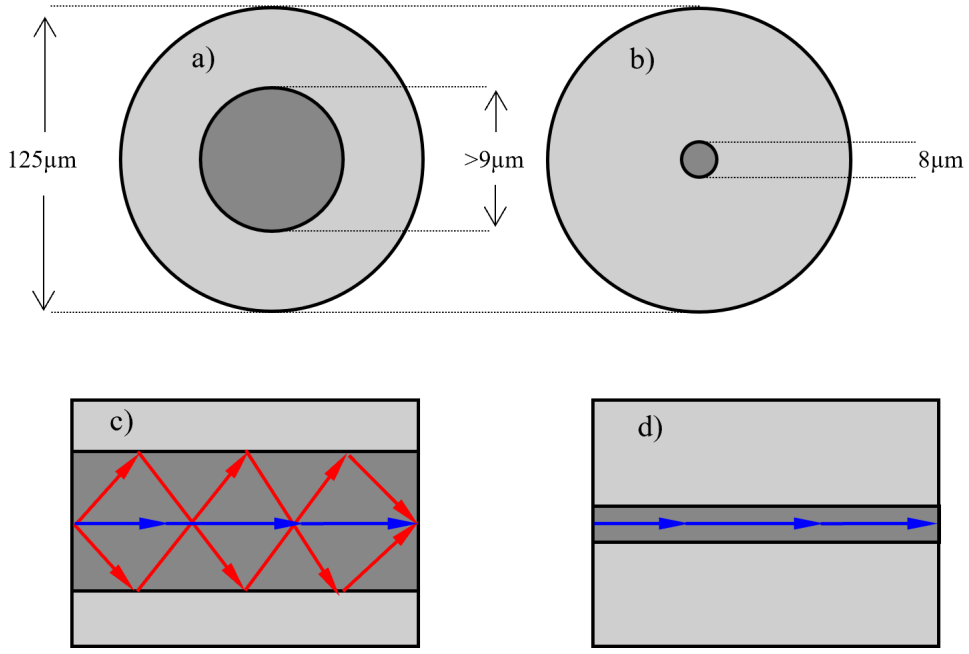

Figure 1.4 (a) A multi mode optical fibre with a core diameter of more than 9 µm is displayed. (b) A single mode optical fibre with a diameter of the core 8 µm. Both (a,b) have the same diameter of the cladding 125 µm. (c) and (d) show the side cross section of both multi mode and single mode, respectively.

The cladding diameter of both single mode and multi mode is approximately 125 µm as shown in Fig. 1.4 a,b. The diameter of the single mode core typically ranges between 2 and 9 µm, whereas the diameter of the multi mode core is larger than that. Due to the narrow diameter of the single mode core, only one mode can travel through to the central axis [2]. When a single mode is present, it can be described by a Gaussian beam profile. This profile characterizes the power distribution carried by the wave, with the highest power located at the centre of the beam and gradually decreasing towards the edges as shown Fig. 1.4 d [47]. However, in multi mode fibres, various modes can travel through the fibre. This is due to the larger core diameter and numerical aperture values of multi mode fibres compared to those of single mode fibres. As a result, multi mode fibres can support a greater range of angles of incidence, allowing for the propagation of multiple modes with different beam profiles as shown Fig. 1.4 c. When operating within a range of 10 km or less and when the quality and form of the beam are not particularly important, multi-mode optical fibre is a suitable option [43].

Fig. 1.5 depicts the normalized propagation constant b as a function of V_{number} for optical fibres with various modes. These modes are represented by hybrid symbols, HE_{mn} and EH_{mn}, which correspond to modes with dominant magnetic and electric fields, respectively. The fibre also supports transverse electric and transverse magnetic modes (TE_{0n} and TM_{0n}). The

azimuthal mode number ($_m$) dictates angular variations around the circumference of the fibre, while the radial mode number ($_n$) determines radial variations from the centre to the outer edge. Among these symbols, HE_{11} specifically denotes the single mode, which is the fundamental mode [43,48,49]. If the V_{number} is increased to a value greater than 2.405, the optical fibre will start to generate multi modes. When the V_{number} is 5, for instance, seven different modes are supported by the fibre. The parameter b is given by [43]:

$$b = \frac{n_{eff} - n_{cladding}}{n_{core} - n_{cladding}} \tag{1.9}$$

where n_{eff} is the effective index or mode index that has physical value in determining the speed of light in an optical fibre. Typically, its value lies between n_{core} and $n_{cladding}$.

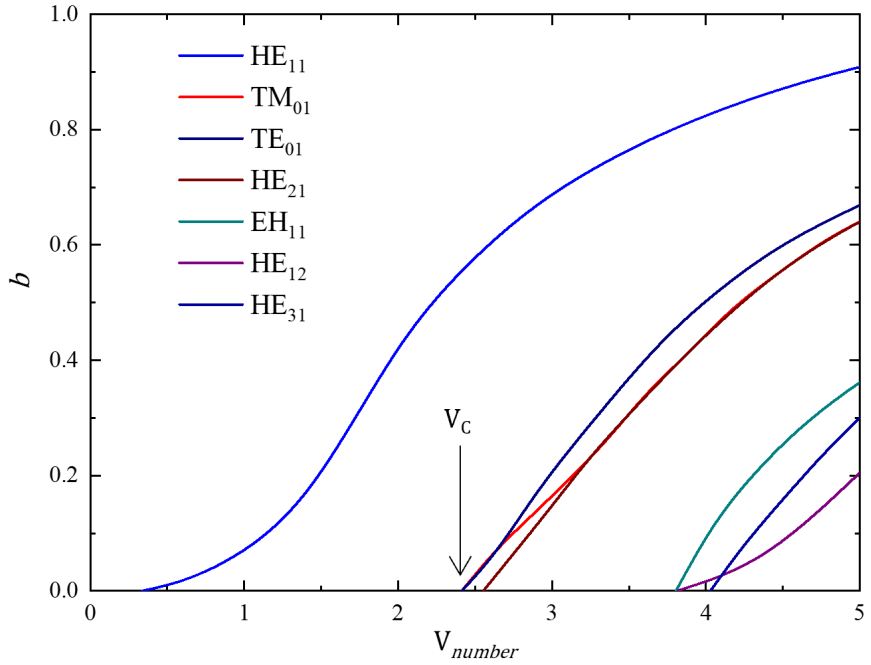

Figure 1.5 b as a function of V_{number} with regard to a few of low-order fibre modes [43].

1.2.1.3 Dispersion of an optical fibre

The variation in the speed of electromagnetic wave pulses that travel through an optical fibre, which causes the pulses to separate widely gradually, can be used to evaluate dispersion in the fibre [43]. There are two types of dispersion that can occur in an optical fibre: intermodal and intramodal [50]. In intermodal, the difference is between the different velocities v of the modes can occur, leading to delays in multi-mode optical fibre. To simplify the case, the modes take different paths ΔL, and the distance travelled influences the arrival time, causing delay ΔT. The delay is given by the following equation using the propagation velocity [43]:

$$v = \frac{c}{n_{core}} = \frac{\Delta L}{\Delta T} \quad \rightarrow \quad \Delta T = \frac{L\,(n_{core})^2}{c\,n_{cladding}}\,\Delta \tag{1.10}$$

where Δ is index difference and given by:

$$\Delta = \frac{n_{core} - n_{cladding}}{n_{core}} \tag{1.11}$$

In intramodal, dispersion can apply to the single mode optical fibre "chromatic dispersion". Chromatic dispersion is a result of the different wavelengths of light travelling at different speeds, which causes the optical signal to spread out or dispersion [50]. The dispersion in optical fibre is determined by the material properties as well as the geometry [43]. The total dispersion parameter D can be determined by combining the material dispersion D_M and waveguide dispersion D_W, where D_M is dependent on material properties and D_W is dependent on both material properties and the waveguide geometry [43]:

$$D = D_M + D_W \tag{1.12}$$

Except for vacuum, which is characterized by no dispersion, all other mediums exhibit some degree of dispersion [2]. The group index n_{g} describes the speed of light pulse travels through an optical fibre. The ratio of the speed of light in a vacuum c to the group velocity v_{g} in an optical fibre is referred to as the n_{g} where the value of v_{g} can be expressed as the ratio of the length of the optical fibre to the time delay produced by different wavelengths while travelling through the optical fibre [2]:

$$n_{\mathrm{g}} = n - \lambda\frac{dn}{d\lambda} \tag{1.13}$$

where n is the refractive index of the medium. Calculating the derivative of the n_{g} with respect to wavelength provides the dispersion of a material D_M [43]:

$$D_M = \frac{1}{c}\,\frac{dn_{\mathrm{g}(cladding)}}{d\lambda} \tag{1.14}$$

where $n_{\mathrm{g}(cladding)}$ is the group index of refraction in the cladding of an optical fibre. The contribution of D_W to the D is determined by fibre characteristics and the index difference Δ [43]. Since D_W is depended on V_{number}, it depends on the size of the core (geometry) and the refractive index (material properties) and is given by [43]:

$$D_W = -\frac{2\pi\Delta}{\lambda^2}\left[\frac{(n_{g(cladding)})^2}{n_{cladding}\,\omega}\,\frac{V_{number}\,d^2(V_{number}\,b)}{dV_{number}{}^2} + \frac{dn_{g(cladding)}}{d\omega}\,\frac{d(V_{number}\,b)}{dV_{number}}\right] \quad (1.15)$$

Fig. 1.6 depicts the parameters D_M and D_W, as well as their sum D, for a standard single-mode fibre, where Δ represents the quantity $\Delta = 5 \times 10^{-3}$. In optical communication systems, the primary effect of D_W is to shift the zero-dispersion wavelength (λ_{ZD}) by approximately 30 to 40 nm, aiming to achieve zero total dispersion (D) around 1310 nm. Within the wavelength range of 1300 to 1600 nm, which is crucial for optical communication, this adjustment also reduces D from its D_M value. Around 1550 nm, the average values of D typically range from 15 to 18 ps/(km-nm), where ps represents pulse spreading over a spectral width of 1 nm and propagating through 1 km of the fibre. This wavelength range is particularly significant in lightwave systems due to the low fibre loss near 1550 nm. In addition, the core radius of an optical fibre is r_{core} = 4 μm; we employ this value for the purposes of this thesis [43].

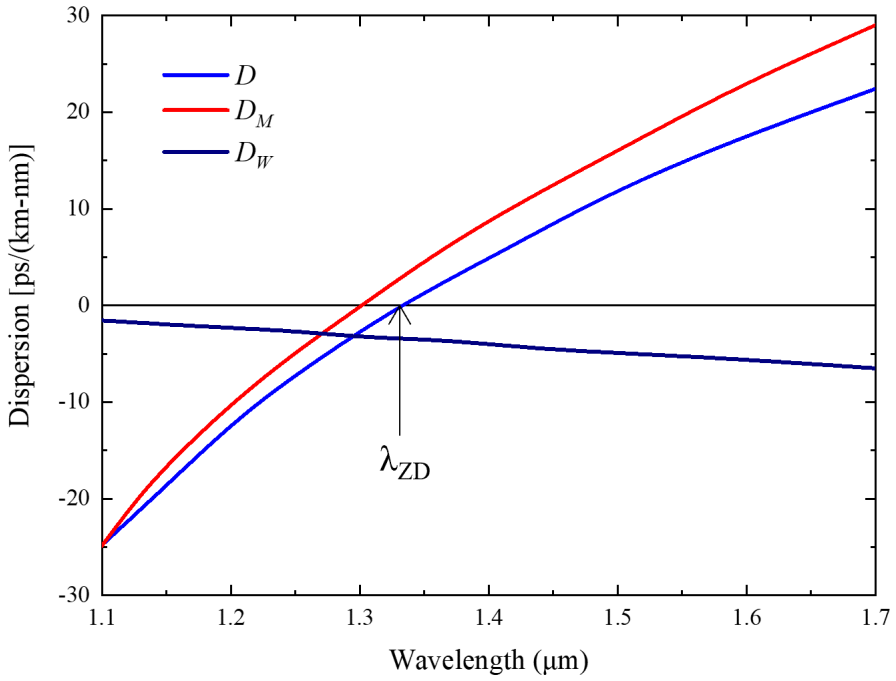

Figure 1.6 Total dispersion and the factors relating of material dispersion and waveguide dispersion for a standard single-mode fibre [43].

1.2.2 Optical microscopy

One of the oldest and most well-known types of imaging technology is the optical microscope, which is usually made up of various lenses [2,51]. Based on the number of lenses, the optical microscope can be divided into two categories: a simple microscope (one lens) and a compound microscope (more than one lens) [3]. The compound microscope is more

commonly used than the simple microscope because it provides a higher level of magnification for the image. Fig. 1.7 shows one type of the compound microscope, which has both an eyepiece and an objective lens. The sample to be imaged is positioned at the focal length *FL* of the objective lens. The image created by the objective lens is placed at the *FL* of the eyepiece, which amplifies it. Since the eyepiece magnifies the image, some compound microscopes have many eyepieces to achieve a larger magnification.

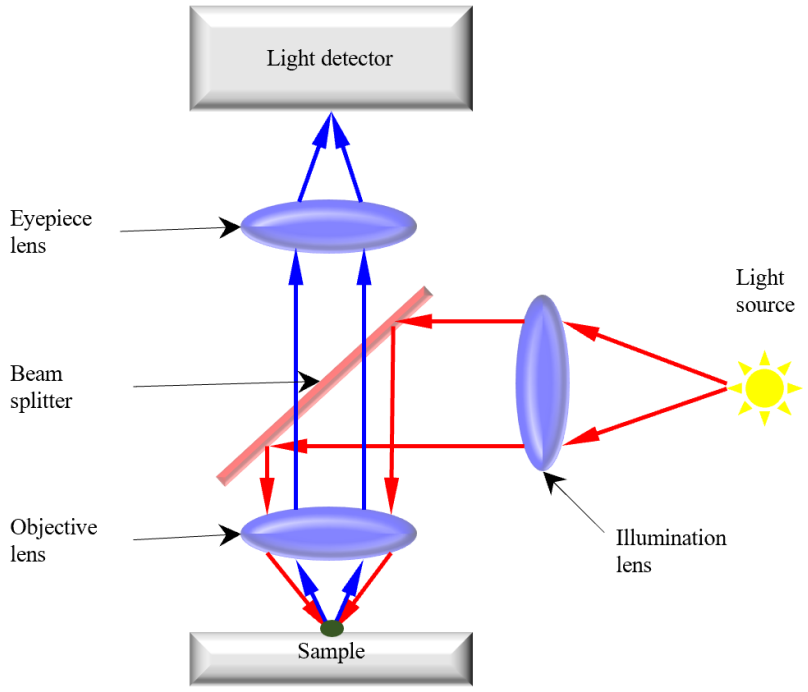

Figure 1.7: The schematic shows the fundamental principle of the compound microscope. The red arrows representing the incident beam from the source to the sample and the blue arrows representing the beam reflected from the sample to the light detector [51].

The examination of small particles is made possible by the use of a magnifying optical microscope [51]. Because of this, it has a wide range of applications in a variety of areas that need the analysis of small samples such as cell biology, chemistry, and physics [52–54]. Within the optical spectrum, the near infrared, visible, and ultraviolet spectral ranges are the most frequently employed for optical microscopy [38,52,54]. The resolution of the images is limited by the diffraction limit, which will be explained in 1.3; image resolution is one of the challenges associated with optical microscopy. As a consequence of this, it is challenging to get a clear picture of images of particles with a size of less than 200 nm when employing methods such as visible light [55–57]. In the following sections, we will talk about the diffraction limit as well as a few applications that try to improve spatial resolution.

1.3 Diffraction limit of electromagnetic waves

Improving the resolution of nanoparticle images in imaging systems is challenging due to a phenomenon known as the diffraction limit of electromagnetic waves [1]. The factors that have the greatest impact on the spatial resolution are the wavelength in the medium λ_m and the numerical aperture of an imaging systems [1,58]. The numerical aperture of an optical microscope system NA_{mic} is given by [1]:

$$\mathrm{NA}_{mic} = n_m \, sin\theta_h \tag{1.16}$$

where n_m is the refractive index of the imaging medium that λ_m travels though it and θ_h is the half-angle of the light that collected from the sample under the objective lens as shown in Fig. 1.8.

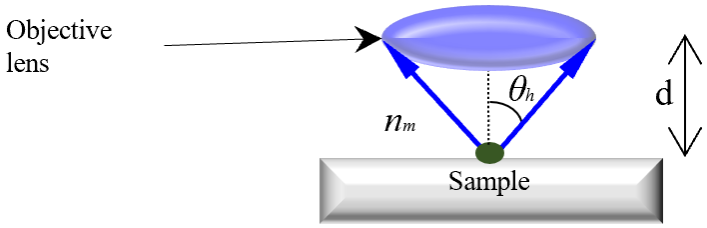

Figure 1.8: The numerical aperture parameters of an optical microscope together with the distance d between the objective lens and the sample are shown [51].

The Abbe resolution formula is one approach to calculate the diffraction limit of electromagnetic waves for optical microscopy systems which is given by [59]:

$$Abbe\ resolution = \frac{\lambda_m}{2\, n_m \, sin\, \theta_h} \tag{1.17}$$

The Eq. 1.17 indicates that in order to reduce the diffraction limit, either a short wavelength or an increase in numerical aperture is required. From Fig. 1.8, when the sample is positioned close to the objective lens by decreasing the distance d, the θ_h can be adjusted until it approaches 90 degrees and $sin\ \theta_h$ can be set to 1 in Eq. 1.17. This adjustment effectively enhances the ability of rays emitted by the sample to penetrate into the objective lens, resulting in improved resolution [47].

The Rayleigh and Sparrow criteria are two commonly used methods for calculating the spatial resolution of an optical system by measuring the spot size [60]. In order to calculate the spatial resolution, Rayleigh performs a measurement of the distance between the centre of the spot that represents the diffraction limit and the position of the first zero of the power distribution. Sparrow determines the spatial resolution of a spot by measuring the full width at

half maximum (*FWHM*) of a spot. The *FWHM* refers to the distance along the transversal axis of the spot at which the power distribution has lost half of its highest value as shown in Fig. 1.9 [61]. This thesis uses the *FWHM* measurement for all of the focal spots since it is the method with the highest accuracy and the easiest method to apply when compared to the criterion of Rayleigh for calculating spatial resolution [60].

It is possible to separate the electromagnetic waves that were emitted by the sample into two ranges: the far field and the near field. The properties of a sample image can be found in both of them. The far field wave that was emitted from the sample travels to the objective lens, bringing with it some properties of the image. However, the near field wave vanishes after travelling a short distance after exiting the sample, and it may not reach the objective lens. The boundary between the near field and far field depends on factors such as the wavelength of light and the size of the aperture or diffracting object, depending on the case [62,63]. Some applications can benefit from the use of near field imaging and achieving high spatial resolution such as near field scanning optical microscopy, superlenses, and PNJ [64–66]. The topics of superlenses and PNJ will be discussed in the following two sections with a primary focus on PNJs as the central theme of this thesis.

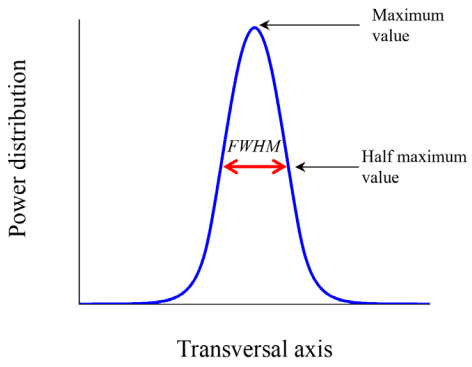

Figure 1.9: Schematic showing the calculation of FWHM [61].

1.4 High spatial resolution devices

This section explores two topics: lenses and PNJs. We investigate the topic of lenses and their applications, such as superlenses, as well as the interesting phenomenon of PNJs and their potential applications in a variety of fields.

1.4.1 Lenses

Lenses have played a significant role in optical systems, operating as transparent materials with curved surfaces that modify the behaviour of light. They have the ability to refract or bend light beams, hence enabling light to converge or diverge. This characteristic allows lenses to

focus properly and magnify images. Lenses can be found in a variety of optical devices, including cameras, telescopes, microscopes, and eyeglasses. The operation of these lenses is based on the refraction process to provide the desired visual effects [2].

Despite the great abilities of conventional lenses, they are constrained by diffraction limit which restricts the resolution they can achieve. As technology and scientific understanding have progressed, the need for higher resolution imaging has forced the development of new types of lenses that are capable of overcoming these diffraction limits.

The introduction of superlenses has fundamentally transformed the abilities of optical systems. Unlike conventional lenses, superlenses utilise the interesting subwavelength imaging concept. This phenomenon enables them to overcome the limitations imposed by the diffraction limit, which has limited the resolution of conventional optical systems [65]. Superlenses achieve this by utilising metamaterials, which have unique subwavelength structures and artificial materials. These artificial materials enable superlenses to exceed the limitations of conventional lenses and achieve high spatial resolutions. They have become an essential element in manipulating the propagation of electromagnetic waves. The first research of metamaterials primarily focused on structures that possessed both negative permittivity $(-\epsilon)$ and negative permeability $(-\mu)$ [67–69]. This was done because structures that exhibited negative refractive index $(-n)$, were considered to have a great deal of application potential in subwavelength optics since they offered the possibility of overcoming the limits imposed by the diffraction limit [70].

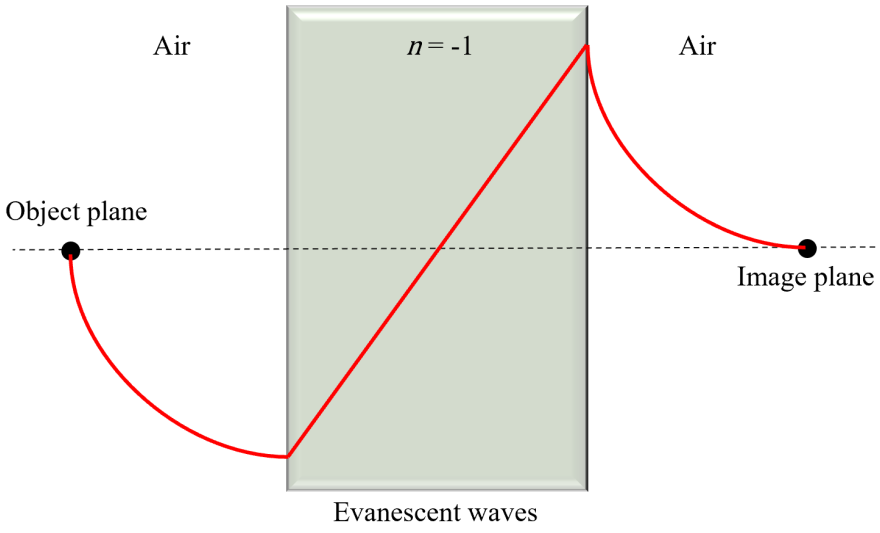

Figure 1.10: Negative index material can amplify evanescent waves across the lens, so the amplitude of evanescent waves at the object and image planes are same [65].

For materials with a positive refractive index, the strength of the evanescent field decreases exponentially, and some of the image data in the evanescent field cannot be captured; however, when using materials with a negative refractive index, the image data in the evanescent field can be captured [2,71–73]. When a lens made of negative index media is placed in close proximity to an emitted object, as shown in Fig. 1.10, the near field evanescent waves have the potential to be considerably inverted all the way through the lens and the reason is that the phenomenon of reflection of Snell's law has been inverted [65,74]. Fig. 1.10 is an illustration of one example of a superlens, the benefit of which relies in its ability to overcome the diffraction limit by maintaining image data in the near field [65,75].

1.4.2 Photonic nanojet (PNJ)

PNJs have made significant contributions to imaging and sensing devices due to their demonstrated ability to detect subwavelength particles [66,76–83]. PNJs can be characterized as the near-field focal spot of a high-intensity electromagnetic wave created at the output surface of a dielectric when it is illuminated by a planewave [66].

In 2004, Z. Chen et al. reported on the utilization of a planewave with a wavelength of 500 nm to illuminate a dielectric cylinder, with a diameter of ten wavelength and a refractive index of 1.7, surrounded by air [66]. After generating the focusing spot at the output surface of the dielectric cylinder, they demonstrated that this PNJ had a *FWHM* of the intensity distribution along the transversal axis smaller than the diffraction limit (less than half a wavelength). The high resolution of PNJs is a result of constructive interference between refracted light on the front surface of the dielectric, which converges the beam to a focusing spot smaller than the diffraction limit [84–86].

The interesting result of PNJs is that they can propagate along the propagation axis for a greater distance than one wavelength without significant diffraction and without involving evanescent waves [87]. Evanescent waves are the near-field components of an electromagnetic wave that decay exponentially with distance from the source [2]. However, in the case of PNJs, they remains confined within the near-field region while continuing to propagate along the incidence axis without significant diffraction [66,88–91].

The size range of the cylinder or sphere dielectrics used to generate PNJ is approximately between 2 λ and 40 λ, where λ is the operator wavelength in freespace [88,92]. A small dielectric with size $<< \lambda$ instead of acting as a small lens, it scatters light [93]. As PNJs have the ability of producing high spatial resolution, having a focal spot with high intensity, and detecting subwavelength particles, multiple studies have employed PNJs in various dielectric shapes such

as spheres, cylinders, cuboids, triangles, ellipses, and non-symmetrical dielectrics [94–100]. Some applications, such as microscopy, imaging of subwavelength particles, Raman spectroscopy, sensing of a single molecule, and medical surgery, have benefited from the use of PNJs [55,56,86,101–103].

PNJs utilizing dielectrics offer promising opportunities, however a challenge is their design as free-standing structures with air as the background medium, limiting their practical applicability. However, an efficient approach to address this challenge involves creating PNJs from optical fibres [85,104–108]. This technique eliminates the requirement for free-standing dielectrics and enables free control of the PNJ's location through mechanical or manual positioning of the entire structure. As a result, the need for free-standing designs is relaxed. Various techniques such as dielectric waveguides, shaped optical fibre tips, core-shell, and graded index techniques have been investigated, showing improved performance of PNJs compared to those generated using planewaves [100,104–106,109–112].

Using a single mode optical fibre is crucial for eliminating higher modes within the fibre [113], as these modes can negatively impact the overall response of the generated PNJ. For instance, in PNJs created with tip-ended optical fibres, higher modes have been found to cause the maximum intensity outside the fibre to shift off-axis [105]. To address this, we selected a single mode optical fibre that operates at telecommunication wavelengths (λ_0 = 1.55 μm). This specific wavelength holds significant importance due to its low fibre loss at 1.55 μm [43].

The refractive index of the dielectric plays a critical role in determining the spatial resolution of PNJs. According the literature, PNJs can be produced at the output surface of a dielectric illuminated with a planewave when the ratio between the refractive index of the dielectric and the surrounding background medium should be less than two [88,93,114–119]. However, recent studies have demonstrated that this condition can be relaxed by utilizing hemispherical high-index dielectrics [94]. The profile of high-index cylindrical (2D) or spherical (3D) dielectrics can be truncated by employing techniques similar to those used in solid immersion lenses, such as the Weierstrass formulation as will be discussed in section 2.2.2. The solid immersion lenses are made with a high refractive index to enhance the resolution of imaging systems [120]. When these designed structures are illuminated by a planewave, they can generate high intensity PNJs near their output surface, opening new opportunities for applications that require high spatial resolution.

The motivation for this thesis is to exploit the advantages of generating PNJs, which have the ability to produce high spatial resolution and have a high-intensity focal spot, by using

optical fibres, which eliminates the need for free-standing dielectrics. To achieve this goal, a dielectric with a high refractive index is placed at the end of a single mode optical fibre. Subsequently, the dielectric is truncated at its output surface, enabling to generate the desired high spatial resolution PNJ at the output surface of the dielectric. The impact of PNJ properties on *FWHM* resolution, *FL* position, depth of focus (DoF), and power enhancement will be the main focus. The proposed device holds potential applications in scenarios where high spatial resolution is critical, particularly in imaging and sensing systems operating at telecommunication wavelengths.

Chapter 2 Key aspects of PNJs, methods and materials

This chapter provides the literature review of PNJs and the methods and materials utilised to create the structure. It studies the influence of incident wavelength and dielectric sizes on PNJ performance, emphasising the impact on spatial resolution, *FL* position, DoF, and power enhancement. Additionally, this chapter analyses the effect of the dielectric refractive index on the production of PNJs. Furthermore, the use of single mode optical fibres, high refractive index dielectric materials, and simulations conducted with CST Studio Suite and COMSOL Multiphysics for accurate and efficient design are discussed.

2.1 Literature review of PNJs

PNJs have developed as an interesting field of photonics research, with promising applications in high resolution imaging [121,122]. These localised light fields are generated when incident light interacts with dielectric to form a high-intensity electromagnetic wave focal point. Understanding the key parameters affecting PNJ performance, such as incident wavelength and dielectric sizes, as well as the refractive index of dielectric, is important for developing and optimising their performance [123].

The influence of incident wavelength and dielectric sizes on the properties of PNJs is discussed below in section 2.1.1. The incident light wavelength is a significant factor in determining the spatial resolution of PNJs. The diffraction effects can be minimised by using shorter wavelengths, leading to higher resolution imaging [124]. Moreover, the size of the dielectric also influences PNJs. The *FWHM* of the PNJs increases as the dielectric diameter increases, affecting image resolution. Additionally, as the dielectric diameter increases, the *FL* moves away from the surface of the dielectric to the freespace, the DoF expands, and the power enhancement of PNJs also increases [125].

We examine the influence of the dielectric index on PNJs in section 2.1.2. The refractive index of both the dielectric and the surrounding background significantly influences the properties and performance of PNJs. The performance of PNJs can be broken down into three sections based on the refractive index of the dielectric ratio to that of the background [78,93–95,114,122,126–128]. When the refractive index of the dielectric is less than that of the background, there is no *FL* formed outside the dielectric. For a refractive index ratio between 1 and 2, *FL*s are located around one wavelength from the output surface of the dielectric. In

contrast, the *FL*s will be generated inside the dielectric when the ratio of the index of refraction of the dielectric to that of the background is greater than 2 [93]. By using high refractive index dielectric materials and truncating them, this thesis enables us to examine the possibility of creating PNJs with a high spatial resolution.

Finally, we perform simulations using parameters from the literature review in section 2.1 and discuss the results to confirm their accuracy and validity. We do not directly take results from other papers. We conduct all simulations using CST Studio Suite, utilizing parameters found in the literature review, and provide references accordingly.

2.1.1 Effect of incident wavelength and dielectric sizes

PNJs can be generated across a wide range of wavelength in the electromagnetic spectrum [129]. The wavelength of the generated PNJs is one of the variables that can impact spatial resolution because shorter wavelengths reduce diffraction effects, resulting in higher resolution imaging. The Abbe resolution in Eq. 1.17 discusses how the wavelength affects the diffraction limit. Additionally, it is important to note that other parameters in Eq. 1.17, such as the numerical aperture, also affect the diffraction limit [129–131].

The first study on PNJs by Z. Chen et al. has discussed that the spatial resolution of the PNJs changes when a planewave with a changing wavelength illuminates a dielectric cylinder [66]. In that work, the ratio between the diameter of the dielectric cylinder and the wavelength of the incident planewave was found to be constant between the two sizes of dielectric cylinders as shown in Fig. 2.1 a,b. Accordingly, when the first diameter (d_1) of a dielectric cylinder is 5 μm and the second diameter (d_2) is 6 μm, the first size of the dielectric cylinder (d_1) is illuminated with a wavelength (λ_1) of 250 nm. The second size of the dielectric cylinder (d_2) is then illuminated with a wavelength (λ_2) of 300 nm. The ratio between the two dielectric cylinder sizes and their corresponding wavelengths remains constant at 20 [66].

The ratio of the refractive index of the dielectric n_d to the refractive index of the background n_b that surrounds it, given as $n_d/n_b = 1.75$, was kept the same in all of the dielectrics in Fig. 2.1. This was done so that the PNJ would continue to be located at the output surface of the dielectric cylinder [129]. More information regarding the refractive index ratio can be found in section 2.1.2.

Fig. 2.1 a,b illustrates the influence of incident wavelength on spatial resolution for two dielectric cylinders. The *FWHM* of the intensity along the transversal axis of the PNJ increases from 120 nm to 130 nm as the incident wavelength increases from $\lambda_1 = 250$ nm to $\lambda_2 = 300$ nm [66]. This indicates that a shorter wavelength should be utilised to improve spatial resolution.

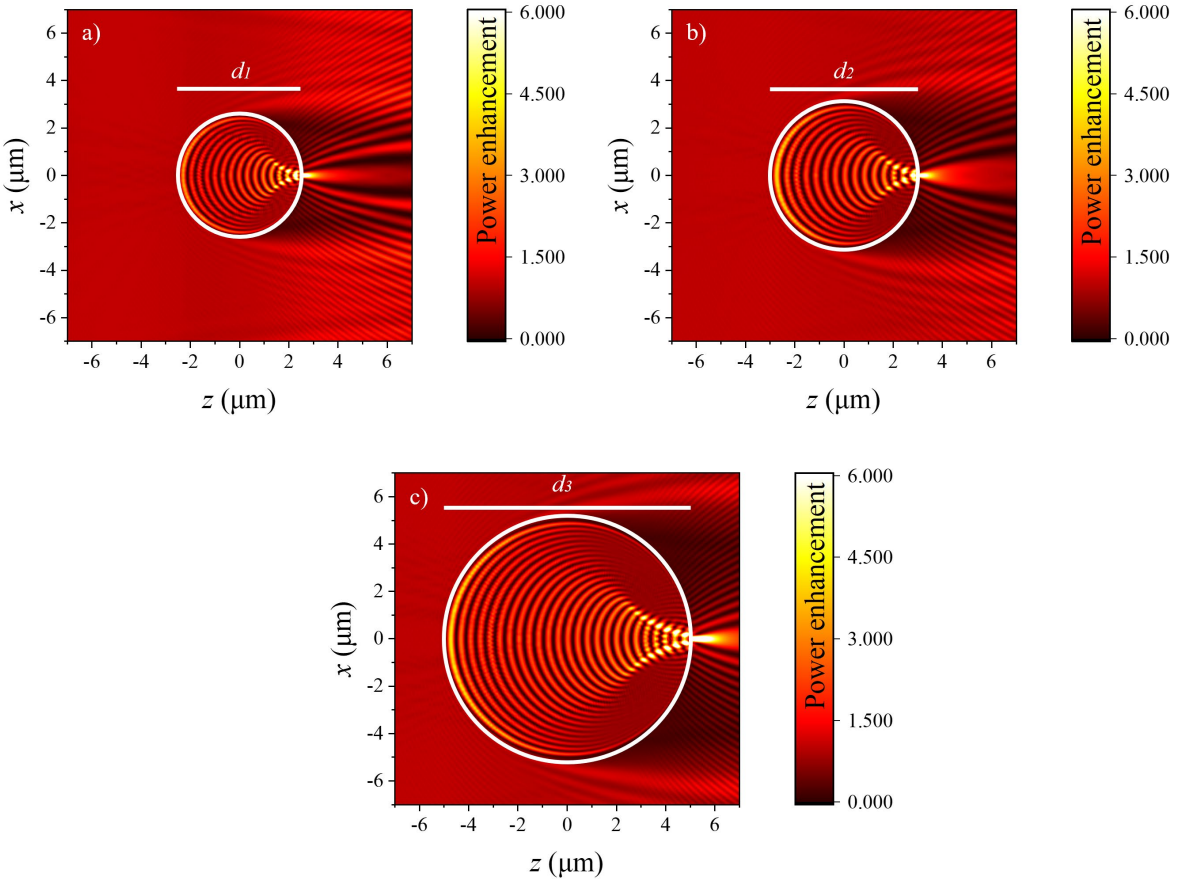

Figure 2.1: The CST Studio Suite is utilised to simulate the structure in which the generated PNJ is located at the output surface of the 2D dielectric cylinder. The simulation represents the power enhancement in the xz plane, where the magnetic field polarized along the x axis with propagation along the z axis. The centre of all dielectric cylinders is at x = z = 0. The ratio of the refractive indexes n_d / n_b = 1.75 for all of them with (a) d_1 = 5 µm and λ_1 = 250 nm, (b) d_2 = 6 µm and λ_2 = 300 nm, and (c) d_3 = 10 µm and λ_2 = 300 nm. The values for the parameters above are obtained from a corresponding reference [66].

The impact of the dielectric diameter on the PNJ was analysed as part of the same study that focused on the dielectric cylinder [66]. After determining that n_d/n_b should be set to a value of 1.75 in order to preserve the location of the PNJ at the output surface, the diameter of the dielectric was increased from d_2 = 6 µm to d_3 = 10 µm while the incident wavelength was constant at λ_2 = 300 nm as shown, respectively, in Fig. 2.1 b,c. Fixing the incident wavelength by changing the dielectric diameter is equivalent to fixing the dielectric diameter while changing the incident wavelength [132,133]. When the dielectric diameter was increased from d_2 to d_3, an increase in the *FWHM* was observed, with the result being a value of 140 nm rather than 130 nm [66]. A larger dielectric enables more light waves to contribute to the formation of the PNJ [76]. As a result, the PNJ formed has a larger diameter, resulting in a larger *FWHM*. It is important to mention that several parameters, such as the wavelength, the shape and size of the dielectric, and the refractive index of the dielectric, can also affect the properties of the PNJ [128].

Not only does the diameter of the dielectric cylinder have an impact on the spatial resolution, but it also has an influence on the length of the PNJ [134]. The DoF is the length of the PNJ along the propagation axis, and it is measured as the distance at which the power enhancement at the *FL* decays to half of its maximum along the propagation direction [135,136]. When the diameter of the dielectric was increased from d_2 to d_3, the DoF of the PNJ expanded from 500 nm to 1000 nm [66]. The main cause of this phenomenon is that a dielectric surface with a larger radius of curvature generates more aberration [137]. Consequently, this larger aberration results in a longer extension of the PNJ length. In specific applications, such as PNJ etching and marking on semiconductors and metals, as well as for improving imaging performance by protecting the dielectric from contacting a specimen, DoF is a significant factor [104,135,138–141].

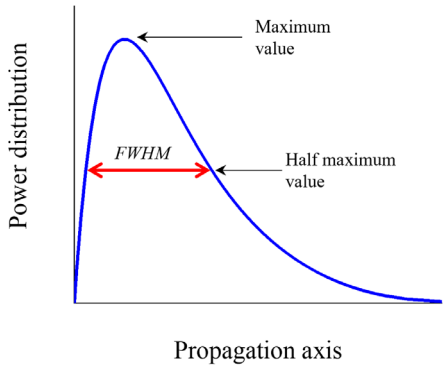

Figure 2.2: Schematic illustrating the calculation of DoF [135].

When a dielectric sphere is considered by Z. Chen et al. [76], the size of the dielectric sphere has an effect on the spatial resolution, the location of the *FL*, and the power enhancement, which is similar to the cylinders from Fig. 2,1, as expected. Fig. 2.3 a-d show dielectric spheres with diameters increasing in the following order: d_4 = 1 μm, d_5 = 2 μm, d_6 = 3.5 μm, and d_7 = 8 μm, respectively, that have been illuminated by a planewave with a wavelength of λ_3 = 400 nm. Additionally, the ratio of the index of refraction of the dielectric sphere and the index of refraction of the background that surrounds it is always the same: n_d/n_b = 1.59. Using $1 < n_d/n_b < 2$, the PNJ would generate at the output surface of the dielectric spheres, as will be discussed in section 2.1.2. In that work, the results demonstrated that as the diameter of the dielectric sphere increased, the *FWHM* also increased, becoming 130 nm, 150 nm, 190 nm, and 210 nm, respectively. Similar to the case of cylinders in Fig. 2.1 b,c as expected, the results in Fig. 2.3 demonstrated a correlation between the variables of dielectric sphere diameter and *FWHM*. Increasing the size of the dielectric allows more light waves to participate in forming the PNJ, leading to a larger *FWHM* [125]. The *FL* of the dielectric sphere

moves further away from the surface of the dielectric sphere and towards the freespace as the diameter of the dielectric sphere increases. In these studies, the n_d/n_b ratio was considered to be less than two in order to achieve *FL* outside of or at the output surface of the dielectric. Recent studies conducted with a dielectric that has a high refractive index in comparison to the background $n_d/n_b > 2$ have shown that *FL* shifts away from the output surface of the dielectric sphere and moves further inside the dielectric sphere as the diameter of the dielectric sphere increases [94]: such a difference in the refractive index compared to the background will be discussed in the following section. Lastly, an increase in the dielectric diameter can increase the power enhancement of the PNJs. This is because more light waves can contribute to the production of the PNJ as the dielectric size increases [137,142].

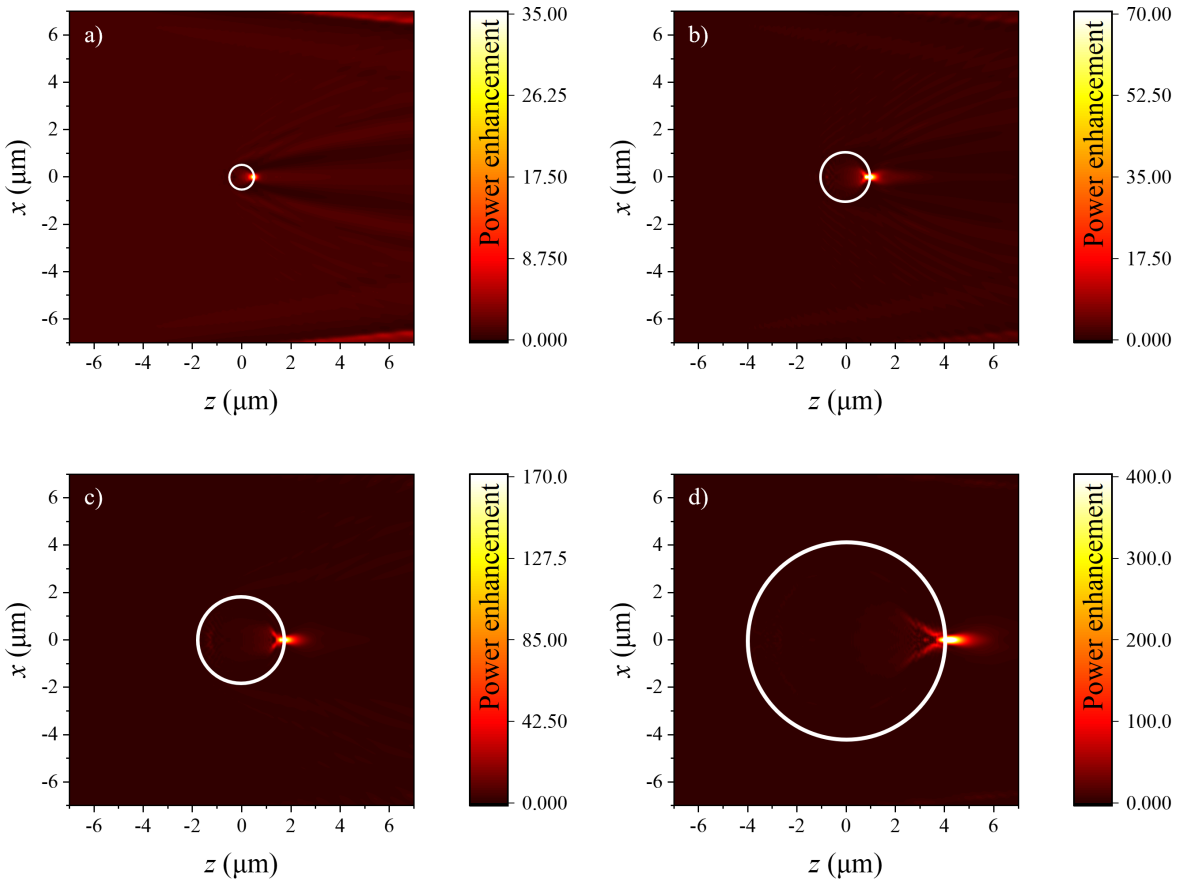

Figure 2.3: The CST Studio Suite is used to simulate the structure in which a dielectric sphere is used to generate the PNJ. The simulation represents the power enhancement in the xz plane, where the polarisation of the magnetic field is along the x axis and propagation is along the z axis. x = z = 0 is the centre of all dielectric spheres. The ratio of the refractive indexes $n_d/n_b = 1.59$ with $\lambda_3 = 400$ nm for all of them for diameter (a) $d_4 = 1$ µm, (b) $d_5 = 2$ µm, (c) $d_6 = 3.5$ µm, and (d) $d_7 = 8$ µm. The values for the parameters here were provided from the respective reference [76].

2.1.2 PNJs with different refractive index of dielectrics

The previous section 2.1.1 studied the properties of PNJs, such as *FWHM*, the position of *FL*, and the power enhancement, where the index of refraction of the dielectric and background

is given by ($1 < n_d/n_b < 2$); however, this section 2.1.2 focuses on the impact of the refractive index of the dielectric in the properties of the PNJs. The index of refraction of the dielectric and the background significantly affects the properties and performance of PNJs [126]. To achieve subwavelength light focusing and satisfy the properties of PNJs, it is important to locate PNJs on the output surface of the dielectric [143]. This positioning improves the efficacy of PNJs by permitting light waves to converge and generate a highly concentrated spot beyond the diffraction limit [127]. The investigation of refractive index of the dielectric can be broken down into three sections in order to find out where the *FL* is located; my thesis will use one of these sections when $n_d/n_b > 2$:

- The first section is when the index of refraction of a dielectric is less than that of the background. If the ratio of the refractive index of the dielectric material (n_d) to that of the surrounding background (n_b) is less than 1 ($n_d/n_b < 1$), no *FL* is generated outside the dielectric material [93]. The illustrated Fig. 2.4 depicts a dielectric sphere being illuminated from the left by a planewave. This simulation was generated using the CST Studio Suite simulation. To ensure consistency with the findings in references [126,128,144], the simulation parameters such as the dielectric sphere diameter, refractive index, and wavelength were all kept identical to the references. In Fig. 2.4 a, the wavelength is $\lambda_4 = 800$ nm, and the electric field is polarized along the *y* axis, while the magnetic field is polarized along the *x* axis, with the wave propagating in the *z* axis direction [144]. The diameter of the dielectric sphere is $d_8 = 5$ μm. Noting that the ratio of the refractive index is greater than one to observe the *FL* distance from the outer surface of the dielectric sphere. The refractive index ratio is $n_d/n_b = 1.096$, and the *FL* is determined outside the dielectric sphere and far from its surface at a distance of approximately 3.6 μm, as seen in Fig. 2.4 a.
- The second section is utilised when the ratio of the refractive index of the dielectric to the index of refraction of the surrounding background falls between 1 and 2 ($1 < n_d/n_b < 2$). Here the PNJs are found at a distance of approximately one wavelength from the output surface of the dielectric [77,78,145,146]. The distance between the PNJs and the output surface of the dielectric decreases when the ratio n_d/n_b increases [130]. For $n_d/n_b = 2$, PNJs are generated exactly on the output surface of the dielectric [93]. Fig. 2.4 b corresponds to the same setup as Fig. 2.4 a, with the difference that the ratio of the refractive index is $n_d/n_b = 1.45$ [144]. The setup in Fig. 2.4 c,d uses a wavelength of $\lambda_5 = 400$ nm and the diameter of the dielectric sphere is $d_9 = 2$ μm

[126]. In Fig. 2.4 c, the ratio of the refractive index is $n_d/n_b = 1.43$, while in Fig. 2.4 d, the ratio of the refractive index is $n_d/n_b = 1.59$. Using these parameters, the PNJs are generated, as in Fig. 2.4 b-d, just at the output surface of the dielectric sphere.

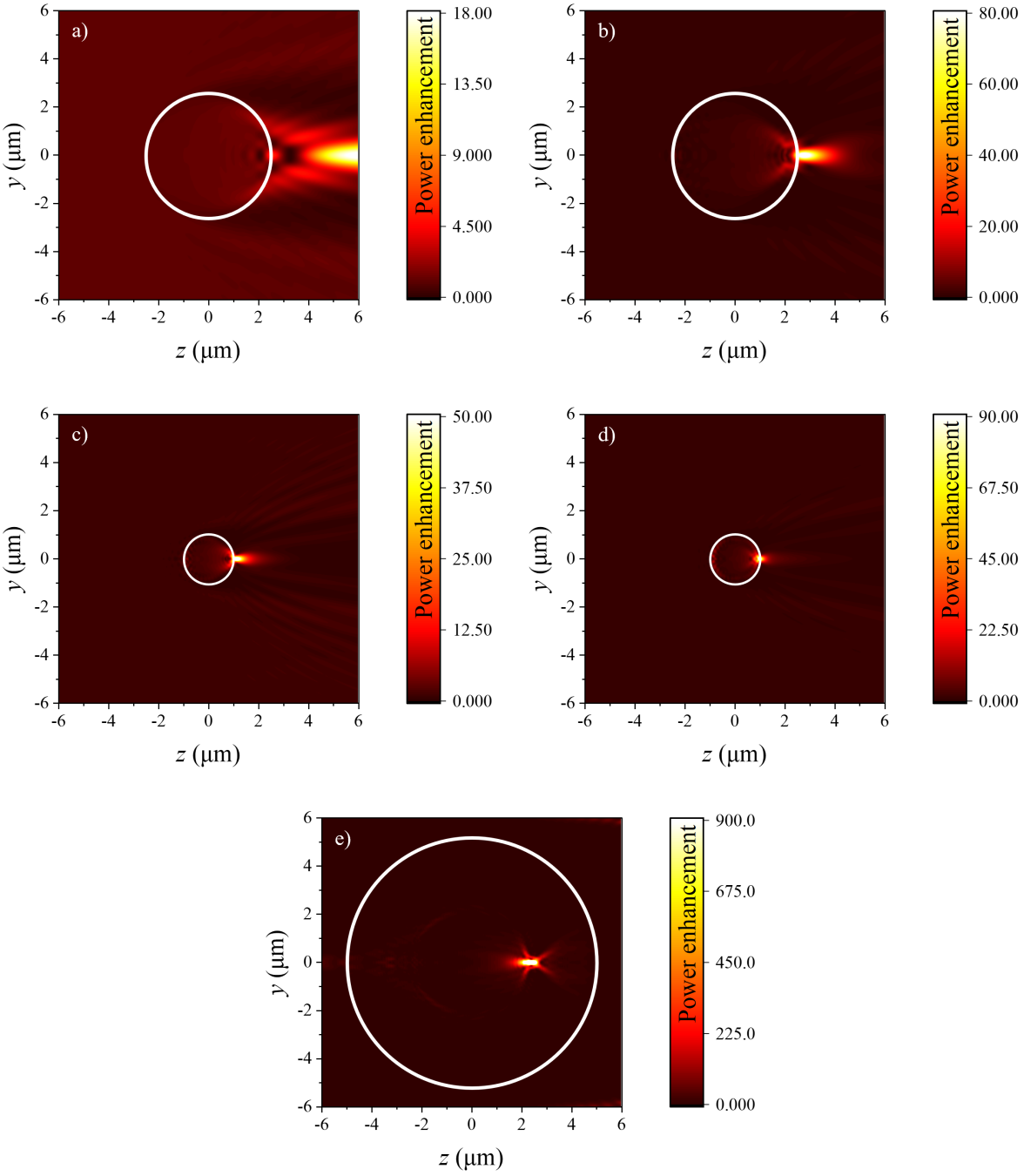

Figure 2.4: To demonstrate the location of the PNJ, a dielectric sphere illuminated by a planewave was simulated using the CST Studio Suite. The simulation represents the power enhancement in the yz plane, where the electric field is polarized along the y axis, and the propagation direction is along the z axis. The centre of all dielectric spheres is located at y = z = 0. The wavelength of (a) and (b) is λ_4 = 800 nm, and the diameter of the dielectric is d_8 = 5 µm. The refractive index ratio is n_d/n_b = 1.096 and 1.45, respectively [144]. *(c) and (d) are illuminated by λ_5 = 400 nm when d_9 = 2 µm. The ratio is n_d/n_b = 1.43 and 1.59, respectively* [126]. *(e) has a ratio n_d/n_b = 2.5 when λ_6 = 515 nm and d_{10} = 10 µm* [128].

- The third section is when the ratio between the index of refraction of the dielectric and that of the surrounding background is higher than two ($n_d/n_b > 2$). As expected,

the PNJs will be generated inside the dielectric because the incident wavelength is strongly refracted on entering the cylinder or sphere dielectrics [93,94,122,128,147]. Fig. 2.4 e depicts the result where a wave is propagating in the z axis direction with a wavelength of λ_6 = 515 nm [128]. The diameter of the dielectric sphere is d_{10} = 10 µm, and the ratio of the refractive index is n_d/n_b = 2.5, as shown in Fig. 2.4 e. Based on these parameters, the PNJs will be located inside the dielectric sphere.

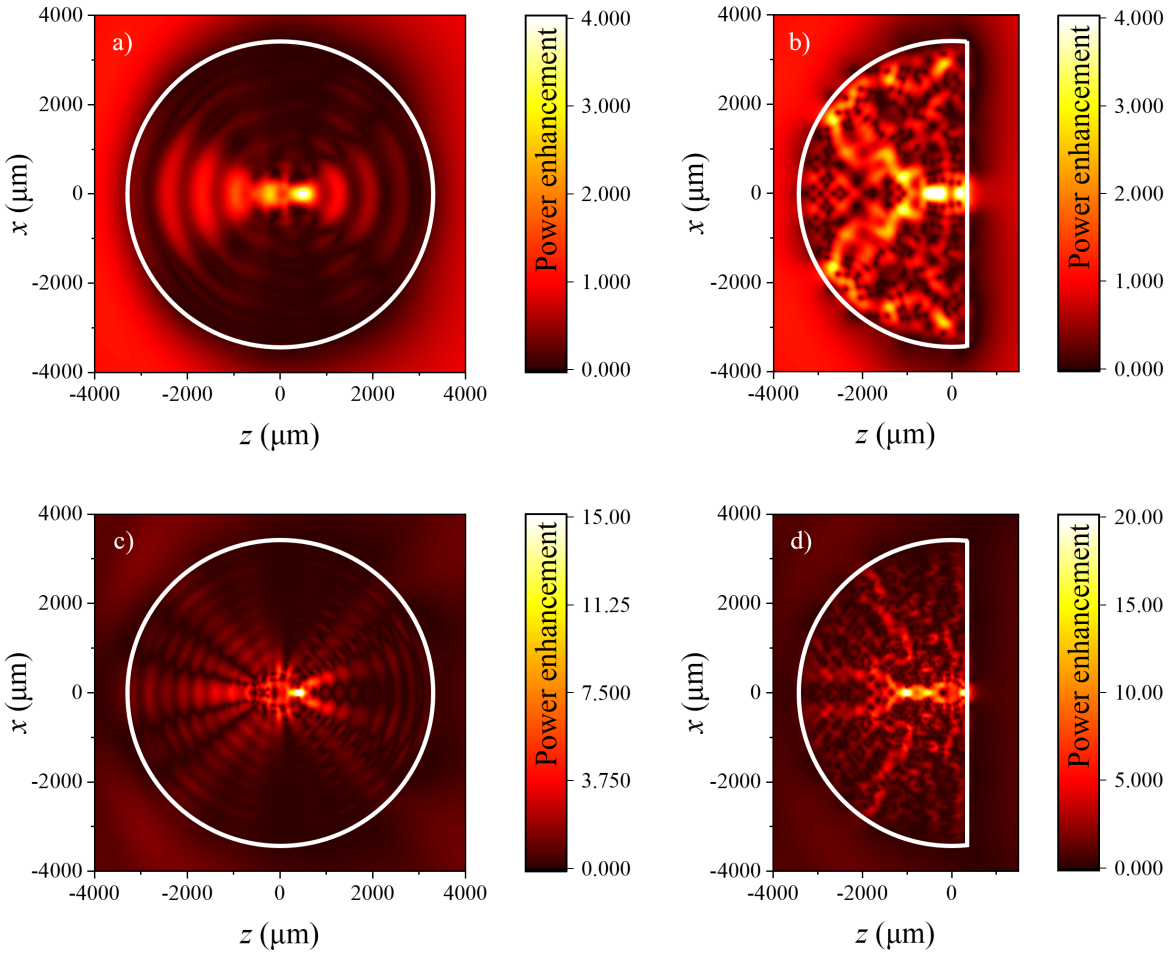

Figure 2.5: CST Studio Suite is utilised to simulate the structure in which a dielectric cylinder is used to generate the PNJ. The simulation represents the power enhancement in the xz plane, where the magnetic field is polarised along the x axis, and the propagation is along the z axis. x = z = 0 represents the centre of all dielectric cylinders. The ratio of the refractive indices is (n_d/n_b) = 9.59 for all the dielectric cylinders with a diameter of d_{11} = 6.6 mm. The dielectric cylinder is illuminated on the left side by λ_7 = 6 mm and λ_8 = 3 mm for (a) and (c), respectively. The truncated dielectric cylinder is illustrated in (b) for (a) and displayed in (d) for (c), respectively. The values for the parameters in this figure were obtained from the relevant reference [94].

The aim of this thesis is to explore the properties of PNJs produced using high refractive index dielectric, with a particular emphasis on the potential for generating PNJs with high spatial resolution after truncating the high refractive index dielectric. In a recent study, a high refractive index dielectric was investigated in comparison to the surrounding background with a refractive index ratio of n_d/n_b = 9.59 [94]. The dielectric used in the study had a fixed diameter

of d_{11} = 6.6 mm when illuminated by a planewave with a changing wavelength from λ_7 = 6 mm to λ_8 = 3 mm, as shown in Fig. 2.5 a,c respectively. PNJs are generated inside the dielectric as expected, similar to the result observed in Fig 2.3 e. The results in Fig. 2.5 a,c indicate that the position of the *FL* changes as wavelength changes from λ_7 = 6 mm to λ_8 = 3 mm. Specifically, as the wavelength decreases with the fixed dielectric size, or when the dielectric size increases with a fixed wavelength [133], the position of the *FL* shifts from being inside and close to the outer surface to being further deep inside the dielectric. The findings in chapter 3 align with the present result here, demonstrating that as the dielectric size increases while maintaining a fixed wavelength, the PNJ's position moves from near the outer surface to further inside the dielectric.

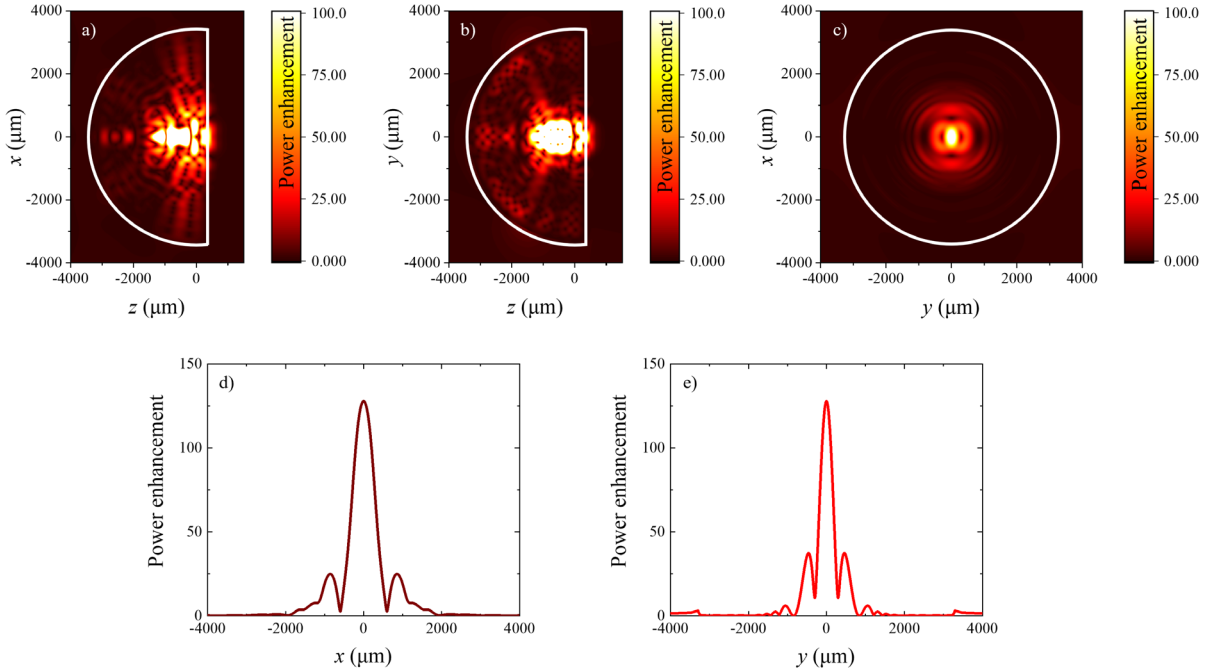

Figure 2.6: To simulate the structure in which a truncated dielectric sphere is utilised to generate the PNJ, the CST Studio Suite is used. The truncated dielectric sphere is illuminated on the left by a wavelength of λ_7 = 6 mm, where x = z = 0 denotes the centre of all dielectric spheres. The simulation represents power enhancement in the xz and yz planes for (a) and (b), respectively. Additionally, the simulation represents the power enhancement on the xy plane (c) at the output surface of the truncated dielectric sphere (front face). The electric field is polarised along the y axis, while the magnetic field is polarised along the x axis. The propagation direction is along the z axis. The diameter of all dielectrics is d_{11} = 6.6 mm, and the refractive index ratio is (n_d/n_b) = 9.59. The power enhancement along the transversal x and y axes is shown in (d) and (e) at the output surface of the truncated dielectric sphere, respectively. Parameter values in this figure were obtained from the relevant reference [94].

Given that the PNJ is formed inside the high refractive index dielectric, it is essential to use an appropriate method for transferring the PNJ from inside the dielectric to its output surface. To do that, the Weierstrass formulation for immersion lenses approach is a suitable method, and it was utilised in a previous study [94]. This method is important to achieving the PNJ at the output surface of the dielectric and will be further discussed in section 2.2.2. The shape of the truncated dielectric cylinder for Fig. 2.5 a and c is depicted in Fig. 2.5 b and d,

respectively. By utilizing this method, PNJs can transfer to freespace from the flat surface of the truncated dielectric cylinder.

Consider the truncated dielectric sphere depicted in Fig. 2.6, which has the same configuration as Fig. 2.5 a but a sphere instead [94]. The output surface of the truncated sphere clearly shows the presence of a PNJ, as demonstrated in Fig. 2.6 a,b. Fig. 2.6 c illustrates the power enhancement on the *xy* plane, specifically on the cross-section of the front face at the output surface where the PNJs are produced. To facilitate comparison, Fig. 2.6 d,e show the results of power enhancement along the *x* axis (at $y = 0$) and *y* axis (at $x = 0$), respectively, at the output surface of the truncated dielectric sphere. These results demonstrate high spatial resolution with $FWHMx = 0.08\lambda_7$ and $FWHMy = 0.06\lambda_7$ along the *x* and *y* axes, respectively [94]. Based on these findings, this thesis will use a high refractive index dielectric truncated at the output surface to achieve high spatial resolution PNJs. The results of chapter 3 will demonstrate that PNJs with the high spatial resolution are generated at the output surface of the truncated cylinder and truncated sphere dielectrics.

2.2 Methods and materials used in the design of my structure

This section provides an overview of the design details for optical fibres and dielectrics. Firstly, we discuss single mode optical fibre, which is crucial for generating PNJs, that operates at 1.55 μm wavelength and its materials. Secondly, we discuss the use of dielectric materials with a high refractive index to improve spatial resolution. Two designs are considered: one design uses the dielectric immersed in the air, whereas the other uses the dielectric immersed in the cladding material as the surrounding background. Lastly, we illustrate the use of CST Studio Suite and COMSOL Multiphysics with an appropriate mesh cell size for highly accurate and efficient simulations.

2.2.1 An optical fibre with a single mode

In this study, we utilize a single mode optical fibre operating at telecom wavelengths ($\lambda_0 = 1.55$ μm), where λ_0 represents the wavelength in freespace. The fibre consists a cylindrical core and cladding, and the use of a single mode optical fibre is necessary to eliminate any higher modes that may exist inside the optical fibre itself [113]. These higher modes have the potential to deteriorate the overall responsiveness of the PNJs [105]. It has been shown that higher modes can cause the maximum intensity outside the centre of the optical fibre to shift off-axis when PNJs are created using tip-ended optical fibres, for example [105]. In this scenario, the core of our single mode optical fibre ($n_{core} = 1.445$) is composed of silicon dioxide that has been slightly

doped with germanium (SiO_2-Ge), and the cladding ($n_{cladding}$ = 1.44) is composed of silicon dioxide (SiO_2). The diameters of the core and cladding are 8 µm and 125 µm, respectively. An illustration of the proposed structure for the single mode optical fibre as schematic is shown in Fig. 2.7 a. In order to provide a comprehensive picture, Fig. 2.7 b illustrates a side view as well as the profile of the fundamental mode of the fibre as a red curve.

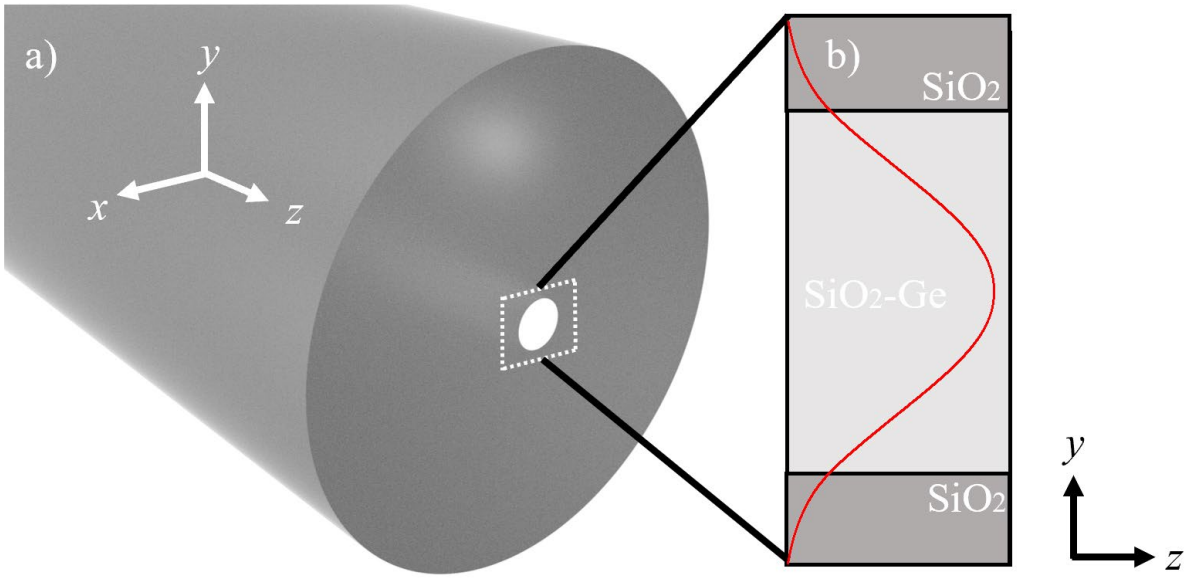

Figure 2.7: (a) A schematic of a single mode optical fibre is presented, while (b) provides a detailed side view of a dotted line within the optical fibre. The power distribution of the fundamental mode inside the optical fibre is depicted as a red line in (b). Additionally, the materials comprising the optical fibre are visible in (b).

For competence, let us make the consideration that the optical fibre is illuminated by an electric field polarised along the *y* axis (E_y) and a magnetic field polarised along the *x* axis (H_x), with propagation along the *z* axis. The polarization of the light does not affect the mechanism of total internal reflection that allows the light to propagate through the optical fibre. However, as the light exits the optical fibre and interacts with the dielectric cylinder or dielectric sphere, the polarisation influences the ability of light to focus sharper [148–154].

By applying Eq. 1.7, one can determine the numerical aperture of the optical fibre NA_f, which represents the ability of the optical fibre to gather light. Based on this equation, the calculated value of NA_f is 0.12. In addition, using Eq. 1.6, the value of V_{number} is 1.94, which determines both the number of modes and the cut-off (λ_c) in the optical fibre. Since the V_{number} is lower than 2.405, this optical fibre is capable of producing only a single mode when using a wavelength of λ_0 = 1550 nm, as discussed in section 1.2.1.2 [43].

2.2.2 High refractive index dielectric materials

Since the proposed structure is to produce a PNJ with high spatial resolution from a high refractive index dielectric, the dielectric is truncated using the Weierstrass formulation for immersion lenses approach, as previously mentioned in section 2.1.2. The Weierstrass formulation is a mathematical expression that describes the shape of an immersion lens, which is a specialized type of lens used in microscopy [155]. When an immersion lens is placed in direct contact with the observed specimen, Weierstrass formulation can achieve high levels of resolution, enabling a thorough examination of the specimen's structures and features [156,157].

The Weierstrass formulation for immersion lenses allows us to truncate the dielectric that has a high refractive index, which is how we overcome this problem [157]. The spatial resolution of the spot focus is improved when the dielectric is truncated using the Weierstrass formulation for immersion lenses [158–160]. This improvement is achieved through the reduction of the spot size when a wave transitions from a truncated dielectric to freespace through a truncated flat surface. During this transition, an angle is formed between the incident wave and the flat surface. If this angle becomes small enough to exceed the critical angle, the wave exits the truncated high index dielectric and enters freespace at a larger refractive angle. Consequently, the spot size decreases, resulting in improved spatial resolution for spot focus [161].

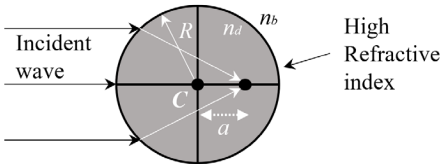

Figure 2.8: The truncated distance is shown in a schematic that corresponds to the Weierstrass formulation for immersion lenses [162].

The truncated dielectric has been implemented in a variety of applications, including optical data storage and microscopy [161,163,164]. Additionally, the truncated dielectric has been employed in situations where a dielectric is illuminated with a Bessel-modulated Gaussian beam [165]. The truncated distance corresponds to the value presented in Eq. 2.18 [94,162,166]:

$$a = \left(1 + \frac{n_b}{n_d}\right) R - R \tag{2.18}$$

where a is the truncated distance from the centre of the dielectric C, from Fig. 2.8, and R is the radius of the dielectric. With this arrangement, the dielectric is truncated along the dashed line depicted in Fig. 2.9. It is essential to note that Eq. 2.18 is valid for immersion lenses

illuminated with a planewave. However, our approach differs as we use the fundamental mode of a single mode optical fibre, as illustrated in Fig. 2.9. While we initially employ Eq. 2.18 as a starting point, the final truncation distance a needs to be optimized, as it will be shown in chapter 3 and 4 below. In the following chapters, we present a detailed investigation of the performance of the proposed high index dielectric particle placed on top of the optical fibre to generate high spatial resolution PNJs.

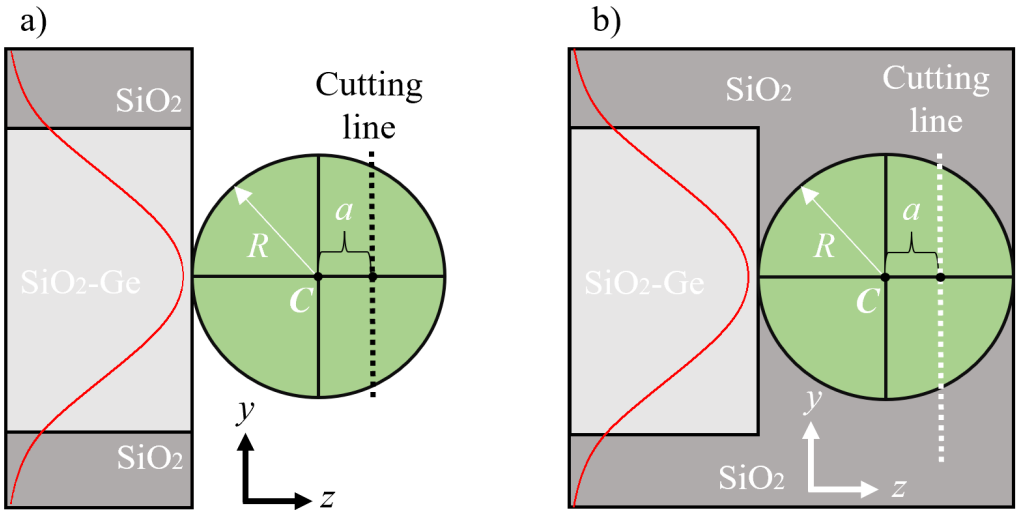

Figure 2.9: (a) When looking at an optical fibre from the side, it resembles Fig. 2.7 b. However, in this case, the dielectric is positioned at the end of the fibre and is surrounded by air. (b) Both the dielectric and the core of the optical fibre are covered by a cladding material. This cladding material has a refractive index value of $n_{cladding}$ = 1.44. In both cases (a,b), the design parameters for the truncated dielectric structure are represented by variables such as a, C, and R.

The first design is a high refractive index dielectric placed at the end of an optical fibre as illustration in Fig. 2.9 a. The structure is evaluated through simulation in chapter 3, both in two-dimensions 2D (using a dielectric cylinder) and in three-dimensions 3D (using a dielectric sphere). The results were discussed in terms of spatial resolution, power enhancement, location of the *FL*, and decay distance with different truncation positions. We selected a refractive index for this dielectric of n_d = 3.3 and without loss of generality, which is close to the value of frequently used materials at telecom wavelengths such silicon [1,19]. The structure is analysed when air (with a refractive index of n_b = 1) is used as the surrounding background. The ratio of the refractive index of the dielectric medium to that of the background medium is greater than two in this scenario $n_d/n_b > 2$. We anticipate that the PNJ will be formed within the high index dielectric because of ($n_d/n_b > 2$) as will be shown in chapter 3 and as demonstrated in [94].

The second design is for the experimental configuration, which involves immersing the dielectric in the cladding material ($n_{cladding}$ = 1.44), as shown in Fig. 2.9 b. The structure is evaluated in 3D using a Ge sphere with a refractive index of n_d = 4.295 and an extinction

coefficient of k = 0.0050938 at 2 µm wavelength [167]. The results were then examined and discussed with respect to different truncated positions. Detailed explanations for these specific values will be provided in chapter 4. Even when the refractive index of the surrounding background is increased to n_b = 1.44 in Fig. 2.9 b, the resulting refractive index ratio between the dielectric material and background medium is greater than two ($n_d/n_b > 2$). Consequently, immersing the dielectric in the cladding material enables to generate the PNJs at the output surface of the dielectric once the dielectric is truncated, as will be seen in chapter 4. It is important to note that this immersion of the dielectric causes a slight modification in the value of parameter a, as described in Eq. 2.18, compared to the value of a in Eq. 2.18 for the setup presented in Fig. 2.9 a. This change is a result of the increased refractive index of both the surrounding background and the dielectric material.

2.3 Utilizing 3D CST microwave studio for structure design

For investigating structures in electromagnetic simulations, accurate and efficient simulators are important. This section will discuss the key aspects of optical fibre and dielectric design for simulation using CST Studio Suite. The 3D simulations of CST Studio Suite require careful consideration of mesh cell sizes to achieve accurate results and improved computing performance. By utilising approximately 10 mesh cells per wavelength and utilising the symmetry of the structure, simulations can be solved faster and with high accuracy [168]. To further reduce simulation time, the cylindrical cladding of an optical fibre can be reshaped into a cubic cladding, reducing the number mesh cells while maintaining the same power distribution values. Increasing the number of mesh cells within and around the dielectric sphere will improve the accuracy of the result.

2.3.1 Simulation of 3D optical fibre configuration

The CST Studio Suite is a commercial 3D simulation software produced by Computer Simulation Technology AG, Germany. It provides a simulation tool for electromagnetic phenomena, such as wave propagation, scattering, diffraction, and absorption. Its most important features are the ability to simulate complex 3D structures and the properties of materials, as well as powerful visualisation capabilities. It is widely used in various industries, including telecommunications and imaging devices [169].

The finite-difference time-domain (FDTD) is a numerical method for simulating electromagnetic phenomena in 3D structures, and it is used in commercial software such as CST Studio Suite. The FDTD method breaks down the simulated structure into small mesh cells

and applies Maxwell's equations to compute the electric and magnetic fields at each mesh cell. FDTD simulations in CST Studio Suite can be used to study a wide range of electromagnetic phenomena, and the accuracy and efficiency of the simulations depend on various factors, such as mesh cell size [170]. Mesh cell sizes are crucial for accurate and efficient structure simulations in commercial software like CST Studio Suite. These small hexahedral mesh cells represent the simulated structure or device, and their size can significantly impact the accuracy of simulation and computational performance. The impact of cell size on the accuracy of my structure has been examined and the results are provided in appendix A. When the mesh cells are smaller, the simulation can capture finer details, allowing for a better understanding of the structure or device and resulting in a more accurate simulation. Additionally, these small cells also make the boundaries of electromagnetic field analysis accurate by capturing the finer details of shape and curvature that can have significant impacts when electromagnetic fields interact with the structure or device [171].

In Fig. 2.10 a, the core of the optical fibre has a diameter of 8 μm, while the cladding has a diameter of 125 μm, as mentioned in section 2.2.1. The optical fibre used in CST Studio Suite has a length of 5 μm. Since the structure is considered as a lossless material, the length of the optical fibre does not have an impact on the simulation results. The waveguide port at the back side excites the single mode optical fibre, with the electric field is (E_y) polarized along the y axis and the magnetic field is (H_x) polarized along the x axis, while propagation is along the z axis. Here, we must determine the minimum wavelength allowed for only a single mode to propagate. By utilising Eq. 1.8, we can determine the minimum wavelength λ_c (cut-off) required for the optical fibre to generate a single mode. According to Eq. 1.8, the cut-off value is λ_c = 1254 nm. In this case, the simulation covers a range of wavelengths, specifically from λ_{min} = 1545 nm to λ_{max} = 1555 nm. To gather information on the distribution of the electromagnetic field, field monitors are utilized in CST Studio Suite. The wavelength chosen from the field monitors is λ_0 = 1550 nm, which is known to experience the least amount of losses in the optical fibre [43].

To achieve accurate results while using CST Studio Suite, it is crucial to determine the appropriate mesh cell size. The size of the mesh cell is determined by the wavelength of λ_0 in freespace. When choosing a mesh cell size within the structure (the cladding and the core) shown in Fig. 2.10, it is recommended to have approximately ten meshes (cells) per wavelength [168]. In this case, the minimum mesh cell size is $0.11\lambda_0$ at both the cladding and the core. Conversely, the maximum mesh cell size is $0.16\lambda_0$ in the air. The use of mesh cell size in this

study was considered appropriate due to previous studies demonstrating its efficiency [144,168,172].

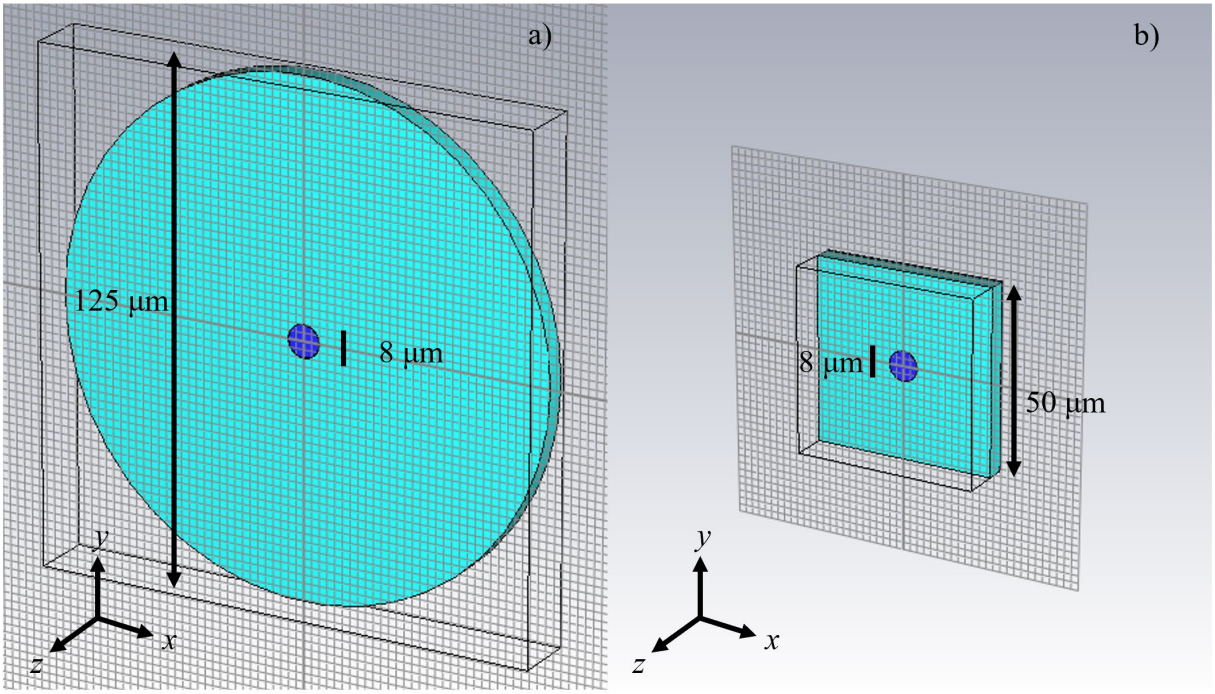

Figure 2.10: The illustration has been obtained from the CST Studio Suite. It displays the structure of an optical fibre, with (a) representing the actual size of the optical fibre (a cylinder cladding), and (b) representing the structure that is being used (a cube cladding).

The symmetry of the structure along the x and y axes allowed it to be divided into four quadrants; thus, we only needed to solve one quadrant to determine the value for all four. As a result, the CST Studio Suite only solves a single quadrant, which leads to a reduction in the solving time. Since the type of symmetry in the CST Studio Suite can be electric or magnetic, the xz plane was selected and made $Ex = 0$; this will eliminate the polarisation of the electric field E along the x axis where the wave propagation is along the z axis. This involved eliminating the tangential component of the electric field parallel to the xz plane and polarising the normal component of the electric field perpendicular to the xz plane along the y axis. Similarly, the yz plane was chosen with $H_y = 0$ to eliminate the magnetic field polarisation along the y axis. This involved eliminating the tangential component of the magnetic field parallel to the yz plane and polarising the normal component of the magnetic field perpendicular to the yz plane along the x axis. In this specific instance, not only should CST Studio Suite solve for only a quarter, but also the polarisation of the electric field of the electromagnetic wave is along the y axis (E_y), and the magnetic field is polarized along the x axis (H_x). By doing that, the structure comprises 8,897,436 mesh cells after applying symmetry, compared to 35,583,744 mesh cells without symmetry.

The 8,897,436 mesh cells still pose a challenge since the mesh cells for a dielectric material must be added. Adding a dielectric material at the end of the optical fibre, as will be shown in section 2.2.2, the total number of mesh cells should be significantly increased, increasing the required solving time. For instance, as illustrated in Fig. 2.14, when the number of mesh cells for the dielectric alone reaches 11,686,533, the solving time is affected even more [171]. To address the time issue and ensure the accuracy of the final result, the cylindrical cladding of the optical fibre was cut and shaped into a cubic shape, resulting in a reduced number of mesh cells, as illustrated in Fig. 2.10 b. CST Studio Suite allows for open boundaries to be selected, which enables the flat surfaces at the edges of a cube to be considered as infinitely long in the *x* and *y* axes, which can be seen in all four directions, top, bottom, right, and left in Fig. 2.10 b. The width of the cube was reduced to 50 μm, while its length has remained the same at 5 μm throughout this process. To ensure consistency in obtaining a single mode inside the optical fibre, the diameter of the cylindrical core has remained unchanged, resulting in the same outcomes depicted in Fig. 2.10 a. The mesh cell size, in Fig. 2.10 a and Fig. 2.10 b, remains unchanged, ranging from a minimum of $0.11\lambda_0$ to a maximum of $0.16\lambda_0$. The total number of mesh cells has been reduced to 1,411,551 due to the cylindrical cladding of the optical fibre being cut and reshaped into a cubic form. Therefore, this value of 1,411,551 is the number of meshes in my structure without dielectric.

Fig. 2.11 illustrates the power distribution planes for a cylinder and a cube cladding, respectively. The dimensions *x*, *y*, and *z* are parameterized to the freespace wavelength, which is set to $\lambda_0 = 1.55$ μm. As depicted in Fig. 2.11, a single mode is clearly generated inside the optical fibre, and this process has been explained in section 1.2.1.2. To locate the difference in power distribution, the ratio of power distribution between cube and cylinder optical fibres is calculated in order to determine the power enhancement. Fig. 2.11 b and Fig. 2.11 d represent the power distribution for the cube optical fibre, while Fig. 2.11 a and Fig. 2.11 c represent the power distribution for the cylinder optical fibre. The power enhancement is obtained by dividing the power distribution along the *z* axis at $x = y = 0$ for the cube optical fibre by the power distribution along the *z* axis at $x = y = 0$ for the cylinder optical fibre, as illustrated in Fig. 2.12. This calculation enables a comparison of the power distributions for the two geometries and facilitates the evaluation of the power enhancement.

In this study, using CST Studio Suite, we observed that the power distribution at the centre in both cylinder and cube claddings of the optical fibre are similar, as illustrated in Fig. 2.12. Both structures have this similarity because the power enhancement along the *z* axis equals 1.

The oscillations on the negative z direction (left side) result from the wave reflecting at the output surface of the optical fibre ($z = 0$). A standing wave is generated when two waves with the same wavelength and amplitude travel in opposite directions and interfere with each other at this point in the process. On the positive z direction (right side), the results are constant over distance because the wave propagates in a freespace without any reflection.

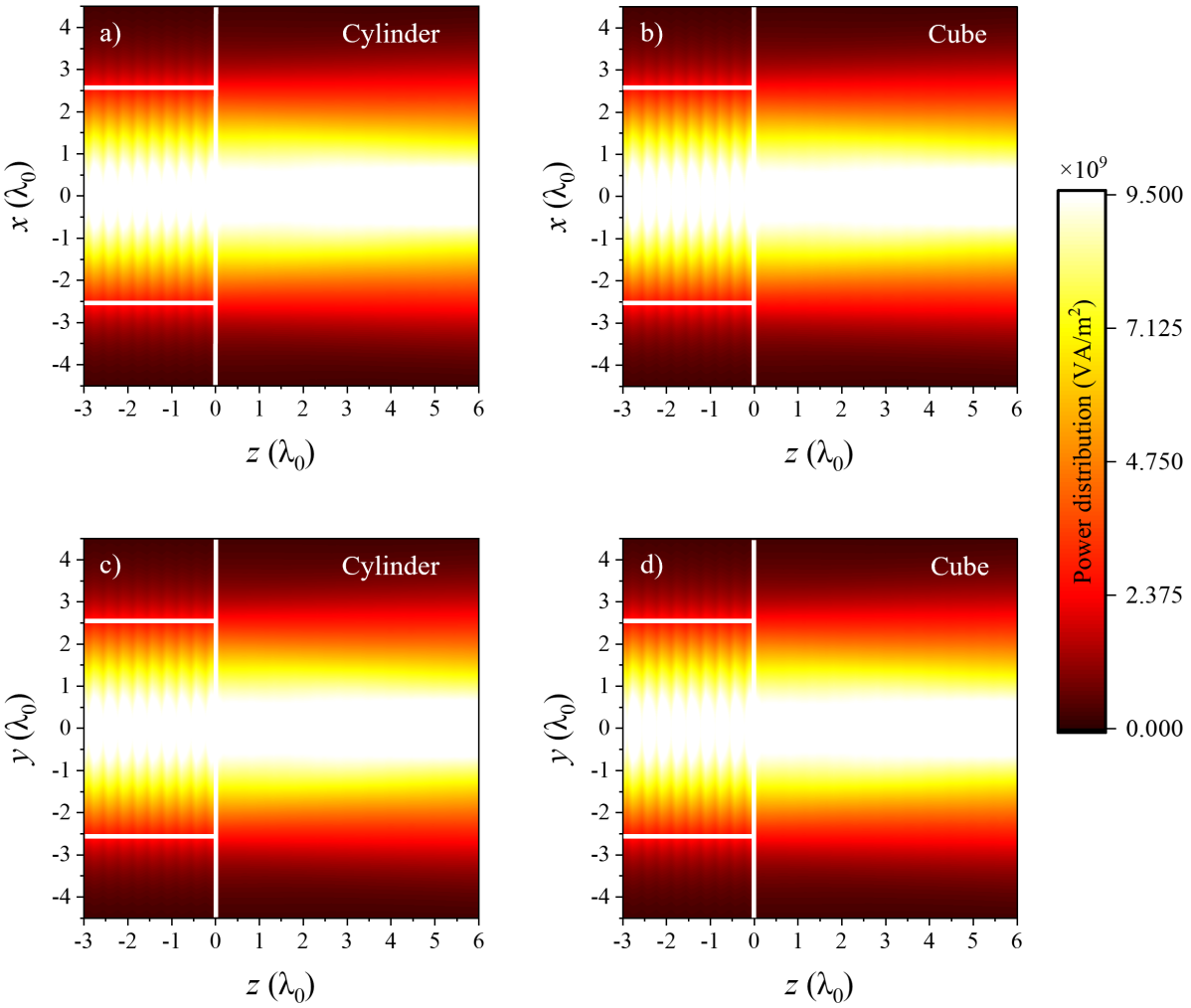

Figure 2.11: (a) The power distribution is on the xz plane at y = 0 for a cylinder cladding, while (b) is the power distribution for a cube cladding. (c) The power distribution is on the yz plane at x = 0 for a cylinder cladding, whereas (d) is the same plane of the power distribution for a cube cladding. The electric field is polarized along the y axis, and the magnetic field is polarized along the x axis. The propagation direction is along the z axis, with the output surface of the optical fibre located at z = 0. The power distribution values in the scale bar have been normalised by a factor of $1e^9$ to provide a clearer picture of the results between 0 and 9.5.

The power distribution of a Gaussian beam can be observed in both cube and cylinder optical fibre preforms along the transversal x and y axes in Fig. 2.11. This Gaussian beam has the highest power distribution at the centre of the optical fibre and gradually decreases towards the edges, allowing Gaussian beams to remain focused over long distances because the centre of the beam provides the majority of the power needed for focusing [47]. Fig. 2.13 compares

the power distribution of the transversal axes of both cylinder and cube claddings in the middle of the fibre to illustrate the differences in the Gaussian beam curves of the two fibre shapes.

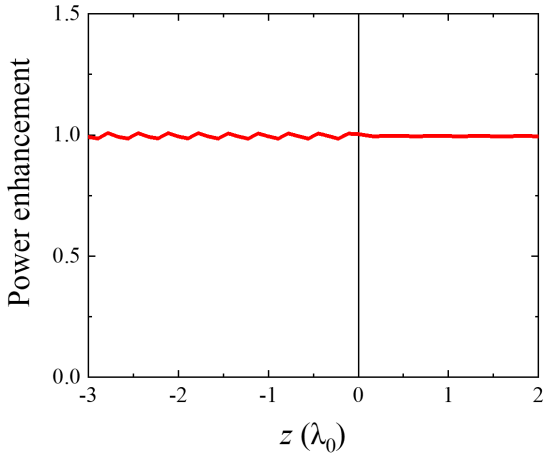

Figure 2.12: The power enhancement along the z axis at the point where x and y both equal zero in the optical fibre. This enhancement compares the power distribution in both structures by dividing the power distribution propagating within a cube optical fibre by the power distribution of a cylinder optical fibre. The power distribution values are extracted from Fig. 2.11 b and Fig. 2.11 a. At z = 0 is the output surface of the optical fibre for two structures.

To evaluate the power distribution of a Gaussian beam at the centre of the optical fibre, the *FWHM* is used along the transversal *x* and *y* axes, as previously mentioned in section 1.3. In the case of cylinder cladding, the *FWHM*s of the power distribution along the transversal *x* and *y* axes at $z = -2.5$ µm are $FWHMx = 3.84\lambda_0$ and $FWHMy = 3.84\lambda_0$, respectively. Similarly, the *FWHM*s of the power distribution for cube cladding are $FWHMx = 3.84\lambda_0$ and $FWHMy = 3.84\lambda_0$. These results indicate that the power distribution in both structures is similar, and that the cube cladding is suitable for simulations, this approximation will then be used in further chapters of this thesis.

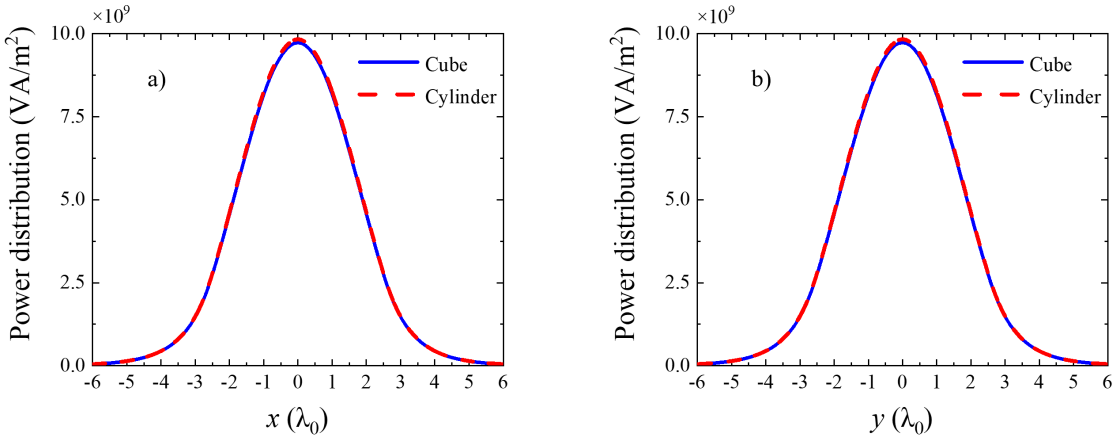

Figure 2.13: At z = - 2.5 µm, the power distribution was calculated for both a cube-shaped and a cylinder-shaped optical fibre along the transverse x and y axes, as shown in (a) and (b), respectively. The cube cladding is depicted by a blue line, while the cylinder cladding is represented by a red dashed line. The values of the power distribution have been normalised by a factor of $1e^9$ for better representation of the results in the range 0 to 10.

2.3.2 Simulation of 3D dielectric setup

Once the optical fibre has been arranged according to the configuration depicted in Fig. 2.11 b,d, a dielectric sphere has to be introduced at the end of the optical fibre. In order to achieve accurate results, the number of hexahedral mesh cells within and surrounding the dielectric sphere was increased, as illustrated in Fig. 2.14. In the dielectric region, the mesh cell size in terms of the wavelength in freespace λ_0 is $0.05\lambda_0$, which is greater than ten meshes (cells) per wavelength. The mesh size is the same in the air region, at $0.16\lambda_0$, and in the cladding and core regions, both at $0.11\lambda_0$. As a result, for a given radius R of the dielectric sphere, the number of mesh cells across the radius is 11 mesh cells for $R = 0.55\lambda_0$ and 31 mesh cells for $R = 1.55\lambda_0$. These particular values of R were chosen based on a previous study and will be discussed further in chapter 3 [94].

The CST Studio Suite enables the selection of local mesh properties, allowing for an increase in the number of mesh cells within an object. To assess the accuracy of the *FL* location in the simulation, we examined the results obtained from varying mesh cell sizes along the radius of the dielectric sphere R, as depicted in appendix A. This thesis uses 40 mesh cells across the radius of the dielectric sphere because it has a negligible effect on the location of the *FL*.

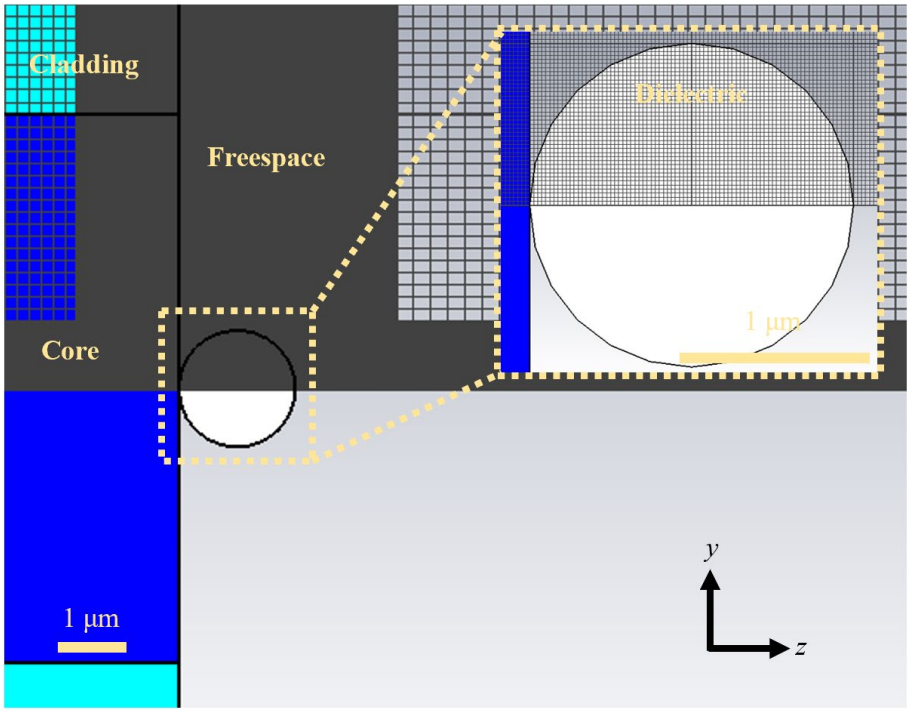

Figure 2.14: The illustration was extracted from the CST Studio Suite, where the mesh cells are depicted as a cross-section of the dielectric sphere in the yz plane. The dielectric sphere has a radius of R = 0.55 λ_0, and the inserting image displays that along its radius there are 40 mesh cells.

2.4 Employing 2D COMSOL Multiphysics for structure design

This section will briefly discuss the structure of optical fibre and dielectric by utilizing the COMSOL Multiphysics. In 2D simulations, the size of the mesh cells is significant, and employing an extremely fine mesh can further improve the accuracy of the results. It is essential to reduce the size of mesh cells within and surrounding the dielectric cylinder in order to improve the accuracy of the results. COMSOL Multiphysics is a powerful simulation software that offers a wide range of tools for modelling and optimizing the behaviour of various optical devices in 2D. With this software, researchers can simulate the interactions between light and different media and structures, including dielectric and optical fibres in 2D [106,139,173,174]. The simulation allows for accurate analysis of light propagation, reflection, refraction, and diffraction, enabling researchers to refine the performance of optical devices and improve their designs. COMSOL Multiphysics for photonics simulation in 2D provides faster simulations than 3D modelling because it simplifies the geometry and decreases the computation time by disregarding the third dimension [159].

The Finite Element Method (FEM) is a numerical technique used for solving Maxwell's equations. The process includes dividing a structure into finite elements, which are simpler and smaller parts. These elements are interconnected, forming a mesh that represents the structure. The method then combines these individual element solutions to produce the overall result for the entire system [175].

COMSOL Multiphysics uses the FEM to simulate by breaking down the mesh cell shape into triangular or quadrilateral elements as shown in Fig. 2.15. In COMSOL Multiphysics, the user first designs a structure by selecting the geometry, material properties, and boundary conditions. The software then generates a mesh of finite elements that breaks down the structure on itself [176]. In Fig. 2.15 a, the 2D fibre structure is immersed in air from top, bottom, right, and left. A port covering the whole 2D fibre, both the core and the cladding, is utilized to illuminate the fibre from the left. The electric field is polarised along the y axis and propagates along the positive z axis. Finally, the refractive index for the core is $n_{core} = 1.445$, the cladding is $n_{cladding} = 1.44$, and the air is $n_b = 1$. When determining the appropriate mesh cell sizes for the structure depicted in Fig. 2.15 a, which includes cladding, core, and freespace regions, it is recommended to aim for approximately ten cells per wavelength [106,174,177]. In this instance, the chosen mesh cell size within the cladding and core regions is $0.1\lambda_0$. In the air region (the right scattering region, which is of particular interest), the mesh size is set at $0.002\lambda_0$.

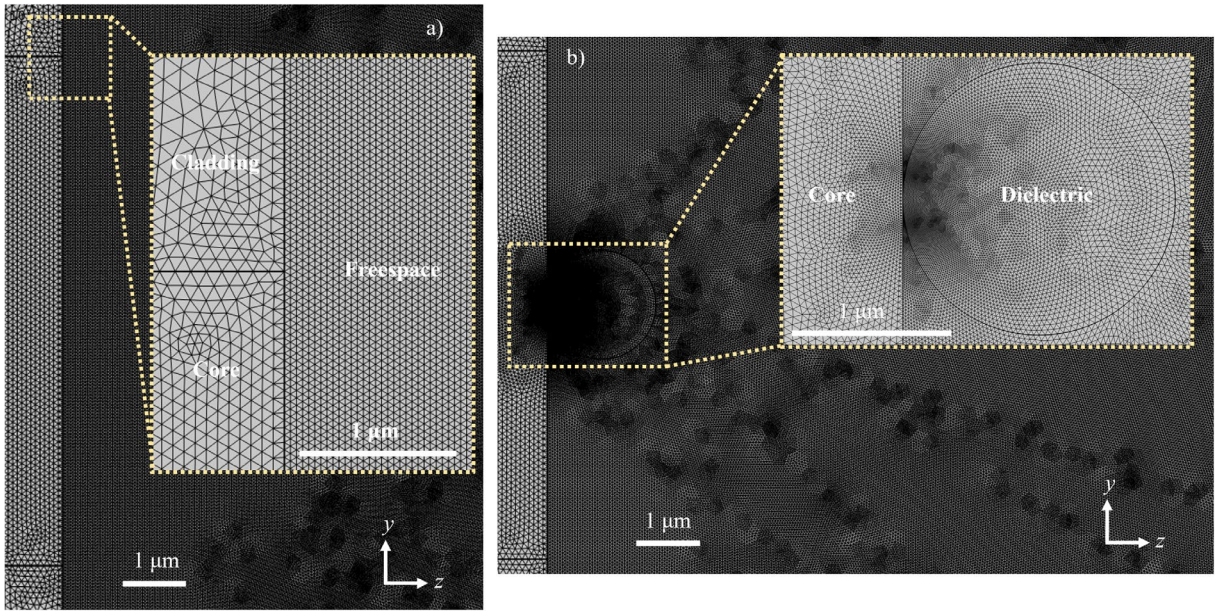

Figure 2.15: The provided figure is generated using COMSOL Multiphysics software, which visualizes the mesh cells as cross-sections. Specifically, the cross-sections represent the optical fibre (a) and the optical fibre with the dielectric cylinder (b) in the yz plane. (a) The inserting image shows the three structural regions of cladding, core, and freespace. (b) The dielectric cylinder has a radius of R = 0.55λ_0, and the inserting image depicts the extremely fine mesh inside and around the dielectric cylinder.

Fig. 2.15 b depicts a dielectric cylinder is placed at the end of an optical fibre. Both the optical fibre and the dielectric are immersed in air, similar to the setup shown in Fig. 2.9 a. To maintain consistency with the 3D scenario, the dielectric material has a refractive index of n_d = 3.3, without losses. The optical fibre illuminates the dielectric cylinder from the left side. For accurate simulation results, the dielectric material mesh cells in COMSOL Multiphysics have a minimum size of 0.0006λ_0. Reducing the mesh cell size has been considered to be appropriate, depending on the effective use and results of previous studies [178]. The mesh cell size in COMSOL Multiphysics is comparatively less than that in CST Studio Suite because to the reduced computational time required for simulations in COMSOL Multiphysics.

Chapter 3 Exploring photonic nanojets for high-resolution spatial focusing in telecommunication wavelengths

In this chapter, we present a technique for achieving high spatial resolution focusing of electromagnetic waves at telecommunication wavelengths (λ_0 = 1.55 μm) by placing high-refractive index dielectrics at the end of an optical fibre. Our technique is to produce PNJs with narrow focusing spots and high intensity. We evaluate the performance of the device in both 2D and 3D configurations using cylindrical and spherical high-index dielectrics placed at the end of an optical fibre, respectively. We demonstrate how PNJs can be shifted towards the output surface by truncating the output profile of the high-index dielectric. By engineering the size and truncation distance of the 2D/3D dielectric particles, this simple modification enables us to obtain a PNJ with a high transversal resolution.

The objective of this work is to present a comprehensive analysis and design process for 3D truncated dielectrics, starting from ideal scenarios of 2D dielectric cylinders and progressing towards more realistic devices. In section 3.1, the effect of varying the full size and truncation distance of idealized 2D dielectric cylinders on their PNJ properties is examined. Moving on to section 3.2, the focus is on investigating the influence of truncated dielectric cylinders with finite transverse length, specifically a 3D high refractive index dielectric cylinder positioned at the end of an optical fibre, on the PNJ. Finally, in section 3.3, the impact of full size, truncated dielectrics, losses, and shape imperfections of dielectric spheres on PNJ parameters such as spatial resolution, power enhancement, location of the *FL*, and decay distance is studied. The proposed structure demonstrates promise for sensing and imaging systems which need high spatial resolution in the near field. The majority of the content in this chapter has been published in the following references [179–181].

3.1 High index dielectric cylinder (2D)

This section focuses on investigating high index dielectric cylinders in 2D using COMSOL Multiphysics software to determine the initial performance of the structure. The section is divided into two parts. Section 3.1.1 evaluates the idealised full 2D dielectric cylinder surrounded by air and illuminated by an optical fibre. We investigate the effect of varying the size of the dielectric cylinder on the performance of the PNJ.

In section 3.1.2, we apply a truncation on the dielectric cylinder in order to generate a PNJ at the output surface of the dielectric. To do this, we utilize the Weierstrass formulation for immersion lenses as a starting point for truncating the dielectric cylinder. Then, we perform a parametric analysis of the structure by changing the distance between the centre of the dielectric cylinder and the flat output surface. This enables us to determine the PNJ at the output surface of the truncated dielectric cylinder.

3.1.1 Full dielectric cylinder

The 2D structure of a full dielectric cylinder surrounded by air on the top, bottom, and right sides is illustrated in Fig. 2.15 b. On the left side, the 2D optical fibre is attached to a full dielectric cylinder. The optical fibre is illuminated, with a wavelength of $\lambda_0 = 1.55$ µm, from the left using a port that covers the whole fibre (core and cladding). The electric field of the light is polarized along the *y* axis, and it propagates in the positive *z* axis direction. Finally, the mesh cells with a maximum and minimum mesh size of 0.1 λ_0 and 0.0006 λ_0, respectively, was utilised, as described in section 2.4.

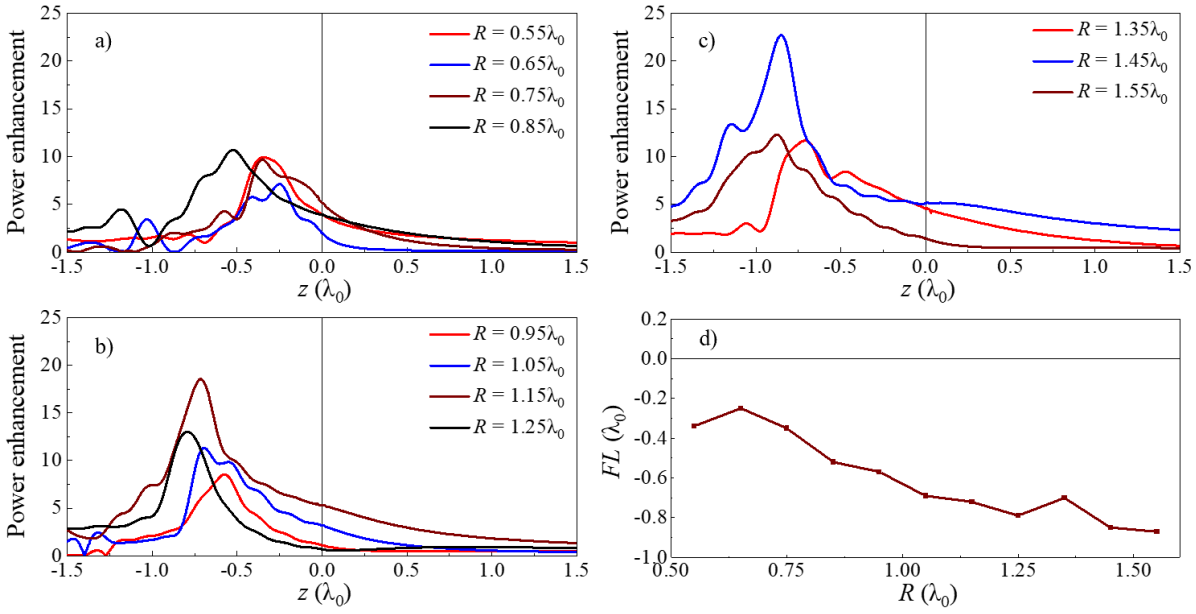

Figure 3.1: The power enhancement along the z axis at y = 0 for all the different values of R is shown in (a-c). (d) The FL for all the different values of R, ranging from R = 0.55λ0 to R = 1.55λ0 with steps of 0.1λ0. In (a-c) and (d), the black lines that run vertically and horizontally at zero, respectively, represent the output surface of the full 2D dielectric cylinders.

We initially determined the size of the dielectric cylinder to be similar to the size used in previous findings utilising cylinders and spheres with a high refractive index as mentioned in section 2.1.2 [94]. According to those results, the radius of the dielectric cylinders and spheres, *R*, in relation to the freespace wavelength λ_7 is $R = 0.55\lambda_7$, where λ_7 has a value of 6 mm. In this study, we employ a similar relationship for the freespace wavelength resulting in $R = 0.55\lambda_0$. To ensure consistency, we also utilised the radius in relation to the wavelength inside

the dielectric cylinder in order to maintain the similar scale with the previous results [94]. In this study, we utilized a dielectric refractive index value (n_d = 3.3) that differs from the one employed in previous findings (n_{d7} = 9.59). Additionally, the wavelength used in this study is also different from that of the previous findings. Based on those results, the radius of the dielectric was approximately $R \approx 5\lambda_{d7}$, where λ_{d7} represents the wavelength inside the dielectric cylinder, calculated as $\lambda_{d7} = \lambda_7 / n_{d7}$. To determine the wavelength inside the dielectric cylinder for this study, we utilized the relationship $\lambda_{d0} = \lambda_0 / n_d$, where λ_{d0} represents the wavelength inside the dielectric in this study. Consequently, employing $R \approx 5\lambda_{d0}$ in this study, the radius of the dielectric cylinder is approximately equivalent to $R \approx 1.52\lambda_0$.

To fully examine the impact of dielectric size on PNJs, we explored dielectric cylinder sizes ranging from $R = 0.55\lambda_0$ to $R = 1.55\lambda_0$, increasing with step of $0.1\lambda_0$. Specifically, we examined dielectric sizes of $0.55\lambda_0$, $0.65\lambda_0$, $0.75\lambda_0$, $0.85\lambda_0$, $0.95\lambda_0$, $1.05\lambda_0$, $1.15\lambda_0$, $1.25\lambda_0$, $1.35\lambda_0$, $1.45\lambda_0$, and $1.55\lambda_0$, and analysed their impact on the performance of the PNJs under study. Fig. 3.1 a-c displays the power enhancement along the *z* axis at the centre of the dielectric cylinder $y = 0$. The enhancement was calculated by dividing the power distribution along the *z* axis when using a dielectric cylinder and an optical fibre by the power distribution on the *z* axis when using an optical fibre only. The black line at $z = 0$ denotes the output surface of the dielectric cylinder, and the positive *z* axis is the freespace. All *FL*s are generated inside the dielectric cylinder, in the negative *z* side, and their locations vary with the dielectric size. *FL* defines the distance from the output surface of the dielectric to the focus of light. These results agree with previous studies given that the ratio of the dielectric index n_d to the refractive index of the surrounding background n_b is greater than 2 (n_d/n_b = 3.3) [88,128]. In order to understand the results regarding the relationship between *FL*s and dielectric size, Fig. 3.1 d shows the *FL* for all *R* values, from $R = 0.55\lambda_0$ to $R = 1.55\lambda_0$ with steps of $0.1\lambda_0$. The *FL* shifts from a position closer to the surface of the dielectric cylinder (on the inside of the cylinder) to a position further inside the dielectric cylinder (deeper inside the cylinder) as the size of the dielectric cylinder increases, which is also in agreement with what was reported in [94]. We chose four sizes as examples to display the power enhancement in *yz* plane, which are $0.55\lambda_0$, $0.85\lambda_0$, $1.25\lambda_0$, and $1.55\lambda_0$. Through Fig. 3.2 a-d, the *FL* can be seen clearly formed inside the dielectric of all sizes. The spatial resolution of these *FL*s inside the dielectrics was calculated as shown in Fig. 3.2 e-h. At the corresponding *FL* for each value of *R*, the *FWHM* of the power enhancement along the transversal *y* axis was determined to be $0.46\lambda_{d0}$, $0.56\lambda_{d0}$, $0.42\lambda_{d0}$, and $0.46\lambda_{d0}$ for $R = 0.55\lambda_0$, $0.85\lambda_0$, $1.25\lambda_0$, and $1.55\lambda_0$, respectively (with $\lambda_{d0} \approx 470$ nm). Here, $0.13\lambda_0$, $0.16\lambda_0$, $0.12\lambda_0$, and $0.13\lambda_0$ represent the corresponding values of the *FWHM*s in terms of the freespace wavelength.

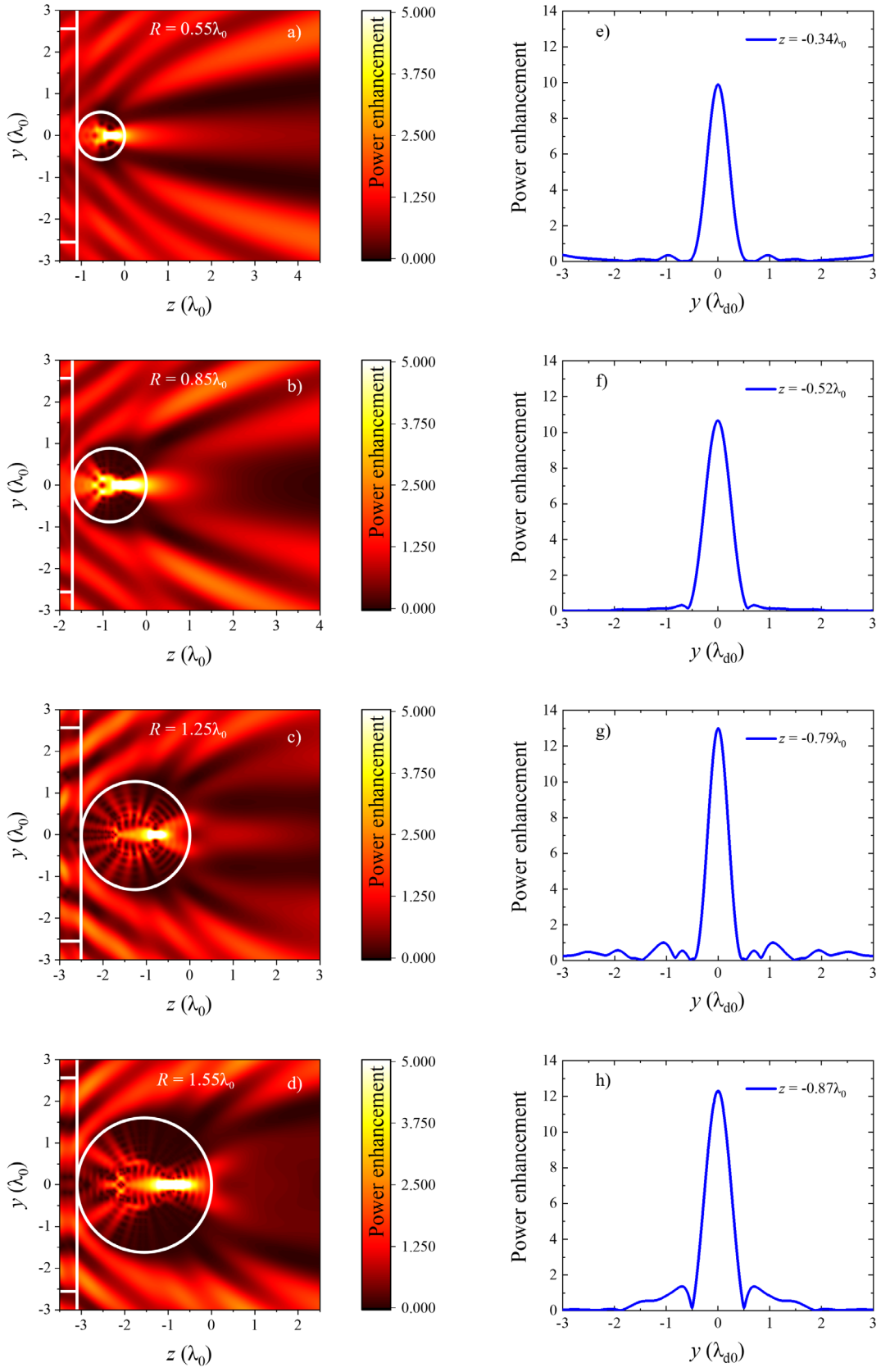

Figure 3.2: Power enhancement on the yz plane taking into consideration a radius R of the full 2D dielectric cylinder of (a) R= 0.55λ0, (b) R= 0.85λ0, (c) R= 1.25λ0, and (d) R= 1.55λ0, respectively. It displays that the contour scales have been saturated from 0 to 5 so that the results can be compared more effectively. The transversal y axis of the power enhancement at the position of the FL (z = FL) for the radius of (e) R= 0.55λ0, (f) R= 0.85λ0, (g) R= 1.25λ0, and (h) R= 1.55λ0 is extracted by using the same values of R as in panels (a-d).

3.1.2 Performance analysis of truncated dielectric cylinder structure with varying truncation distance

To get the PNJ out from inside to the outside of the dielectric cylinder, the dielectric cylinder is truncated using Eq. 2.18. To do this, we select the radius of the dielectric cylinder to $R = 1.55\lambda_0$ (so that the wavelength inside the dielectric cylinder is similar to the previous work under planewave illumination [94]). In continuation with the previous work, we also analysed the dielectric size with $R = 0.55\lambda_0$. This size assures that the wavelength in freespace is similar to the previous work in terms of the wavelength in freespace. The results demonstrated that PNJs are generated at the output surface of the dielectric cylinder, however their power enhancement values are close to 1. The detailed results of this analysis can be found in appendix B i. When employing Eq. 2.18 with $R = 1.55\lambda_0$, the resulting value for a is $a \approx 0.47\lambda_0$. This represents the distance between the centre of the dielectric cylinder and the output flat surface, which is the cutting line, as depicted in Fig. 2.9 a. Importantly, the illumination differs from a planewave (as considered in [94]) when the dielectric is at the end of an optical fibre. Because of this difference in illumination, it is anticipated that will need to have a slight adjustment made to it in order to account for such a change in illumination. To achieve this, a parametric study of the performance of the structure is carried out, taking into consideration values of a (for the fixed $R = 1.55\lambda_0$), which range from $\sim 0.39\lambda_0$ to $\sim 0.55\lambda_0$ with steps of $\sim 0.006\lambda_0$ (600 nm to 860 nm with a step of 10 nm).

By truncating the dielectric cylinder, we are able to generate *FL*s outside of it for all values of a, as shown in Fig. 3.3 a (in the positive vertical axis). The outer *FL*s from the dielectric surface range from $0.05\lambda_0$ to $0.32\lambda_0$. The closest *FL* to the dielectric flat surface obtains at $a \approx 0.52\lambda_0$. To evaluate the spatial resolution of the obtained *FL*s, we calculate the *FWHM* based on the *FL* locations appearing outside the dielectric cylinder, as illustrated in Fig. 3.3 b. The *FWHM* values range from $0.28\lambda_0$ to $0.45\lambda_0$ for all values of a, indicating spatial resolutions smaller than the diffraction limit, which is less than half the wavelength [56,83]. Notably, the highest spatial resolution achieved is $0.28\lambda_0$ when a is between $0.50\lambda_0$ to $0.54\lambda_0$. We also evaluate the power enhancement at the *FL* position. As shown in Fig. 3.3 c, the power enhancement values range from 2 to 9 based on different values of a. The result indicates that the highest values of the power enhancement are achieved when a is increased, specifically up to $a \sim 0.55\lambda_0$. However, due to the location of the generated PNJs is moved further from the output surface of the 2D truncated dielectric, the spatial resolution is slightly reduced as expected [95,110].

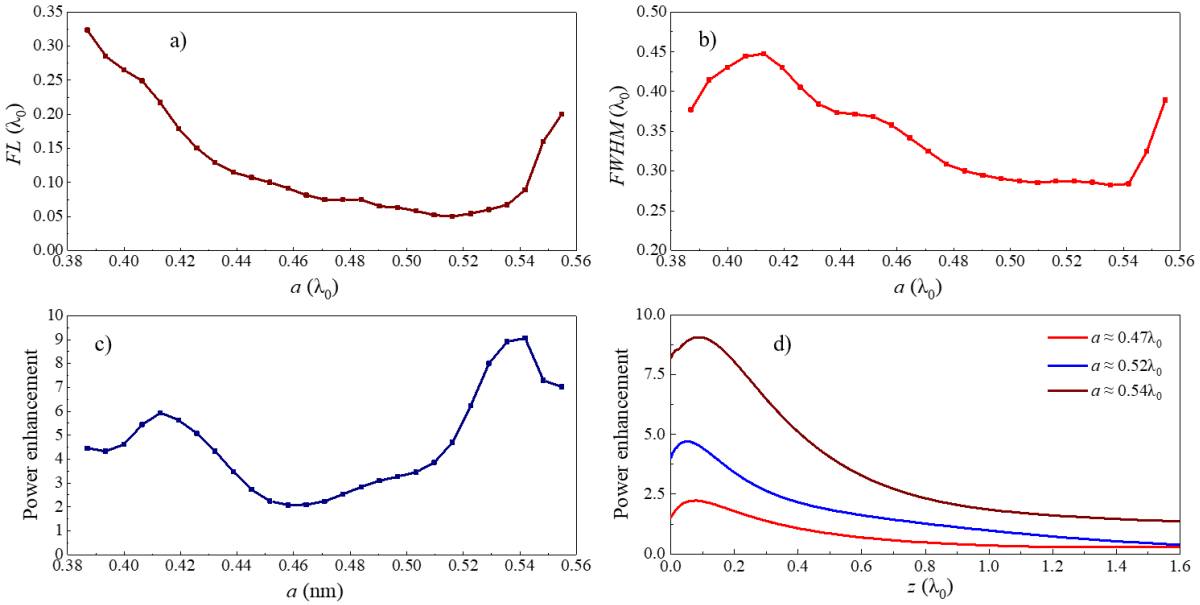

Figure 3.3: (a) The FL of a truncated dielectric cylinder is shown with different values of a. The output surface of all truncated dielectric cylinders is represented by the zero on the horizontal axis. Additionally, the FWHM (b) and power enhancement (c) can be determined as functions of a, specifically at the position of the FL, for a truncated 2D dielectric cylinder with $R = 1.55\lambda_0$. (d) The power enhancement along the propagation z axis when y = 0 is for $a \approx 0.47\lambda_0$, $0.52\lambda_0$, and $0.54\lambda_0$. The output surface of the truncated dielectric cylinder is at z = 0.

In Fig. 3.3 d, where the *FL*s appears outside the truncated dielectric cylinder, we present three examples of the power enhancement along the *z* axis in which *a* equals the exact value from Eq. 2.18 ($a \approx 0.47\lambda_0$), the closest *FL* to the flat surface of the truncated dielectric cylinder ($a \approx 0.52\lambda_0$), and the highest power enhancement ($a \approx 0.54\lambda_0$). The power enhancement along the *z* axis for all values of *a* is illustrated in appendix B ii. The present study demonstrates that adjusting the truncation position has the ability to influence the convergence or divergence of light as it passes the truncated dielectric cylinder. This adjustment generates PNJs with high spatial resolution [159,161,182]. The results presented in Fig. 3.3 c demonstrate the highest power enhancement achieved at approximately 9 when the parameters *R* and *a* were set to $1.55\lambda_0$ and $0.54\lambda_0$, respectively. Fig. 3.4 a illustrates the power enhancement on the *yz* plane for the truncated dielectric cylinder, demonstrating the formation of PNJ outside of the truncated dielectric cylinder. Furthermore, the power enhancement along the transverse *y* axis at the *FL* is also seen in Fig. 3.4 b, where it is up to 9 times more than in structures without the truncated dielectric cylinder.

Based on the results from Fig. 3.3 b, the best structure is determined by the value of *a* that enables the excitation of a PNJ with the narrowest *FWHM* and closest *FL* to the output surface. We find that when the *FL* approaches the surface of the truncated dielectric cylinder, the spatial resolution of PNJ increases, and this is in agreement with what was reported in [94,95,110]. As explained above, for the case with $R = 1.55\lambda_0$, the truncated 2D dielectric cylinders with $a \approx$

$0.50\lambda_0$ to $0.54\lambda_0$ generate the PNJs with the highest resolution, whereas the design with $a \approx 0.52\lambda_0$ produces the *FL* that is closest to the output surface. By considering into account these conditions, the best structure for $R = 1.55\lambda_0$ would be determined to be $a \approx 0.52\lambda_0$. This value of a is close to but not exact to the one obtained with Eq. 2.18, $a \approx 0.47\lambda_0$, as expected given that the illumination is no longer a planewave. As expected by Eq. 2.18, different values of a will be required if a different value of R is selected. For completeness, the power enhancement on the *yz* plane for the truncated dielectric cylinder with $a \approx 0.52\lambda_0$ and the power enhancement along the y axis at the position of the *FL* ($z = 0.05\lambda_0$) are shown in Fig. 3.4 c,d, respectively. According to these results, the ability of generating PNJs with high spatial resolution is achieved with a transversal resolution of $FWHM = 0.28\lambda_0$ and a power enhancement at the *FL* that is 4 times higher than the case without the truncated dielectric cylinder.

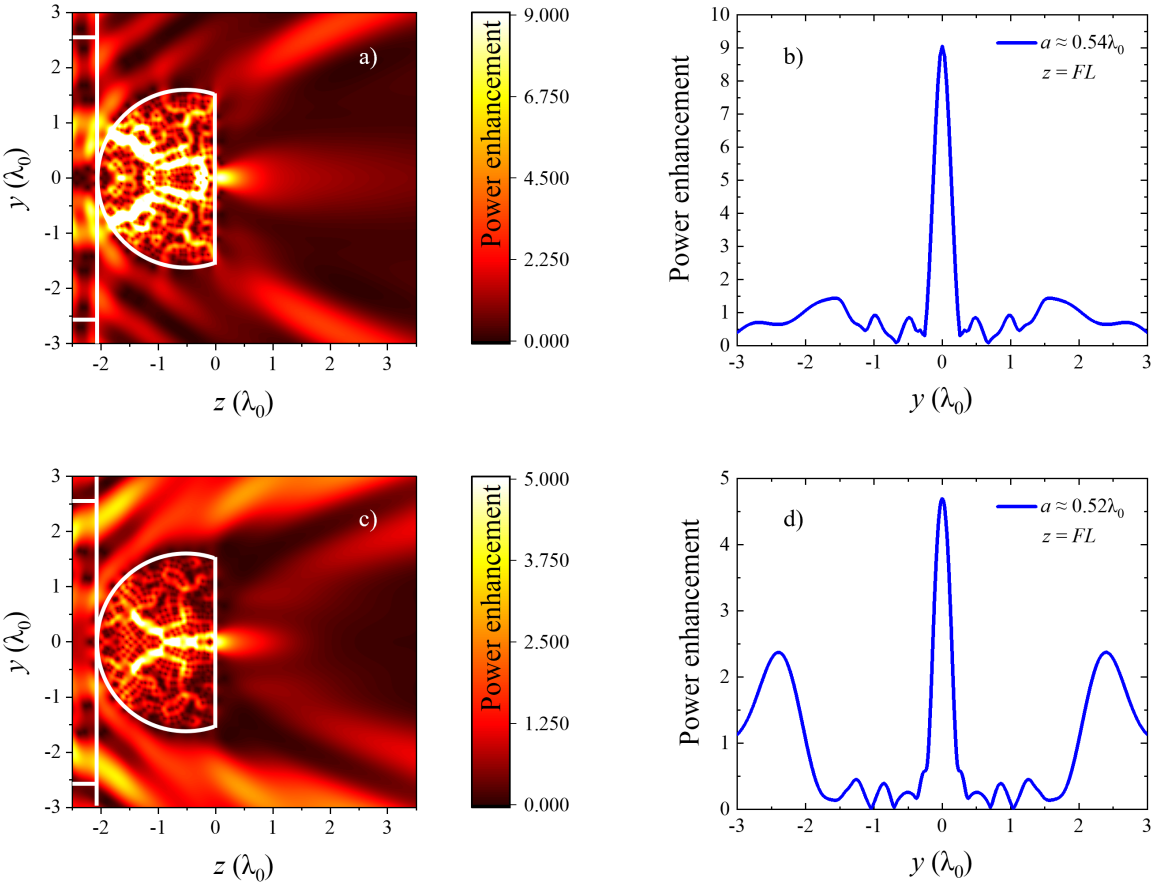

Figure 3.4: Power enhancement on the yz plane for $R = 1.55\lambda_0$ and (a) $a \approx 0.54\lambda_0$ (c) $a \approx 0.52\lambda_0$. Power enhancement along y axis at the FL, extracted from panel (a) for (b) and extracted from panel (c) for (d).

In summary, the results shown in Fig. 3.1 demonstrate that the generated PNJ is inside the dielectric cylinders when using ideal full 2D high index dielectric cylinders placed on top of the optical fibre. However, by truncating the output profile, as depicted in Fig. 3.3, the PNJ

can be generated close to the output flat surface of the truncated dielectric cylinder. Finally, we have examined 2D dielectric cylinders with a truncated output surface.

3.2 Investigation of non-ideal 2D cylinders: dielectrics with finite sizes

In this section, we examine the scenario where a 3D high refractive index dielectric cylinder is positioned at the end of an optical fibre. These cylinders are not fully 2D and the purpose is to demonstrate the influence of utilizing these truncated dielectric cylinders with finite transverse length on the PNJ. In our investigation, we consider truncating the dielectric cylinder at its output, with *a* value of $0.52\lambda_0$, similar to what is illustrated in Fig. 3.4 c,d. This particular value of *a* was chosen because it produces the best structure in 2D, which is characterized by the excitation of a PNJ with the narrowest *FWHM* and the closest *FL* to the output surface.

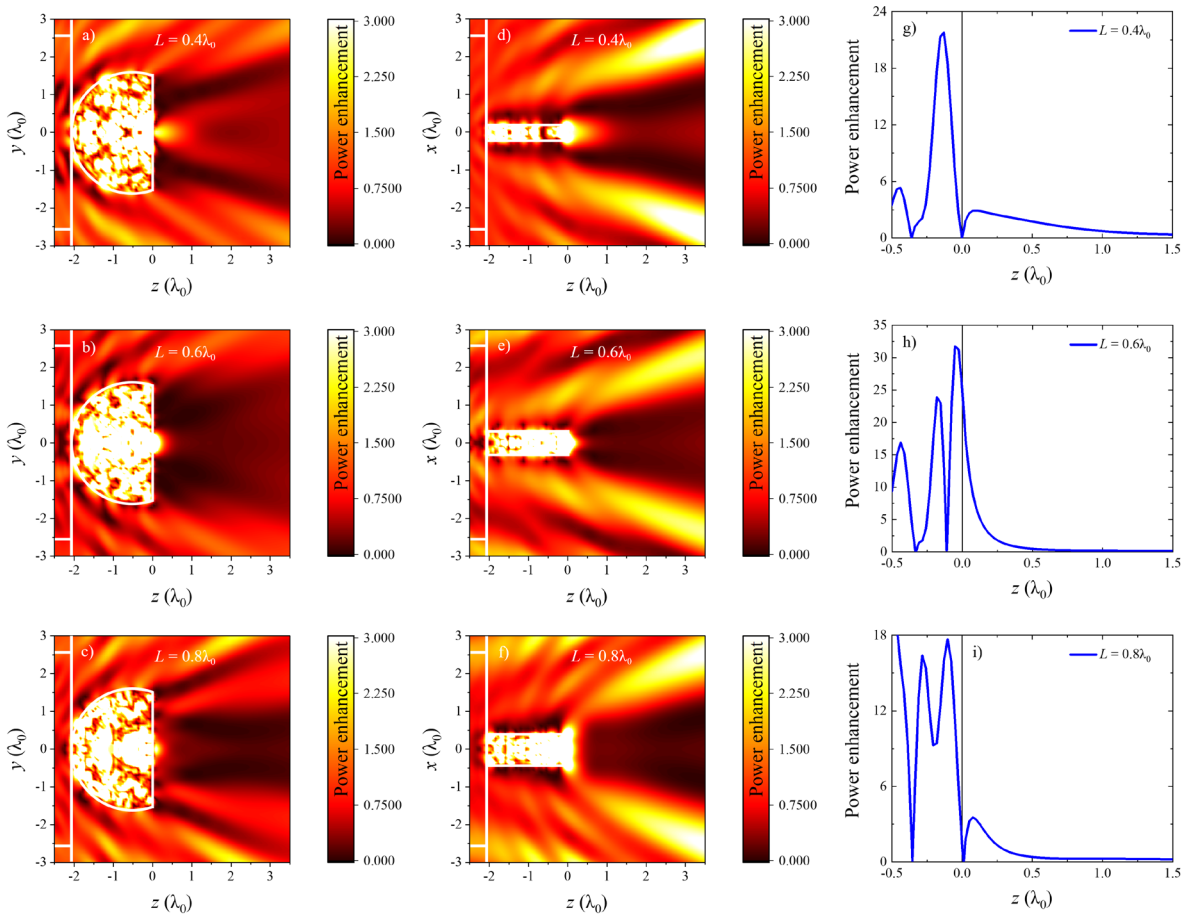

Figure 3.5: (a-c) Considering transversal lengths of $0.4\lambda_0$, $0.6\lambda_0$, $0.8\lambda_0$, respectively, power enhancement in the yz plane for the truncated 3D dielectric cylinder with $R = 1.55\lambda_0$ and $a = 0.52\lambda_0$ (to make it better to view the results, the contour scales have been saturated from 0 to 3). (d-f) Similar to (a-c), but with the xz planes where the transversal lengths of the truncated dielectric cylinders are clear to see. (g-i) Calculated power enhancement along the z axis with y = x = 0 based on the results presented in (a-f).

As illustrations in Fig. 3.5, we present the results of power enhancement on the *yz* and *xz* planes for truncated dielectric cylinders with transversal lengths (*L*) along the *x* axis. These transversal lengths are $L = 0.4\lambda_0$, $0.6\lambda_0$, and $0.8\lambda_0$, as depicted in Fig. 3.5 a,d, Fig. 3.5 b,e, and Fig. 3.5 c,f, respectively. For completeness, we also provide the results of power enhancement along the propagation *z* axis, shown in Fig. 3.5 g, h, and i, corresponding to each transversal length of $0.4\lambda_0$, $0.6\lambda_0$, and $0.8\lambda_0$, respectively. The different *L* values of finite truncated dielectric cylinders, which have been chosen as an example, enable us to evaluate the impact on the properties of the PNJ. The results obtained show that a PNJ is generated outside the truncated dielectric cylinder in two cases: when the transversal length is $L = 0.4\lambda_0$, the *FL* is $FL = 0.1\lambda_0$, and when the transversal length is $L = 0.8\lambda_0$, the *FL* is $FL = 0.08\lambda_0$. However, for the case with a transversal length of $L = 0.6\lambda_0$, the *FL* is located inside the dielectric. As the length of the truncated dielectric cylinder increases, the power enhancement also increases due to the increased refraction of light, as seen in Fig. 3.5 g, h, and i. Consequently, a modification in the length of the truncated dielectric cylinder impacts the position of the PNJ, in agreement with what was reported in [143,183]. These findings demonstrate how finite truncated cylinders can generate PNJs with different *FL*s, depending on the transversal dimension of the dielectric, as expected [182]. Despite using finite 3D configurations, it is important that the results are comparable to those discussed in Fig. 3.4 c,d, which present ideal 2D configurations, particularly in terms of the locations of the PNJs. This indicates that even with the truncation and finite dimensions, the PNJ properties are consistent with those observed in ideal configurations.

3.3 High index dielectric sphere (3D configuration)

In this section, the CST Studio Suite is used to analyse the impact of various factors on the properties of PNJs generated by 3D high index dielectric spheres in order achieve a more realistic design. There are four parts in this section. Firstly, in section 3.3.1, we examine the influence of the full size of the dielectric sphere on PNJ characteristics such as power enhancement and the location of the *FL*. Moving on to section 3.3.2, the effects of varying truncation distances in dielectric spheres on PNJs are investigated. In section 3.3.3, we further explore how dielectric losses affect the position of the *FL*, power enhancement, and spatial resolution of the PNJs. Lastly, in section 3.3.4, we investigate the potential impact of decay distance and shape imperfections of the truncated hemispherical dielectric on PNJ parameters. The results presented in this section enables us to determine the PNJ with a high spatial resolution for use in sensing and imaging systems.

3.3.1 Analysis of difference sphere sizes

As shown in Fig. 2.14, the 3D structure of a full dielectric sphere is surrounded by air. The optical fibre is attached to a full dielectric sphere on the left side. The optical fibre is illuminated from the left using a port that covers the fibre, including both the core and cladding. The wavelength of the light used is λ_0 = 1.55 μm. To maintain consistency with the results presented in section 3.1.1, in which the structure was analysed in ideal 2D scenarios, the same methods are used for this 3D analysis. Specifically, we examine a range of dielectric sizes from $R = 0.55\lambda_0$ to $1.55\lambda_0$, with steps of $0.1\lambda_0$. For the simulation, we considered an electric field (E_y) polarized along the y axis and a magnetic field (H_x) polarized along the x axis, with propagation is along the z axis. Finally, maximum and minimum mesh size for a refined hexahedral mesh were $0.16\lambda_0$ and $0.016\lambda_0$, respectively, as mentioned in 2.3.

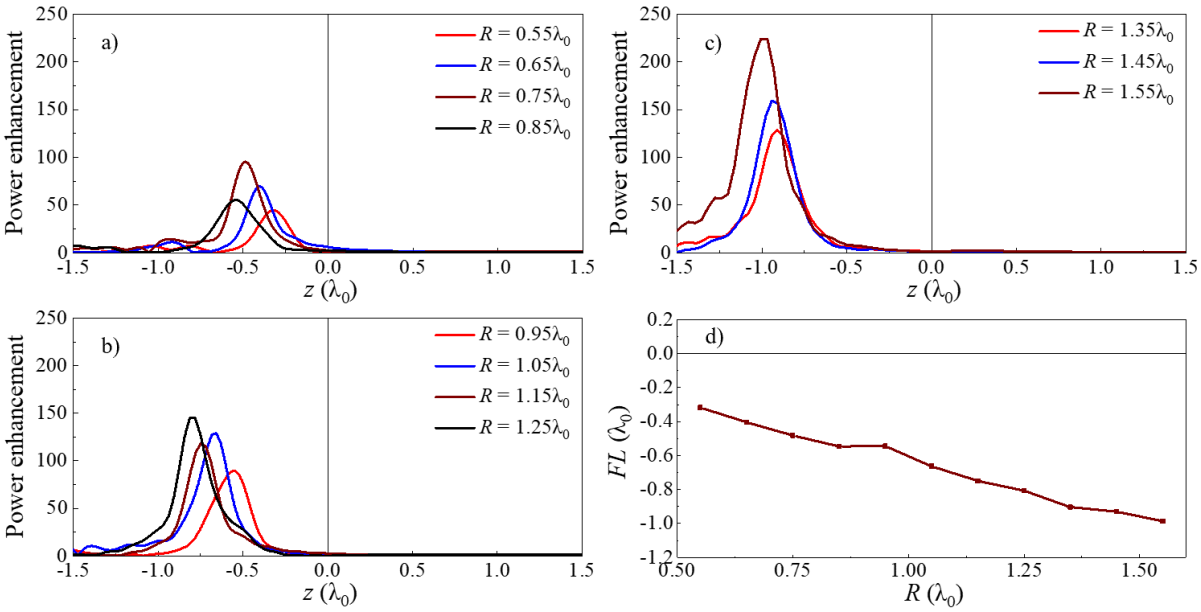

Figure 3.6: The power enhancement along the z axis at x = y = 0 for all the different values of R is shown in (a-c). (d) The FL for all the different values of R, ranging from R = 0.55λ0 to R = 1.55λ0 with steps of 0.1λ0. In (a-c) and (d), the black lines that run vertically and horizontally, respectively, represent the output surface of the full 3D dielectric spheres.

In Fig. 3.6 a-c, we evaluate the power enhancement along the z axis at the centre of the structure ($x = y = 0$). All the *FL*s are generated along the negative z axis, which means that the focal spots are formed inside the dielectric sphere, with varying distances depending on the size of the dielectric sphere. As expected and consistent with the results discussed in section 3.1.1, where full 2D cylinders were used (as depicted in Fig. 3.1), we find that the *FL*s for the full 3D dielectric spheres are also generated within the dielectric. This is due to the relatively high value of the n_d in comparison to n_b. Specifically, the ratio of n_d/n_b is 3.3, which is greater than the value of 2. Consequently, *FL*s are generated within the dielectric spheres [88,128]. Additionally, the results presented here display similarities to the findings we presented at a

conference (refer to appendix C i). However, it is important to note that these results apply specifically to a smaller size of the 3D dielectric sphere, where the formation of *FL*s are inside the dielectric sphere.

In accordance with what has been reported in [76,142], the power enhancement increases as the size of the dielectric spheres increases, because more light waves can contribute to the production of the *FL*. The *FL* distances range from - 0.97λ_0 to - 0.32λ_0 from the outer surface of the dielectric sphere as shown in Fig. 3.6 d. Also, as the size of the dielectric sphere increases, the *FL* moves from a location that is closer to the surface of the dielectric sphere (on the inside of the sphere) to a location further within the dielectric sphere (deeper inside the sphere), which is also in line with what was reported in [94].

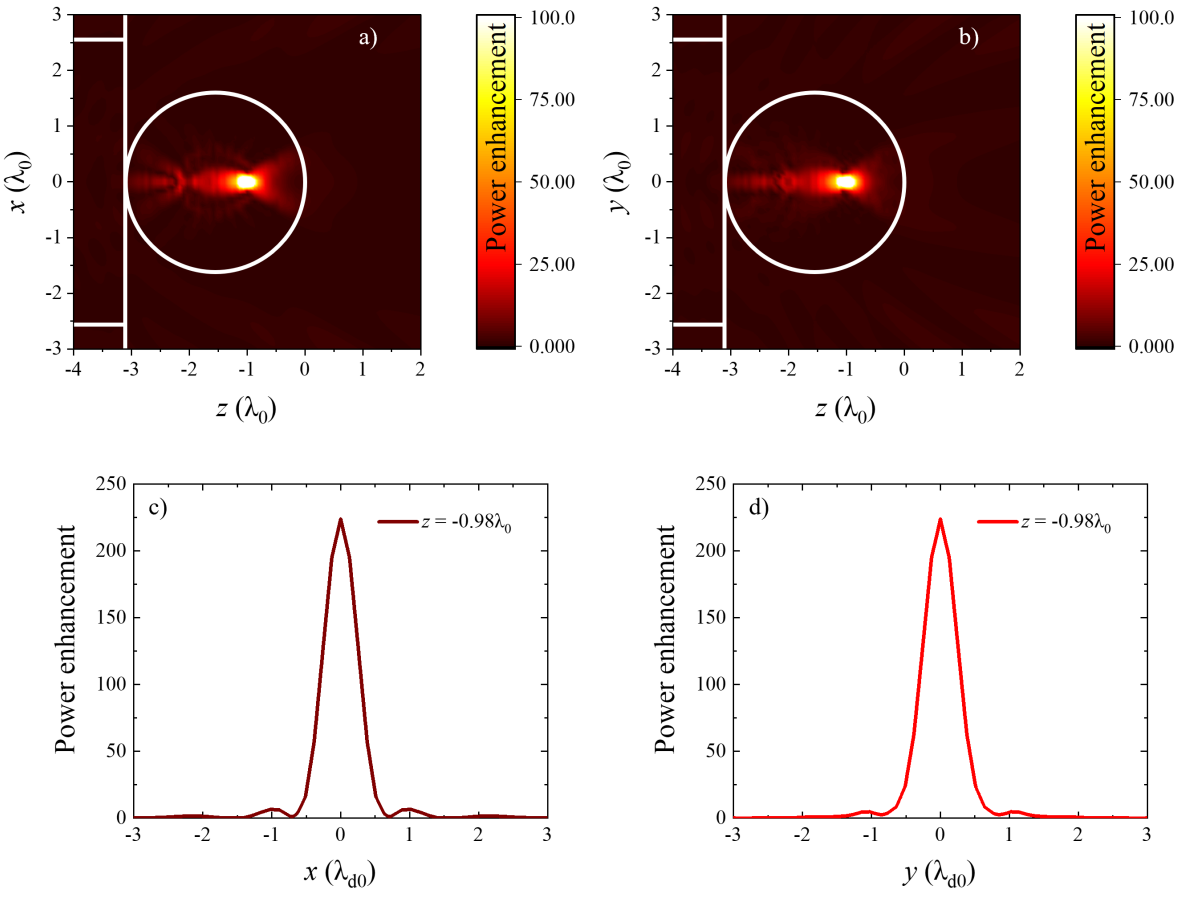

Figure 3.7: (a,b) The power enhancement results are shown on the xz and yz planes for a full 3D dielectric sphere with a radius R = 1.55λ_0. The contour scales are saturated between 0 and 100 to allow better observation of the results. (c,d) The power enhancement extracted from the results in (a,b) is presented along the x and y axes, respectively. The calculations were performed at a specific position along z axis, z = - 0.97λ_0.

In order to be consistent with section 3.1.2, we determined the size of the dielectric sphere to be R = 1.55λ_0. This size, in relation to the wavelength within the dielectric sphere, has a similar scale with the previous results [94]. We find from Fig. 3.6 a-c for R = 1.55 λ_0 that it has

the highest power enhancement. From here, in Fig. 3.7 a,b show the power enhancement in two planes *xz*, *yz* respectively for a dielectric sphere with a radius of $R = 1.55\lambda_0$. We clearly find the *FL* is inside the dielectric as expected and at a distance of $- 0.97\lambda_0$ from the outer surface of the dielectric. The spatial resolution of the focus inside the dielectric was calculated at a distance of $- 0.97\lambda_0$ in the *z* axis and is given by the value $FWHMs = 0.56\lambda_d$ for both *x* and *y* axes where λ_d is the wavelength inside the dielectric sphere, shown in Fig. 3.7 c,d.

3.3.2 Exploring the impact of varying truncation distance on PNJs in truncated dielectric spheres

To move the PNJ from the inside of the dielectric sphere to its output surface, the dielectric sphere is truncated using Eq. 2.18. To do that, we choose the radius of the dielectric sphere to be $R = 1.55\lambda_0$ as mentioned in section 3.1.2. When the dielectric sphere is truncated using Eq. 2.18, the Eq. 2.18 gives a value of $a \approx 0.47\lambda_0$, and then the value of *a* is changed from $\sim 0.39\lambda_0$ to $\sim 0.55\lambda_0$ with steps of $\sim 0.006\lambda_0$ (600 nm to 860 nm with a step of 10 nm). Using this setup, Fig. 3.8 a illustrates the results of the obtained *FL* as a function of the truncated distance *a*. As observed, PNJs are generated inside the 3D truncated dielectric sphere, unlike the ideal 2D situation discussed in section 3.1.2. Furthermore, when the results from Fig. 3.8 a and Fig. 3.3 a are compared, it can be seen that the PNJs in the 3D setup are closer (but still inside) to the output surface than those produced with the 2D setup (between $- 0.06\lambda_0$ and $- 0.02\lambda_0$ from the output surface for the 3D configuration). This is in agreement with what was reported in [94] under planewave illumination where it was demonstrated how PNJs generated inside dielectrics but were able to leak out into freespace.

To determine the spatial resolution of the generated PNJs, the *FWHM* of the power enhancement along the *x* and *y* axes at the output flat surface of the truncated dielectric sphere ($z = 0$) for all values of *a* was calculated as shown in Fig. 3.8 b. The resulting *FWHM* values, as a function of the value of *a*, on the *x* axis (represented by the blue line) ranged from $0.21\lambda_0$ to $0.31\lambda_0$, while those on the *y* axis (represented by the red line) ranged from $0.16\lambda_0$ to $0.21\lambda_0$. All *FWHM* values are less than half the wavelength and this is better than the spatial resolution shown within the full dielectric sphere in Fig. 3.7 c,d. Here, it is observed that the modification of the truncation position has the potential to enhance the convergence or divergence of light as it passes the truncated dielectric sphere. This modification provides a narrower *FWHM*, resulting in improved spatial resolution [159,161,182].

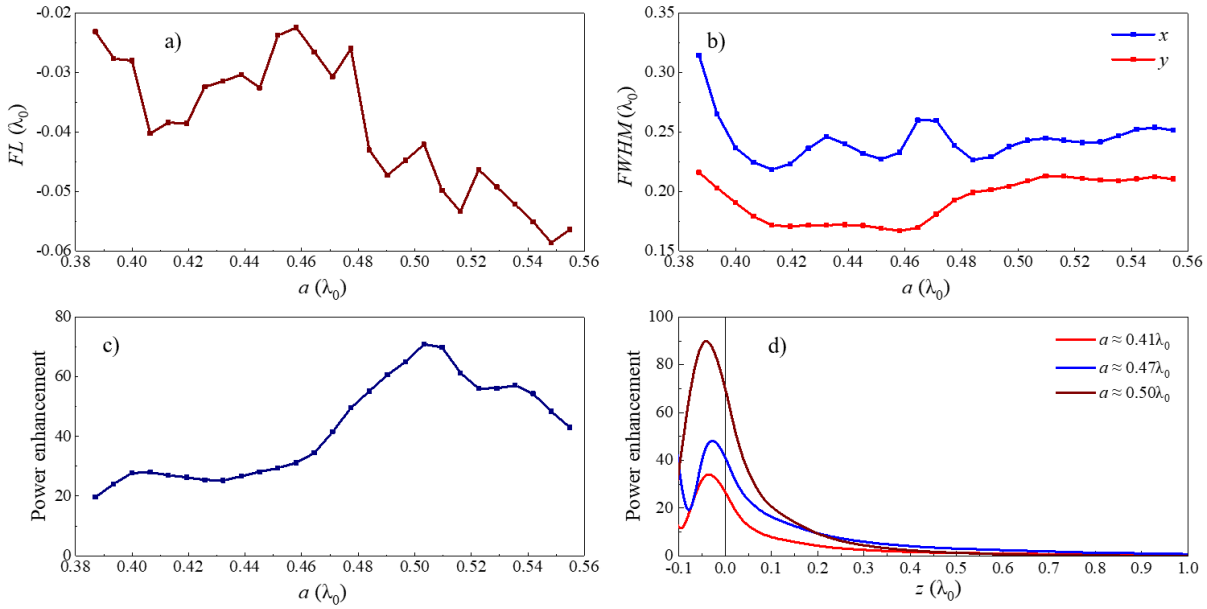

Figure 3.8: (a) Position of the FL for different values of a inside the 3D truncated dielectric sphere. (b,c) FWHM and power enhancement as a function of a calculated at z = 0, respectively, for 3D truncated dielectric spheres with a radius of R = 1.55λ0. (d) When x = y = 0, the power enhancement along the propagation z axis is for a ≈ 0.41λ0, 0.47λ0, and 0.50λ0. The output surface of truncated dielectric spheres is located at z = 0.

We determine the power enhancement at the output flat surface of the truncated dielectric sphere ($z = 0$). As shown in Fig. 3.8 c, the power enhancement values range approximately from 20 to 70 based on different values of a. Fig. 3.8 d presents three examples of power enhancement along the z axis, where the FLs are positioned inside a truncated dielectric sphere. These examples of three different values of the a: one in which a is equivalent to the exact value determined by Eq. 2.18 ($a \approx 0.47\lambda_0$), another in which a demonstrates the highest spatial resolution ($a \approx 0.41\lambda_0$), and the third in which a provides the highest power enhancement ($a \approx 0.50\lambda_0$). For an in-depth examination of the power enhancement along the z axis across all values of a, see appendix C ii. In agreement with what was reported in [66,76], it has been observed that the 3D design provides higher power enhancement of the PNJs in Fig. 3.8 c compared to the case of 2D in Fig. 3.3 c.

The results shown in Fig. 3.8 c provide the highest power enhancement obtained at ~ 70 (at $z = 0$) when the values of parameters R and a were given as $1.55\lambda_0$ and $0.50\lambda_0$, respectively. Fig. 3.9 a,b displays the best power enhancement in xz and yz planes. It is observed that the FL is located within the truncated dielectric sphere, with a portion of it leaking outside the truncated dielectric sphere, as shown in Fig. 3.8 d, as expected [94]. The transverse axes of the power enhancement at $z = 0$ for both x and y are shown in Fig. 3.9 c,d, respectively. The power enhancement on the outside flat surface of the truncated dielectric sphere, specifically at $x = y = z = 0$, is approximately 70 with a spatial resolution of $FWHMx = 0.24\lambda_0$ along the x axis and $FWHMy = 0.20\lambda_0$ along the y axis.

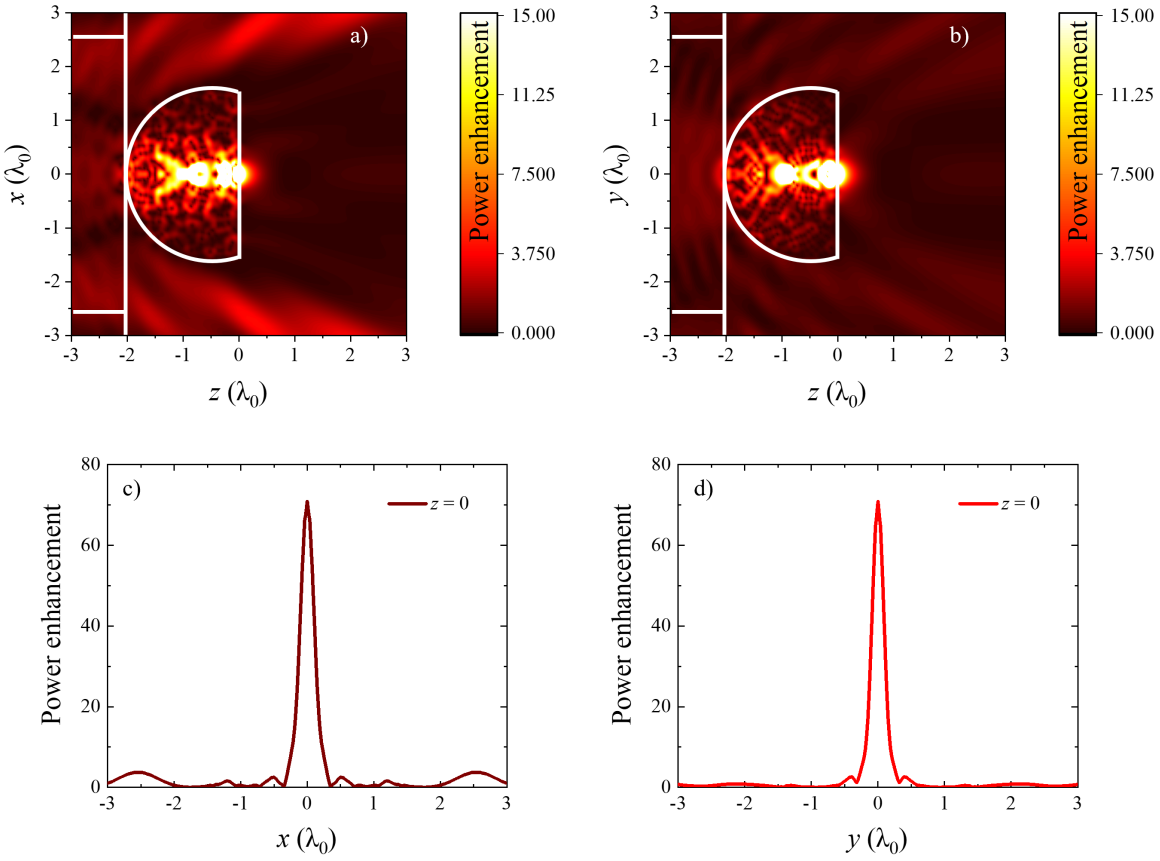

Figure 3.9: (a,b) Power enhancement for the truncated dielectric sphere with $R = 1.55\lambda_0$ and $a \approx 0.50\lambda_0$ on the xz and yz planes, respectively. The contour scales are saturated from 0 to 15, making it easier to view the results and compare them. (c,d) The power enhancement along the x and y axes, evaluated at z = 0, was extracted from (a,b), respectively.

In Fig. 3.8 b, we observed the spatial resolution of different values of a for 3D truncated dielectric sphere. The best structure for $R = 1.55\lambda_0$ can be obtained by taking into consideration the smallest *FWHM* along the x and y axes, resulting in a value of approximately $a \approx 0.41\lambda_0$. Fig. 3.10 a,b depicts the power enhancement on the xz plane (where $y = 0$) and the yz plane (where $x = 0$) for a truncated dielectric sphere with $a \approx 0.41\lambda_0$. This value of a is close to, but not equal to the value obtained from Eq. 2.18, $a \approx 0.47\lambda_0$, as expected the illumination no longer a planewave, as discussed in section 3.1.2. The analysis demonstrated that the design in Fig. 3.10 a,b generated a PNJ within the truncated dielectric sphere that leaks into freespace. To better understand this behaviour, the power enhancement along the z axis in the centre of the structure (where $x = y = 0$) was extracted from Fig. 3.10 a,b and then displayed in Fig. 3.8 d. The PNJ was found to be positioned at $z = -0.04\lambda_0$ and decayed as it exited the output flat surface of the truncated dielectric sphere into freespace at $z = 0$, with a power enhancement of approximately 27 at that position. The spatial resolution of the generated PNJ was analysed in term of wavelength in freespace. In Fig. 3.10 c,d, the power enhancement along the transversal x and y axes at $z = 0$ was plotted (extracted from Fig. 3.10 a,b, respectively). The results

demonstrated that the highest spatial resolution in the x and y axes was obtained for $a \approx 0.41\lambda_0$ with $FWHMx = 0.21\lambda_0$ and $FWHMy = 0.17\lambda_0$ respectively. When comparing the spatial resolution of the result in Fig. 3.10 c,d with the literature review that uses an optical fibre structure, it is seen that Fig. 3.10 c,d demonstrates a higher spatial resolution in comparison to literature review [85,104–108]. The results of this study illustrate the ability to produce PNJs with both high intensity and high spatial resolution at the output surface of a truncated 3D high index dielectric sphere positioned at the end of an optical fibre.

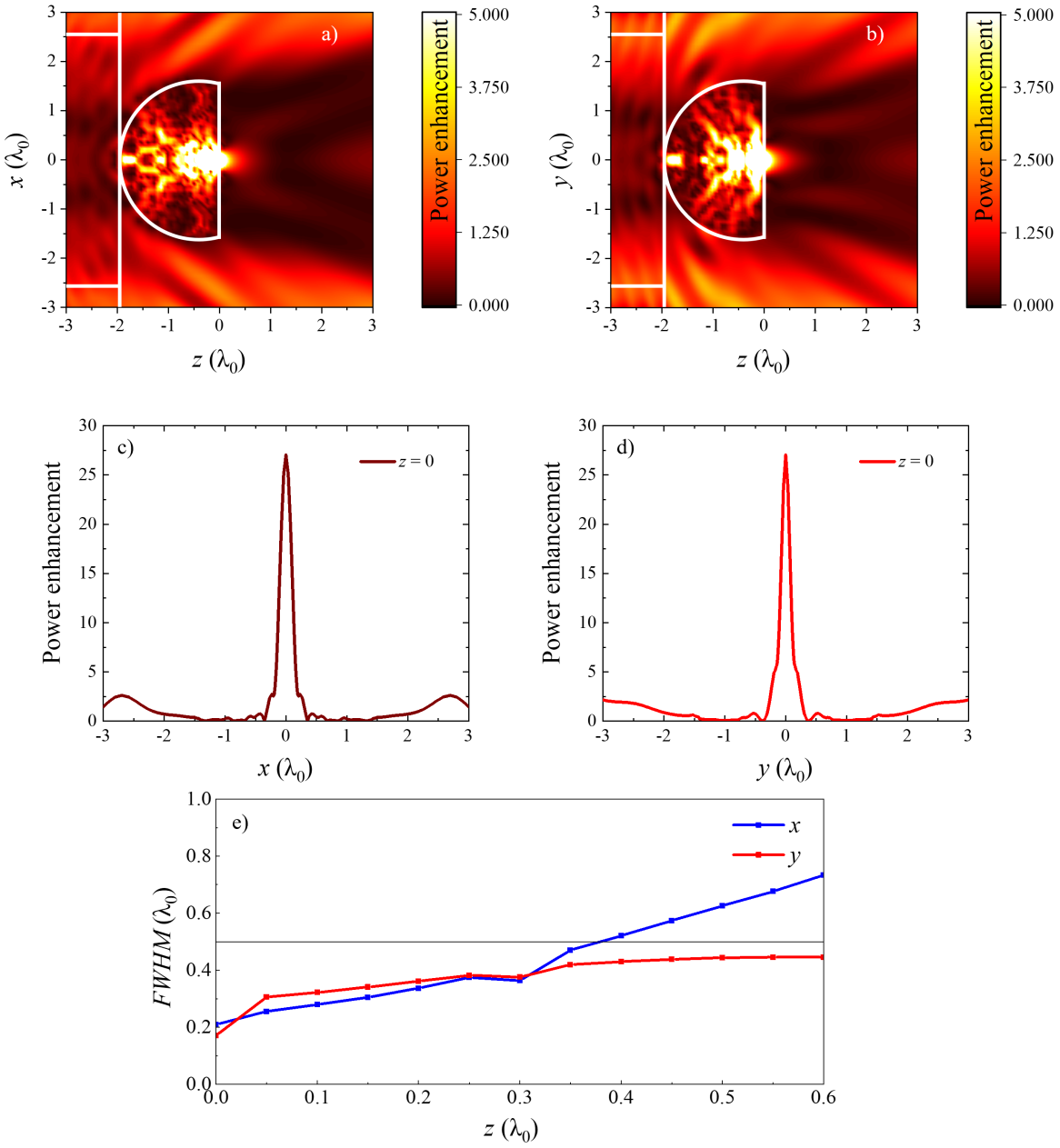

Figure 3.10: (a,b) The power enhancement of a truncated dielectric sphere is presented, with parameters $R = 1.55\lambda_0$ and $a \approx 0.41\lambda_0$ on the xz and yz planes, respectively. To facilitate result visualization and comparison, the contour scales are saturated from 0 to 5. (c,d) The power enhancement along the x and y axes was extracted at $z = 0$ from (a,b), respectively. (e) The values of the FWHMs along the x and y axes as a function along z axis extracted from Fig. 3.8 d at $a \approx 0.41\lambda_0$ is shown. The black horizontal line indicates the point at which the FWHM equals $0.5\lambda_0$.

We analyse the spatial resolution of the PNJ along the z axis (propagation axis) for $a \approx 0.41\lambda_0$. as presented in Fig. 3.8 d. However, as we move away from $z = 0$ and progress towards the positive z axis (i.e., into freespace), the power enhancement gradually decays. This decay of the power enhancement impacts the spatial resolution along the transverse x and y axes. To evaluate the effect of this decay on spatial resolution, we calculated *FWHM* of the power enhancement along the transverse x and y axes at different positions along z axis. These positions along the z axis are from $z = 0$ to $z = 0.6\lambda_0$ with a step size of $0.05\lambda_0$, as illustrated in Fig. 3.10 e. The results clearly demonstrate that the spatial resolution decreases as we move away from the PNJ starting at $z = 0$, as expected [95,110]. However, the spatial resolution along the z axis remains less than half the wavelength of the x axis from $z = 0$ to $z = 0.35\lambda_0$ (approximately 0 to 550 nm). The design depicted in Fig. 3.10 demonstrates its ability to generate a PNJ from a truncated dielectric sphere. The PNJ illustrates high power enhancement and spatial resolution in both the propagation axis and transverse axes, resulting in a spatial resolution of less than half a wavelength. This significant result is consistent with the motivation of this thesis, which is to produce PNJs with high spatial resolution and power enhancement through the use of optical fibres, eliminating the requirement for free-standing dielectrics and improving the practical application potential.

3.3.3 The impact of material losses on PNJ properties

The investigation of the results depicted in Fig. 3.1 to 3.10 has been performed assuming that the truncated dielectrics have negligible losses. In this section, we analyse the effect of dielectric losses on the properties of the PNJ generated by a truncated dielectric sphere. To do that, we selected the best design shown in Fig. 3.10, a 3D truncated dielectric sphere with dimensions $a \approx 0.41\lambda_0$ and $R = 1.55\lambda_0$.

The loss tangent, represented by (tan δ), is a parameter utilized for determining the loss or dissipation of energy in a dielectric material when illuminated by electromagnetic waves. In the case of a dielectric material that does not exhibit magnetic properties, the tan δ is the ratio of the imaginary part of permittivity divided by the real part of permittivity [184,185]. Fig. 3.11 depicts the results of including dielectric losses ranging from tan δ values of 0.005 to 0.03 with steps of 0.005. The power enhancement along the propagation z axis decreases as tan δ increases, and the PNJ location changes slightly ($\sim 0.001\lambda_0$) across the full range of tan δ values considered, as depicted in Fig. 3.11 a, as expected [186,187].

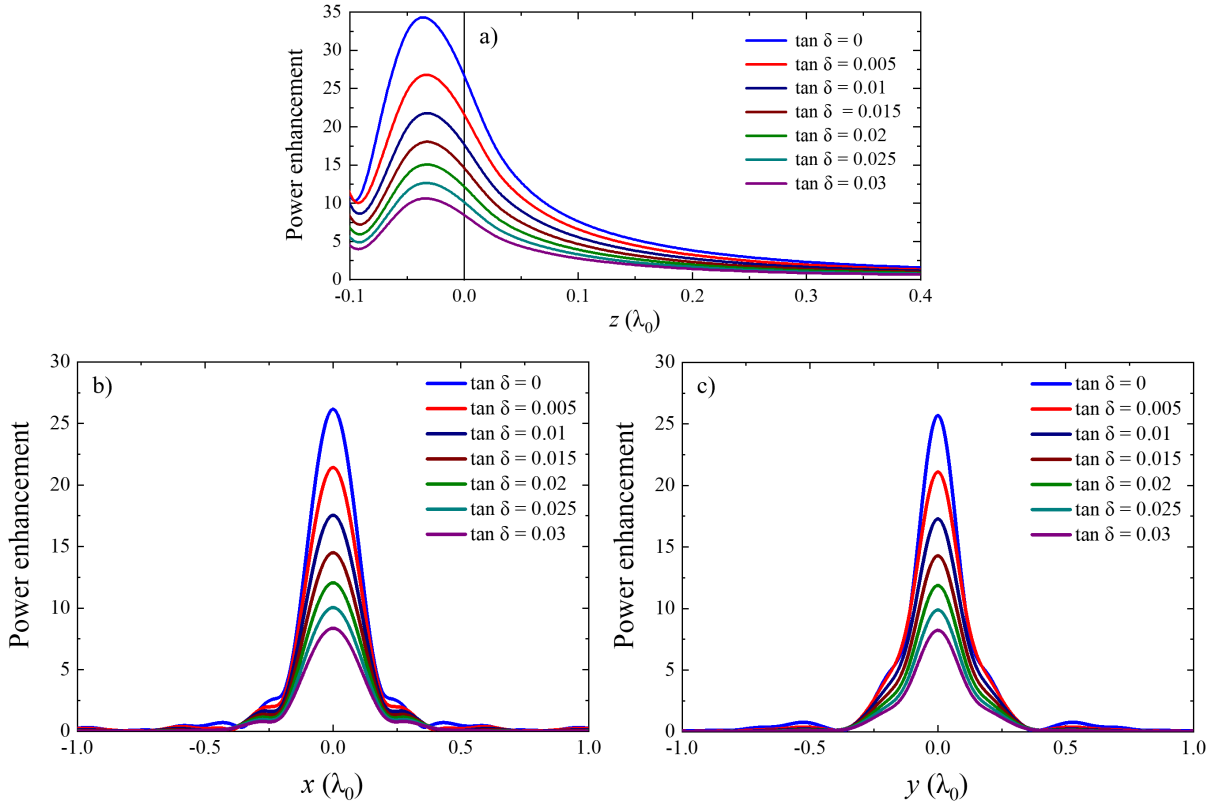

Figure 3.11: (a) Power enhancement along the propagation axis at x = y = 0 for a truncated dielectric sphere when a ≈ 0.41λ₀ and R = 1.55λ₀, as shown in Fig. 3.10, while dielectric losses with tan δ values ranging from 0 to 0.03 in steps of 0.005 are considered. (b,c) Power enhancement for the same different values of tan δ along the transverse x and y axes at z = 0 is presented, respectively.

Furthermore, we examine the impact of introducing losses on the spatial resolution of the generated PNJs by evaluating the *FWHM* of the power enhancement along the *x* and *y* axes (calculated at $z = 0$), as depicted in Fig. 3.11 b,c respectively, for the different values of tan δ. The values of the *FWHM* have been extracted from Fig. 3.11 b,c, respectively, for *FWHMx* and *FWHMy*, and are shown as blue and red lines in Fig. 3.12 a. The resolution of the generated PNJ is affected by dielectric losses, resulting in $FWHMx \approx 0.25\lambda_0$ and $FWHMy \approx 0.18\lambda_0$ for high losses with tan δ = 0.03, as expected. Additionally, the power enhancement values at $z = 0$ are obtained from Fig. 3.11 a with different tan δ values and illustrated in Fig. 3.12 b, where the power enhancement decreases from approximately 27 to 8 as the losses increase. The results demonstrate that as losses increase, the power enhancement of the PNJ decreases. When there is less power enhancement at the PNJ due to these losses, the calculation of the *FWHM* is affected. Specifically, the decrease in maximum power enhancement shifts the position of the full width downwards, thereby increasing the distance along the transverse axes of the PNJ, as explained in Fig. 1.9. However, the overall spatial resolution remains comparable to the scenario without losses. Specifically, the spatial resolution of the generated PNJs remains below

~ 0.25λ_0 in both transversal axes. This demonstrates the ability of the structure to generate PNJs when including the dielectric loss.

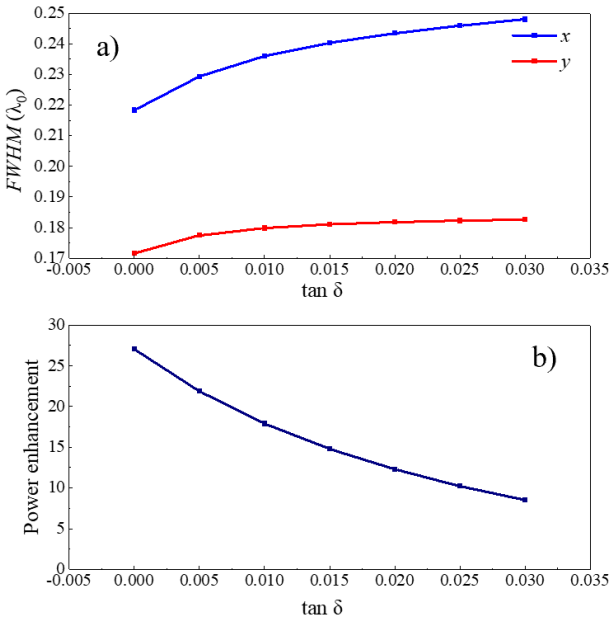

Figure 3.12: (a) The FWHM values for the x (blue) and y (red) axes are displayed with different tan δ values ranging from tan δ = 0 to 0.03 with a step size of 0.005. These calculations are determined at z = 0 for a truncated dielectric sphere with a ≈ 0.41λ_0 and R = 1.55λ_0. (b) The power enhancement is determined at z = 0 using the same tan δ values as in (a).

3.3.4 Effects of imperfections on the truncated hemispherical dielectric on PNJ and decay distance

From an experimental viewpoint, it is crucial to investigate the impact of potential imperfections in the shape of a truncated hemispherical dielectric when it is attached to an optical fibre. Various geometrical errors may arise, such as a non-fully flat output surface, a non-fully spherical back surface, or an imperfect curvature of the radius (deviating from a perfect hemisphere). To show the impact of possible fabrication imperfections, we examine a modified structure depicted in Fig. 3.13, which includes the addition of a cylinder at the back of the configuration discussed in Fig. 2.9 a. To achieve this, we chose for the best design, as depicted in Fig. 3.10 which is a 3D truncated dielectric sphere with parameters of $a \approx 0.41\lambda_0$ and $R = 1.55\lambda_0$, and we added the cylinder to the back. In this study, we maintain the same refractive index with the 3D truncated dielectric sphere for the cylinder at the back. This configuration not only accounts for fabrication imperfections but also eliminates the requirement of using a fully hemispherical shape for the 3D dielectric. Consequently, there is no need for a single point of the hemisphere to touch the top of the optical fibre, as shown in Fig. 3.10 a,b. By employing this setup, we analyse the effect on the spatial resolution and power enhancement of the generated PNJ while varying the radius (*Rcy*) of the added cylinder. The radius is changed from $Rcy = 0.025\lambda_0$ to $0.925\lambda_0$ with a step size of $0.05\lambda_0$.

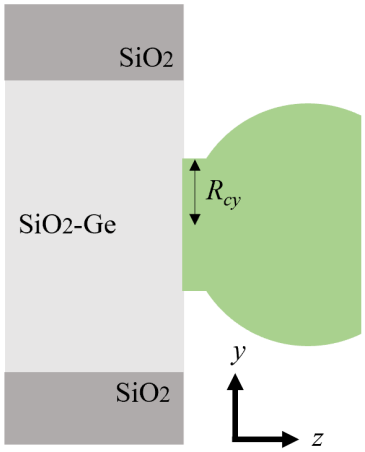

Figure 3.13: Depicts the schematic representation of Fig. 2.9 a, in which a cylinder is added to the back side of the truncated dielectric sphere, denoted by the radius Rcy.

Fig. 3.14 a presents the spatial resolution on the transversal x and y axes at $z = 0$ as blue and red lines, respectively. The obtained results indicate that all designs achieve values of *FWHM* less than $0.25\lambda_0$ and $0.20\lambda_0$ for the x and y axes, respectively. For comprehensive analysis, we also evaluate the power enhancement at $z = 0$, as shown in Fig. 3.14 b. The calculated power enhancement values vary from approximately 27 to 65, depending on the different values of *Rcy* used in the experiments.

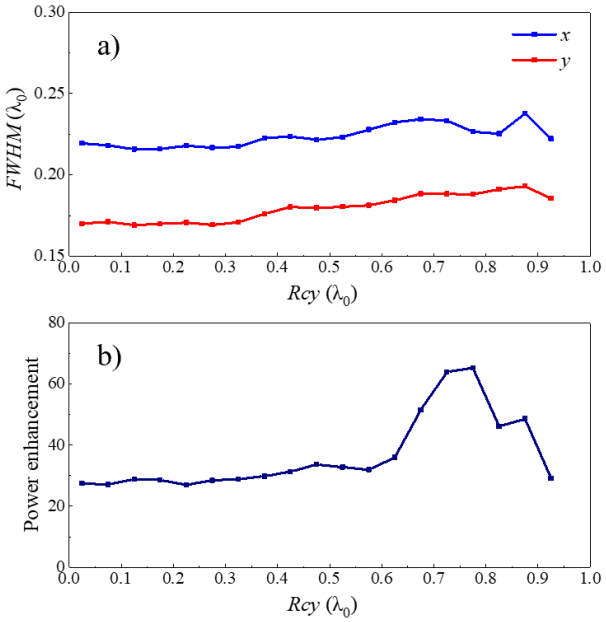

Figure 3.14: (a) FWHM values for the x axis (blue) and y axis (red) are shown with different values of Rcy, ranging from Rcy = 0.025λ_0 to 0.925λ_0 with a step size of 0.05λ_0. These calculations are performed at z = 0 for a truncated dielectric sphere with a ≈ 0.41λ_0 and R = 1.55λ_0. (b) The power enhancement is calculated at z = 0 using the same values of Rcy as described in (a).

A longer decay distance in a PNJ has significant advantages, making it a crucial parameter for a variety of applications [137,174]. For example, it enables the PNJ to have a longer working distance, which is advantageous for applications such as optical sensing and imaging, where

the PNJ must reach and interact with samples situated at a particular distance from the dielectric [139]. In addition, a greater working distance reduces the risk of sample damage because the PNJ can be focused from a respectable distance [131]. Moreover, a longer decay distance enables the PNJ to maintain its narrow width across a longer length, which is advantageous for specific applications including semiconductor and metal PNJ etching and marking [104,135,138]. Additionally, it can enhance imaging performance by preventing the dielectric from getting into interacting with the specimen [140]. In general, the decay distance is an important factor that significantly affects the performance and application of PNJs in a variety of cases. In Fig. 3.15 a, we present a detailed analysis of the decay distance of the PNJ. Specifically, we compare the decay distance of a truncated dielectric structure without a cylinder at the back (Fig. 3.10) with truncated dielectric spheres that have a cylinder of varying radii added at the back (Fig. 3.13). We chose a wide range of cylinder radii values, from *Rcy* = $0.125\lambda_0$ to $0.775\lambda_0$, to include the highest spatial resolution and power enhancement values, as seen in Fig. 3.14.

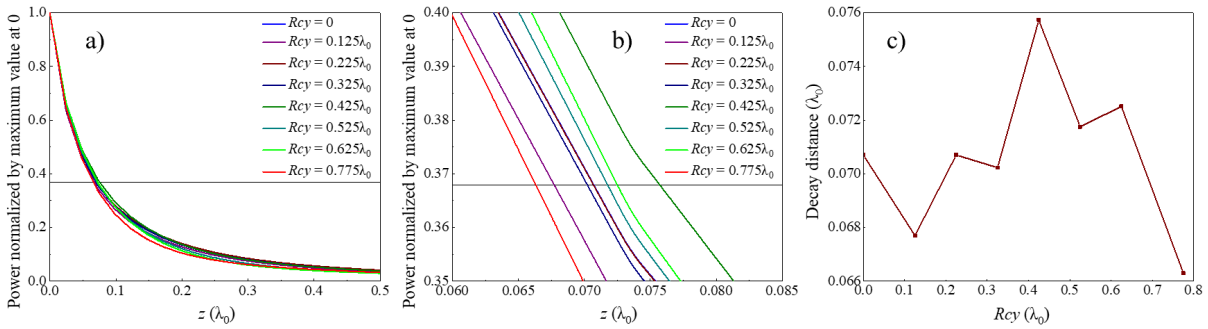

Figure 3.15: (a) Comparison of power distribution decay for truncated dielectric structures with and without a cylinder at the back. The power distribution is normalized by dividing each value by its value at the output surface. The horizontal black line represents the value of 1/e (= 0.367). (b) Zoomed-in view of the decay distance from (a) to show the intersection of the power normalized curves with the 1/e black line. (c) A decay distance as a function of the cylinder radius varies from Rcy = 0 to Rcy = 0.775λ0.

To evaluate the decay distance, we determine the distance from the output surface of the truncated dielectric sphere to the point where the power distribution decreases to 1/*e* (where 1/*e* = 0.367) [183]. In Fig. 3.15 a, we normalize the power distribution values by dividing each value by its corresponding value at the output surface (located at $z = 0$). This normalization sets all values to start at 1, providing a relative comparison. The horizontal black line in Fig. 3.15 a represents the value of 1/*e*. To enable a better view of the decay distance, Fig. 3.15 b provides a zoomed-in view, displaying the points where the curves intersect with the 1/*e* line at various locations. In Fig. 3.15 c, we compare the decay distance of a truncated dielectric sphere without a cylinder at the back to the same structure with the addition of a cylinder of radii ranging from *Rcy* = $0.125\lambda_0$ to $0.775\lambda_0$. We observe that adding a cylinder at the back has a slightly impact

on the decay distance of the structure. For instance, the difference in decay distance between a truncated dielectric sphere without a cylinder at its back and the smallest decay distance after adding a cylinder at its back with *Rcy* = 0.775λ_0 is approximately 0.005λ_0. Consequently, the influence of fabrication imperfections on the decay distance of the structure is negligible when adding a cylinder at the back.

Based on the results shown in Fig. 3.14 a, the impact of the *Rcy* on the spatial resolution of the PNJ generated is negligible for *Rcy* values ranging from 0.025λ_0 and 0.325λ_0. For example, when a cylinder of *Rcy* = 0.325λ_0 is added at the back of the 3D truncated dielectric sphere, the spatial resolution on the transverse axes (*x* and *y*) at *z* = 0, as depicted in Fig. 3.16 c,d, is determined to be *FWHMx* = 0.21λ_0 and *FWHMy* = 0.17λ_0,, respectively. The power enhancement on the *xz* and *yz* planes for this specific value of *Rcy* (0.325λ_0) is illustrated in Fig. 3.16 a,b respectively. Importantly, this resolution is similar to the one achieved without the addition of a cylinder at the back region of the 3D truncated dielectric sphere, as shown in Fig. 3.10 c,d.

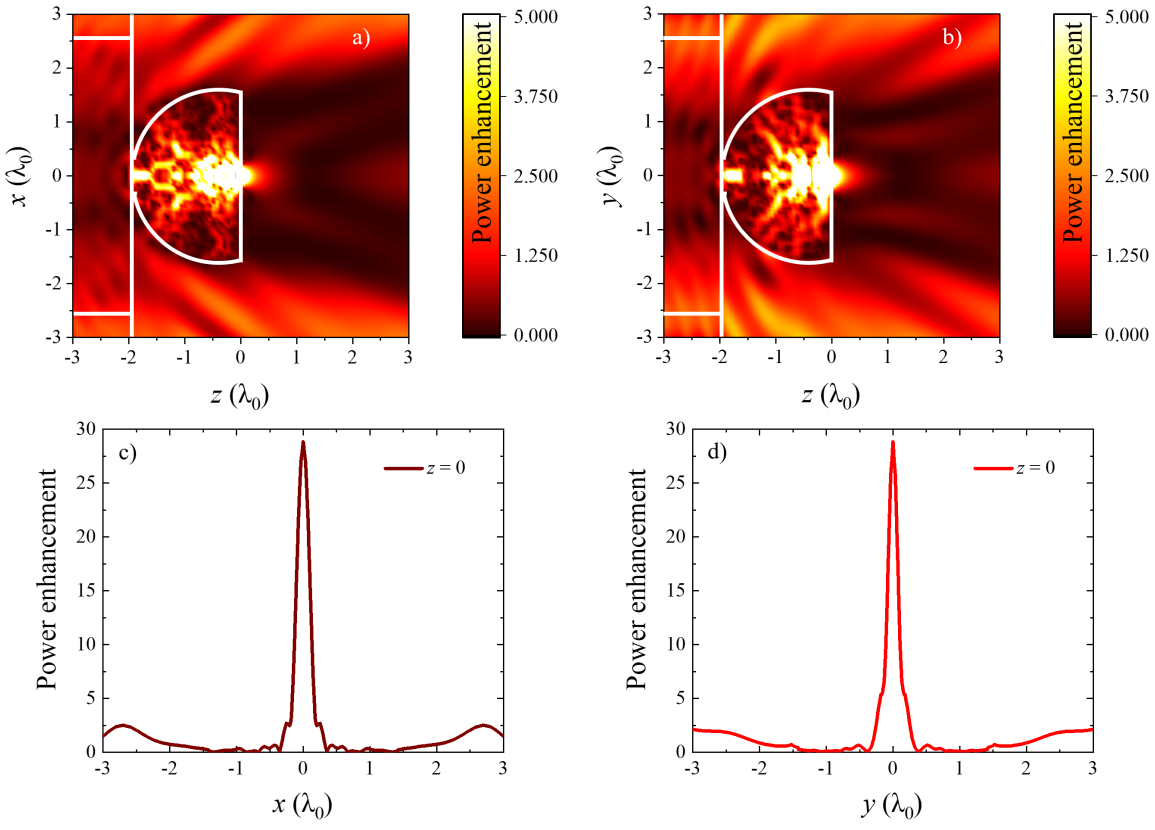

Figure 3.16: The power enhancement resulting from the addition of a back cylinder with a radius of Rcy = 0.325λ_0 to the truncated dielectric sphere with a ≈ 0.41λ_0 and R = 1.55λ_0 is calculated in four different plots: (a) the xz plane at y = 0, (b) the yz plane at x = 0, (c) the transverse x axis at z = 0, (d) and the transverse y axis at z = 0.

For completeness, we show results similar to those from Figs. 3.16 a-d for Fig. 3.17 a-d, but with $Rcy = 0.775\lambda_0$, which represents the highest power enhancement ~ 65. These findings show that the proposed design demonstrates a spatial resolution of $0.22\lambda_0$ along the *x* axis and $0.18\lambda_0$ along the *y* axis, shown Fig. 3.17 c,d. This demonstrates that the structure has the ability to generate PNJs with a high spatial resolution, even when the back surface of the 3D truncated spherical dielectric has imperfect curvature but flat.

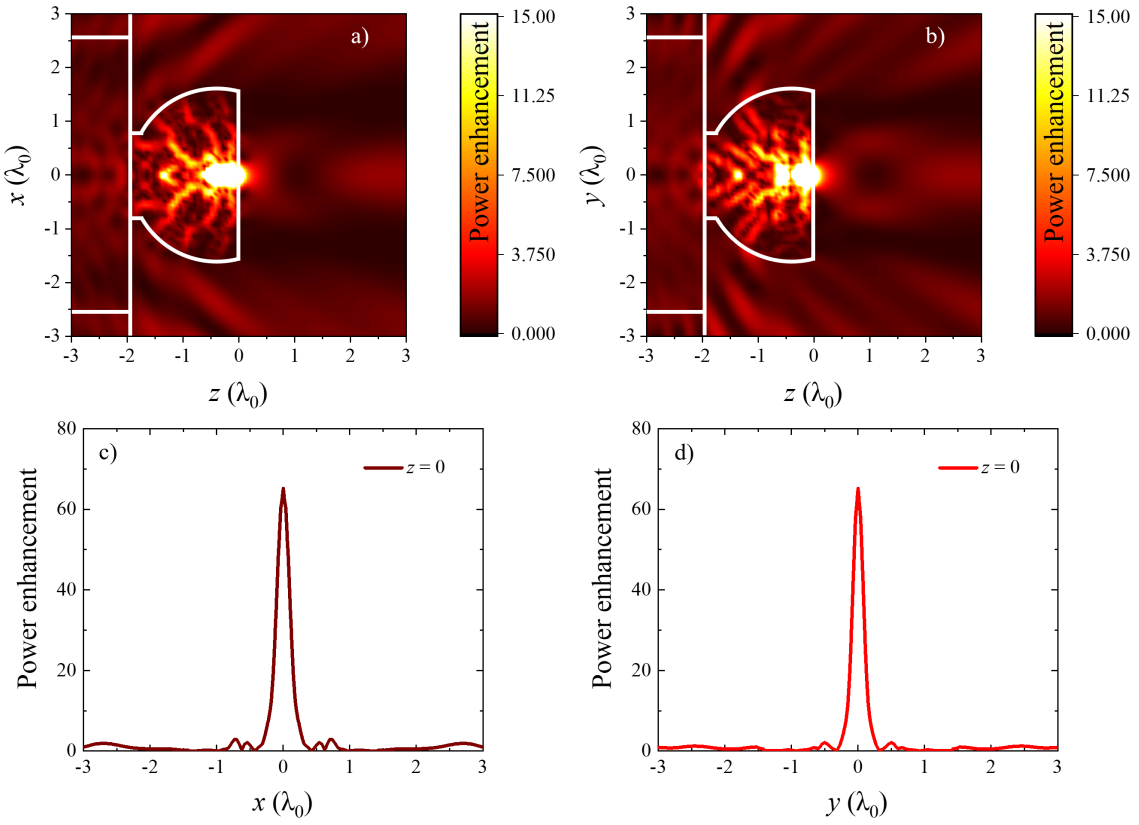

Figure 3.17: The power enhancement resulting from adding of a back cylinder with a radius of Rcy = 0.775λ0 to the truncated dielectric sphere with a ≈ 0.41λ0 and R = 1.55λ0 is evaluated in four different plots: (a) the xz plane at y = 0, (b) the yz plane at x = 0, (c) the transverse x axis at z = 0, (d) and the transverse y axis at z = 0.

In summary, the findings presented in section 3.3 illustrate the potential of utilising 3D high index dielectrics at the end of an optical fibres to produce high spatial resolution PNJs by truncating the profile of the dielectric particles at their output surface. The present study provides an analysis of the impact of dielectric losses and potential fabrication errors on the spatial resolution and power enhancement of the PNJ. The results indicate that although these factors can affect the PNJ's resolution and power enhancement, the *FWHM* of the generated PNJs remains below $0.25\lambda_0$ for all the considered values of losses and fabrication errors.

3.4 Comparison of dielectric cylinder and sphere

The comparison between the different shapes and parameters of dielectric structures demonstrates different properties of PNJs regarding *FL*, *FWHM*, and power enhancement, as shown in Table 1. For the truncated dielectric cylinder, two sets of parameters were selected, as illustrated in Fig. 3.4. With a *R* of $1.55\lambda_0$ and *a* of approximately $0.52\lambda 0$, the *FL* was $0.05\lambda_0$. This positive *FL* indicates that the focal point is generated outside the truncated dielectric cylinder. The *FWHM* was consistent at $0.28\lambda_0$, suggesting stable spatial resolution. Additionally, the power enhancement was four times higher compared to the case without the truncated dielectric cylinder. When the *a* was slightly increased to approximately $0.54\lambda_0$ while keeping the radius constant, the *FL* moved further from the output surface of the truncated dielectric cylinder to be $0.089\lambda_0$. The *FWHM* remained the same at $0.28\lambda_0$, but the power enhancement more than doubled to nine times.

Shape	**Parameters**	***FL***	***FWHM***	**Power enhancement**
Truncated dielectric cylinder	$R = 1.55\lambda_0$ $a \approx 0.52\lambda_0$	$FL = 0.05\lambda_0$	$FWHM = 0.28\lambda_0$	4 times
	$R = 1.55\lambda_0$ $a \approx 0.54\lambda_0$	$FL = 0.089\lambda_0$	$FWHM = 0.28\lambda_0$	9 times
Truncated dielectric sphere	$R = 1.55\lambda_0$ $a \approx 0.41\lambda_0$	$FL = -0.038\lambda_0$	$FWHMx = 0.21\lambda_0$ $FWHMy = 0.17\lambda_0$	27 times
	$R = 1.55\lambda_0$ $a \approx 0.5\lambda_0$	$FL = -0.042\lambda_0$	$FWHMx = 0.24\lambda_0$ $FWHMy = 0.2\lambda_0$	70 times

Table 1: A comparison of the best results in chapter 3 between the truncated dielectric cylinder and the truncated dielectric sphere is presented. The results are compared based on FL, FWHM, and power enhancement. The results presented in Fig. 3.4 were used for the truncated dielectric cylinder, while the results displayed in Figs. 3.9 and 3.10 were used for the truncated dielectric sphere.

In contrast, the truncated dielectric sphere demonstrated different properties of PNJs. With the same *R* of $1.55\lambda_0$ and *a* of approximately $0.41\lambda_0$, the *FL* was $-0.038\lambda_0$, as shown in Fig. 3.10. This negative *FL* indicates that the focal point is generated inside the truncated dielectric sphere. The *FWHM* values varied between the *x* axis and *y* axis, with $0.21\lambda_0$ and $0.17\lambda_0$, respectively, suggesting higher spatial resolution compared to the truncated dielectric cylinder. The power enhancement was significantly higher at 27 times, as expected [66,76].

When a was increased to approximately $0.5\lambda_0$, the *FL* slightly changed to - $0.042\lambda_0$, as shown in Fig. 3.9. The *FWHM* values increased slightly to $0.24\lambda_0$ along the x axis and $0.2\lambda_0$ along the y axis, while the power enhancement increased significantly to 70 times. Adjusting the truncation position can have an impact on the *FL*, spatial resolution, and power enhancement [159,161,182].

In summary, the truncated dielectric cylinder provides a positive *FL* with consistent spatial resolution and a slight change in power enhancement. The focal point is outside the truncated dielectric cylinder, and the power enhancement increases with a small modification in the truncated distance. On the other hand, the truncated dielectric sphere offers a negative *FL*, indicating the focal point is inside the truncated dielectric sphere. It also provides higher spatial resolution with changing *FWHM* values and significantly greater power enhancement, which increases with changes in the truncated distance. Overall, the truncated dielectric sphere demonstrates better results in terms of spatial resolution and power enhancement when compared with the truncated dielectric cylinder, even if they have different *FL* positions.

Chapter 4 Experimental exploration of high spatial resolution photonic nanojets with Ge spheres immersed in optical fibres

In this chapter, we provide an approach to achieve high spatial resolution PNJs of electromagnetic waves at $\lambda_0 = 2$ μm using Ge spheres immersed in optical fibre cladding. The Ge sphere is positioned at the end of the core within the optical fibre, with both the Ge sphere and the core fully immersed in the cladding material. In our method, the structure is used to generate small spot PNJs that have high intensity. When truncating the output profile of the Ge sphere, we demonstrate that the PNJs can be generated at the output surface with a high spatial resolution.

This work is an exploration of simulations and experiments that seek to show the potential of these structures. We demonstrate an evaluation and design process beginning with simulations of 3D Ge spheres and progressing to experimental devices. In section 4.1, the result of changing the full size and truncation distance of Ge spheres on their PNJ properties is evaluated. In section 4.2, the purpose is to create the structures in the photonic lab, specifically to fabricate a Ge sphere that is positioned at the end of the core of an optical fibre. The proposed design opens the door for a new sensing and imaging device with high spatial resolution PNJs. Some results of this design have been participated in the conference [188,189].

4.1 Determine the size and truncation distance of the dielectric prior to the experimental phase

This section examines the performance of the structure by investigating a Ge sphere in 3D using CST Studio Suite. Ge is selected due to its unique properties, such as its ability to respond to a carbon dioxide (CO_2) laser, which makes it appropriate for forming into a sphere [190]. The section is divided into two parts that investigate the results of the Ge sphere with different parameters such as R and a. The investigation of the full Ge sphere immersed in cladding material and illuminated by the core of an optical fibre is presented in section 4.1.1. Section 4.1.2 involves truncating the output profile of the Ge sphere in order to generate a PNJ at the output surface of the truncated high index Ge sphere.

4.1.1 Evaluating the results of different sizes of a full Ge sphere

Our purpose is to investigate the size of the dielectric sphere before performing an experiment. The structure depicted in Fig. 2.9 b illustrates a full dielectric sphere that is

completely immersed in cladding material with ($n_{cladding}$ = 1.44). The selection of this particular design was based on its ability to be fabricated in a photonic lab at Newcastle University, making it simple to control the dielectric sphere within the cladding material. The choosing of the dielectric material is determined based on the available equipment in the photonic lab. Ge is a material that has the ability to change its shape when subjected to a CO_2 laser [190]. Therefore, Ge is selected as the optimal material due to its ability to be fabricated into a Ge sphere using a CO_2 laser, as demonstrated in section 4.2.5. Ge has a high absorption at wavelengths used in telecommunications, consequently wavelengths longer than 1.55 μm are utilised [191,192]. In this chapter, we use light with a wavelength of λ_0 = 2 μm since this particular wavelength has the ability to propagate through Ge [193]. The refractive index of the Ge material was found to be n_d = 4.295, while the extinction coefficient is found to be k = 0.0050938 at a wavelength of 2 μm [167].

In order to ensure consistency with the results reported in chapter 3 and the previous findings [94], the same methods in chapter 3 are employed in this study to determine the size of the Ge sphere. Since the refractive index of the Ge sphere and the illuminated wavelength are different from those in chapter 3, the range of Ge sizes will also be different, refer to section 3.1.1 for details. We investigate Ge sizes ranging from $R = 0.55\lambda_0$ to $1.25\lambda_0$, with steps of $0.1\lambda_0$. As a result, we have the ability to examine the range of Ge sizes by taking into consideration both the wavelength in freespace and the wavelength within the Ge sphere. In particular, we investigated the effects of Ge sizes of $R = 0.55\lambda_0$, $0.65\lambda_0$, $0.75\lambda_0$, $0.85\lambda_0$, $0.95\lambda_0$, $1.05\lambda_0$, $1.15\lambda_0$, and $1.25\lambda_0$ on the performance of the PNJs.

In the simulation, the refractive index and extinction coefficient values for the Ge material are utilised by inserting their data from appendix D, Fig. D 2 b,c into the CST Studio Suite. The port in the simulation, attached to the optical fibre, illuminates light with wavelengths that range from λ_{min} = 1.5 μm to λ_{max} = 2.5 μm. It is important to note that this range above the cut-off wavelength λ_c, where λ_c is equal to 1.254 μm as determined by Eq 1.8, results in the optical fibre producing only a single mode. λ_0 = 2 μm is the wavelength selected from the field monitors in the CST Studio Suite. Finally, the electric field is polarised along the y axis, while the magnetic field is polarised along the x axis. The propagation is along the z axis.

The evaluation of the power enhancement along the z axis at $x = y = 0$ is shown in Fig. 4.1 a-c. As expected, [94], all the *FL*s appear inside the Ge sphere at different distances based on the size of the Ge sphere, which is consistent with the results described in Fig. 3.6. This is

because the n_d has a relatively higher value than the n_b. In particular, the ratio of n_d to n_b is 2.98, which is higher than 2. Accordingly, *FL*s appear within the Ge spheres [88,128].

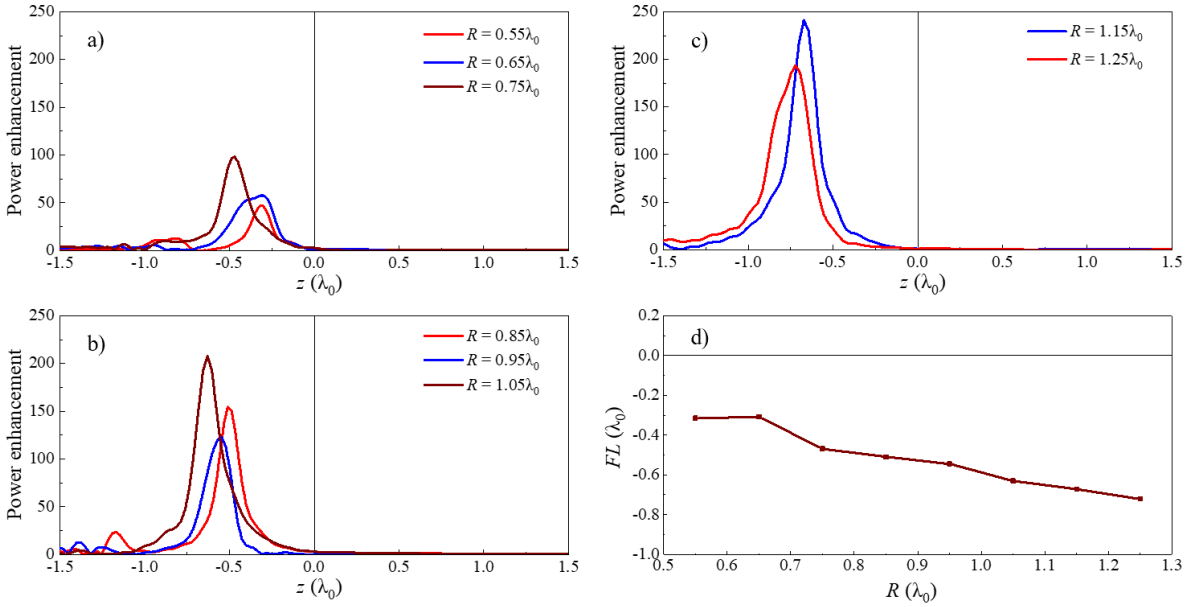

Figure 4.1: The power enhancement along the z axis at the centre of the structure (x = y = 0) is depicted (a-c) for all values of R. These values range from R = 0.55λ₀ to R = 1.25λ₀, with steps of 0.1λ₀. (d) The FLs are shown as a function of all values of R. The output surface of the Ge spheres is represented in (a-c) and (d) by the vertical and horizontal black lines, respectively.

As indicated in Fig. 4.1 d, the *FL* is positioned between - 0.72λ_0 and - 0.3λ_0 from the output surface of the Ge sphere. When examining the result in Fig. 4.1 d and comparing it to the result in Fig. 3.6 d, we observe that the *FL* is closer to the outer surface of the Ge sphere in Fig. 4.1 d, as a result of the slight difference in ratio between n_d and n_b. The *FL* also shifts from a point closer to the surface (inside) of the Ge sphere to the centre of the Ge sphere, as the size of the Ge sphere increases in Fig. 4.1 d, in agreement with what was reported in [94].

4.1.2 Analysis of the results for varying truncation distance of the dielectric sphere on PNJs performance

In order to reposition the PNJ from the inside of the Ge sphere to its output surface, the truncation of the Ge sphere is performed using Eq. 2.18. To do this, the radius of the Ge sphere is selected as $R = 1.15\lambda_0$, ensuring that the wavelength within the Ge sphere aligns with the parameters provided in chapter 3 and previous studies [94]. When the Ge sphere is truncated using Eq. 2.18, it provides a value of $a = 0.385\lambda_0$. Subsequently, the value of a is slight changed from $0.285\lambda_0$ to $0.485\lambda_0$ in steps of $0.005\lambda_0$ to account for the change in illumination from a planewave as discussed in chapter 3.

The impact of truncating the Ge sphere on the *FL* as a function of the truncated distance a is shown in Fig. 4.2 a. Depending on whether the *FL* is positioned inside or outside the

truncated Ge sphere, the difference in the value of a can be divided into two parts. When a ranges from $0.305\lambda_0$ to $0.485\lambda_0$, the *FL* is generated within the truncated Ge sphere. In particular, the *FL* locations shift toward the output flat surface of the truncated Ge sphere as a decreases. The *FL* aligns exactly at the output surface ($z = 0$) of the truncated Ge sphere where $a = 0.305\lambda_0$.

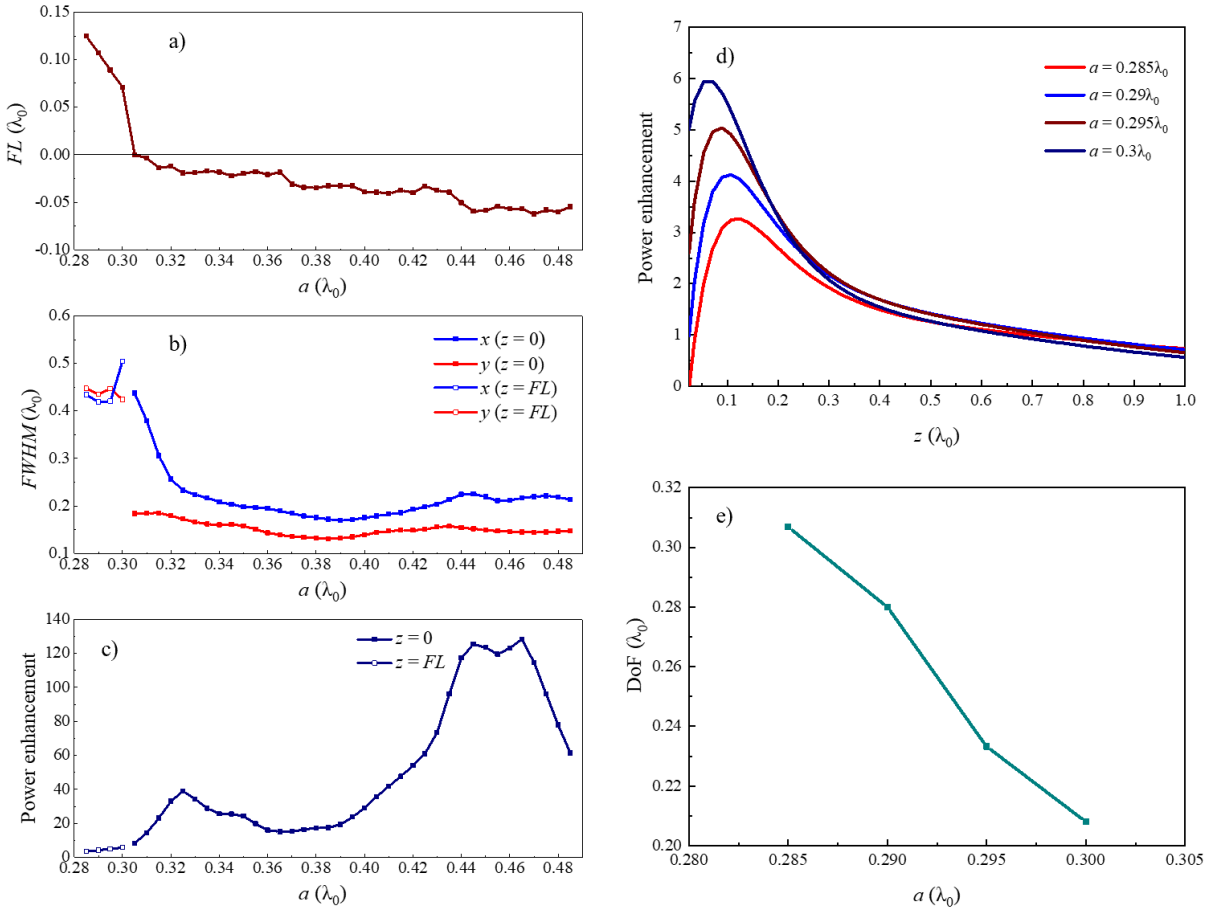

Figure 4.2: (a) For a radius of $R = 1.15\lambda_0$, the FL of a truncated Ge sphere is presented with various a values. The zero on the vertical axis is the output surface of all truncated Ge spheres. (b,c) FWHM and power enhancement calculated at $z = FL$ when the PNJ forms outside of the truncated Ge sphere and at $z = 0$ when the PNJ forms inside of the truncated Ge sphere. (d) The power enhancement along the propagation z axis for a equals from $0.285\lambda_0$ to $0.3\lambda_0$ when $x = y = 0$. $z = 0$ is the location of the output surface of truncated Ge spheres. (e) When the PNJ forms outside of the truncated Ge sphere, the DoF have been calculated from the results shown in (d).

Interestingly, the *FL*s can be obtained outside of the truncated Ge sphere for a values between $0.285\lambda_0$ and $0.3\lambda_0$ along the positive vertical axis. The distance between the surface of the truncated Ge sphere and the outside *FL*s ranges from $0.07\lambda_0$ to $0.12\lambda_0$. As a values increases, the *FL* moves to the output surface of the truncated Ge sphere, which is consistent with the results discussed in Fig. 3.3 a. To better demonstrate these results, we illustrate the power enhancement along the z axis where the PNJ forms outside of the truncated Ge sphere in Fig.4.2 d. It demonstrates that the PNJ shifts towards the output surface of the truncated Ge sphere when the value of a increases. Adjusting the truncation position improves the convergence or

divergence of light as it passes through the truncated Ge sphere, as demonstrated by the production of PNJs at the output flat surface [159,182].

The spatial resolution is determined based on the location of the PNJ. For example, when the PNJ appears outside of the truncated Ge sphere, the *FWHM* of the power enhancement along the transversal *x* and *y* axes is calculated at the location of the *FL* ($z = FL$). However, the *FWHM* of the power enhancement along the transversal *x* and *y* axes is calculated just at the output flat surface of the truncated Ge sphere ($z = 0$) when the PNJ appears inside the truncated Ge sphere and close to its outer surface. The *FWHM* values as a function of all *a* values are depicted in Fig. 4.2 b, where the *x* axis is represented by a blue line and the *y* axis is represented by a red line. The resulting *FWHM* values are ranged from $0.16\lambda_0$ to $0.5\lambda_0$ on the *x* axis and ranged from $0.13\lambda_0$ to $0.44\lambda_0$ on the *y* axis. It has been demonstrated the spatial resolution is higher when the PNJ is generated within the truncated Ge sphere, $a = 0.305\lambda_0$ to $0.485\lambda_0$, compared to the spatial resolution achieved when the PNJ is formed outside the truncated Ge sphere. The reason for this is that the high index of the Ge reduces the wavelength inside the truncated Ge sphere, resulting in a smaller spot size when we calculate the spot size at $z = 0$ [161]. In addition, the power enhancement is determined at the *FL* ($z = FL$) when the PNJ is located outside, and just at the output flat surface of the truncated Ge sphere ($z = 0$) when the PNJ is located inside, as depicted in Fig. 4.2 c. The value of the power enhancement ranges from 3 to 130 depending on the value of *a*. Finally, the DoF is evaluated from the PNJ that is generated outside of the truncated Ge sphere, the DoF being calculated from Fig. 4.2 d and presented in Fig. 4.2 e. As the PNJ moves closer to the output surface of the truncated Ge sphere (as *a* increases), the angle of refraction of the light that exits the truncated Ge sphere increases. The divergence of light outside a truncated Ge sphere increases when the PNJ moves towards the output surface of the truncated Ge sphere, resulting in a decrease in the DoF, which agrees with the findings presented in [159].

We will present the power enhancement in the *xz* and *yz* planes for three different cases. In the first case, the *FL* generated outside the truncated Ge sphere has the highest spatial resolution. The second case has the highest power enhancement. The third case has the optimal structure and produces the highest spatial resolution. Fig. 4.2 b shows that $a = 0.29\lambda_0$ provides the highest spatial resolution of the PNJ outside the truncated Ge sphere. The PNJ is located at a distance of $0.1\lambda_0$ from the outer surface of the truncated Ge sphere as in Fig. 4.2 a. The power enhancement in the *xz* (at $y = 0$) and *yz* (at $x = 0$) planes at $R = 1.15\lambda_0$ and $a = 0.29\lambda_0$ is shown in Fig. 4.3 a,b. The PNJ is clearly generated outside of the truncated Ge sphere. As depicted in

Fig. 4.2 e, this PNJ has a DoF along the propagation z axis of $0.28\lambda_0$. The PNJ has a spatial resolution of $FWHMx = 0.41\lambda_0$ and $FWHMy = 0.43\lambda_0$, as shown in Fig. 4.3 c,d, with a power enhancement of 4. This result demonstrates that the PNJ can be generated outside of the truncated high refractive index dielectric compared to the background $n_d/n_b > 2$. The finding is very similar to the one depicted in appendix C iii, which was presented at the conference [188,189].

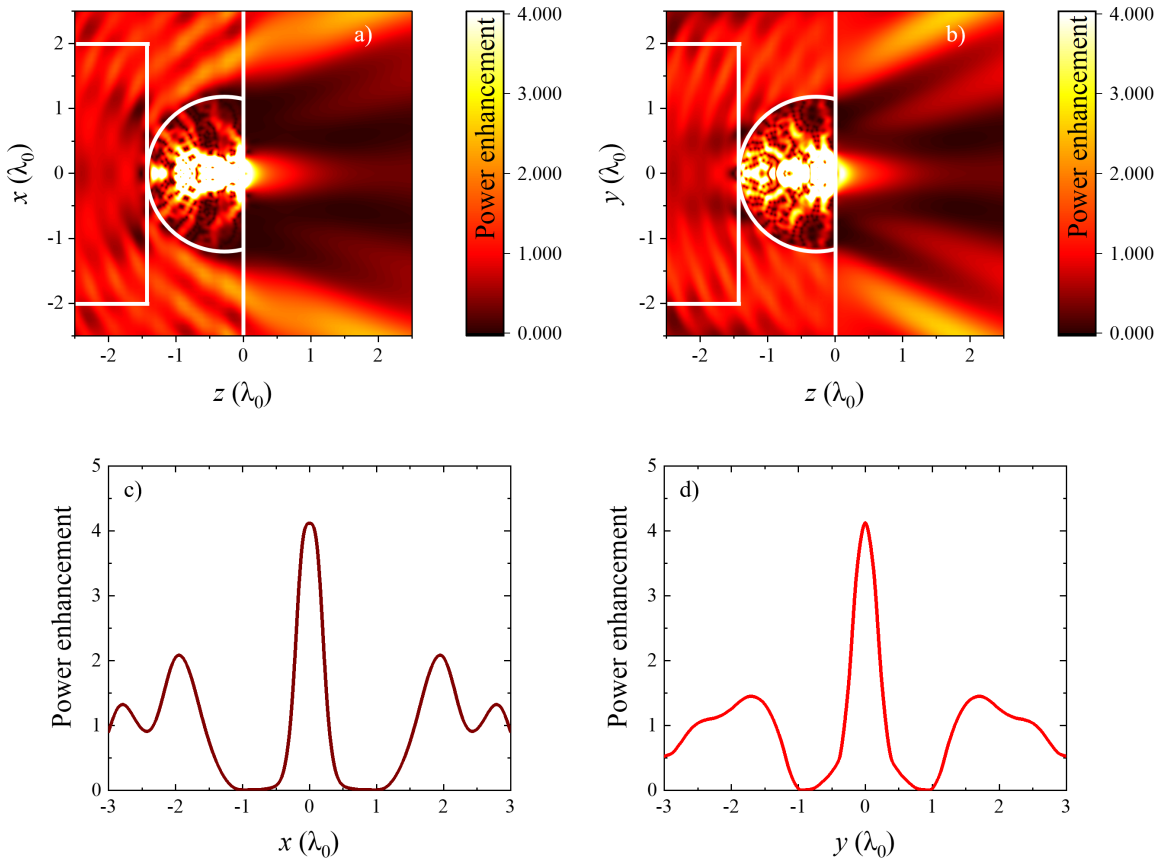

Figure 4.3: (a,b) The power enhancement results for a truncated Ge sphere with $R = 1.15\lambda_0$ and $a = 0.29\lambda_0$ are displayed on the xz and yz planes. The values of the power enhancement scale bar have been saturated between 0 and 4 in order that the results can be observed more clearly. (c,d) The power enhancement is extracted from (a,b) and is displayed along the x and y axes, respectively. The values have been determined at the position of the FL that appears on the output surface, at $z = 0.1\lambda_0$.

The highest power enhancement is observed ~ 130 (at $z = 0$) when the parameters R and a have been set to values of $1.15\lambda_0$ and $0.465\lambda_0$, respectively, as illustrated in Fig. 4.2 c. The results of the best power enhancement is shown in the xz (at $y = 0$) and yz (at $x = 0$) planes in Fig. 4.4 a,b, respectively. It can be observed that the PNJ is located within the truncated Ge sphere. There is a distance of - $0.05\lambda_0$ between PNJ and the output surface in Fig. 4.2 a, and some of the PNJ can be seen leaking out of the truncated Ge sphere. Fig. 4.4 c,d depict the transverse x and y axes of the power enhancement at $z = 0$, respectively. With a spatial resolution

of $FWHMx = 0.21\lambda_0$ and $FWHMy = 0.14\lambda_0$, it can be seen that the power enhancement on the outside flat surface of the truncated Ge sphere, particularly at $x = y = z = 0$, is ~ 130.

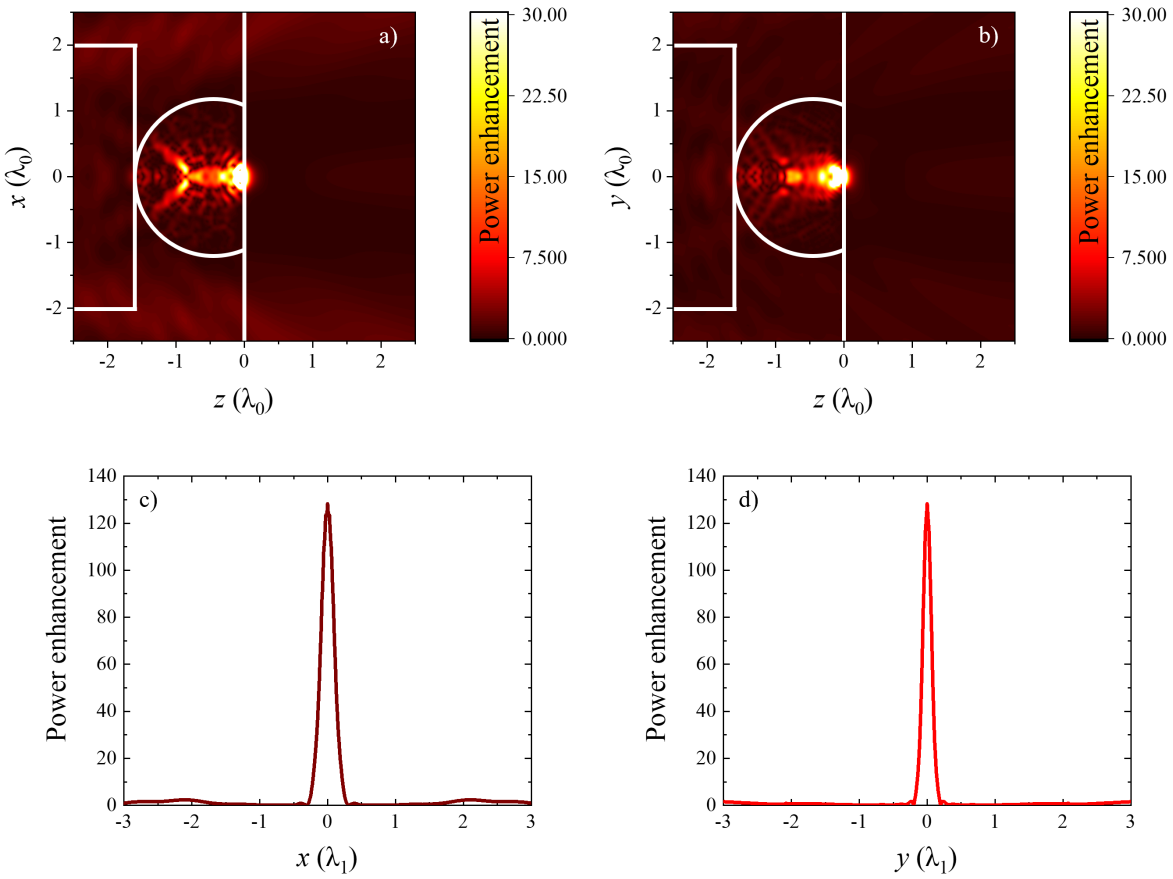

Figure 4.4: (a,b) The xz and yz planes illustrate the power enhancement results for truncated Ge sphere with $R = 1.15\lambda_0$ and $a = 0.465\lambda_0$. (c,d) The power enhancement along the x and y axes, when evaluated at $z = 0$, is obtained from (a,b), respectively.

In this study, a similar method is employed in Fig. 3.10 to determine the best structure. The optimal configuration for $R = 1.15\lambda_0$ can be achieved by considering the minimum *FWHM* values along the x and y axes, leading to a value of $a = 0.39\lambda_0$ as shown in Fig. 4.2 b. The power enhancement for a truncated Ge sphere with $a = 0.39\lambda_0$ is shown in Fig. 4.5 a,b on the xz plane (where $y = 0$) and yz plane (where $x = 0$). The results in Fig. 4.5 a,b showed that the structure produced a PNJ inside the truncated Ge sphere that leaked into freespace. Fig. 4.5 d illustrates the power enhancement along the z axis at the centre ($x = y = 0$) of the structure. The results demonstrates that the position of the PNJ is determined to be located inside at $z = -0.03\lambda_0$. Additionally, it is observed that the PNJ has a decay when it exits from the output surface of the truncated Ge sphere ($z = 0$) into freespace. This decrease has a power enhancement of approximately 19 at $z = 0$. The spatial resolution of the generated PNJ is determined by analysing the power enhancement along the transversal x and y axes at $z = 0$. The values of the

power enhancement are extracted from Fig. 4.5 a,b, and then shown in Fig. 4.5 c. According to the results, $a = 0.39\lambda_0$ produces the best spatial resolution along the x and y axes with $FWHMx = 0.16\lambda_0$ and $FWHMy = 0.13\lambda_0$, respectively. A higher spatial resolution is observed in Fig. 4.5 c when compared to the literature review that employs an optical fibre structure [85,104–108]. The findings demonstrate that it is possible to generate PNJs with high spatial resolution at the output surface of a truncated Ge sphere located at the end of an optical fibre.

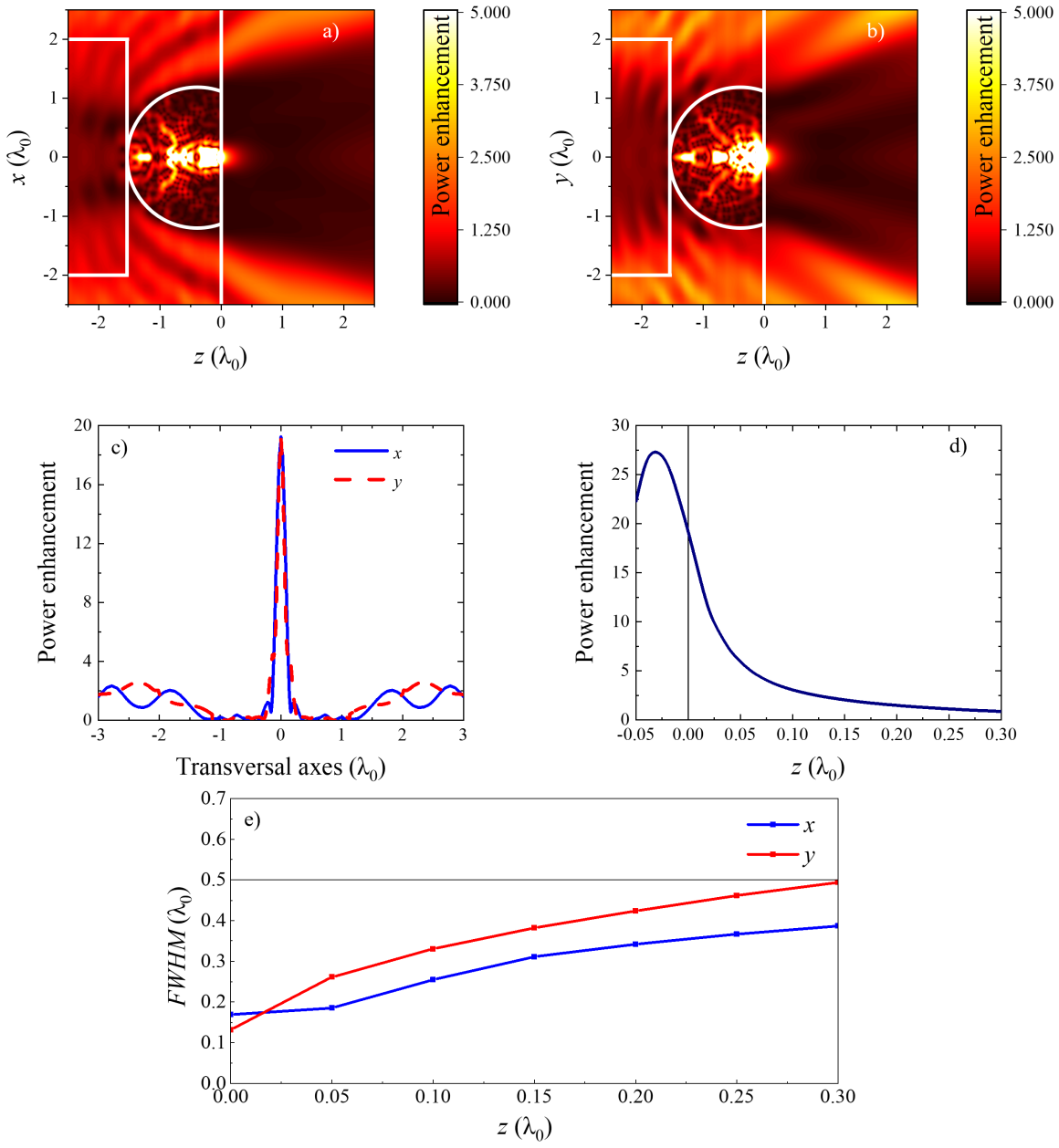

Figure 4.5: (a,b) With the parameters $R = 1.15\lambda_0$ and $a = 0.39\lambda_0$ on the xz and yz planes, respectively, the power enhancement of a truncated Ge sphere is illustrated. (c) At $z = 0$, the power enhancement along the x and y axes, represented by blue and red dashed lines, is extracted from (a,b). (d) From the panels (a,b), the power enhancement along the z axis at $y = x = 0$ is shown. (e) Extracted from (d) are the FWHM values on the x and y axes as a function of the z axis. The horizontal black line represents the location where the FWHM equals $0.5\lambda_0$.

In order to determine the impact of power enhancement decay on spatial resolution, we determine the *FWHM*s of the power enhancement along the transverse x and y axes at various locations along the z axis. As can be seen in Fig. 4.5 e, these locations along the z axis range from $z = 0$ to $z = 0.3\lambda_0$ with a step size of $0.05\lambda_0$. The results indicate that starting at $z = 0$ and moving away from the PNJ, the spatial resolution decreases. This result aligns with our expectations [95,110] and is consistent with the observations presented in Fig. 3.10 e. The motivation of this thesis, detailed in chapter 1, is directly supported by the optimization of the structure described in Fig. 4.5, which generates PNJs using optical fibres, which achieves high spatial resolution and power enhancement.

4.2 Preparing the structure in the photonic lab: preliminary results

In section 4.2, a practical approach is used as the experimental structure is fabricated in the photonic lab at Newcastle University. This section provides an explanation of the fabrication process, illustrating how theoretical ideas are transformed into physical devices. We start by cleaving and filling a large capillary with Ge powder. The subsequent steps involve splicing a large capillary to a small capillary, transforming Ge, tapering capillaries, and using a CO_2 laser to form Ge into spheres. Finally, the Ge lens is spliced with an optical fibre. While these preliminary results are promising, we agree that there were a few challenges during the process, including obtaining the desired spherical shape.

4.2.1 Producing the structure: a step-by-step process

This section provides a simplified overview of the photonic device fabrication procedure. The sections that follow will provide detailed descriptions of each step along with the corresponding results. We start by bringing a large capillary, an empty core diameter of 150 µm +/- 4 µm, a cladding diameter of 363 µm +/- 10 µm (made of silicon dioxide SiO_2), as shown in the Fig. 4.6 a. The reason for using a large capillary is that Ge can be easily filled into an empty core of 150 µm +/- 4 um [194]. The large capillary is filled with Ge. After filling, the large capillary is spliced to the small capillary, as depicted in Fig. 4.6 b. The empty core diameter of the small capillary is 5 µm +/- 2 µm, and the cladding diameter is 363 µm +/- 10 µm (which is made of silicon dioxide SiO_2). Following the splicing process, the Ge material is transferred from the large capillary to the small capillary using a furnace and gas pressure.

The small capillary is then tapered from a cladding diameter of 363 µm +/- 10 µm to a diameter of 125 µm to be equal to an optical fibre. As depicted in Fig. 4.6 c, the Ge (core) diameter will decrease from 5 µm +/- 2 µm to 1.72 µm as a result. When the cladding diameter

of the small capillary approaches the size of an optical fibre (as mentioned in section 2.2.1), the shape of the Ge material changes from cylinder to spheres by using a CO_2 laser, as depicted in Fig. 4.6 d [195,196]. The small capillary containing Ge spheres is cleaved to prepare it for splicing with an optical fibre. As shown in Fig. 4.6 e, the Ge sphere of $R = 1.15\lambda_0$ is positioned at both the end and the centre of the core of the optical fibre. As depicted in Fig. 4.6 f, the small capillary is cleaved again to create just one Ge sphere of $R = 1.15\lambda_0$ at the end of the optical fibre. In the last step, the end of the device is polished until the desired truncated value of $a = 0.39\lambda_0$ is achieved.

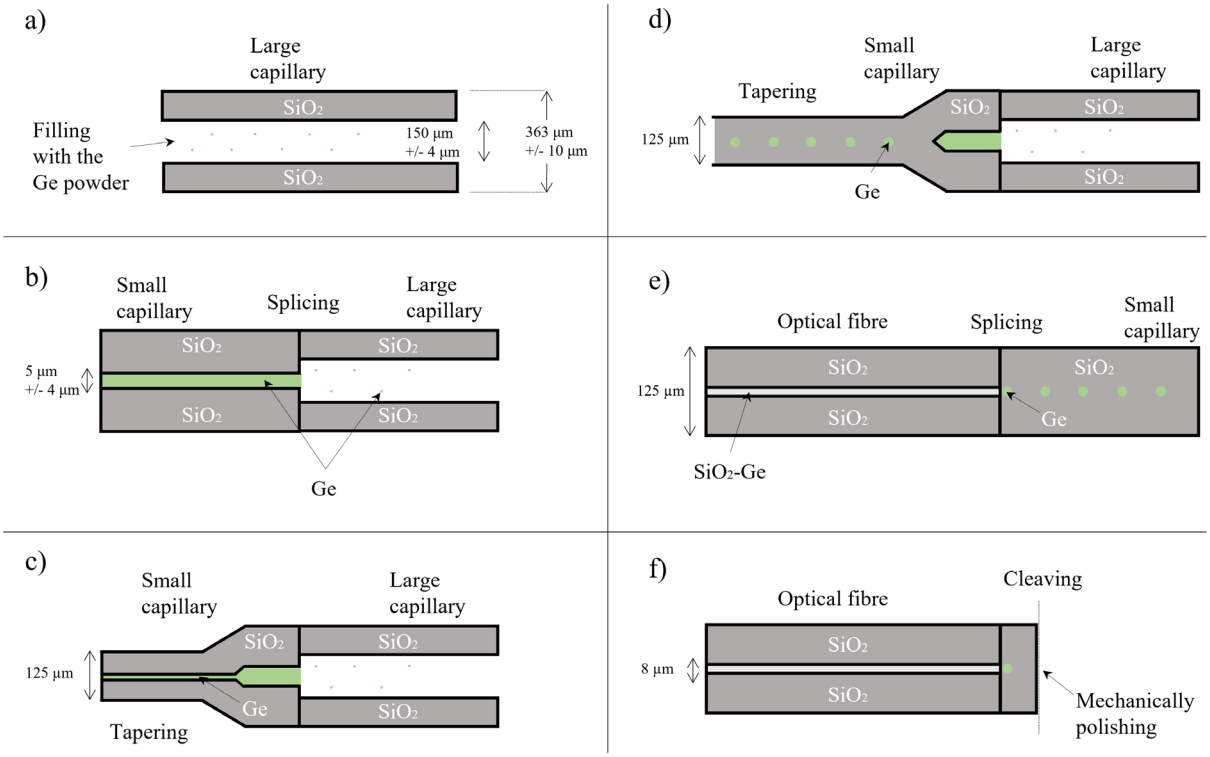

Figure 4.6: From (a) to (f) are presented the steps required to fabricate the device in the photonics lab. (a) The large capillary, which has an outer diameter of 363 µm +/- 10 µm and an inner diameter of 150 µm +/- 4 µm, is filled with Ge powder. (b) The small capillary, which has an outer diameter of 363 µm +/- 10 µm and an inner diameter of 5 µm +/- 2 µm, is spliced to large capillary containing Ge materials in order to transfer Ge material from the large capillary to the small capillary. (c) The same in (b) after the small capillary has been tapered, that contains Ge materials, from the outer diameter of 363 µm +/- 10 µm to 125 µm. (d) The CO_2 laser is utilised to illuminate the tapered small capillary, resulting in a transformation of the cylindrical shape of the core Ge material into a spherical shape. (e) This step involves cleaving the tapered small capillary containing the Ge spheres at the edge of the desired size Ge sphere. Subsequently, the desired size Ge sphere is spliced to an optical fibre, positioning it at the end of the core of the optical fibre. The step from (e) is cleaved again to create a single Ge sphere of the desired size at the end of the core of an optical fibre, which is then polished to the desired value of a.

4.2.2 Preparation: cleaving and filling the large capillary with Ge powder

We begin by cleaving the large flexible fused silica capillary using a scribe to make its end flat, as shown in appendix D (Fig. D.1 a,c). The large capillary has a coating thickness of approximately 20 µm on each side. After the cleaving process, the end of the large capillary must be cleaned to remove the coating before being filled with Ge powder and spliced to a small

capillary (the splicing process will be discussed in 4.2.3). It is necessary to remove the coating since it can affect with following processes, such as adding Ge powder and performing capillary splicing. To clean the large capillary, a Large Diameter Splicing System machine (LDS), shown in Fig. D.1 d,f in appendix D, with appropriate parameters is utilised. The arc control of the machine has been set as it will apply 35 of arc power at the end of the large capillary [197]. Also, the sweep speed of the arc power is set to 250 µm/s, and the length of the sweep is set to 2000 µm. This process turns the large capillary end into pure SiO_2 without any coating.

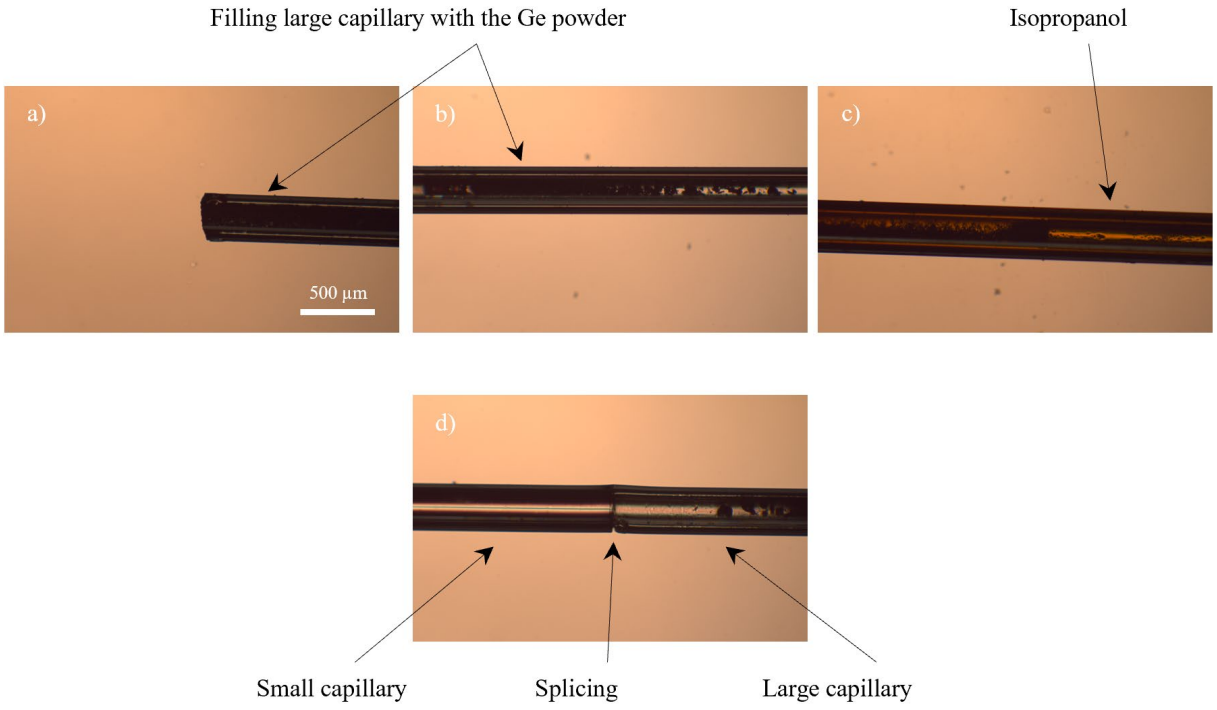

Figure 4.7: The images are taken using an optical microscope in the photonics lab. From (a-c) we can see the large capillary after it has been filled with Ge powder. This sample was imaged immediately as it was filled with Ge powder, therefore the isopropanol is clearly visible in (c). The isopropanol is used to facilitate the entry of the Ge powder into the large capillary. (d) After allowing approximately one day for the isopropanol to evaporate from sample (a-c), it is spliced to a small capillary to transfer Ge material from the large capillary to the small capillary.

After the cleaning is complete, the Ge powder is mixed with isopropanol, as represented in Fig. D.2 a in appendix D [197]. This mixture makes inserting Ge powder into the large clean capillary easy. After the Ge powder has been inserted into the large capillary (as indicated in Fig. 4.7 a-c), the large capillary is allowed to sit for approximately one day to allow the isopropanol to evaporate before splicing the large capillary with small capillary.

4.2.3 Connecting the large capillary to the small capillary for Ge transfer

We performed a splice to connect a large clean capillary filled with Ge powder with a small flexible fused silica capillary. As illustrated in appendix D (Fig. D.1 b), the small capillary has an empty core diameter of 5 µm +/- 2 µm, a cladding diameter of 363 µm +/- 10 µm (made of silicon dioxide SiO_2), and a coating thickness of approximately 20 µm on each side. The use

of a core diameter 5 µm +/- 2 µm is considered acceptable in terms of the practicality of splicing [194,197]. Before splicing, the small capillary had to be cleaved to provide a flat surface. Additionally, we utilised the same cleaning procedure as with the large capillary to remove the coating.

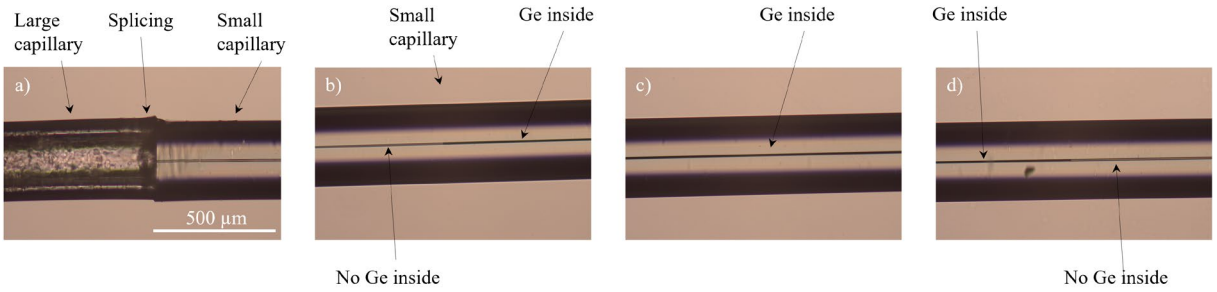

Figure 4.8: (a) After splicing the large and small capillaries together and inserting them into a furnace until the Ge material melts within the large capillary, gas pressure is applied within the large capillary towards the small capillary in order that the melted Ge material can be transferred within 5 µm +/- 2 µm of the small capillary. (b-d) are an extension of (a); the Ge material begins in the middle of the small capillary with a black colour in (b), fills the entire small capillary in (c), and then ends in the middle of (d).

To achieve the splice, an LDS machine was utilised. The prefuse power has been set to 63, and the prefuse time has been set to 0.5 seconds in order to heat both capillaries. Next, we applied an arc power of 65 for 0.4 seconds while pushing the capillaries toward each other at a distance of 30 µm. This step ensured a strong splice. Subsequently, we maintained an arc power of 65 for 2 seconds without applying any pushing force, further securing the splice. Finally, we used a pull distance of 12 µm for each capillaries, pulling them apart for 2 seconds with an arc power of 55. This step allowed for the straightening of the capillaries as shown in Fig. 4.7 d.

After completing the splice, the large and small capillaries are placed in a furnace, with the location of splicing positioned in the centre of the furnace, as shown in Fig. D.1 e in appendix D. The furnace subjects both the Ge material and SiO_2 to a heat level of 1000 degrees. Ge is melted in a furnace heated to 1000 degrees, whereas SiO_2 (cladding) is unaffected because SiO_2 melts at 1100 degrees [190]. The spliced capillaries were left into the furnace for approximately 10 minutes until the Ge powder melted. Following melting, we turned on the gas pressure (argon gas because unreactive) connected to the large capillary side as shown in Fig. D.1 h in appendix D [194]. We applied gas pressure 40 – 50 bar for approximately 15 minutes to facilitate the transfer. The gas pressure pushed the melted Ge into the small capillary, allowing it to flow through the small capillary diameter. Therefore, the gas pressure enabled the transfer of melted Ge from the large capillary to the small capillary, as shown in Fig. 4.8 a-d.

4.2.4 Shaping the Ge cylindrical fibre through tapering

The results presented in this section were achieved through a collaborative effort with Christian Johnson-Richards. After filling the small capillary with Ge, the small capillary is then tapered. The initial diameter of the cladding is around 363 µm +/- 10 µm, and the aim is to reduce it to 125 um until it is similar to the diameter of an optical fibre. For this task, we use an LDS machine that can taper the small capillary. The small capillary is held in place by two handles on LDS machine as shown in appendix D (Fig. D.1 f). While the arc is fixed and applying power, the handles move in the same direction, with one moving faster than the other to allow for tapering. The arc initially generates 70 of power over a 100 µm length to provide heating. Subsequently, the arc power increases to 75 as it reduces the diameter from 363 µm +/- 10 µm to 125 µm along a downward slope length 1000 µm. This higher power level is maintained at 75 over a 3 cm waist length to achieve a 33% diameter reduction. The process then switches to an upward slope, where the arc works on increasing the diameter from 125 µm back to 363 µm +/- 10 µm along a 1000 µm length.

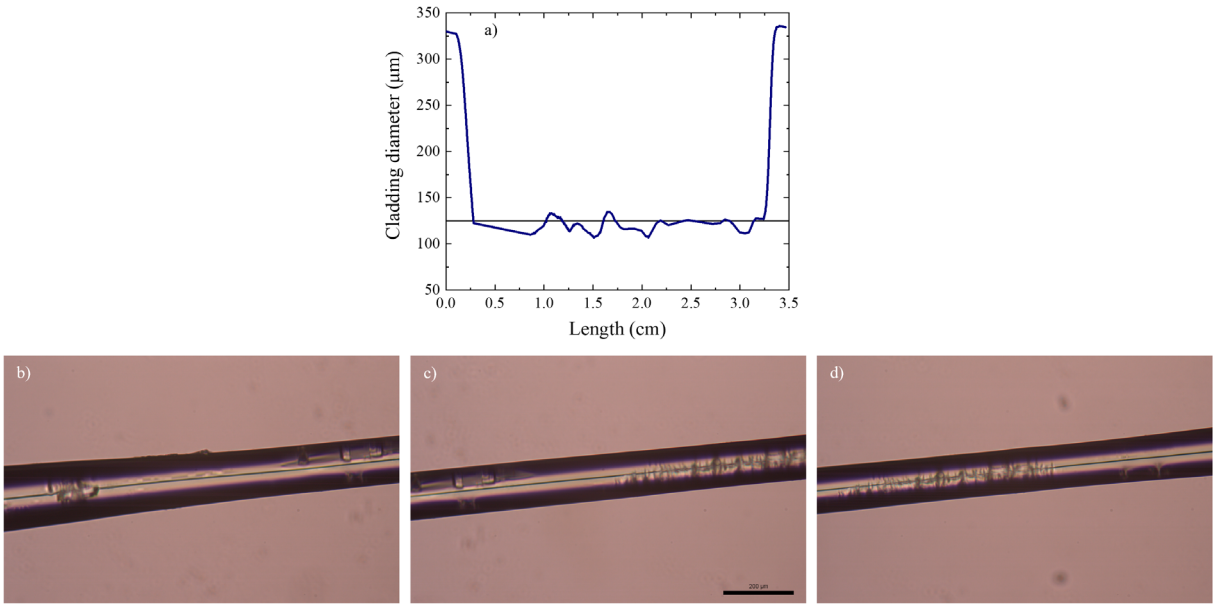

Figure 4.9: (a) The cladding diameter of the small capillary containing the Ge material is tapered from 363 µm +/- 10 µm to 125 µm across a length of approximately 3 cm. (b-d) When the cladding diameter of the tapered small capillary reached 125 µm, which is similar to the diameter of an optical fibre, and the tapered small capillary contained Ge material, three examples are presented.

As a result of these processes, the LDS machine has a taper length of approximately 3 cm, as shown in Fig. 4.9 a, where the data has been extracted from LDS. In Fig. 4.9 a, it is evident that the cladding diameter reaches 125 µm, which is similar to the diameter of an optical fibre. In addition, we display in Fig. 4.9 b-d three points of view taken when the cladding diameter approaches 125 µm. These images provide evidence of an existence of Ge within the

core. To determine the Ge core diameter after tapering, we begin with a cladding diameter of 363 µm +/- 10 µm and taper it down to 125 µm. We can calculate the ratio between the diameters of the cladding before and after tapering and then apply this ratio to the diameter of the core before tapering. This will determine the diameter of the core after tapering. When the cladding diameter reaches 125 µm after tapering, the core diameter is expected to be approximately 1.72 µm.

4.2.5 Formation of a Ge sphere using CO_2 laser

In this step, I collaborated with Luke Stocks to utilize a CO_2 laser, as illustrated in appendix D (Fig. D.1 g). A CO_2 laser is chosen due to the ability it has to transform a cylindrical fibre core into a series of sphere forms [195,196]. We began by placing the small tapered capillary filled with Ge on two holders along its edges. The CO_2 laser adjusts using lenses and mirrors available in the photonics lab to produce a CO_2 laser with a focal point of 565 µm. The sample is then illuminated by moving the two holders from one to the other through the focal point of the CO_2 laser. The speed of the holders has an important role in determining the size of the spheres; accordingly, the slower the speed of the holders, the smaller the spheres [195]. In our experiments, the holders speed is set to 20 µm/s.

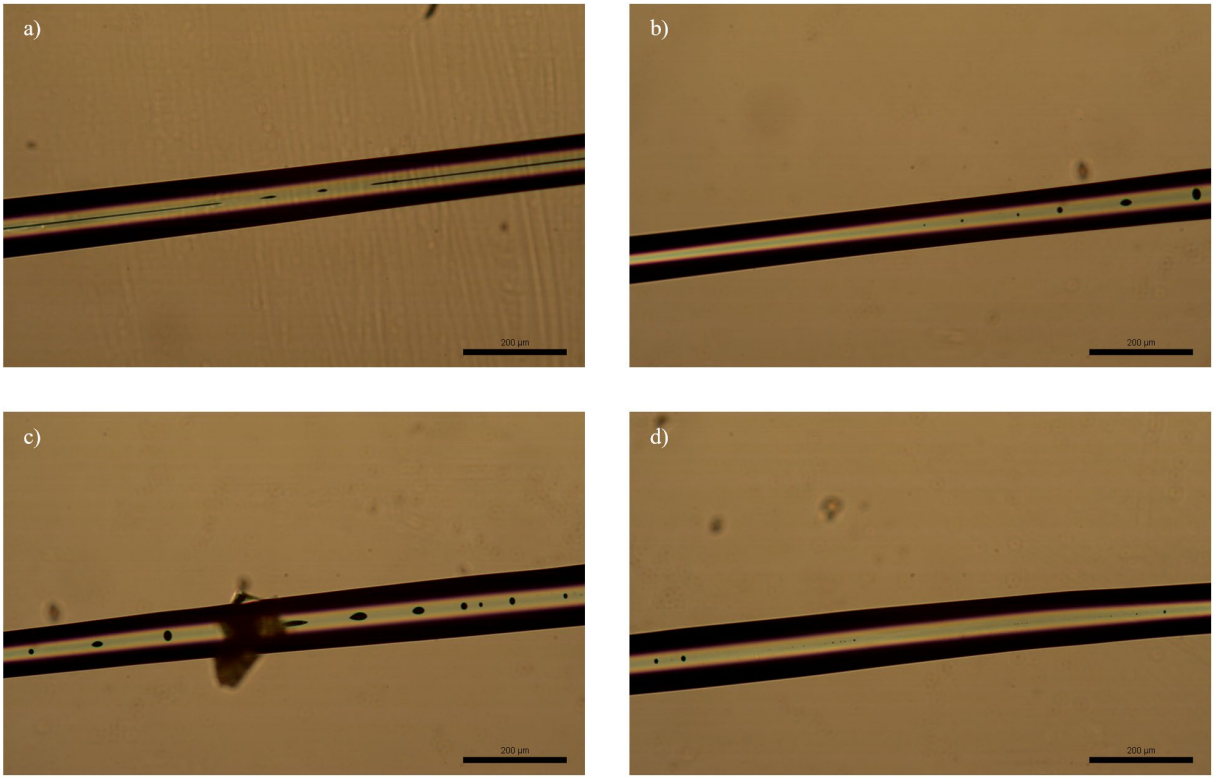

Figure 4.10: (a-d) After subjecting the sample, which is the tapered small capillary containing the Ge material, to the CO_2 laser, a group of lenses in different shapes of Ge material are formed. In (b), the sample contains lenses that are approximately similar in size as the desired lens in Fig. 4.1 c, which are the first three lenses from the left. These three lenses are used to splice with an optical fibre.

We determined the suitable power setting for the CO_2 laser after multiple attempts and carefully testing. It has been observed that 750 mW power is effective, as lower power levels failed to produce spherical shapes, whereas higher power levels caused the whole sample to bend. The size of the cylinder core significantly influences the size of the spheres. As shown in Fig. 4.9 a, the diameter of the cladding is irregular, reflecting the irregularity of the diameter of the Ge core. There are also slight bends in the sample, as depicted in Fig. 4.9 b-c, which influence the location of the Ge core at the focal point of the CO_2 laser. Due to the differences in Ge core diameter and the presence of bend in the sample, we expect the formation of spheres with different sizes and irregular shapes. The sample obtained in the photonics lab is shown in Fig. 4.10 a-d, where we observe the existence of Ge spheres of different sizes and irregular shapes. The first step in implementing sample cleaving is to select the Ge lens size from the sample that closely corresponded with the desired size, as depicted in Fig. 4.5. The first three Ge lenses located from the left side of Fig. 4.10 b have been chosen. The following section 4.2.6 shows cleaving the sample in Fig. 4.10 b and splicing it with optical fibre.

4.2.6 Cleaving Ge spheres from cylindrical fibres and splicing them to an optical fibre

The results in this section were obtained by collaboration with Christian Johnson-Richards. After selecting the sample in Fig. 4.10 b, we perform a cleaving process between the first Ge lens on the left side and the second Ge lens, utilizing the LDS depicted in appendix D (Fig. D.1 j). This specific cleaving point is chosen for ease of splicing each Ge lens with an optical fibre. In Fig. 4.11 a, we can observe the sample after cleaving, containing the second, third, and fourth Ge lenses. Cleaving the sample accurately to form the Ge lens at the end can be quite challenging. Consequently, when splicing the sample to an optical fibre, as shown in Fig. 4.11 b, we observe that the distance between the end of the optical fibre core and the Ge lens is approximately 34 µm. It is important to note that the splicing process can introduce some distortion to the shape of the optical fibre core, as illustrated in Fig. 4.11 b.

The cleaving procedure repeats for Fig. 4.11 b, with the third Ge lens positioned at the end of the sample, as illustrated in Fig. 4.11 c. The third Ge lens is located at the end of the sample, and we carefully splice the sample to an optical fibre from its right side, as illustrated in Fig. 4.11 d. In Fig. 4.11 d, we can observe two Ge lenses, each spliced to an optical fibre. The Ge lens on the right side is clearly attached to the core of the optical fibre. To create the best possible device in the photonics lab, we cleave the sample in the middle, between these two Ge lenses, and make use of the right Ge lens, as shown in Fig. 4.11 e. In Fig. 4.11 e, it is necessary to perform polishing on the right side of the sample until the Ge lens is reached the

end of the sample. When performing a closer examination of Fig. 4.11 e, which has been zoomed in Fig. 4.12 a, it is shown that the Ge lens has an elliptical form.

The Ge elliptic lens in Fig. 4.12 a has the following dimensions: its width on one side measures $1.76\lambda_0$, while its length is $2.4\lambda_0$. The Ge elliptic lens is attached to the core of the optical fibre; however, it is not positioned centrally on its output surface. The Ge elliptic lens is positioned at a distance of approximately $0.8\lambda_0$ from the centre of the core. It is important to note, for splicing reasons such as capillaries heating and pushing, the diameters of both the optical fibre core and cladding are greater than 8 µm and 125 µm, respectively. The diameter of the core, when attached to the Ge elliptic lens, is approximately 11.2 µm and gradually reduces to its normal size of 8 µm. Although the increase in the radius of the core of the optical fibre, it still only supports single mode. Using Eq. 1.6, we determine that the value of V_{number} is 2.11, which is less than 2.405; consequently, a single mode is generated.

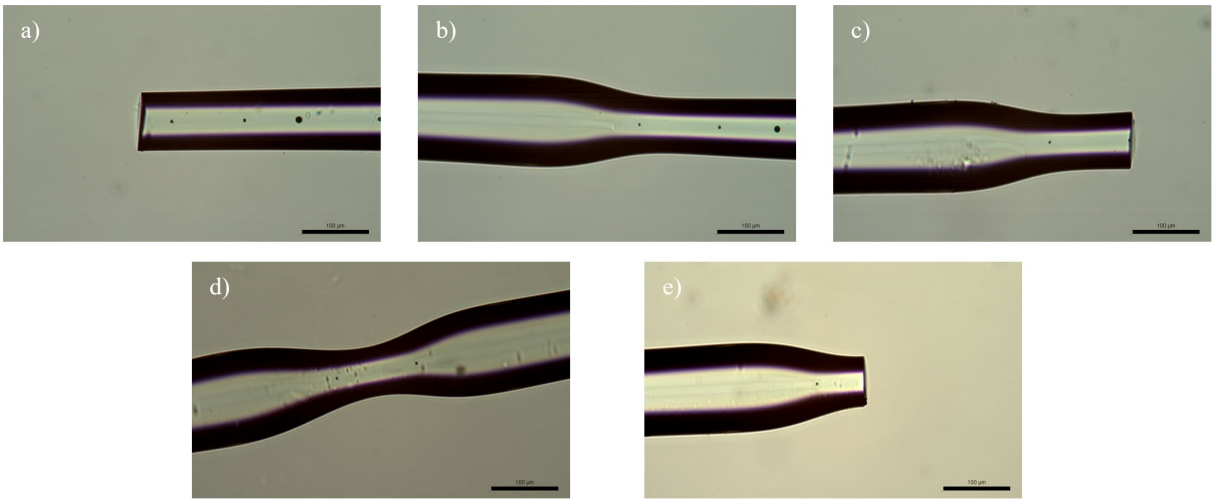

Figure 4.11: (a) The sample in Fig, 4.10 b is cleaved between the first and second Ge lenses, and here we can observe the second, third, and fourth Ge lenses. (b) The left side of (a) is spliced with an optical fibre. Due to the slightly higher refractive index of the core compared to the cladding, the core of an optical fibre can be observed. We can also observe core distortions caused by splicing, and the second Ge lens is 34 µm away from the output surface of the core. (c) The third Ge lens is at the end of the sample where (b) is cleaved directly on the third Ge lens. (d) The right side of (c) is spliced to an optical fibre, and the third lens is placed at the end of the core. (e) The right sample in (d) is depicted, which is cleaved between the two lenses. The light of the optical microscope is increased so that the Ge lens on the end of the core can be observed more clearly.

Since the shape of the Ge lens is elliptical, and it is not positioned at the centre of the end of an optical fibre, the *FL* inside this Ge elliptic lens will be expected to not have a uniform shape and low power enhancement. This is due to the power distribution within a single mode optical fibre is described by a Gaussian beam, as mentioned in section 1.2.1.2 and shown in Fig. 2.11. In Gaussian beam, the power distribution is at its highest value in the centre of the optical fibre and gradually decreases as the power distribution move away from the centre. Since a portion of the Ge elliptic lens aligns with the optical axis, which is in the middle of the

core inside the optical fibre, and another part is located away from the centre of the core as shown in Fig. 4.12 a, the refraction of light within the Ge elliptic lens will have different characteristics.

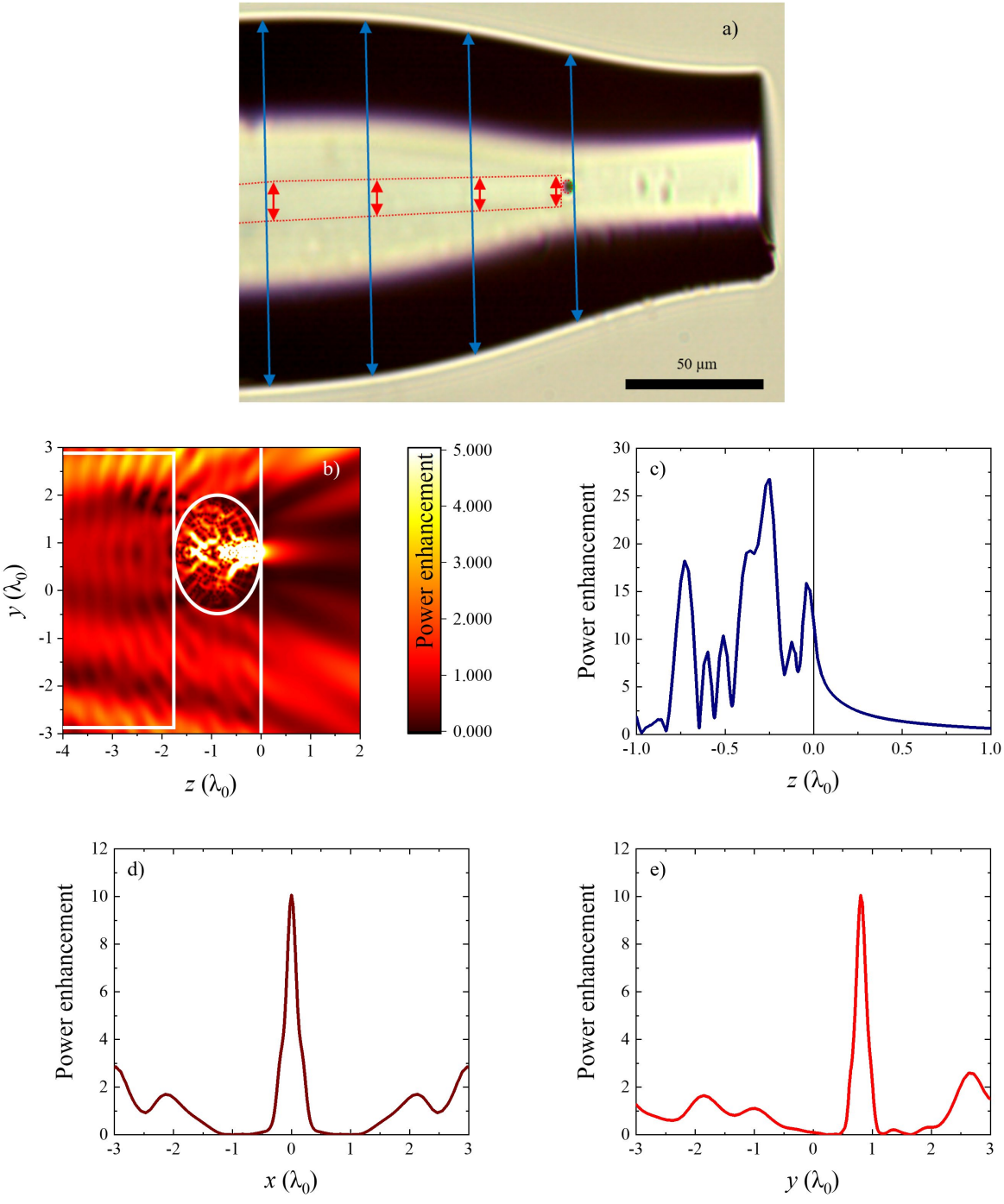

Figure 4.12: (a) The magnified image of Fig. 4.11 e is presented to investigate the size and location of the Ge elliptic lens inside the device, along with the size of an optical fibre after splicing. The red arrows measure the core diameter of an optical fibre, while the blue arrows measure the cladding diameter of an optical fibre. The circumferences of the Ge elliptic lens and core of an optical fibre are indicated by a dashed red line. (b) The structure is simulated by using the CST Studio Suite. The Ge elliptic lens is illuminated on the left by an optical fibre with a wavelength of λ_0 = 2 µm, where z = 0 denotes the output surface of the Ge elliptic lens. The diameter of the core in an optical fibre is defined to be 5.6λ_0. The result illustrates the power enhancement in the yz plane with the centre of the Ge elliptic lens at (x = 0, y = 0.8λ_0, z = - 0.88λ_0). The parameter values for (b) are determined from (a). (c) From panel (b), the power enhancement along the z axis at x = 0 and y = 0.8λ_0 is displayed. (d,e) At z = 0, the power enhancement along the x axis (at y = 0.8λ_0) and the y axis (at x = 0) are illustrated, respectively.

The Ge elliptic lens size shown in Fig. 4.12 a is not the desired size as shown in Fig. 4.5. Before polishing the structure shown in Fig. 4.12 a, we must examine this Ge elliptic lens. The results depicted in Fig. 4.12 b illustrate the simulation result of the sample provided in Fig. 4.12 a, assuming that the sample had been polished until the outer surface of the Ge elliptic lens was reached. Fig. 4.12 b depict a Ge elliptic lens positioned at the output surface of the core of the optical fibre, which has an 11.2 μm diameter. Fig. 4.12 b shows the position of the Ge elliptic lens at a distance of $0.8\lambda_0$ from the centre ($y = 0$) of the y axis, where $x = 0$. Accordingly, the results demonstrate not having of a uniform spot-shaped focus point inside the Ge elliptic lens, as expected. The power enhancement along the z axis as it propagates through the centre of the Ge elliptic lens, where $x = 0$ and $y = 0.8\lambda_0$, is shown in the Fig. 4.12 c. By comparing between the power enhancement depicted in Fig. 4.12 c and the power enhancement illustrated in Fig. 4.1 a-c, it is evident that the power enhancement observed in Fig. 4.1 a-c is higher than Fig. 4.12 c, as expected. This emphasises the importance of aligning the Ge lens exactly at the centre of the core of the optical fibre. To determine the impact of the Ge elliptic lens's position on power enhancement, we examined different positions for the Ge elliptic lens at the end of the optical fibre. The results demonstrate that the power enhancement decreases as the Ge elliptic lens moves away from the centre of the optical fibre, as illustrated in Fig. E.1 appendix E. We clearly observe that the *FL* is not produced outside the Ge elliptic lens, where the outside is in the direction of the positive z axis, as expected since the ratio of the dielectric index of refraction to the surrounding background is greater than two ($n_d/n_b > 2$). When we evaluate the power enhancement at $z = 0$, we find that it reaches the value of 10, which is due to the *FL* generated inside and close to the surface of the Ge elliptic lens at $z = -0.04\lambda_0$. To evaluate the spatial resolution of the generated PNJs, we calculated the *FWHM* of the power enhancement along the x axis (at $y = 0.8\lambda_0$) and y axis (at $x = 0$) at the output flat surface of the Ge elliptic lens ($z = 0$), as depicted in Fig. 4.12 d,e respectively. The obtained spatial resolution values are $FWHMx = 0.22\lambda_0$ at $x = 0$, and $FWHMy = 0.21\lambda_0$ at $y = 0.8\lambda_0$, and the power enhancement is 10. Even though the value of the spatial resolution in Fig. 4.12 d,e is less than half the wavelength, it is not greater than the value of the spatial resolution for the structure we seek in Fig. 4.5.

Given that the Ge elliptic lens is not located in the centre of an optical fibre, it is expected that the PNJs would not achieve high power enhancement. For further details regarding a decrease in power enhancement as the Ge elliptic lens moves from the centre of the optical fibre, see Fig. E.1 appendix E. Fig. 4.13 a depicts the power enhancement in the yz plane (at $x = 0$) for the truncated Ge elliptic lens. Since the width of the full Ge elliptic lens measures $1.76\lambda_0$, we initially employ Eq. 2.18, which provides $a = 0.295\lambda_0$. When the Ge elliptic lens is

truncated, the *FL* appears outside the structure with low power enhancement. Fig. 4.13 b depicts the power enhancement along the z axis at $x = 0$ and $y = 0.8\lambda_0$ in order to represent the *FL*. It is observed that the *FL* of the truncated Ge lens, which has a power enhancement of 1.8, is located at a distance of $0.19\lambda_0$ from the output flat surface. Fig. 4.13 c illustrates the power enhancement along the x axis at the *FL* of the truncated Ge elliptic lens at $y = 0.8\lambda_0$ and $z = 0.19\lambda_0$, while Fig. 4.13 d shows the power enhancement along the y axis at $x = 0$ and $z = 0.19\lambda_0$. As expected, the *FL*s have been shifted from the centre of the structures with spatial resolution values of $FWHMx = 0.63\lambda_0$ at $x = 0$, and $FWHMy = 0.51\lambda_0$ at $y = 0.8\lambda_0$. Finally, we evaluate and compare the results of a Ge elliptical lens, a truncated Ge elliptical lens, a Ge sphere, and a truncated Ge sphere in order to determine whether Ge elliptical lenses work better than Ge spheres. This comparison is illustrated in Fig. E.2, which can be found in appendix E. The comparison of the results obtained from Ge elliptical lenses and Ge spheres demonstrates that the Ge spheres, seen in Fig. 4.5, provide the highest spatial resolution in chapter 4.

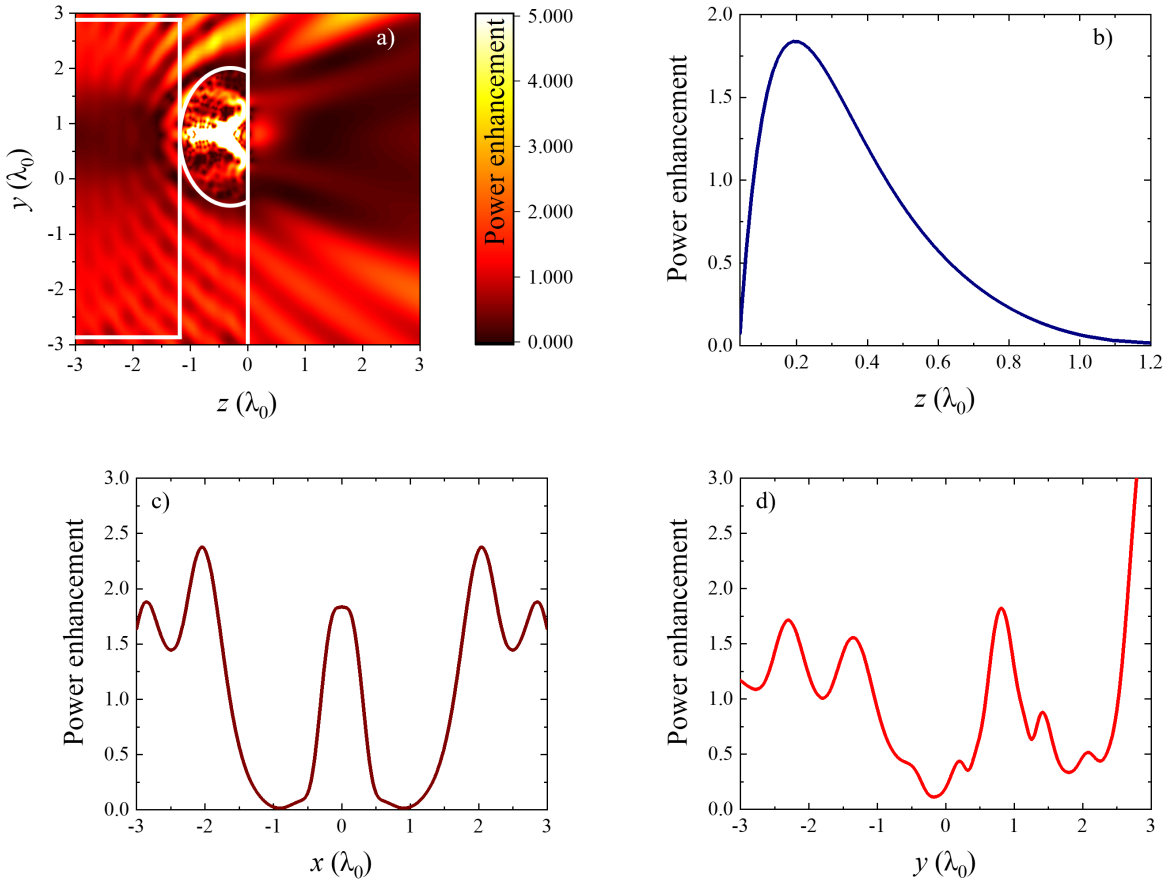

Figure 4.13: The results show the power enhancement in the yz plane for (a) with the same structure as Fig. 4.12 b, but after the full Ge elliptic lens has been truncated. At the point where $x = 0$ and $y = 0.8\lambda_0$, (b) illustrates the power enhancement along the z axis, which is located in the centre of the truncated Ge lens. The output surface of the truncated Ge elliptic lens is located at $z = 0$. (c,d) The power enhancement along the transversal x and y axes at the FL where $z = 0.19\lambda_0$ are displayed, respectively.

As mentioned in section 4.2, it is important to note that the results presented here are preliminary. Further experimental work is required to achieve the desired size, which is producing a Ge sphere with a specific radius, $R = 1.15\lambda_0$. Due to time limitations during the Ph.D stage and the restrictions imposed by the covid-19 pandemic, the results presented in this section 4.2 represent the best achievable results obtained from the photonic lab.

4.3 Comparing truncated Ge spheres and elliptic lenses

Various properties of PNJs with respect to *FL*, *FWHM*, and power enhancement can be observed by comparing different lens shapes and parameters, as shown in Table 2. For the truncated Ge sphere, three sets of parameters were chosen. With R of $1.15\lambda_0$ and a of approximately $0.29\lambda_0$, the *FL* was $0.1\lambda_0$, as shown in Fig. 4.3. This positive *FL* indicates that the focal point is generated outside the truncated Ge sphere. The *FWHM* values were $0.41\lambda_0$ along the x axis and $0.43\lambda_0$ along the y axis, suggesting spatial resolution less than half the wavelength. The power enhancement was four times higher compared to the case without the truncated Ge sphere. When a was increased to approximately $0.465\lambda_0$ while keeping R constant, the *FL* changed to - $0.057\lambda_0$, indicating a shift of the focal point inside the truncated Ge sphere as shown in Fig. 4.4. The *FWHM* values at the output surface of the truncated Ge sphere decreased significantly to $0.21\lambda_0$ along the x axis and $0.14\lambda_0$ along the y axis, indicating higher spatial resolution. The power enhancement achieved 130 times, which was the highest in chapter 4. For the third set of parameters, with a of approximately $0.39\lambda_0$, the *FL* was - $0.032\lambda_0$, indicating the focal point is inside the sphere as shown in Fig. 4.5. The *FWHM* values were $0.16\lambda_0$ along the x axis and $0.13\lambda_0$ along the y axis, with a power enhancement of 19 times. These results show that adjusting the truncation position has a significant impact on the *FL*, spatial resolution, and power enhancement, as expected [159,161,182].

For the Ge elliptic lens, with a width of $1.76\lambda_0$ and a length of $2.4\lambda_0$, the *FL* was - $0.04\lambda_0$ which indicates that the focal point is generated inside the Ge elliptic lens as shown in Fig. 4.12. The *FWHM* values in the x and y axes were $0.22\lambda_0$ and $0.21\lambda_0$, respectively, indicating that the spatial resolution was less than the diffraction limit. The power enhancement was ten times higher compared to the case without the Ge elliptic lens. In the case of the truncated Ge elliptic lens as shown in Fig. 4.13, with the same width and length but with a of $0.295\lambda_0$, the *FL* changed to $0.19\lambda_0$, indicating that the focal point is outside the lens. The *FWHM* values increased to $0.63\lambda_0$ along the x axis and $0.51\lambda_0$ along the y axis, indicating lower spatial resolution. The power enhancement decreased to 1.8 times.

Shape	Parameters	*FL*	*FWHM*	Power enhancement
Truncated Ge sphere	$R = 1.15\lambda_0$ $a = 0.29\lambda_0$	$FL = 0.1\lambda_0$	$FWHMx = 0.41\lambda_0$ $FWHMy = 0.43\lambda_0$	4 times
	$R = 1.15\lambda_0$ $a = 0.465\lambda_0$	$FL = -0.057\lambda_0$	$FWHMx = 0.21\lambda_0$ $FWHMy = 0.14\lambda_0$	130 times
	$R = 1.15\lambda_0$ $a = 0.39\lambda_0$	$FL = -0.032\lambda_0$	$FWHMx = 0.16\lambda_0$ $FWHMy = 0.13\lambda_0$	19 times
Ge elliptic lens	Width = $1.76\lambda_0$ Length = $2.4\lambda_0$	$FL = -0.04\lambda_0$	$FWHMx = 0.22\lambda_0$ $FWHMy = 0.21\lambda_0$	10 times
Truncated Ge elliptic lens	Width = $1.76\lambda_0$ Length = $2.4\lambda_0$ $a = 0.295\lambda_0$	$FL = 0.19\lambda_0$	$FWHMx = 0.63\lambda_0$ $FWHMy = 0.51\lambda_0$	1.8 times

Table 2: The best results in chapter 4 obtained from the truncated Ge sphere, Ge elliptic lens, and the truncated Ge elliptic lens are compared. The results are evaluated by comparing them using FL, FWHM, and power enhancement. The results displayed in Fig. 3.3, Fig. 3.4, and Fig. 3.4 were utilized for the truncated Ge sphere, respectively. The results displayed in Figs. 4.12 and 4.13 were used for the Ge elliptic lens and the truncated Ge elliptic lens, respectively.

In summary, the truncated Ge sphere shows varying *FL*s with higher spatial resolution and significant power enhancement, especially when the focal point is inside the sphere. Adjusting the truncation position impacts the *FL*, *FWHM*, and power enhancement significantly. In contrast, the Ge elliptic lens provides a negative *FL*, resulting in spatial resolution that is below the diffraction limit, along with slightly reduced power enhancement. When truncated, the lens demonstrates a positive *FL* with decreased spatial resolution and lower power enhancement. Consequently, the truncated Ge sphere demonstrates higher power enhancement and spatial resolution compared to the Ge elliptic lens.

Chapter 5 Conclusions and future work

5.1 Conclusions

Chapter 3:

In chapter 3, we explored the interesting subject of high spatial resolution focusing of electromagnetic waves, particularly at telecommunication wavelengths (λ_0 = 1.55 μm), using techniques involving high refractive index dielectrics placed at the end of optical fibres. The main achievement in this chapter is the demonstration of the success of PNJs in generating narrow, highly focusing spots, showing significant promise for improving spatial resolution in applications where high spatial resolution is needed, such as imaging and sensing systems.

We investigated into the effects of varying the size and truncation distance of idealized 2D dielectric cylinders on their PNJ properties. By manipulating these parameters, we successfully achieved improved spatial resolution with narrow focal spots ($FWHM = 0.28\lambda_0$) and a power enhancement four times higher than the case without the truncated dielectric cylinder, where $R = 1.55\lambda_0$ and $a \approx 0.52\lambda_0$. We considered 3D scenarios with finite truncated dielectric cylinders as part of this research. This enabled us to show how different transverse lengths affect the properties of PNJs and show how the proposed structure can be used in different configurations. We explored the impact of various factors, including the size, truncation distances, losses, and shape imperfections of dielectric spheres on PNJ parameters. In the truncated dielectric sphere, a resolution of $FWHMx = 0.21\lambda_0$ and $FWHMy = 0.17\lambda_0$ was successfully achieved, resulting in a power enhancement of 27. This achievement was made possible by employing a design which includes a dielectric sphere with $R = 1.55\lambda_0$ and $a \approx 0.41\lambda_0$. We achieved that adjusting the truncation position of dielectric structures, such as spheres and cylinders, is significant in improving light convergence or divergence, resulting in the creation of PNJs with higher spatial resolution. We demonstrated how effective the proposed structure is by showing that in the case with losses and fabrication imperfections, it is still possible to achieve valuable spatial resolutions and power enhancements, making it an appropriate structure for practical applications.

The results in chapter 3 offer great promise for sensing and imaging devices that need high spatial resolution working at telecommunication wavelengths. The ability to create PNJs

through the manipulation of dielectric geometries and parameters offers an opportunity for sensing and imaging applications.

Chapter 4:

The design proposed in chapter 4 achieves a new sensing and imaging device with high spatial resolution PNJs. It provides that by focusing electromagnetic waves at a wavelength of $\lambda_0 = 2$ μm with high spatial resolution. Our study is based on placing a Ge sphere at the end of the optical fibre core, where they are completely immersed by the cladding material. This technique uses PNJs to generate small high intensity spots, which enables an optical fibre for a new application device.

Our exploration, which combines simulations and experimental methods to investigate the parameters that determine the efficiency of this design. This chapter provides an overview of the progression from theoretical modelling to practical implementation in the photonic lab. Ge was chosen as the material for the dielectric because it has unique properties, such as its ability to responds to a CO_2 laser, allowing it change into a sphere. We evaluated how different factors, such as the R and a, influenced the performance of the PNJs. We achieved that truncating the Ge sphere resulted in a transversal resolution of $FWHMx = 0.16\lambda_0$ and $FWHMy = 0.13\lambda_0$, along with a power enhancement of 19. These achievements were made possible by a truncated Ge sphere with $R = 1.15\lambda_0$ and $a = 0.39\lambda_0$. We moved from theory to practice when we started making an experiment structure in the photonic lab. Here, we reviewed over the steps that are needed to turn theoretical ideas into real devices. We proceeded by cleaving a large capillary and filling it with Ge powder. Then we completed several procedures, such as splicing, tapering, and shaping with a CO_2 laser, to make Ge spheres inside small capillary. Finally, we were able to successfully splice the Ge lens with the core of an optical fibre. Although challenges, such as achieving the desired Ge sphere size, appeared during this process, these preliminary results are promising.

Our proposed design in chapter 4 provides a promising approach to create a new device of sensing and imaging systems with PNJs that operate at $\lambda_0 = 2$ μm and have high spatial resolution. Section 4.2 provides the foundation for future developments in this field by attempting to achieve the required size in experiments, aligning it with theoretical models.

Challenges:

In chapter 3, a structural concept was introduced which initially appeared to have promise. However, as we investigated into the practical aspects of implementing it in our photonic lab,

we found some limitations. These limitations centred on the challenges of fabricating a dielectric sphere within an air medium. Additionally, it was challenged to exactly position the dielectric sphere at the end of the core of an optical fibre and then truncate it to meet our desired parameters. Consequently, we decided to investigate the structure described in chapter 4 as it has the possibility for the fabrication of a Ge sphere within a cladding material. The new approach not only addresses these manufacturing difficulties, but it also demonstrates to be more suitable to the capabilities of our photonic lab, such as placing the Ge sphere at the end of the core of an optical fibre.

It is important to mention the limitations we found during the fabrication process for the structure described in section 4.2. These limitations were mainly imposed due to the covid-19 pandemic, which significantly restricted our ability to access the photonic lab. Unfortunately, these limitations, along with the time limits of a Ph.D stage, prevented us from achieving the desired size. Despite with these challenges, section 4.2 is an appropriate starting point for future work in this field. It shows the importance of addressing the desired parameters of the structure when comparing theoretical models with experimental observations.

5.2 Future work

- In future study, we aim to use a fabrication method described in a recent 2023 study [92]. In this method, full and truncated dielectric spheres are attached at the end of an optical fibre using nanoparticles self-assembly in a water dispersion. When H_2O molecules evaporate at room temperature and atmospheric pressure, a device that has the shape of a sphere or a truncated sphere forms. The dielectric is attached from its truncated side to the end of the optical fibre, while the curved side remains unattached to the optical fibre. Chapter 3 will adopt a similar process to determine sphere size and truncation distance, Si will be used for the dielectric. Once attached to the optical fibre, the truncated sphere is spliced from the curved side to the optical fibre. Following this, the truncated dielectric sphere will be cleaved from the optical fibre at the point where it is attached to the truncated side. Subsequently, we illuminate the optical fibre with a 1.55 μm laser to evaluate spatial resolution. This approach corresponds the recent 2023 study to chapter 3, providing a method for fabricating the structures.

- Experimental demonstration, after achieving, in future study, the desired size of the structure in chapter 4, we will evaluate spatial resolution by illuminating the optical fibre with a 2 μm laser as shown in Fig. 5.1.

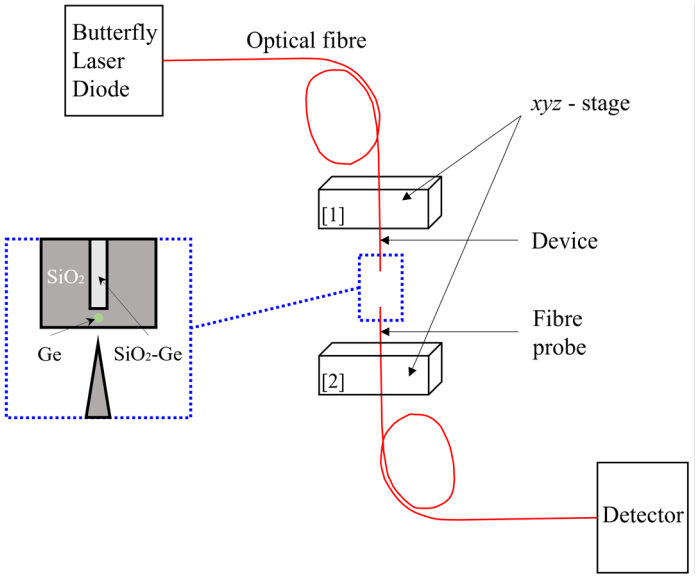

Figure 5.1: The device is connected to a Butterfly Laser Diode in the photonics lab. The Butterfly Laser Diode operates at wavelength 2 μm. As shown in the blue box, the device consists of an optical fibre with a Ge lens placed at its end. The device is securely inserted and properly adjusted on a stage 1. The detector is connected to a fibre probe with a tapered head, as depicted in the blue box. The fibre probe is placed on the adjustable stage 2. Finally, the Butterfly Laser Diode is turned on and the spatial resolution of the device is calculated.

- After achieving a high spatial resolution with our devices, we employ this resolution in future work to detect subwavelength particles. The process of detection involves the calculation of particle scattering after they are immersed in a PNJs. Backscattering is calculated when metal and dielectric particles are used, while forward scattering is calculated when dielectric particles are used [4,198,199].

Appendix A: Optimizing mesh cell sizes for accurate results

We investigated the results of the *FL* location obtained from varying mesh cell sizes along the radius of the dielectric sphere *R*, where these mesh cells are shown in Fig. A.1 a. The results in Fig. A.1 b,c illustrate the power enhancement, which was calculated by dividing the power distribution obtained on the *yz* plane ($x = 0$) when using a dielectric sphere with an optical fibre by the power distribution obtained on the *yz* plane ($x = 0$) when using only the optical fibre. The wavelength utilized is $\lambda_0 = 1.55$ μm, and the electric field is polarized along the *y* axis, while the magnetic field is polarized along the *x* axis, with the wave propagating in the *z* direction.

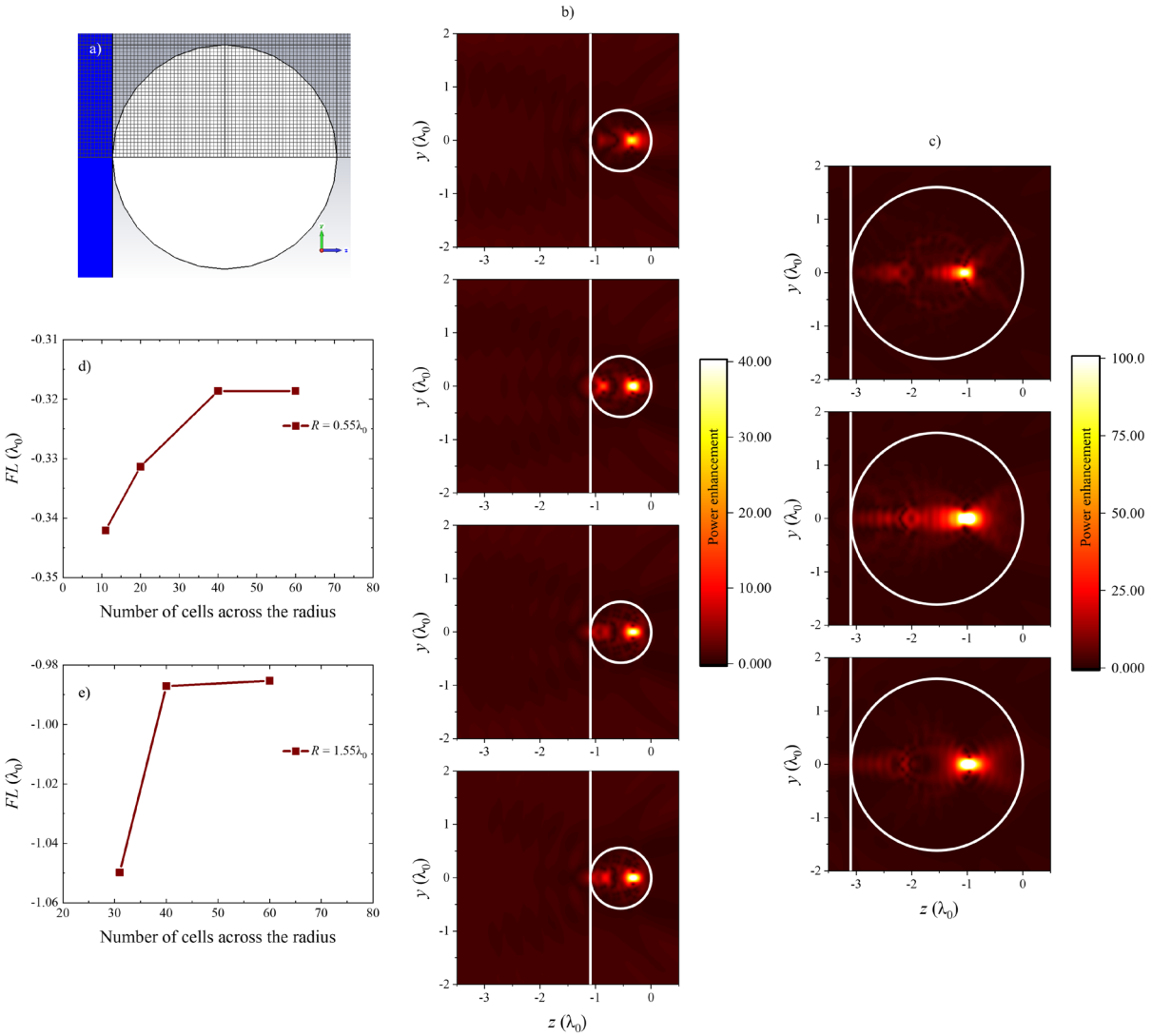

Figure A 1: (a) This illustration was obtained from CST Studio Suite and shows the mesh cells in a cross-section of the dielectric sphere. (b) The dielectric sphere has a size of $R = 0.55\lambda_0$, and the number of mesh cells along the radius of the dielectric sphere increases from top to bottom by 11, 20, 40, and 60. (c) The dielectric sphere has a size of $R = 1.55\lambda_0$, and the number of mesh cells along the radius of the dielectric sphere increases from top to bottom by 31, 40, and 60. The output surface of the dielectric sphere is located at $z = 0$. (d) and (e) The position of the FL is shown as a function of the number of mesh cells across the radius of the dielectric sphere for both $R = 0.55\lambda_0$ and $1.55\lambda_0$, respectively.

For competence, we conducted an analysis of the number of mesh cells along the radius of a dielectric sphere. Specifically, we examined cases where the radius was $R = 0.55\lambda_0$, and the number of mesh cells along the radius was either 11, 20, 40, or 60. Additionally, we investigated situations where the radius was $R = 1.55\lambda_0$ and the number of mesh cells along the radius was either 31, 40, or 60. The number of mesh cells within the dielectric sphere has been increased, along with an increase in the number of cells surrounding its boundary. Specifically, 6 additional cells have been added along both the *x* and *y* axes, and 70 cells have been added along the *z* axis due to propagation in the *z* axis.

Fig. A.1 d,e show the accuracy of the *FL* position as the number of cells in the dielectric sphere varies at $R = 0.55\lambda_0$ and $R = 1.55\lambda_0$, respectively. Increasing the number of mesh cells from 40 to 60 does not affect the accuracy of the location of the *FL* for $R = 0.55\lambda_0$, as shown in Fig. A.1 d. However, for $R = 1.55\lambda_0$, increasing the number of mesh cells from 40 to 60 causes the *FL* position to shift by approximately 10 nm, as depicted in Fig. A.1 e. Based on these results, this thesis uses 40 mesh cells across the radius of the dielectric sphere or cylinder because it has a negligible effect, approximately $0.006\lambda_0$, on the location of the *FL*.

Appendix B: Analysis of the performance of PNJs with various sizes of truncated dielectric cylinders

i. Small truncated dielectric cylinder ($R = 0.55\lambda_0$)

In this section, we investigate the performance of the truncated dielectric cylinder in 2D when the dielectric size is similar to the dielectric size in the previous study [94]. This study is similar to the study in section 3.1.2 as it uses the Weierstrass formulation for immersion lenses as a starting point to determine the truncation distance. Subsequently, we perform a parametric study by varying the truncation distance between the centre of the dielectric cylinder and the output flat surface. The dielectric cylinder is truncated by applying Eq. 2.18 to move the PNJ from the inside to the outside of the dielectric cylinder. We chose the dielectric size of $R = 0.55\lambda_0$ in order to make it equivalent to the dielectric size in the previous study based on the freespace wavelength [94]. Using Eq. 2.18, we determine that $a \approx 0.16\lambda_0$ and change a from $0.096\lambda_0$ to $0.225\lambda_0$ in steps of $\sim 0.006\lambda_0$.

The difference in a value can be divided into two sections based on the location of the *FL*, whether it is inside or outside the truncated dielectric cylinder. For example, when a is equal to from $0.096\lambda_0$ to $0.122\lambda_0$, the *FL* appears outside the truncated dielectric cylinder, as shown in Fig. B.1 a, which illustrates the power enhancement along z axis when the y axis equal to zero. We can see clearly that the power enhancement increased as the value of a increased. Also, the positions of the *FL* shifted slightly to the output flat surface of the truncated dielectric cylinder as the values of a increased. The *FL* locations are shown in Fig. B.1 b, and they are close to the outer surface of the truncated dielectric cylinder, and the distance between them and the outer surface ranges from approximately $0.05\lambda_0$ to $0.09\lambda_0$.

The observation obtained from Fig. B.1 b indicates that an increase in the value of a results in a shift in the position of the *FL* towards the direction of the flat surface of the truncated dielectric cylinder. This behaviour is consistent with the findings presented in Fig. 3.3 a when the *FL*s are obtained at the output surface of the truncated dielectric cylinder. When looking at the power enhancement on the *FL* that appears outside the truncated dielectric cylinder, we find that all its values are close to 1. When the power enhancement is equal to 1, this indicates that the power distribution through the structure consisting of an optical fibre and a truncated dielectric cylinder is equal to the power distribution through the optical fibre only. When looking at Fig. B.1 c, it is observed that certain power enhancement values have values less

than 1 within the range of $a = 0.096\lambda_0$ to $0.109\lambda_0$, while others achieve a value slightly higher than 1 at $a = 0.116\lambda_0$ and $0.122\lambda_0$.

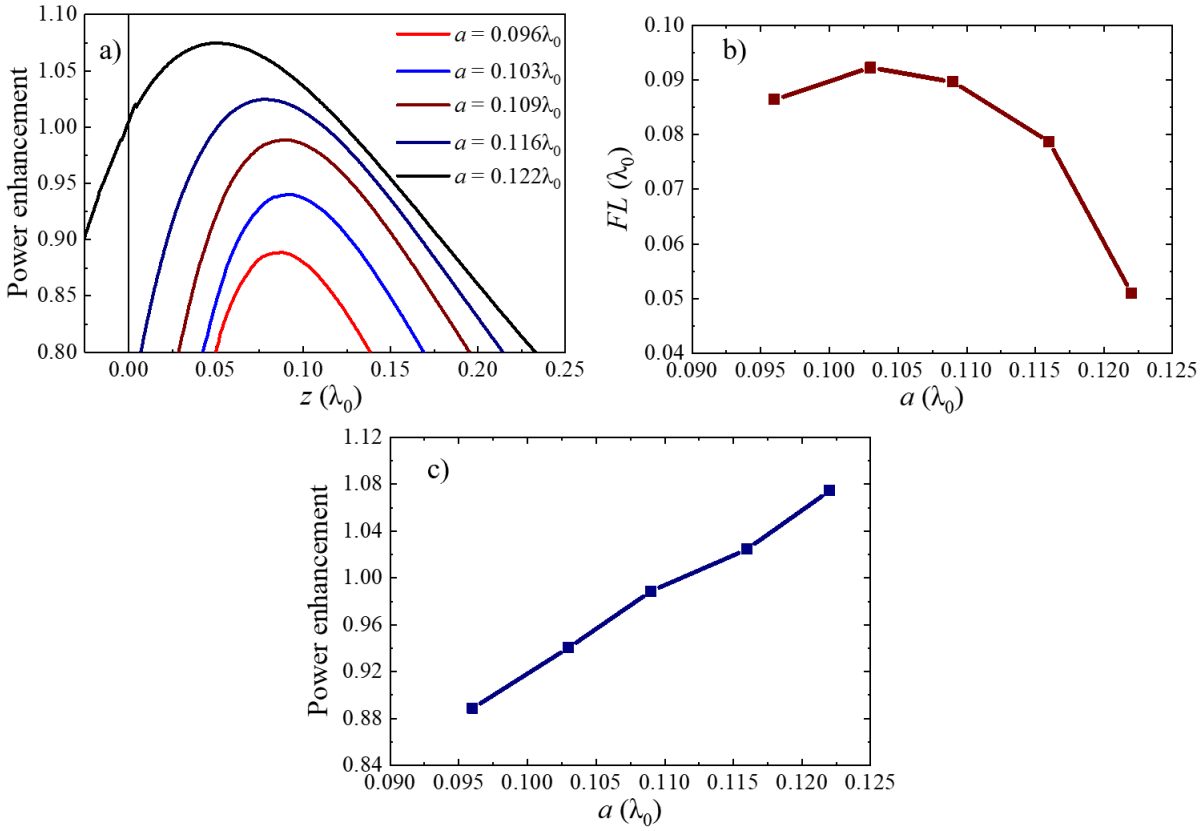

Figure B 1: (a) The power enhancement along the propagation z axis at y = 0 for the values between $0.096\lambda_0$ and $0.122\lambda_0$ is illustrated when the FLs appear at the output surface of the truncated dielectric cylinder, at the positive z axis. (b) and (c) The FL and power enhancement as a function of a are shown, respectively.

To evaluate the spatial resolution of these *FL*s, the *FWHM*s of the power enhancement as it passes through the *FL*s are calculated on the transverse *y* axis. In Fig. B.2 a-c, we clearly find the value of the power enhancement at $y = 0$ (at $a = 0.096\lambda_0$ to $0.109\lambda_0$) less than 1, but the value of the power enhancement at $y = 0$ ($a = 0.116\lambda_0$ and $0.122\lambda_0$) is slightly higher than 1 as shown in Fig. B.2 d,e. The values of *FWHM* at $a = 0.096\lambda_0$ to $0.122\lambda_0$ are shown in Fig. B.2 f. All spatial resolution values are less than $0.5\lambda_0$, and the spatial resolution increases when the value of *a* is increased. The spatial resolution is improved as expected [95,110] due to the generated PNJs are moved closer to the output surface of the 2D truncated dielectric cylinder. It has been observed that the best spatial resolution ($FWHM = 0.24\lambda_0$) is achieved at a value of $a = 0.122\lambda_0$. Furthermore, it is seen that the power enhancement reaches its maximum value (>1) when the *FL* is positioned outside the truncated dielectric cylinder. Fig. B.2 g illustrates the power enhancement in the *yz* plane for $a = 0.122\lambda_0$ and $R = 0.55\lambda_0$. In this case, the *FL* is clearly observed outside the truncated dielectric cylinder. It is important to note that the observed power enhancement has been scaled from 0 to 1.

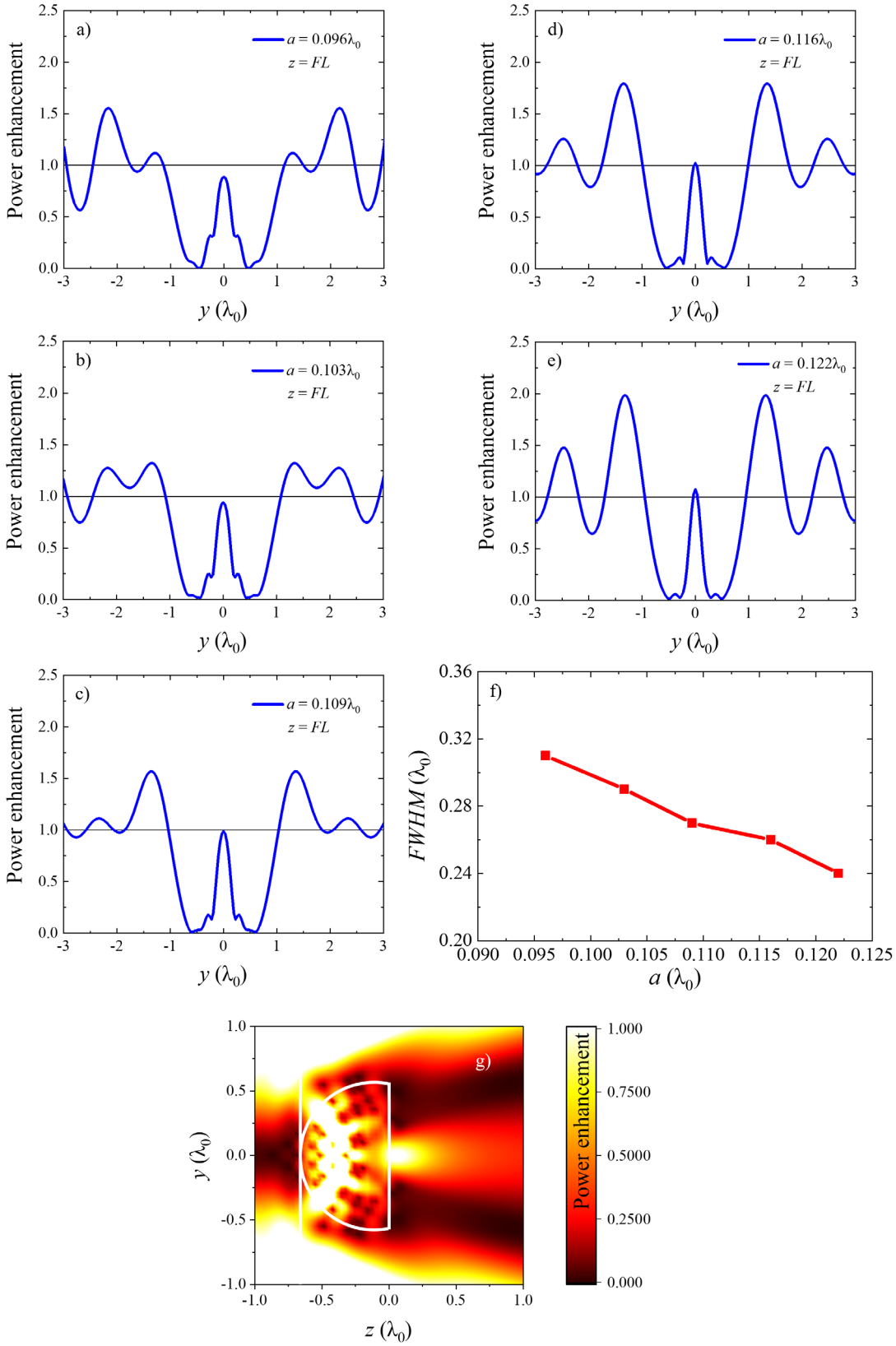

Figure B 2: The power enhancement along transversal y axis at the position of the FL that appear in the output surface of the truncated dielectric cylinder is shown for (a) $a = 0.096\lambda_0$, (b) $a = 0.103\lambda_0$, (c) $a = 0.109\lambda_0$, (d) $a = 0.116\lambda_0$, and (e) $a = 0.122\lambda_0$. The black line at the power enhancement at 1 shows when the power distribution through the structure constituted of an optical fibre and a truncated dielectric cylinder is the same to the power distribution through the optical fibre alone. (f) The FWHM is shown as a function of various values of a, which have been calculated from (a-e). (g) The power enhancement for $a = 0.122\lambda_0$ and $R = 0.55\lambda_0$ is illustrated in the yz plane.

To move forward at the values of a from $0.129\lambda_0$ to $0.225\lambda_0$, we observe that all *FL*s appear inside the truncated dielectric cylinder, as shown in Fig. B.3 a-c, where zero in the propagation z axis means the flat outer surface of the truncated dielectric cylinder. The locations of the *FL*s and the power enhancement vary when a value is changed, as expected. Fig. B.3 d illustrates the *FL* locations as a function of the values of a, so that the results can be observed more clearly. In this case, the *FL* axis has a negative scale, indicating the presence of the *FL* within the truncated dielectric cylinder. This result differs with the observations in Fig. B.1 b, where the *FL* axis has a positive scale. *FL*s range approximately from $0.06\lambda_0$ to $0.08\lambda_0$ from the surface of the truncated dielectric cylinder.

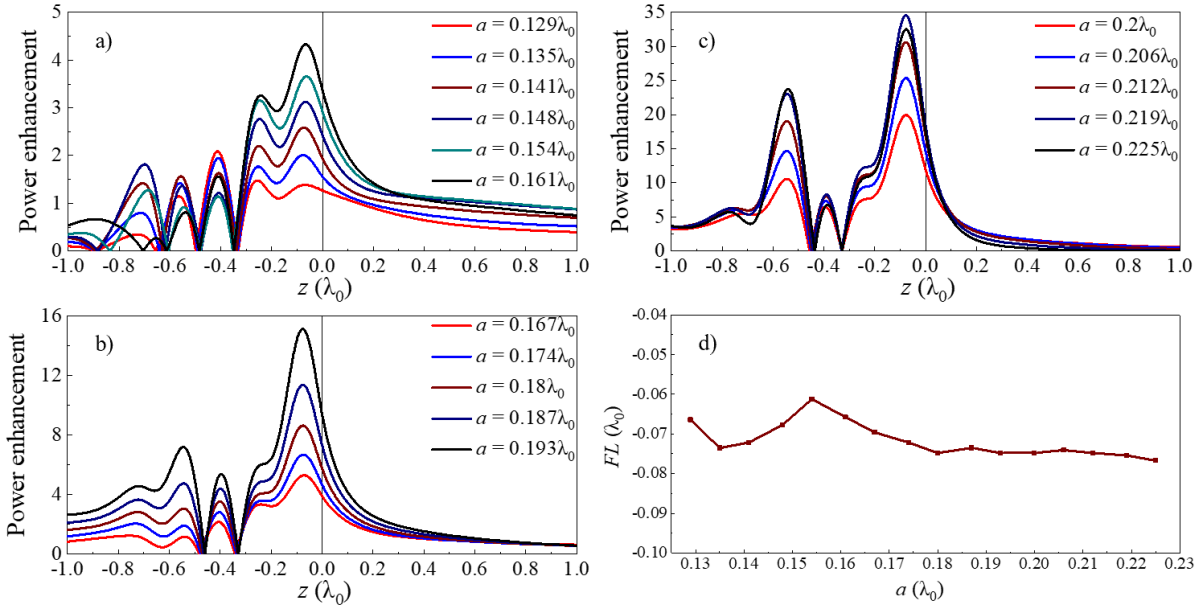

Figure B 3: (a-c) The power enhancement along the propagation z axis when y = 0 for a = 0.129λ0 to 0.225λ0 is illustrated. The vertical black line at z = 0 is the output surface of the truncated dielectric cylinder. (d) The FL as a function of different values of a is displayed.

The *FWHM* and the power enhancement on the outer surface of the truncated dielectric cylinder are calculated specifically at the $z = 0$ for $a = 0.129\lambda_0$ to $0.225\lambda_0$, as seen in Fig. B.4 a,b respectively. In this analysis, it is shown that as the value of a increases, there is a decrease in spatial resolution and an increase in power enhancement. However, all spatial resolution values on the truncated dielectric cylinder surface are less than half a wavelength. These values are ranged from $0.17\lambda_0$ to $0.39\lambda_0$, while the corresponding power enhancement values vary from 1 to 18.

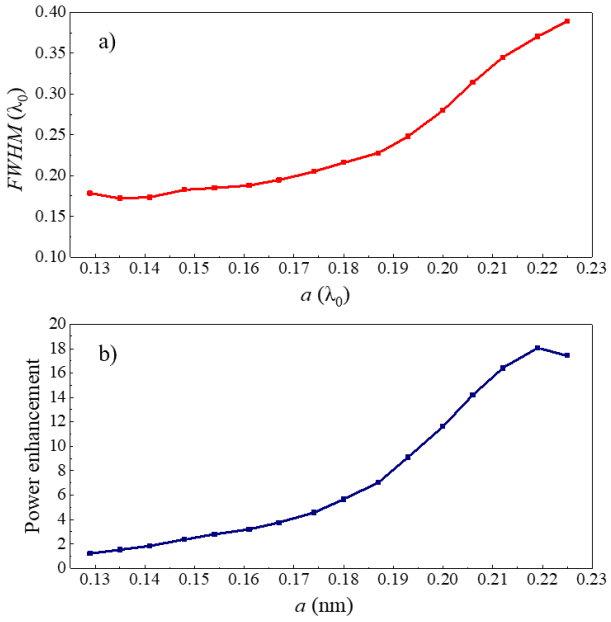

Figure B 4: (a) and (b) The FWHM and the power enhancement as a function of the different values of a (from a = 0.129λ₀ to 0.225λ₀) are illistrated. These values have been calculated at just the output flat surface of truncated dielectric cylinder where z = 0.

The best spatial resolution is obtained at $a = 0.135\lambda_0$, while the highest power enhancement is achieved at $a = 0.219\lambda_0$, as shown in Fig. B.4 a,b respectively. Fig. B.5 a illustrates the power enhancement in *yz* plane for the best spatial resolution when $a = 0.135\lambda_0$ and $R = 0.55\lambda_0$. This result clearly demonstrates that a *FL* is generated within the truncated dielectric cylinder and close to its outer surface. Fig. B.5 b depicts the power enhancement along the *y* axis at the outer surface of the lens ($z = 0$). The *FWHM* at $y = 0$ has been calculated to be $0.17\lambda_0$ with a power enhancement of 1.5. Furthermore, Fig. B.5 c shows the result of the highest power enhancement in the *yz* plane, which is achieved at $a = 0.219\lambda_0$. Fig. B.5 c is similar to the result depicted in Fig. B.5 a, where a *FL* is produced within the truncated dielectric cylinder close to its output surface. At the value of $a = 0.219\lambda_0$, the spatial resolution determines $0.37\lambda_0$, while the power enhancement is seen to be 18, as depicted in Fig. B.5 d.

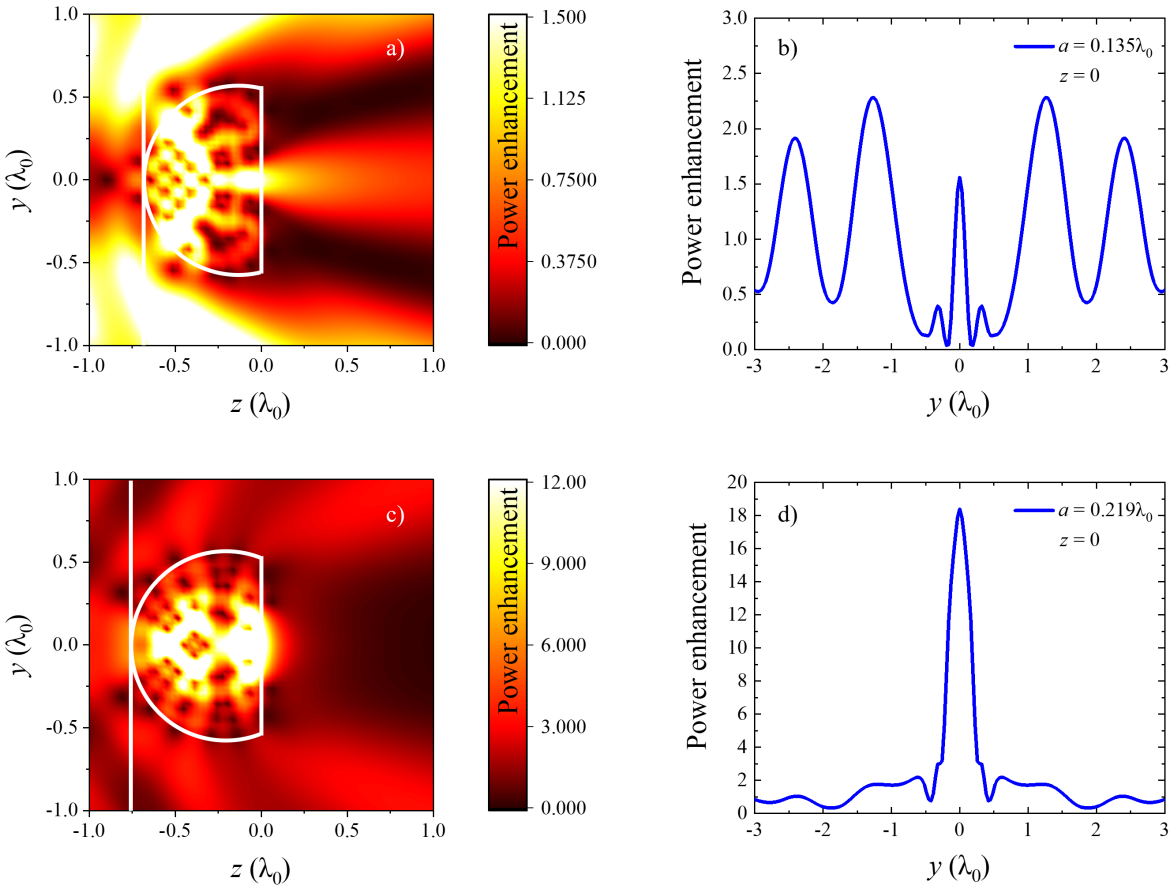

Figure B 5: The power enhancement on the yz plane, where R = 0.55λ0, is shown for (a) a = 0.135λ0 and (c) a = 0.219λ0. The power enhancement along the y axis at the z = 0 is extracted from panels (a) and (c) for panels (b) and (d), respectively.

ii. Varying truncation distances of dielectric cylinder for $R = 1.55\lambda_0$

This section is a continuation of section 3.1.2, in which the structure of a truncated dielectric cylinder is investigated in 2D using COMSOL Multiphysics. The radius of the dielectric cylinder is determined to be $R = 1.55\lambda_0$, providing that the wavelength inside the dielectric cylinder is similar to that of previous studies performed under planewave illumination [94]. The dielectric cylinder is truncated using Eq. 2.18 in order to move the PNJ from the inside to the output surface. By applying Eq. 2.18, where R has the value of $1.55\lambda_0$, the value of a is approximately $0.47\lambda_0$.

The performance analysis of the structure includes a parametric study in which the truncated distance a is changed while the value of R remains constant at $1.55\lambda_0$. The range of a has been set between $0.387\lambda_0$ and $0.554\lambda_0$, with steps of $\sim 0.006\lambda_0$. We are able to produce PNJs outside the dielectric cylinder by truncating the output profile. This demonstration is observed for all investigated a values, as depicted along the positive vertical axis of Fig. B.6.

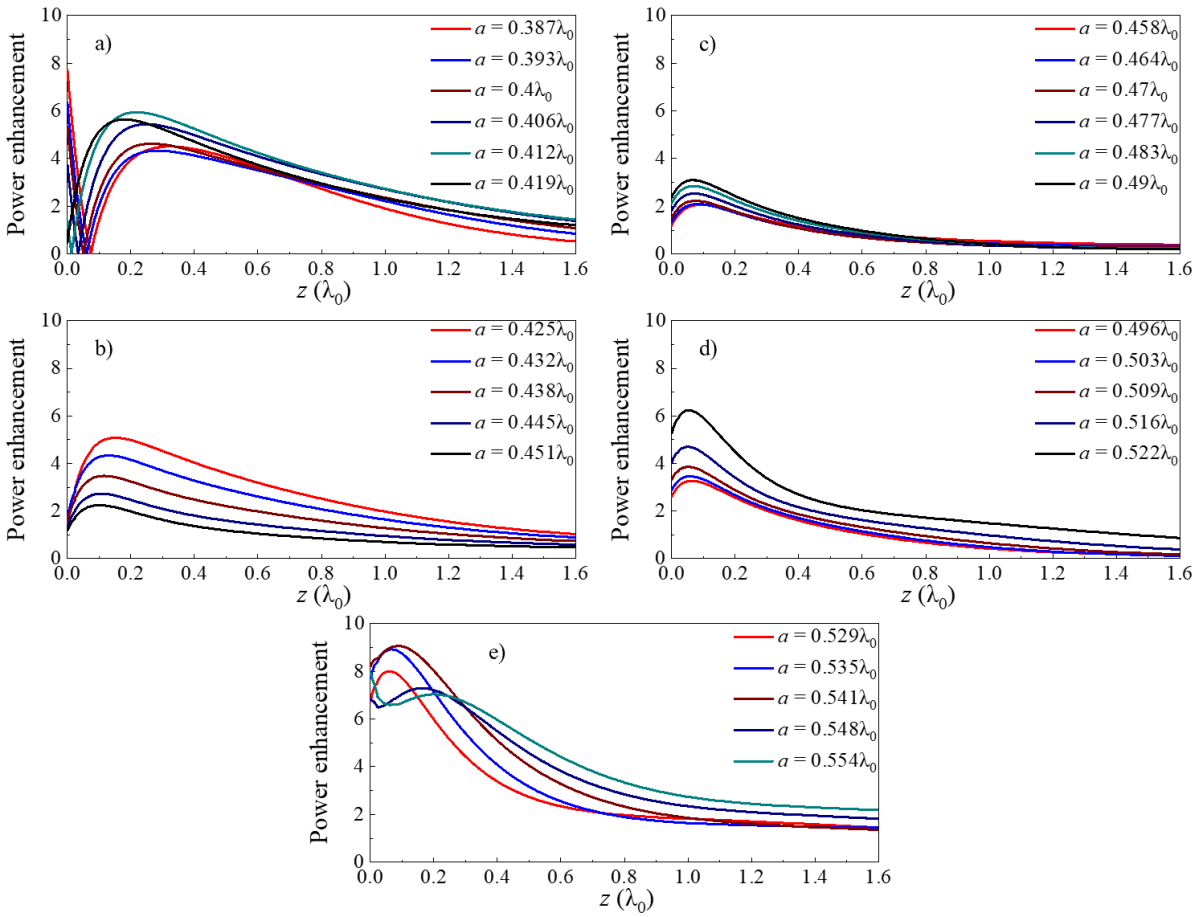

Figure B 6: The power enhancement along the propagation z axis at y = 0, where the radius of the dielectric cylinder is R = 1.55λ_0, ranges from a = 0.387λ_0 to 0.554λ_0, with steps of ~ 0.006λ_0. z = 0 represents the output surface of the truncated dielectric cylinder.

Appendix C: Investigation of PNJ performance with varied sizes of truncated dielectric spheres

i. Analysis of PNJ performance using small dielectric spheres

The results of a small size of the 3D dielectric sphere are analysed and participated in a conference [180]. Here, we only employ a dielectric size equal to one wavelength inside the dielectric sphere $R = 0.5\lambda_{d0}$ due to in the previous study, we take into account the refractive index of the dielectric and relate it to the size of the dielectric until it becomes $R = 5\lambda_{d0}$ [94]. Fig. C.1 a illustrates the power distribution on the *xz* plane of a full dielectric sphere, showing the expected presence of the *FL* within the dielectric sphere [88]. The *FL* is located at a distance of 150 nm from the dielectric surface within the dielectric sphere, as depicted in Fig. C.1 b. To determine the spatial resolution of the *FL*, the *FWHM* of the power distribution inside the dielectric at the *FL* is calculated, given that $FWHMx = 0.44\lambda_d$ with respect to the wavelength inside the dielectric sphere as shown in Fig. C.1 c.

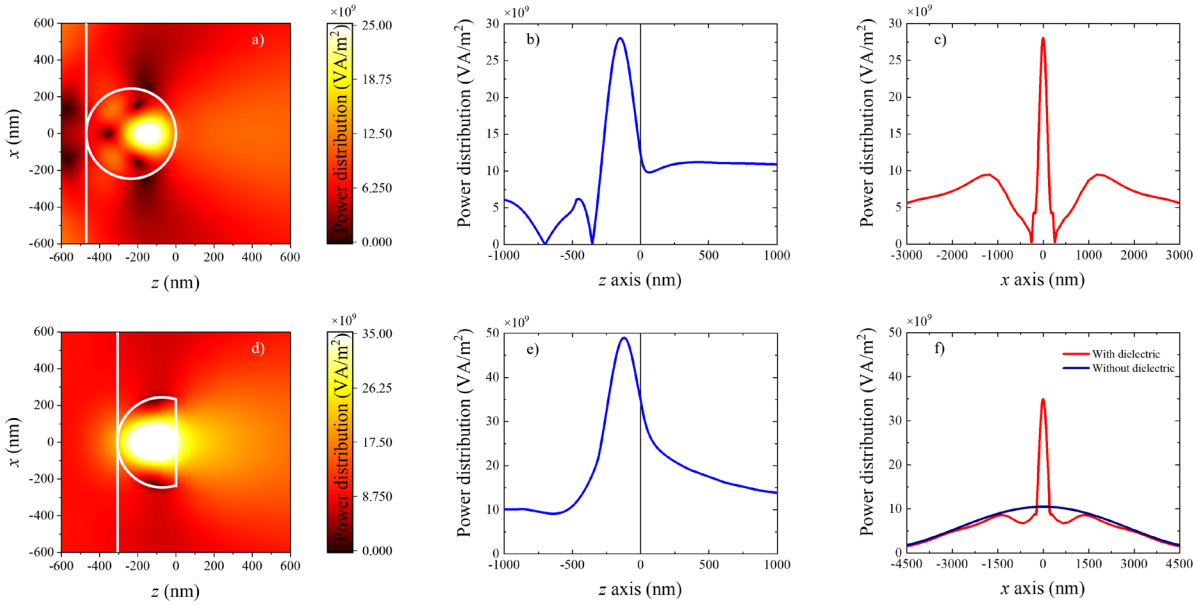

Figure C 1: (a) The power distribution on the xz plane is determined for a dielectric sphere placed at the end of the optical fibre. (b) The power distribution at x = y = 0 along the z axis is determined from panel (a). (c) The power distribution along the transversal x axis within the dielectric sphere at the focal spot is determined by the structure of panel (a). (d) The power distribution on the xz plane is determined for a truncated dielectric sphere placed at the end of the optical fibre. (e) Power distribution along the z axis at x = y = 0 extracted from panel (d). (f) The power distribution along the transversal x axis is determined just at the output surface of the truncated dielectric sphere (z = 0), considering both the scenario with the truncated dielectric sphere (rad) and the scenario without it (navy). The values of the power distribution scale bar have been normalised by a value of $1e^9$ to provide a better image of the results.

The dielectric sphere has been truncated using Eq. 2.18 for $R = 0.5\lambda_{d0}$, resulting in the calculation of $a = 71$ nm. Fig. C.1 d shows the power distribution in the *xz* plane where $y = 0$

after truncating the dielectric sphere. The findings indicate that the *FL* is located within the truncated dielectric sphere at a distance of 122 nm from the surface of the dielectric. Furthermore, a portion of the focus has the ability of leaking into freespace through the flat surface of the truncated dielectric sphere, as depicted in Fig. C.1 e. *FWHM* along the *x* and *y* axes of the power distribution on the outer surface of the truncated dielectric sphere are $FWHMx = 0.22\lambda_0$ and $FWHMy = 0.19\lambda_0$, respectively. In Fig. C.1 f, the red line represents the power distribution along the *x* axis at the output surface of the truncated dielectric sphere, whereas the navy line represents the power distribution along the *x* axis at the end of the optical fibre without a dielectric. Fig. C.1 f provides a clear representation of how the truncated dielectric sphere improves power distribution. We observe that the spatial resolution of the optical fibre with the truncated dielectric sphere is higher than the spatial resolution of the optical fibre without a truncated dielectric sphere, as it is equal to $FWHMx = 3.84\lambda_0$ and $FWHMy = 3.84\lambda_0$ without a truncated dielectric sphere as shown in Fig. 2.13. We also find that the power distribution using the truncated dielectric sphere is approximately 4 times higher than the power distribution by the optical fibre without the truncated dielectric sphere.

ii. Exploring the effects of varying truncation distance on PNJs with a dielectric sphere of $R = 1.55\lambda_0$

This section continues the investigation of the structure of a truncated dielectric sphere in 3D using the CST Studio Suite introduced in section 3.3.2. The radius of the dielectric sphere has been determined to be $R = 1.55\lambda_0$. To shift the PNJ from the inside to the outer surface of the truncated dielectric sphere, we apply Eq. 2.18 to truncate the dielectric sphere. Applying Eq. 2.18, where *R* is equal to $1.55\lambda_0$, obtains $a \approx 0.47\lambda_0$. The evaluation of the truncated dielectric sphere includes performing a parametric study, with modifying the value of *a*, while keeping the value of $R = 1.55\lambda_0$. The range of *a* has been chosen to be from $0.387\lambda_0$ to $0.554\lambda_0$, with steps of $0.006\lambda_0$. By truncating the dielectric sphere, it is possible to generate PNJs inside and very close to the output surface of the truncated dielectric sphere, as depicted in Fig. C.2 a-e (along with the negative *z* axis). In these results, it is seen that the focus is able to leak into the freespace via the flat surface of the truncated dielectric sphere.

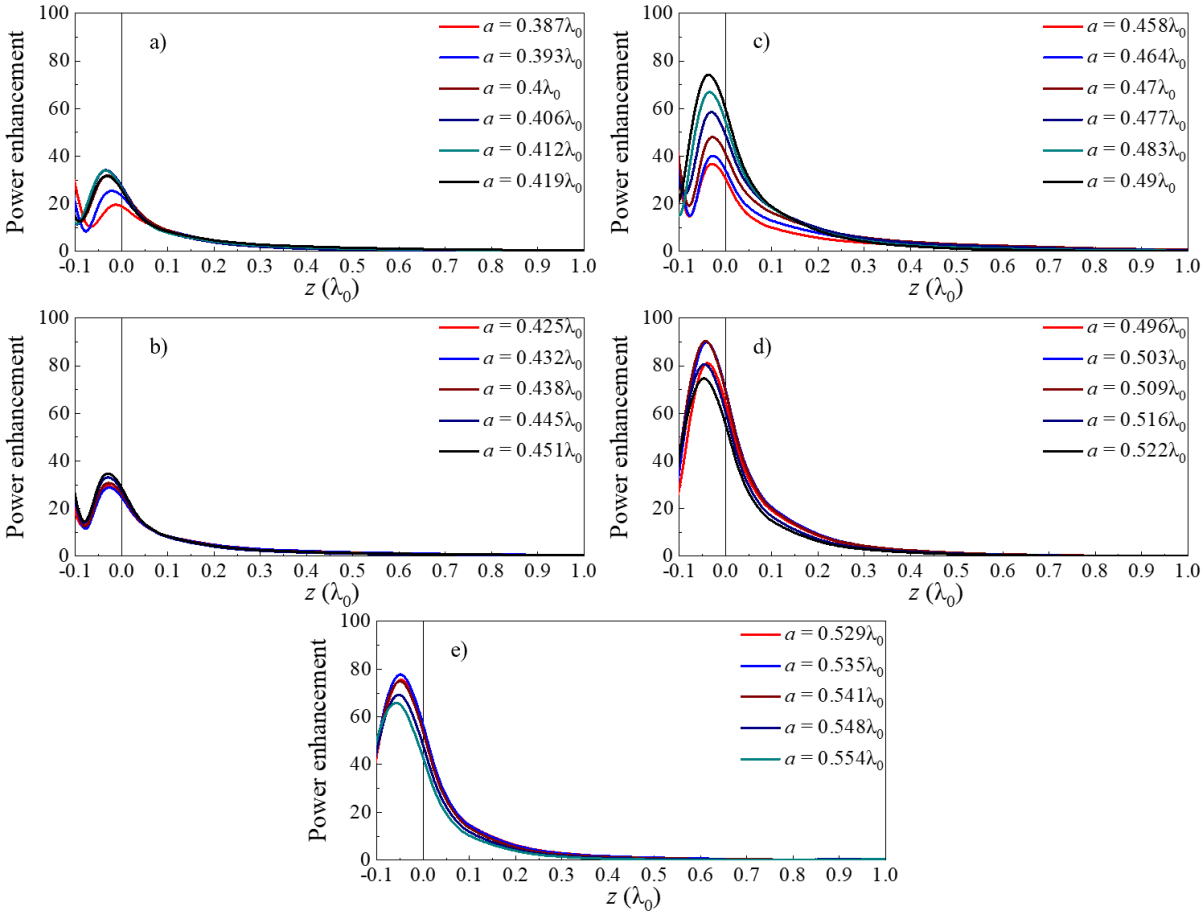

Figure C 2: At the position where x = y = 0, the power enhancement along the propagation z axis ranges from a = 0.387λ₀ to 0.554λ₀, with steps of ~ 0.006λ₀. The radius of the dielectric sphere is R = 1.55λ₀. The value of z = 0 denotes the output surface of the truncated dielectric sphere.

iii. PNJ outside of the truncated high refractive index dielectric

The findings presented in this section were participated to a conference [188,189]. We demonstrate the production of a PNJ at the output surface of an engineered dielectric sphere with a high refractive index placed at the end of an optical fibre. A dielectric sphere is positioned at one end of the core of an optical fibre, and the core and dielectric sphere are completely immersed in a cladding material. The structure has a core and cladding diameter of 8 m and 125 m, respectively, working at a wavelength of $\lambda_0 = 1.55$ μm. The core and cladding have a refractive index of $n_{core} = 1.445$ and $n_{cladding} = 1.44$, respectively. The radius of the dielectric sphere is $R = 1.51\lambda_0$, and its refractive index is $n_d = 3.3$. At the output surface, the background is air, with $n_b = 1$.

The *FL* appears inside the dielectric sphere as expected and are illustrated in Fig. C.3 a because of the difference between the refractive index of the dielectric sphere and the surrounding background is higher than 2. The *FWHM* of the power enhancement at the transversal *x* and *y* axes within the dielectric sphere at the *FL* is calculated in order for evaluating

the spatial resolution of the *FL*. The resulting values are $FWHMx = 0.50\lambda_{d0}$ and $FWHMy = 0.59\lambda_{d0}$, with respect to the wavelength within the dielectric sphere, and the approximate power enhancement is 160, as shown in Fig. C.3 b.

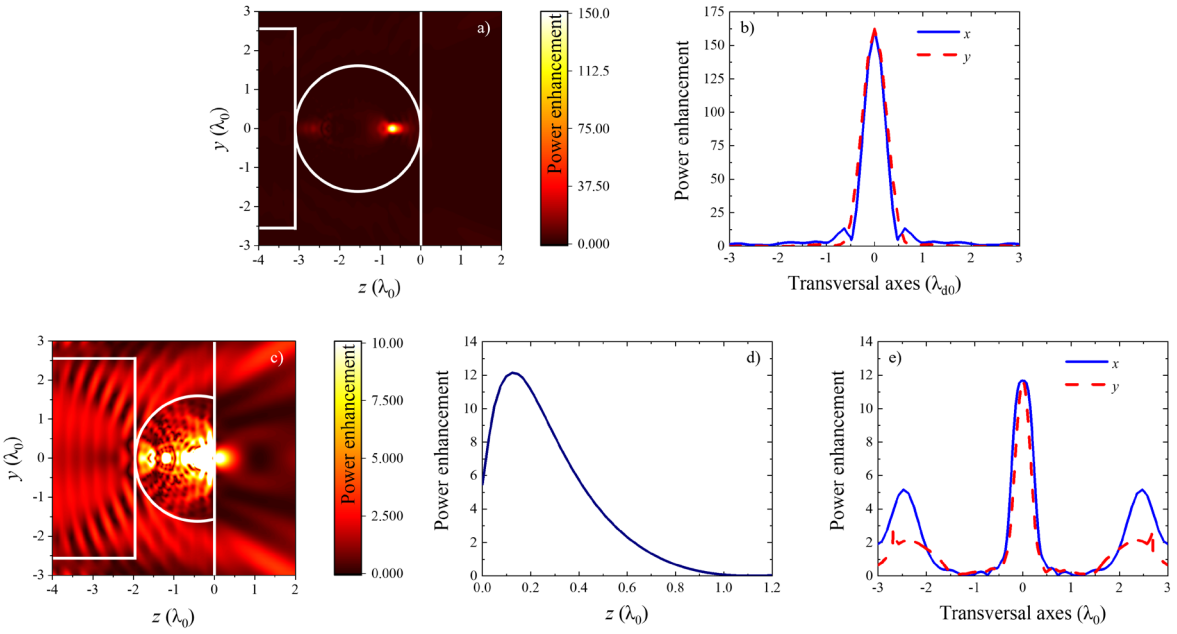

Figure C 3: (a,c) Power enhancement on the yz plane at x = 0 for both full dielectric sphere and truncated dielectric sphere, respectively. (b,e) Power enhancement along the transversal axes x (blue) and y (dashed red) at the FL position for a full dielectric sphere at $z = -0.68\lambda_0$ and a truncated dielectric sphere at $z = 0.12\lambda_0$, respectively. (d) At the centre of the truncated dielectric sphere, power enhancement on the z axis (x = y = 0) is shown. The PNJ can be observed outside the truncated dielectric sphere along the positive z axis, with the outer surface located at z = 0.

As shown in Fig. C.3 c, we can truncate both the dielectric sphere and the cladding to create a flat surface at the output of the dielectric sphere. $0.46\lambda_0$ is the distance between the centre of the truncated dielectric sphere and its flat surface on the right. The power enhancement on the *yz* plane is shown in Fig. C.3 c, where the PNJ is generated outside of the truncated dielectric sphere. In order to make it easier to observation of the position of the PNJ beyond the truncated dielectric sphere, Fig. C.3 d illustrates the power enhancement along the *z* axis at $x = y = 0$, which is the centre of the structure. Based on these findings, the PNJ is transferred outside of the truncated dielectric sphere at a distance of $0.12\lambda_0$, given that the outside flat surface is at $z = 0$ and the power distribution is 12 times greater than without the truncated dielectric sphere. To evaluate the resolution of this PNJ, we determine the *FWHM* at $z = 0.12\lambda_0$, which is the location of the PNJ, as depicted in Fig. C.3 e. Along the *y* and *x* axes, the values are $FWHMy = 0.36\lambda_0$ and $FWHMx = 0.48\lambda_0$, respectively. The results demonstrate that the PNJs can be generated at the output surface of a high index dielectric sphere placed at the end of the core of an optical fibre and immersed in cladding material. The PNJs have been shown to have a spatial resolution on the transverse axis that is less than half the wavelength.

Appendix D: Overview of the experimental configuration and materials used

This section discusses the materials and equipment used for device fabrication in the photonics lab at Newcastle University. A large empty capillary with the product ID TSP150375 Fused Silica Capillary, purchased from CM Scientific, is displayed in Fig. D.1 a after it has been cleaved and cleaned. It has an empty core with a diameter of 150 µm +/- 4 µm and a silicon dioxide (SiO_2) cladding with a diameter of 363 µm +/- 10 µm. One end is filled with Ge, as shown in Fig. D.2 a, and the other end is connected by gas pressure, as shown in Fig. D.1 h. The small capillary in Fig. D.1 b, which is made of SiO_2, has a core diameter of 5 µm +/- 2 µm and a cladding diameter of 363 µm +/- 10 µm after being cleaved and cleaned. It was purchased from CM Scientific and has the product ID TSP150375 Fused Silica Capillary. One end of Fig. D.1 b is spliced to the Ge filled end of the larger capillary.

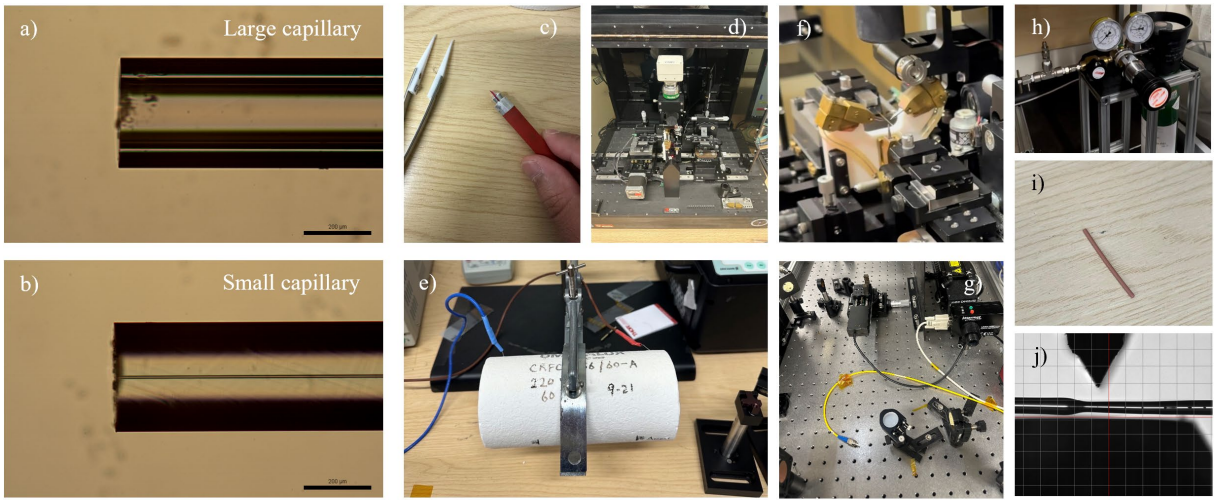

Figure D 1: (a,b) These image illustrate the clean, empty capillary, including both large and small sizes, respectively. (c) The image displays the use of a scribe and tweezers for cleaving and handling capillaries, respectively. (d) The LDS machine is utilised for steps that include splicing and tapering capillaries. (e) The image shows the furnace used for melting the Ge. (f) This image provides a magnified view of (d), illustrating the hands holding the capillary and the surrounding arc. (g) The CO_2 laser is utilised to transform cylindrical Ge into spherical shapes. (h) This illustration depicts a gas pressure connection with a large capillary. (i) This image shows a tubing sleeve connecting the large capillary to the gas pressure. (j) The illustration shows an image from the LDS machine that shows how carefully the small tapered capillary with Ge spheres inside was cleaved.

In Fig. D.1 c, a scribe and tweezer are used to cleave and handle capillaries. The scribe was purchased from Thorlabs, and the ID is S90R - Ruby DualScribe Fiber Optic Scribe. We rely on Fig. D.1 d, the LDS machine, to facilitate processes such as splicing and tapering capillaries, as well as cleaving after the formation of Ge spheres within the small capillary. Fig. D.1 f depicts a magnified image of Fig. D.1 d, displaying the hands holding the capillary and

the arc around it. Fig. D.1 e is the furnace used to melt Ge. This process involves inserting the small capillary, which has been spliced to the larger capillary containing the Ge, into the furnace, which causes the Ge to melt. In Fig. D.1 h, a gas pressure is shown with one end of the large capillary being connected to it. After approximately ten minutes of running the furnace, we turn on the gas pressure to make the molten Ge to move from the large capillary to the smaller capillary. Fig. D.1 i shows a tubing sleeve that was purchased from Cole-Parmer. It is compatible with capillaries ranging in diameter from 350 to 390 µm and has the ID of Idex F-230 tubing sleeve. It connects the large capillary to the gas pressure. The large capillary is inserted into the tubing sleeve, and the nut is tightened to connect the tubing sleeve to the gas pressure. Fig. D.1 g is an image of the CO_2 laser, showing where the small capillary with the Ge core is carefully placed on holders. These holders enable the small capillary to be moved passing the focal point of the CO_2 laser. Fig. D.1 j shows an image from the LDS machine that shows how the small tapered capillary that contains the Ge spheres was carefully cleaved. In this process, the sample is placed on a stage and the needle is used to apply pressure to the sample. Subsequently, the sample is gently pulled from both sides using hands holding the capillary of the LDS machine until the desired cleavage is achieved.

Fig. D.2 a shows Ge powder that has been mixed with isopropanol to make it easier to insert in the large capillary. Fig. D.2 b,c shows the optical properties of Ge, particularly its refractive index and extinction coefficient at different wavelengths. These exact values about Ge were carefully input into the CST Studio Suite simulation, which produced the results shown in section 4.1.

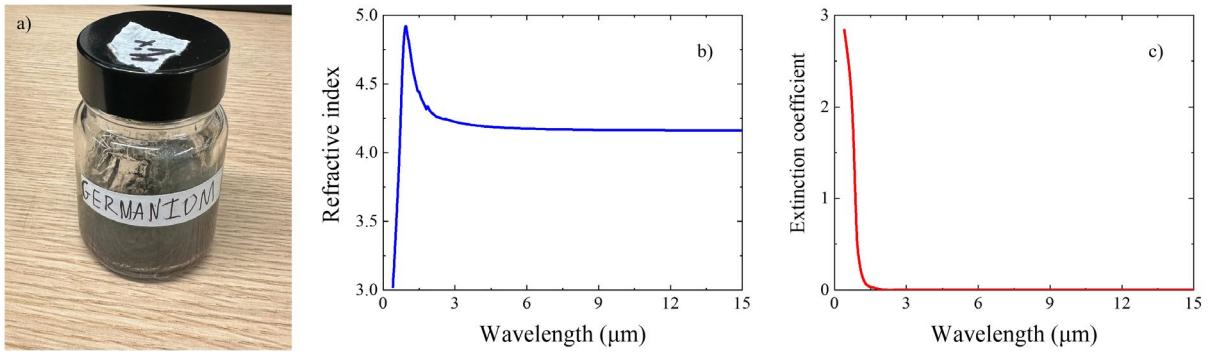

Figure D 2: (a) The image shows the Ge powder used to create a sphere. (b,c) The refractive index and extinction coefficient of Ge show as a function of the different wavelengths [167].

Appendix E: Evaluating power enhancement sensitivity of Ge elliptic lenses based on positional differences and comparative analysis of lens shapes

The impact of power enhancement on the position of the Ge elliptic lens is investigated in this section. In this discussion, we evaluate the power enhancement sensitivity of the full Ge elliptic lens position based on the simulation results shown in Fig. 4.12. The Fig. 4.12 depicts the simulation results of a sample provided in the lab, where the full Ge elliptic lens was positioned $0.8\lambda_0$ away from the centre of the core of the optical fibre on the *y* axis. The results in Fig. E.1 (a-c) depict three different positions of full Ge elliptic lenses along the *y* axis. The positions of the full Ge elliptic lens along the *y* axis are as follows: $0\lambda_0$, $0.2\lambda_0$, and $0.4\lambda_0$, respectively. The results clearly show that the *FL* is generated inside the full Ge elliptic lens, as expected. However, when determining the power enhancement at the output surface of the full Ge elliptic lens, the power enhancement decreases as the full Ge elliptic lens is moved away from the centre of the optical fibre, as expected, and illustrated in Fig. E.1 (d).

To compare the Ge elliptic lens positioned in the centre of the core of the optical fibre with the results presented in Fig. 4.12 (c), Fig. E.2 (a) depicts the power enhancement along the *z* axis when it propagates in the centre of the Ge elliptic lens. The positions of *FL* within the Ge elliptic lens are similar between Fig. 4.12 (c) and Fig. E.2 (a). The power enhancement along the *x* axis (at $y = z = 0$) and *y* axis (at $x = z = 0$) at the output surface of the Ge elliptic lens is illustrated in Fig. E.2 (b). The results demonstrates that, as expected, the *FL* is generated at the centre of the structure at $x = y = 0$. When calculating the spatial resolution of the generated *FL*, we obtain that the values for spatial resolution are $FWHMx = 0.20\lambda_0$ and $FWHMy = 0.18\lambda_0$. This spatial resolution of Fig. E.2 (b) is higher than the spatial resolution of Fig. 4.12 (d,e), and this is due to the position of the Ge elliptic lens, which impacts the spatial resolution.

When the Ge elliptic lens in the centre of the core of the optical fibre is truncated, as illustrated in Fig. E.2 (c), and this result is compared to the one of the truncated Ge lenses in Fig. 4.13 (a), it is observed that both results generate *FL*s outside the truncated Ge elliptic lens. Fig. E.2 (d) illustrates the power enhancement along the *z* axis of the truncated Ge elliptic lens as it propagates in the centre of the truncated Ge elliptic lens in order that the generated *FL*s outside the lens can be observed more clearly outside of the truncated Ge elliptic lens. This demonstrates that, similar the result in Fig. 4.13 (b), the *FL* is generated at a distance of $0.19\lambda_0$ from the output surface of the truncated Ge elliptic lens. In order to determine the spatial

resolution of the *FL* generated, the power enhancement along the *x* axis (at $y = 0$ and $z = 0.19\lambda_0$) and *y* axis (at $x = 0$ and $z = 0.19\lambda_0$) are illustrated in Fig. E.2 (e,f), respectively. In Fig. E.2 (e,f), the *FL* is generated at the centre of the structure, as expected. This is in difference with Fig. 4.13 (c,d), where the *FL* is positioned $y = 0.8\lambda_0$ away from the centre of the optical fibre core. In Fig. E.2 (e,f), the spatial resolution results are, respectively, $FWHMx = 0.62\lambda_0$ and $FWHMy = 0.46\lambda_0$. The spatial resolution observed in Fig. E.2 (e,f) is higher to that of Fig. 4.13 (c,d) due to the truncated Ge elliptic lens is positioned at the centre of the core of the optical fibre.

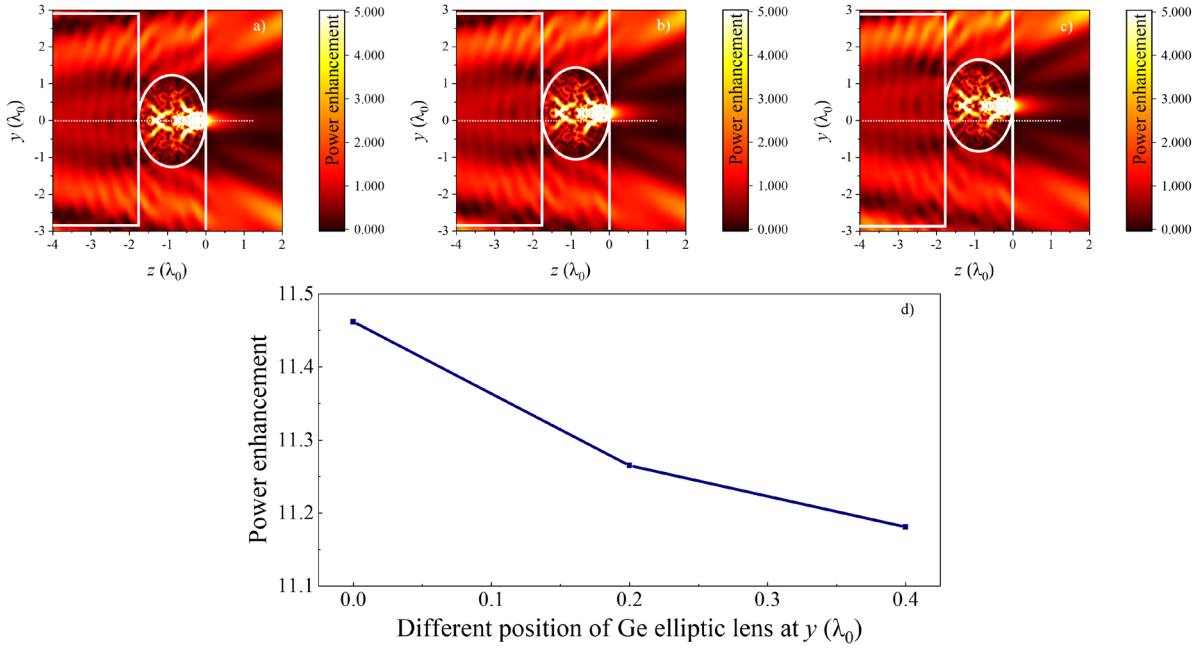

Figure E 1: (a-b) To observe the sensitivity of the Ge elliptic lens position, the structure is simulated using the CST Studio Suite in an arrangement similar to Fig. 4.12 (b), but with a different y axis position. The values of the parameters for (a-c) were obtained from Fig. 4.12 (a), but with different y axis positions. The output surface of all Ge elliptic lenses is denoted by z = 0, and the Ge elliptic lens is illuminated on the left by an optical fibre with a wavelength of $\lambda_0 = 2$ μm and a core diameter of $5.6\lambda_0$. The power enhancement in the yz plane is shown with the centre of the Ge elliptic lenses at ($x = 0$, $z = -0.88\lambda_0$), where (a) $y = 0\lambda_0$, (b) $y = 0.2\lambda_0$, and (c) $y = 0.6\lambda_0$, respectively. The horizontal white dashed line along z at y=0 is presented to better illustrate the change in the position of the Ge elliptic lens at the y axis. (d) The power enhancement is illustrated as a function of the position of the Ge elliptic lens at $y = 0\lambda_0$, $0.2\lambda_0$, and $0.6\lambda_0$, where $z = x = 0$.

Finally, we compare the results of a Ge elliptic lens, a truncated Ge elliptic lens, a Ge sphere, and a truncated Ge sphere in terms of spatial resolution, power enhancement, and *FL* location to determine the optimal lens shape when these lenses are positioned in the centre of the core of the optical fibre. When examining the results for the Ge sphere in Fig. 4.1 and the Ge elliptic lens in Fig. E.1 (a) and Fig. E.2 (a,b), it is evident that the *FL* is located within the lens. This is as expected, as the ratio between the index of refraction of the dielectric and the surrounding background is greater than two. However, the *FL* distance of a Ge elliptic lens is closer to its outer surface than that of a Ge sphere. Therefore, we observe that the spatial resolution and the power enhancement at the output surface of the Ge elliptic lens are higher

than that of the Ge sphere. On the other hand, the comparison results between the truncated Ge elliptic lens in Fig. E.2 (c-f) and the truncated Ge sphere in Figs. 4.3 to 4.5 demonstrate that the truncated Ge sphere provides higher spatial resolution and power enhancement than the truncated Ge elliptic lens. Consequently, in chapter 4, the truncated Ge sphere with a radius of $1.15\lambda_0$ and *a* value of $0.39\lambda_0$, as shown in Fig. 4.5, is still considered the most optimal structure.

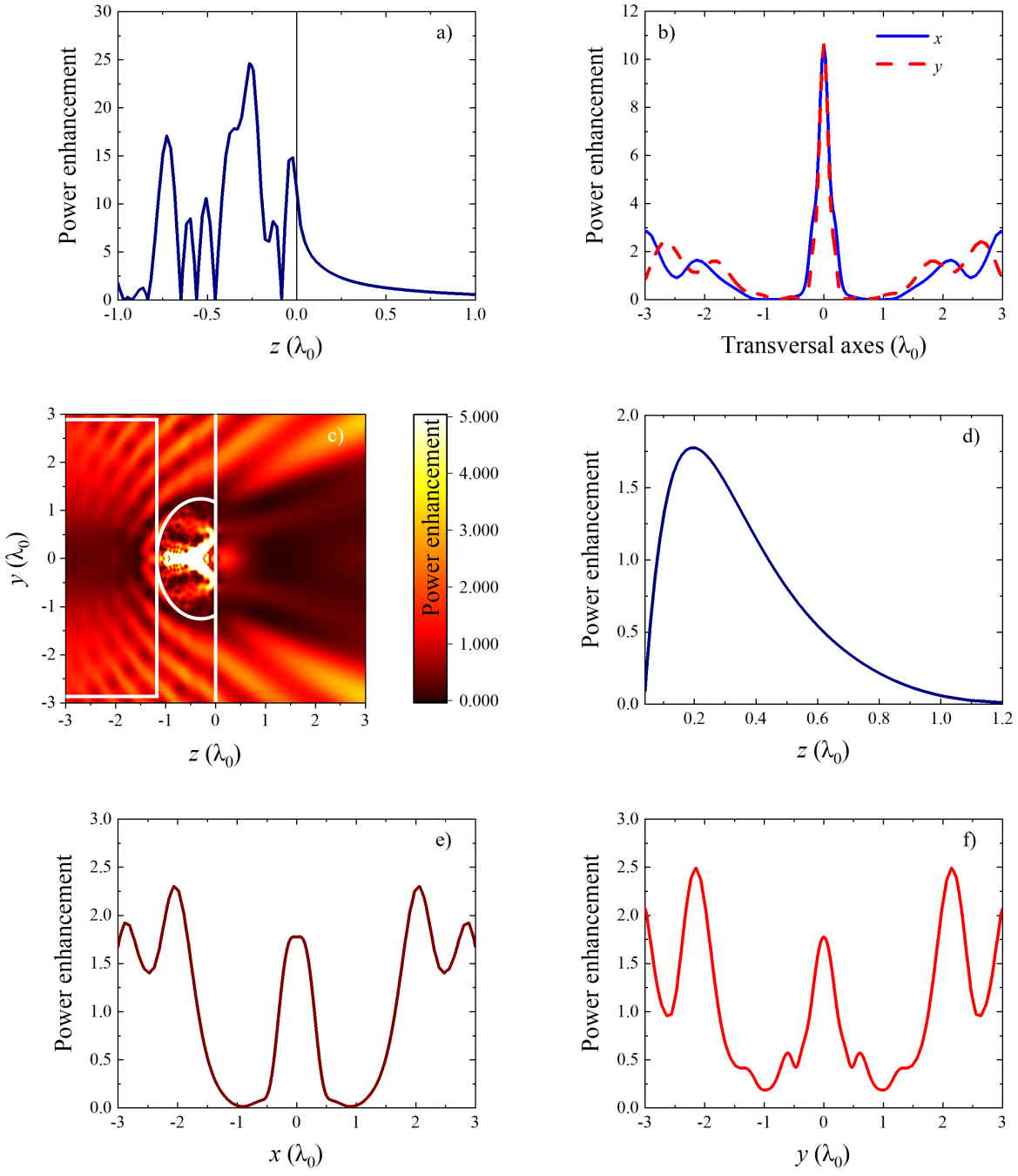

Figure E 2: (a) The power enhancement along the z axis at x = y = 0 is shown, where extracted from Fig. E.1 a. (b) The power enhancement is shown by a blue line along the x axis (at y = 0) and a red dashed line along the y axis (at x = 0) at z = 0 (extracted from Fig. E.1 a). The power enhancement for (c) with the same structure as Fig. E.1 a is presented in the yz plane after the full Ge elliptic lens has been truncated. The power enhancement along the z axis is illustrated in (d) at the centre of the truncated Ge lens, where x = y = 0. z = 0 is the location of the output surface of the truncated Ge elliptic lens. (e,f) The power enhancement at the FL where z = 0.19λ0 is presented along the transversal x and y axes, respectively.

Acronyms

5G	Fifth generation communication
a	The truncated distance from the centre of the dielectric
AM	Amplitude modulation
b	The normalized propagation constant
c	The speed of the light in a vacuum
CO_2	Carbon dioxide laser
D	The total dispersion parameter
D_M	The material dispersion
DNA	Deoxyribonucleic acid
DoF	The depth of focus
D_W	The waveguide dispersion
$\boldsymbol{E}$	The electric field
EH_{mn}	Hybrid symbols for electric fields
FDTD	Finite-difference time-domain
FEM	Finite Element Method
FIR	Far infrared
FL	Focal length
FM	Frequency modulation
$FWHM$	The full width at half maximum
Ge	Germanium
H	The magnetic field
HE_{mn}	Hybrid symbols for magnetic fields
IR	Infrared

ISO	International Organization for Standardization
k	The extinction coefficient
L	The transversal lengths of the dielectric
LDS	Large Diameter Splicing System machine
m	The azimuthal mode number
m_e	Electron mass
MIR	Medium infrared
n	The radial mode number
N	Electrons per unit volume
n	The refractive index
ñ	The complex refractive index
$n_{cladding}$	The refractive index for the cladding
n_{core}	The refractive index for the core
n_{eff}	The effective index or mode index
NA_{mic}	The numerical aperture of an optical microscope system
NA_f	The numerical aperture of an optical fibre
n_b	The refractive index of the background
n_d	The refractive index of the dielectric
n_g	The group index
$n_{\mathrm{g}(cladding)}$	The group index of refraction in the cladding of an optical fibre
NIR	Near infrared
$\boldsymbol{P}$	The electric polarisation
PNJ	Photonic nanojet
q_e	Electron charge
R	The radius of the dielectric

r_{core}	The radius of the core
Rcy	The radius of the added cylinder
Si	Silicon
SiO_2	Silicon dioxide
SiO_2-Ge	Silicon dioxide with germanium
tan δ	The loss tangent
TE_{0n}	Transverse electric modes
TM_{0n}	Transverse magnetic modes
v	The speed of an electromagnetic wave in a medium
V_{number}	Normalized frequency
V_c	The cut-off number
v_g	The group velocity
Δ	The index difference
ΔL	The different paths for the modes
ΔT	The delay for the modes
ϵ	Permittivity
θ_c	The critical angle
θ_g	The angle of incident light
θ_h	The half-angle of the light that collected from the sample under the objective lens
λ_0	The wavelengths in freespace
λ_c	The cut-off wavelength
λ_d	The wavelengths in dielectric
λ_{ZD}	The zero-dispersion wavelength
μ	Permeability
ω	The frequency

References

1. M. Born and E. Wolf, *Principles of Optics*, 7th ed. (New York: Cambridge University, 1999).
2. E. Hecht, *Optics*, Fifth Edit (Pearson Education Limited, 2017).
3. R. A. Serway and J. W. Jewett, *Physics for Scientists and Engineers*, Sixth Edit (Thomson Brooks/Cole, 2004).
4. M. I. Skolnik, *Introduction to Radar Systems*, Second Edi (McGraw-Hill Book Company, 1980).
5. Rabbit and Dynamic, *An Introduction to Wi-Fi* (2008).
6. G. Chittimoju and U. D. Yalavarthi, "A Comprehensive Review on Millimeter Waves Applications and Antennas," J. Phys. Conf. Ser. **1804**(1), 1–7 (2021).
7. F. Kamutzki, S. Schneider, J. Barowski, A. Gurlo, and D. A. H. Hanaor, "Silicate dielectric ceramics for millimetre wave applications," J. Eur. Ceram. Soc. **41**(7), 1–33 (2021).
8. Y.-S. Lee, *Principles of Terahertz Science and Technology* (Springer, 2009).
9. M. Navarro-Cía, M. S. Vitiello, C. M. Bledt, J. E. Melzer, J. A. Harrington, and O. Mitrofanov, "Terahertz wave transmission in flexible polystyrene-lined hollow metallic waveguides for the 25-5 THz band," Opt. Express **21**(20), 23748–23755 (2013).
10. D. Dragoman and M. Dragoman, "Terahertz fields and applications," Prog. Quantum Electron. **28**(1), 1–66 (2004).
11. F. Vatansever and M. R. Hamblin, "Far infrared radiation (FIR): Its biological effects and medical applications," Photonics Lasers Med. **1**(4), 255–266 (2012).
12. F. Hou, Y. Zhang, Y. Zhou, M. Zhang, B. Lv, and J. Wu, "Review on Infrared Imaging Technology," Sustainability **14**(18), 1–26 (2022).
13. E. Tournié, L. Monge Bartolome, M. Rio Calvo, Z. Loghmari, D. A. Díaz-Thomas, R. Teissier, A. N. Baranov, L. Cerutti, and J. B. Rodriguez, "Mid-infrared III–V semiconductor lasers epitaxially grown on Si substrates," Light Sci. Appl. **11**(1), 1–13

(2022).

14. J. X. Liu, S. L. Mei, X. H. Chen, and C. J. Yao, "Recent advances of near-infrared (Nir) emissive metal complexes bridged by ligands with n- and/or o-donor sites," Crystals **11**(2), 1–22 (2021).

15. I. Martinić, S. V. Eliseeva, T. N. Nguyen, V. L. Pecoraro, and S. Petoud, "Near-Infrared Optical Imaging of Necrotic Cells by Photostable Lanthanide-Based Metallacrowns," J. Am. Chem. Soc. **139**(25), 8388–8391 (2017).

16. S. E. Creutz, R. Fainblat, Y. Kim, M. C. De Siena, and D. R. Gamelin, "A Selective Cation Exchange Strategy for the Synthesis of Colloidal Yb3+-Doped Chalcogenide Nanocrystals with Strong Broadband Visible Absorption and Long-Lived Near-Infrared Emission," J. Am. Chem. Soc. **139**(34), 11814–11824 (2017).

17. B. J. Müller, S. M. Borisov, and I. Klimant, "Red- to NIR-Emitting, BODIPY-Based, K+-Selective Fluoroionophores and Sensing Materials," Adv. Funct. Mater. **26**(42), 7697–7707 (2016).

18. N. Sharma, A. D. Ankalgi, U. Thakur, M. S. Ashawat, and N. Sharma, "Advancement of Near Infrared techniques in diagnosis and treatment of cancer," J. Drug Deliv. Ther. **12**(4-S), 192–198 (2022).

19. A. Manickavasagan and H. Jayasuriya, *Imaging with Electromagnetic Spectrum* (Springer Heidelberg New York Dordrecht London, 2014).

20. N. Dong, J. Cui, and J. Xu, "Variable spot size optical system for a dual-wavelength laser therapy device," J. Innov. Opt. Health Sci. **13**(4), 1–7 (2020).

21. C. Yeh, *Applied Photonics* (Academic Press, 1994).

22. R. Menzel, *Photonics: Linear and Nonlinear Interactions of Laser Light and Matter*, 1 st editi (Springer-Verlag Berlin Heidelberg New York, 2001).

23. H. Al-Taiy, N. Wenzel, S. Preußler, J. Klinger, and T. Schneider, "Ultra-narrow line-width, stable and widely tuneable laser source for coherent optical communication systems," Eur. Conf. Opt. Commun. ECOC **39**(20), 5826–5829 (2014).

24. F. Wang, W. Du, Q. Yuan, D. Liu, and S. Feng, "Wander of a Gaussian-Beam Wave Propagating through Kolmogorov and Non-Kolmogorov Turbulence along Laser-Satellite Communication Uplink," Atmosphere (Basel). **13**(2), 1–12 (2022).

25. W. D. Kimura, *Electromagnetic Waves and Lasers*, Second Edi (IOP Publishing, Temple

Circus, Temple Way, Bristol, BS1 6HG, UK, 2020).

26. I. S. Amiri, S. R. Bin Azzuhri, M. A. Jalil, H. M. Hairi, J. Ali, M. Bunruangses, and P. Yupapin, "Introduction to photonics: Principles and the most recent applications of microstructures," Micromachines **9**(9), 1–25 (2018).

27. A. Gorin, A. Jaouad, E. Grondin, V. Aimez, and P. Charette, "Fabrication of silicon nitride waveguides for visible-light using PECVD: a study of the effect of plasma frequency on optical properties," Opt. Express **16**(18), 13509–13516 (2008).

28. K. S. Gill, "Ruby Laser," Int. J. Innov. Res. Sci. Eng. Technol. **11**(4), 2320–6710 (2022).

29. M. F. S. Ferreira and M. C. Paul, *Optical Fiber Technology and Applications* (IOP Publishing, Temple Circus, Temple Way, Bristol, BS1 6HG, UK, 2021).

30. R. P. Feynman, "There's Plenty of Room at the Bottom," Am. Phys. Soc. Pasadena (1959).

31. A. Lininger, G. Palermo, A. Guglielmelli, G. Nicoletta, M. Goel, M. Hinczewski, and G. Strangi, "Chirality in Light-Matter Interaction," Adv. Mater. **2107325**, 1–31 (2022).

32. V. Morozhenko, *Infrared Radiation* (InTech, 2012).

33. A. Aboshosha, A. Nasr, and M. Hassan, "Improved Thermographic Object Detection relying-on Image Processing and Sensorial Development of Quantum IR Photodetectors," Menoufia J. Electron. Eng. Res. **19**(1), 63–80 (2009).

34. Y. Ozaki, C. Huck, S. Tsuchikawa, and S. B. Engelsen, *Near-Infrared Spectroscopy* (Springer Nature Singapore Pte Ltd, 2021).

35. E. D. Palik, *Handbook of Optical Constants of Solids* (Academic Press, Boston, 1985).

36. P. O. Chapuis, S. Volz, C. Henkel, K. Joulain, and J. J. Greffet, "Effects of spatial dispersion in near-field radiative heat transfer between two parallel metallic surfaces," Phys. Rev. B - Condens. Matter Mater. Phys. **77**(3), 1–9 (2008).

37. B. H. Stuart, *Infrared Spectroscopy: Fundamentals and Applications* (John Wiley & Sons, Ltd, 2004).

38. E. N. Lewis, L. H. Kidder, I. W. Levin, V. F. Kalasinsky, J. P. Hanig, and D. S. Lester, "Applications of fourier transform infrared imaging microscopy in neurotoxicity," Ann. N. Y. Acad. Sci. **820**, 234–247 (1997).

39. A. Korkin, P. S. Krsti´c, and J. C. Wells, *Nanotechnology for Electronics, Photonics,*

and Renewable Energy (Springer New York Dordrecht Heidelberg London, 2010).

40. W. M. Haynes, D. R. Lide, and T. J. Bruno, *CRC Handbook of Chemistry and Physics*, 95th Editi (CRC Press is an imprint of Taylor & Francis Group, an Informa business, 2014).

41. F. Begum and P. E. Abas, "Near infrared supercontinuum generation in silica based photonic crystal fiber," Prog. Electromagn. Res. C **89**(January), 149–159 (2019).

42. E. A. Stepanidenko, I. D. Skurlov, P. D. Khavlyuk, D. A. Onishchuk, A. V Koroleva, E. V Zhizhin, I. A. Arefina, D. A. Kurdyukov, D. A. Eurov, V. G. Golubev, A. V Baranov, A. V Fedorov, E. V Ushakova, and A. L. Rogach, "Carbon Dots with an Emission in the Near Infrared Produced from Organic Dyes in Porous Silica Microsphere Templates," Nanomaterials **12**, 1–14 (2022).

43. G. P. Agrawal, *Fiber-Optic Communication Systems*, Third Edit (Wiley-Interscience, 2002), **6**.

44. L. Rechtman and D. M. Marom, "Rectangular versus circular fiber core designs: New opportunities for mode division multiplexing?," in *Optical Fiber Communication Conference, OFC 2017* (2017), pp. 1–3.

45. N. K. Fontaine, R. Ryf, H. Chen, A. V. Benitez, J. E. Antonio Lopez, R. Amezcua Correa, B. Guan, B. Ercan, R. P. Scott, S. J. Ben Yoo, L. Grüner-Nielsen, Y. Sun, and R. J. Lingle, "30×30 MIMO transmission over 15 spatial modes," in *Optical Fiber Communication Conference, OFC 2015* (2015), pp. 1–3.

46. G. P. Agrawal, *Nonliear Fiber Optics*, Third Edit (Academic Press, 2001).

47. D. Meschede, *Optics, Light and Lasers*, Second Edi (WILEY-VCH Verlag GmbH & Co. KGaA, 2007).

48. T. R. Woliński, "Polarization in optical fibers," Acta Phys. Pol. A **95**(5), 749–760 (1999).

49. X. Lian, G. Farrell, Q. Wu, W. Han, F. Wei, and Y. Semenova, "Mode Transition in Conventional Step-Index Optical Fibers," in *2019 18th International Conference on Optical Communications and Networks, ICOCN 2019* (2019), (August), pp. 1–3.

50. R. S. Quimby, *Photonics and Lasers* (A Wiley-Interscience, 2006).

51. S. Kamaraj, S. S. Dhanabalan, A. Thirumurugan, and S. A. Hevia, *Microscopic Techniques for the Non-Expert* (Springer Nature Switzerland AG, 2022).

52. C. Wong, M. E. Pawlowski, and T. S. Tkaczyk, "Simple ultraviolet microscope using off-the-shelf components for point-of-care diagnostics," PLoS One **14**(4), 1–11 (2019).

53. R. Chen, K. Agarwal, C. J. R. Sheppard, J. C. H. Phang, and X. Chen, "A complete and computationally efficient numerical model of aplanatic solid immersion lens scanning microscope," Opt. Express **21**(12), 14316–14330 (2013).

54. I. C. Baianu, "Applications Of Microspectroscopy, Hyperspectral Chemical Imaging And Fluorescence Microscopy In Chemistry, Biochemistry, Biotechnology, Molecular And Cell Biology," Nat. Preced. 1–12 (2011).

55. Z. Wang, W. Guo, L. Li, B. Luk'Yanchuk, A. Khan, Z. Liu, Z. Chen, and M. Hong, "Optical virtual imaging at 50 nm lateral resolution with a white-light nanoscope," Nat. Commun. **2**(1), 1–6 (2011).

56. S. Lee and L. Li, "Rapid super-resolution imaging of sub-surface nanostructures beyond diffraction limit by high refractive index microsphere optical nanoscopy," Opt. Commun. **334**, 253–257 (2015).

57. Y. Zihan and L. Sylvain, "Whispering gallery mode resonance contribution in photonic nanojet simulation," Opt. Express **29**(24), 39249–39255 (2021).

58. D. C. Dilworth, *Lens Design*, Second Edi (IOP Publishing, Temple Circus, Temple Way, Bristol, BS1 6HG, UK, 2020).

59. H. Köhler, "On Abbe's theory of image formation in the microscope," Opt. Acta (Lond). **28**(12), 1691–1701 (1981).

60. Q. Wu, G. D. Feke, R. D. Grober, and L. P. Ghislain, "Realization of numerical aperture 2.0 using a gallium phosphide solid immersion lens," Appl. Phys. Lett. **75**(26), 4064–4066 (1999).

61. A. N. K. REDDY and D. K. SAGAR, "Half-Width at half-Maximum, full-Width at half-Maximum analysis for resolution of asymmetrically apodized optical systems with slit apertures," Pramana - J. Phys. **84**(1), 117–126 (2015).

62. C. Girard and A. Dereux, "Near-field optics theories," Reports Prog. Phys. **59**(5), 657–699 (1996).

63. M. J. Mendes, I. Tobías, A. Martí, and A. Luque, "Light concentration in the near-field of dielectric spheroidal particles with mesoscopic sizes," Opt. Express **19**(17), 16207–16222 (2011).

64. E. Betzig, A. Lewis, A. Harootunian, M. Isaacson, and E. Kratschmer, "Near Field Scanning Optical Microscopy (NSOM): Development and Biophysical Applications," Biophys. J. **49**(1), 269–279 (1986).

65. X. Zhang and Z. Liu, "Superlenses to overcome the diffraction limit," J. Magn. Magn. Mater. **7**, 435–441 (2008).

66. Z. Chen, A. Taflove, and V. Backman, "Photonic nanojet enhancement of backscattering of light by nanoparticles: a potential novel visible-light ultramicroscopy technique," Opt. Express **12**(7), 1214–1220 (2004).

67. V. G. Veselago, "The electrodynamics of substances with simultaneously negative values of ϵ and μ," Sov. Phys. Uspekhi **10**(4), 509–514 (1968).

68. V. Pacheco-Peña, B. Orazbayev, V. Torres, M. Beruete, and M. Navarro-Cía, "Ultra-compact planoconcave zoned metallic lens based on the fishnet metamaterial," Appl. Phys. Lett. **103**(18), 1–7 (2013).

69. V. Pacheco-Peña, M. Navarro-Cía, and M. Beruete, "Epsilon-near-zero metalenses operating in the visible," Opt. Laser Technol. **80**, 1–18 (2016).

70. A. Poddubny, I. Iorsh, P. Belov, and Y. Kivshar, "Hyperbolic metamaterials," Nat. Photonics **7**(12), 958–967 (2013).

71. A. R. McGurn, *Introduction to Nonlinear Optics of Photonic Crystals and Metamaterials*, Second Edi (IOP Publishing, Temple Circus, Temple Way, Bristol, BS1 6HG, UK, 2021).

72. D. R. Smith and D. Schurig, "Electromagnetic Wave Propagation in Media with Indefinite Permittivity and Permeability Tensors," Phys. Rev. Lett. **90**(7), 1–4 (2003).

73. R. M. Walser, A. P. Valanju, and P. M. Valanju, "Extremely Low Frequency Plasmons in Metallic Mesostructures," Phys. Rev. Lett. **76**(25), 4773–4776 (1996).

74. D. Bílková, "Modern methods of parametric estimation: Estimation using L-moments and TL-moments," Phys. Rev. Lett. **84**(18), 4184–4187 (2000).

75. J. B. Pendry and S. A. Ramakrishna, "Near-field lenses in two dimensions," J. Phys. Condens. Matter **14**(36), 8463–8479 (2002).

76. X. Li, Z. Chen, A. Taflove, and V. Backman, "Optical analysis of nanoparticles via enhanced backscattering facilitated by 3-D photonic nanojets," Opt. Express **13**(2), 526–533 (2005).

77. W. Zhang and H. Lei, "Fluorescence enhancement based on cooperative effects of a photonic nanojet and plasmon resonance," Nanoscale **12**(12), 6596–6602 (2020).

78. V. Pacheco-Peña, M. Beruete, I. V. Minin, and O. V. Minin, "Terajets produced by dielectric cuboids," Appl. Phys. Lett. **105**(8), 1–4 (2014).

79. Y. Miao, X. Gao, G. Wang, Y. Li, X. Liu, and G. Sui, "Microsphere-lens coupler with 100 nm lateral resolution accuracy in visible light," Appl. Opt. **59**(20), 6012–6017 (2020).

80. I. V. Minin, O. V. Minin, I. A. Glinskiy, R. A. Khabibullin, R. Malureanu, A. V. Lavrinenko, D. I. Yakubovsky, A. V. Arsenin, V. S. Volkov, and D. S. Ponomarev, "Plasmonic nanojet: an experimental demonstration: publisher's note," Opt. Lett. **45**(13), 3244–3247 (2020).

81. A. Kovrov, A. Novitsky, A. Karabchevsky, and A. S. Shalin, "A Photonic Nanojet as Tunable and Polarization-Sensitive Optical Tweezers," Ann. Phys. **530**(9), 1–5 (2018).

82. H. Yang, R. Trouillon, G. Huszka, and M. A. M. Gijs, "Super-Resolution Imaging of a Dielectric Microsphere Is Governed by the Waist of Its Photonic Nanojet," Nano Lett. **16**(8), 4862–4870 (2016).

83. Y. Wen, H. Yu, W. Zhao, F. Wang, X. Wang, L. Liu, and W. J. Li, "Photonic Nanojet Sub-Diffraction Nano-Fabrication With in situ Super-Resolution Imaging," IEEE Trans. Nanotechnol. **18**, 226–233 (2019).

84. H. Yang, R. Trouillon, G. Huszka, and M. A. M. Gijs, "Super-Resolution Imaging of a Dielectric Microsphere Is Governed by the Waist of Its Photonic Nanojet: Supporting Information," Nano Lett. **16**(8), 4862–4870 (2016).

85. Y. Li, H. Xin, X. Liu, Y. Zhang, H. Lei, and B. Li, "Trapping and Detection of Nanoparticles and Cells Using a Parallel Photonic Nanojet Array," ACS Nano **10**(6), 5800–5808 (2016).

86. H. Yang, M. Cornaglia, and M. A. M. Gijs, "Photonic nanojet array for fast detection of single nanoparticles in a flow," Nano Lett. **15**(3), 1730–1735 (2015).

87. A. Devilez, B. Stout, N. Bonod, and E. Popov, "Spectral analysis of three-dimensional photonic jets," Opt. Express **16**(18), 14200–14212 (2008).

88. A. Heifetz, S. C. Kong, A. V. Sahakian, A. Taflove, and V. Backman, "Photonic nanojets," J. Comput. Theor. Nanosci. **6**(9), 1979–1992 (2009).

89. C. Y. Liu and C. C. Li, "Photonic nanojet induced modes generated by a chain of dielectric microdisks," Optik (Stuttg). **127**(1), 267–273 (2016).

90. D. Lu, M. Pedroni, L. Labrador-Páez, M. I. Marqués, D. Jaque, and P. Haro-González, "Nanojet Trapping of a Single Sub-10 nm Upconverting Nanoparticle in the Full Liquid Water Temperature Range," Small **17**(7), 1–8 (2021).

91. V. Pacheco-Peña, J. A. Riley, C. Y. Liu, O. V. Minin, and I. V. Minin, "Diffraction limited photonic hook via scattering and diffraction of dual-dielectric structures," Sci. Rep. **11**(1), 1–9 (2021).

92. Y. Yue, X. Hu, R. Wang, and X. Qiao, "Generation of long photonic nanojet by a self-assembled microdevice on optical fiber," Opt. Laser Technol. **159**(December 2022), 1–6 (2023).

93. B. S. Luk'yanchuk, R. Paniagua-Domínguez, I. Minin, O. Minin, and Z. Wang, "Refractive index less than two: photonic nanojets yesterday, today and tomorrow [Invited]," Opt. Mater. Express **7**(6), 1820–1847 (2017).

94. V. Pacheco-Peña and M. Beruete, "Photonic nanojets with mesoscale high-index dielectric particles," J. Appl. Phys. **125**(8), 1–7 (2019).

95. I. V. Minin, O. V. Minin, V. Pacheco-Peña, and M. Beruete, "Localized photonic jets from flat, three-dimensional dielectric cuboids in the reflection mode," Opt. Lett. **40**(10), 2329–2332 (2015).

96. A. D. Kiselev and D. O. Plutenko, "Mie scattering of Laguerre-Gaussian beams: Photonic nanojets and near-field optical vortices," Phys. Rev. A - At. Mol. Opt. Phys. **89**(4), 1–22 (2014).

97. I. V. Minin, O. V. Minin, and Y. E. Geints, "Localized em and photonic jets from non-spherical and non-symmetrical dielectric mesoscale objects: Brief review," Ann. Phys. **527**(7–8), 491–497 (2015).

98. L. Yue, O. V. Minin, Z. Wang, J. N. Monks, A. S. Shalin, and I. V. Minin, "Photonic hook: a new curved light beam," Opt. Lett. **43**(4), 771–774 (2018).

99. P. Ferrand, J. Wenger, A. Devilez, M. Pianta, B. Stout, N. Bonod, E. Popov, and H. Rigneault, "Direct imaging of photonic nanojets," Opt. Express **16**(10), 6930–6940 (2008).

100. T. Agrawal, S. Dey, and P. B. Bisht, "Single nanoparticle sensing and waveguide

applications using photonic nanojet from an array of shaped microparticles," Opt. Commun. **529**(129110), 1–6 (2022).

101. V. R. Dantham, P. B. Bisht, and C. K. R. Namboodiri, "Enhancement of Raman scattering by two orders of magnitude using photonic nanojet of a microsphere," J. Appl. Phys. **109**(10), 1–4 (2011).

102. J. Wenger and H. Rigneault, "Photonic methods to enhance fluorescence correlation spectroscopy and single molecule fluorescence detection," Int. J. Mol. Sci. **11**(1), 206–221 (2010).

103. V. N. Astratov, A. Darafsheh, M. D. Kerr, K. W. Allen, N. M. Fried, A. N. Antoszyk, and H. S. Ying, "Photonic nanojets for laser surgery," SPIE Newsroom 1–3 (2010).

104. R. Pierron, G. Chabrol, S. Roques, P. Pfeiffer, J.-P. Yehouessi, G. Bouwmans, and S. Lecler, "Large-mode-area optical fiber for photonic nanojet generation," Opt. Lett. **44**(10), 2474–2477 (2019).

105. J. Zelgowski, A. Abdurrochman, F. Mermet, P. Pfeiffer, J. Fontaine, and S. Lecler, "Photonic jet subwavelength etching using a shaped optical fiber tip," Opt. Lett. **41**(9), 2073–2076 (2016).

106. D. Bouaziz, G. Chabrol, A. Guessoum, N.-E. Demagh, and S. Lecler, "Photonic Jet-Shaped Optical Fiber Tips versus Lensed Fibers," Photonics **8**(9), 1–7 (2021).

107. Z. Li, J. Yang, S. Liu, X. Jiang, H. Wang, X. Hu, S. Xue, S. He, and X. Xing, "High throughput trapping and arrangement of biological cells using self-assembled optical tweezer," Opt. Express **26**(26), 34665–34674 (2018).

108. Y. Li, X. Liu, X. Yang, H. Lei, Y. Zhang, and B. Li, "Enhancing Upconversion Fluorescence with a Natural Bio-microlens," ACS Nano **11**(11), 10672–10680 (2017).

109. I. V. Minin, O. V. Minin, V. Pacheco-Peña, and M. Beruete, "All-dielectric periodic terajet waveguide using an array of coupled cuboids," Appl. Phys. Lett. **106**(25), 1–5 (2015).

110. C. Liu, "Ultra-elongated photonic nanojets generated by a graded-index microellipsoid," Prog. Electromagn. Res. Lett. **37**, 153–165 (2013).

111. M. Salhi and P. G. Evans, "Photonic nanojet as a result of a focused near-field diffraction," J. Opt. Soc. Am. B **36**(4), 1031–1036 (2019).

112. C. Y. Liu, "Superenhanced photonic nanojet by core-shell microcylinders," Phys. Lett.

Sect. A Gen. At. Solid State Phys. **376**(23), 1856–1860 (2012).

113. P. Sharma, R. K. Arora, S. Pardeshi, and M. Singh, "Fibre Optic Communications : An Overview," Int. J. Emerg. Technol. Adv. Eng. **3**(5), 474–479 (2013).

114. V. Pacheco-Peña, I. V. Minin, O. V. Minin, and M. Beruete, "Comprehensive analysis of photonic nanojets in 3D dielectric cuboids excited by surface plasmons," Ann. Phys. **528**(9–10), 684–692 (2016).

115. V. Pacheco-Peña, I. V. Minin, O. V. Minin, and M. Beruete, "Increasing surface plasmons propagation via photonic nanojets with periodically spaced 3D dielectric cuboids," Photonics **3**(1), 1–7 (2016).

116. I. V Minin, O. V Minin, V. Pacheco-Peña, and M. Beruete, "Subwavelength, standing-wave optical trap based on photonic jets," Quantum Electron. **46**(6), 555–557 (2016).

117. A. Heifetz, K. Huang, A. V. Sahakian, X. Li, A. Taflove, and V. Backman, "Experimental confirmation of backscattering enhancement induced by a photonic jet," Appl. Phys. Lett. **89**(22), 1–4 (2006).

118. V. Pacheco-Peña, M. Beruete, I. V. Minin, and O. V. Minin, "Multifrequency focusing and wide angular scanning of terajets," Opt. Lett. **40**(2), 245–248 (2015).

119. B. Wei, S. Gong, R. Li, I. V. Minin, O. V. Minin, and L. Lin, "Optical Force on a Metal Nanorod Exerted by a Photonic Jet," Nanomaterials **12**(2), 1–15 (2022).

120. S. M. Mansfield and G. S. Kino, "Solid immersion microscope," Appl. Phys. Lett. **57**(24), 2615–2616 (1990).

121. A. Darafsheh, "Photonic nanojets and their applications," J. Phys. Photonics **3**(2), 1–21 (2021).

122. I. V. Minin, Y. E. Geints, A. A. Zemlyanov, and O. V. Minin, "Specular-reflection photonic nanojet: physical basis and optical trapping application," Opt. Express **28**(15), 22690–22704 (2020).

123. G. Gu, P. Zhang, S. Chen, Y. Zhang, and H. Yang, "Inflection point: a perspective on photonic nanojets," Photonics Res. **9**(7), 1–45 (2021).

124. A. Karabchevsky, T. Elbaz, A. Katiyi, O. Prager, and A. Friedman, "Super-Resolution Imaging and Optomechanical Manipulation Using Optical Nanojet for Nondestructive Single-Cell Research," Adv. Photonics Res. **3**(2), 1–15 (2022).

125. X. Cui, D. Erni, and C. Hafner, "Optical forces on metallic nanoparticles induced by a photonic nanojet," Opt. Express **16**(18), 13560–13568 (2008).

126. S.-C. Kong, A. Taflove, and V. Backman, "Quasi one-dimensional light beam generated by a graded-index microsphere: errata," Opt. Express **17**(5), 3722–3731 (2009).

127. G. Gu, J. Song, H. Liang, M. Zhao, Y. Chen, and J. Qu, "Overstepping the upper refractive index limit to form ultra-narrow photonic nanojets - supporting information," Sci. Rep. **7**(1), 1–6 (2017).

128. V. Gašparić, T. G. Mayerhöfer, D. Zopf, D. Ristić, J. Popp, and M. Ivanda, "To generate a photonic nanojet outside a high refractive index microsphere illuminated by a Gaussian beam," Opt. Lett. **47**(10), 2534–2537 (2022).

129. S. C. Kong, A. V. Sahakian, A. Heifetz, A. Taflove, and V. Backman, "Robust detection of deeply subwavelength pits in simulated optical data-storage disks using photonic jets," Appl. Phys. Lett. **92**(21), 1–3 (2008).

130. S. Lecler, S. Haacke, N. Lecong, O. Crégut, J.-L. Rehspringer, and C. Hirlimann, "Photonic jet driven non-linear optics: example of two-photon fluorescence enhancement by dielectric microspheres," Opt. Express **15**(8), 4935–4942 (2007).

131. J. Zhu and L. L. Goddard, "All-dielectric concentration of electromagnetic fields at the nanoscale: The role of photonic nanojets," Nanoscale Adv. **1**(12), 4615–4643 (2019).

132. K. J. Yi, H. Wang, Y. F. Lu, and Z. Y. Yang, "Enhanced Raman scattering by self-assembled silica spherical microparticles," J. Appl. Phys. **101**(6), 1–5 (2007).

133. S. Lecler, S. Perrin, A. Leong-Hoi, and P. Montgomery, "Photonic jet lens," Sci. Rep. **9**(1), 1–8 (2019).

134. A. V. Veluthandath and G. S. Murugan, "Photonic nanojet generation using integrated silicon photonic chip with hemispherical structures," Photonics **8**(12), 1–9 (2021).

135. J. A. Riley, N. Healy, and V. Pacheco-Peña, "Plasmonic meniscus lenses," Sci. Rep. **12**(1), 1–11 (2022).

136. S. Legaria, V. Pacheco-Peña, and M. Beruete, "Super-oscillatory metalens at terahertz for enhanced focusing with reduced side lobes," Photonics **5**(4), 10–16 (2018).

137. J. Zhu and L. L. Goddard, "Spatial control of photonic nanojets," Opt. Express **24**(26), 30444–30464 (2016).

138. R. Pierron, S. Lecler, J. Zelgowski, P. Pfeiffer, F. Mermet, and J. Fontaine, "Etching of semiconductors and metals by the photonic jet with shaped optical fiber tips," Appl. Surf. Sci. **418**, 452–455 (2017).

139. G. Wu and M. Hong, "Optical nano-imaging via microsphere compound lenses working in non-contact mode," Opt. Express **29**(15), 23073–23082 (2021).

140. A. Darafsheh, N. I. Limberopoulos, J. S. Derov, D. E. Walker, and V. N. Astratov, "Advantages of microsphere-assisted super-resolution imaging technique over solid immersion lens and confocal microscopies," Appl. Phys. Lett. **104**(6), 1–4 (2014).

141. H. Luo, H. Yu, Y. Wen, J. Zheng, X. Wang, and L. Liu, "Direct writing of silicon oxide nanopatterns using photonic Nanojets," Photonics **8**(5), 1–8 (2021).

142. A. M. Kapitonov and V. N. Astratov, "Observation of nanojet-induced modes with small propagation losses in chains of coupled spherical cavities," Opt. Lett. **32**(4), 409–411 (2007).

143. G. Gu, J. Song, H. Liang, M. Zhao, Y. Chen, and J. Qu, "Overstepping the upper refractive index limit to form ultra-narrow photonic nanojets," Sci. Rep. **7**(1), 1–8 (2017).

144. Z. B. Wang, W. Guo, A. Pena, D. J. Whitehead, B. S. Luk'yanchuk, L. Li, Z. Liu, Y. Zhou, and M. H. Hong, "Laser micro/nano fabrication in glass with tunable-focus particle lens array," Opt. Express **16**(24), 19706–19711 (2008).

145. Y. C. Li, H. B. Xin, H. X. Lei, L. L. Liu, Y. Z. Li, Y. Zhang, and B. J. Li, "Manipulation and detection of single nanoparticles and biomolecules by a photonic nanojet," Light Sci. Appl. **5**(12), 1–9 (2016).

146. A. Heifetz, J. J. Simpson, S.-C. Kong, A. Taflove, and V. Backman, "Subdiffraction optical resolution of a gold nanosphere located within the nanojet of a Mie-resonant dielectric microsphere," Opt. Express **15**(25), 17334–17342 (2007).

147. V. Gašparić, T. G. Mayerhöfer, D. Zopf, D. Ristić, J. Popp, and M. Ivanda, "To generate a photonic nanojet outside a high refractive index microsphere illuminated by a Gaussian beam (Supplemental Document)," Opt. Lett. **47**(10), 1–11 (2022).

148. A. Darafsheh and D. Bollinger, "Systematic study of the characteristics of the photonic nanojets formed by dielectric microcylinders," Opt. Commun. **402**(June), 270–275 (2017).

149. R. Chen, J. Lin, P. Jin, M. Cada, and Y. Ma, "Photonic nanojet beam shaping by

illumination polarization engineering," Opt. Commun. **456**(August 2019), 1–10 (2020).

150. Y. Liu, B. Wang, and Z. Ding, "Influence of incident light polarization on photonic nanojet," Chinese Opt. Lett. **9**(7), 072901–072903 (2011).

151. A. Darafsheh, N. Mojaverian, N. I. Limberopoulos, K. W. Allen, A. Lupu, and V. N. Astratov, "Formation of polarized beams in chains of dielectric spheres and cylinders," Opt. Lett. **38**(20), 4208–4211 (2013).

152. P. B. Johnson, A. Karvounis, H. J. Singh, C. J. Brereton, K. N. Bourdakos, K. Lunn, J. J. W. Roberts, D. E. Davies, O. L. Muskens, M. G. Jones, and S. Mahajan, "Superresolved polarization-enhanced second-harmonic generation for direct imaging of nanoscale changes in collagen architecture," Optica **8**(5), 674–685 (2021).

153. M.-S. Kim, T. Scharf, S. Mühlig, C. Rockstuhl, and H. P. Herzig, "Engineering photonic nanojets," Opt. Express **19**(11), 10206–10220 (2011).

154. Y. Li, H. Xin, Y. Zhang, and B. Li, "Optical Fiber Technologies for Nanomanipulation and Biodetection: A Review," J. Light. Technol. **39**(1), 251–262 (2021).

155. M. Yoshita, K. Koyama, Y. Hayamizu, M. Baba, and H. Akiyama, "Improved high collection efficiency in fluorescence microscopy with a Weierstrass-sphere solid immersion lens," Japanese J. Appl. Physics, Part 2 Lett. **41**(7 B), 858–860 (2002).

156. S. Yadav, G. Kaur, C. Technology, and U. Pradesh, "Aplanatic Point Analysis of Solid Immersion Lens in Photonics," Int. J. Adv. Eng. Technol. **8**(3), 385–396 (2015).

157. L. P. Ghislain, V. B. Elings, K. B. Crozier, S. R. Manalis, S. C. Minne, K. Wilder, G. S. Kino, and C. F. Quate, "Near-field photolithography with a solid immersion lens," Appl. Phys. Lett. **74**(4), 501–503 (1999).

158. Y. Zhang and X. Ye, "Three-zone phase-only filter increasing the focal depth of optical storage systems with a solid immersion lens," Appl. Phys. B Lasers Opt. **86**(1), 97–103 (2007).

159. Z. Zhen, Y. Huang, Y. Feng, Y. Shen, and Z. Li, "An ultranarrow photonic nanojet formed by an engineered two-layer microcylinder of high refractive-index materials," Opt. Express **27**(6), 9178–9188 (2019).

160. S. B. Ippolito, B. B. Goldberg, and M. S. Ünlü, "Theoretical analysis of numerical aperture increasing lens microscopy," J. Appl. Phys. **97**(5), 1–12 (2005).

161. B. D. Terris, H. J. Mamin, D. Rugar, W. R. Studenmund, and G. S. Kino, "Near-field

optical data storage using a solid immersion lens," Appl. Phys. Lett. **65**(4), 388–390 (1994).

162. K. A. Serrels, E. Ramsay, P. A. Dalgarno, B. D. Gerardot, J. A. O'Connor, R. H. Hadfield, R. J. Warburton, and D. T. Reid, "Solid immersion lens applications for nanophotonic devices," J. Nanophotonics **2**(1), 1–29 (2008).

163. K. Karrai, X. Lorenz, and L. Novotny, "Enhanced reflectivity contrast in confocal solid immersion lens microscopy," Appl. Phys. Lett. **77**(21), 3459–3461 (2000).

164. A. N. Vamivakas, R. D. Younger, B. B. Goldberg, A. K. Swan, M. S. Ünlü, E. R. Behringer, and S. B. Ippolito, "A case study for optics: The solid immersion microscope," Am. J. Phys. **76**(8), 758–768 (2008).

165. X. Dong, T. Geng, and S. Zhuang, "Focus shaping of Weierstrass solid immersion lens by an axisymmetric Bessel-modulated Gaussian beam," Opt. Appl. **43**(2), 247–259 (2013).

166. Francis Arthur Jenkins and H. E. White, *Fundamentals of Optics*, Fourth Edi (The McGraw-Hill Companies, Inc., 2001).

167. T. Amotchkina, M. Trubetskov, D. Hahner, and V. Pervak, "Characterization of e-beam evaporated Ge, YbF3, ZnS, and LaF3 thin films for laser-oriented coatings," Appl. Opt. **59**(5), 40–47 (2020).

168. L. Yue, B. Yan, J. N. Monks, R. Dhama, Z. Wang, O. V. Minin, and I. V. Minin, "Photonic Jet by a Near-Unity-Refractive-Index Sphere on a Dielectric Substrate with High Index Contrast," Ann. Phys. **530**(6), 1–6 (2018).

169. J. Yang, I. Ghimire, P. C. Wu, S. Gurung, C. Arndt, D. P. Tsai, and H. W. H. Lee, "Photonic crystal fiber metalens," Nanophotonics **8**(3), 443–449 (2019).

170. D. E. McCoy, A. V. Shneidman, A. L. Davis, and J. Aizenberg, "Finite-difference Time-domain (FDTD) Optical Simulations: A Primer for the Life Sciences and Bio-Inspired Engineering," Micron **151**, 1–19 (2021).

171. CST, *CST Studio Suite High Frequency Simulation* (CST Studio Suite, 2020).

172. V. Pacheco-Peña, N. Engheta, S. Kuznetsov, A. Gentselev, and M. Beruete, "Experimental Realization of an Epsilon-Near-Zero Graded-Index Metalens at Terahertz Frequencies," Phys. Rev. Appl. **8**(3), 1–10 (2017).

173. G. Wu and M. Hong, "Optical nano-imaging via microsphere compound lenses working

in non-contact mode: supplement," Opt. Express **29**(15), 1474545–1474552 (2021).

174. D. Bouaziz, S. Perrin, T. Hajj, G. Chabrol, A. Guessoum, N.-E. Demagh, and S. Lecler, "Direct imaging of a photonic jet at shaped fiber tips," Opt. Lett. **46**(20), 5125–5128 (2021).

175. E. J. F. Dickinson, H. Ekström, and E. Fontes, "COMSOL Multiphysics®: Finite element software for electrochemical analysis. A mini-review," Electrochem. commun. **40**, 71–74 (2014).

176. COMSOL, *Introduction To COMSOL Multiphysics* (COMSOL Multiphysics, 2019).

177. C. Rubio, D. Tarrazó-Serrano, O. V. Minin, A. Uris, and I. V. Minin, "Wavelength-scale gas-filled cuboid acoustic lens with diffraction limited focusing," Results Phys. **12**(February), 1905–1908 (2019).

178. G. Gu, J. Song, M. Chen, X. Peng, H. Liang, and J. Qu, "Single nanoparticle detection using a photonic nanojet," Nanoscale **10**(29), 14182–14189 (2018).

179. W. Aljuaid, J. A. Riley, N. Healy, and V. Pacheco-Peña, "On-fiber high-resolution photonic nanojets via high refractive index dielectrics," Opt. Express **30**(24), 43678–43690 (2022).

180. W. Aljuaid, N. Healy, and V. Pacheco-Peña, "High-refractive-index Nanosparticles on Optical Fibres for High-Resolution Lensing Applications," in *14th International Congress on Artificial Materials for Novel Wave Phenomena – Metamaterials 2020 New York, USA, Sept. 28th – Oct. 3rd, 2020* (2020), pp. 1–3.

181. W. Aljuaid, J. A. Riley, N. Healy, and V. Pacheco-Peña, "On-fiber high-resolution photonic nanojets via high refractive index dielectrics: supplement," Opt. Express **30**(24), 21304746–21304748 (2022).

182. C. Y. Liu and F. C. Lin, "Geometric effect on photonic nanojet generated by dielectric microcylinders with non-cylindrical cross-sections," Opt. Commun. **380**, 287–296 (2016).

183. D. Ju, H. Pei, Y. Jiang, and X. Sun, "Controllable and enhanced nanojet effects excited by surface plasmon polariton," Appl. Phys. Lett. **102**(17), 1–5 (2013).

184. M. N. Afsar and H. Chi, "Millimeter wave complex refractive index, complex dielectric permittivity and loss tangent of extra high purity and compensated silicon," Int. J. Infrared Millimeter Waves **15**(7), 1181–1188 (1994).

185. A. C. Lynch, "Relationship Between Permittivity and Loss Tangent," **118**(1), 244–246 (1971).

186. J. B. Pendry, "Negative refraction makes a perfect lens," Phys. Rev. Lett. **85**(18), 3966–3969 (2000).

187. J. Zhang, "Evolutionary optimization of compact dielectric lens for farfield sub-wavelength imaging," Sci. Rep. **5**, 1–11 (2015).

188. W. Aljuaid, J. A. Riley, N. Healy, and V. Pacheco-Peña, "Producing Photonic Nanojet Outside of Immersed High Refractive Index Engineered dielectrics on Optical Fibers," in *16th International Congress on Artificial Materials for Novel Wave Phenomena – Metamaterials 2022 Siena, Italy, Sep. 12th –17th, 2022* (2022), pp. 1–3.

189. W. Aljuaid, J. A. Riley, N. Healy, and V. Pacheco-Peña, "Attaching truncated dielectric particles to optical fibres to produce high resolution focusing for potential imaging and sensing systems (poster)," in *UK Semiconductor Conference* (2022), p. 1.

190. H. Chen, S. Fan, G. Li, M. A. Schmidt, and N. Healy, "Single Crystal Ge Core Fiber Produced via Pressure Assisted Melt Filling and CO2 Laser Crystallization," IEEE Photonics Technol. Lett. **32**(2), 81–84 (2020).

191. V. Sorianello, A. Perna, L. Colace, G. Assanto, H. C. Luan, and L. C. Kimerling, "Near-infrared absorption of germanium thin films on silicon," Appl. Phys. Lett. **93**(11), 3–6 (2008).

192. L. Colace and G. Assanto, "Germanium on silicon for near-infrared light sensing," IEEE Photonics J. **1**(2), 69–79 (2009).

193. A. Osman, M. Nedeljkovic, J. Soler Penades, Y. Wu, Z. Qu, A. Z. Khokhar, K. Debnath, and G. Z. Mashanovich, "Suspended low-loss germanium waveguides for the longwave infrared," Opt. Lett. **43**(24), 5997–6000 (2018).

194. H. W. Lee, M. A. Schmidt, R. F. Russell, N. Y. Joly, H. K. Tyagi, P. Uebel, and P. S. J. Russell, "Pressure-assisted melt-filling and optical characterization of Au nano-wires in microstructured fibers," Opt. Express **19**(13), 12180–12189 (2011).

195. J. Zhang, K. Li, T. Zhang, P. J. S. Buenconsejo, M. Chen, Z. Wang, M. Zhang, Z. Wang, and L. Wei, "Laser-Induced In-Fiber Fluid Dynamical Instabilities for Precise and Scalable Fabrication of Spherical Particles," Adv. Funct. Mater. **27**(43), 1–8 (2017).

196. J. Zhang, K. Li, T. Zhang, P. J. S. Buenconsejo, M. Chen, Z. Wang, M. Zhang, Z. Wang,

and L. Wei, "Laser-Induced In-Fiber Fluid Dynamical Instabilities for Precise and Scalable Fabrication of Spherical Particles Supporting Information for," Adv. Funct. Mater. **27**(43), 1–11 (2017).

197. R. D. Paiva, A. M. M. C. Mallmann, J. C. Santos, and T. B. L. Kist, "Polyimide removal, cleaving, and fusion splicing of cylindrical and square fused silica capillaries for new separation and detection layouts in capillary electrophoresis and chromatography," J. Sep. Sci. **44**(12), 2438–2448 (2021).

198. W. C. Chew, *Lectures on Electromagnetic Field Theory* (Purdue University, 2019).

199. D. J. Lockwood, "Rayleigh and Mie Scattering," Encycl. Color Sci. Technol. **218**(1), 1–12 (2015).

Conferences: International and National

- Attended the CLEO Virtual Conference 2020.
- Participated in Metamaterials 2020 Conference, the 14th International Congress on Artificial Materials for Novel Wave Phenomena.
- Participated in the UK Semiconductors Conference 2022.
- Participated in Metamaterials 2022 Conference, the 14th International Congress on Artificial Materials for Novel Wave Phenomena.

Publications

- **W. Aljuaid**, J. A. Riley, N. Healy, and V. Pacheco-Peña, "On-fibre high-resolution photonic nanojets via high refractive index dielectrics," Opt. Express 30(24), 43678–43690 (2022).
- **W. Aljuaid**, N. Healy, and V. Pacheco-Peña, "High-refractive-index Nanosparticles on Optical Fibres for High-Resolution Lensing Applications," in 14th International Congress on Artificial Materials for Novel Wave Phenomena – Metamaterials 2020 New York, USA, Sept. 28th – Oct. 3rd, 2020 (2020), pp. 1–3.
- **W. Aljuaid**, J. A. Riley, N. Healy, and V. Pacheco-Peña, "Attaching truncated dielectric particles to optical fibres to produce high resolution focusing for potential imaging and sensing systems," in UK Semiconductor Conference (2022), p. 1.
- **W. Aljuaid**, J. A. Riley, N. Healy, and V. Pacheco-Peña, "Producing Photonic Nanojet Outside of Immersed High Refractive Index Engineered dielectrics on Optical Fibers," in 16th International Congress on Artificial Materials for Novel Wave Phenomena – Metamaterials 2022 Siena, Italy, Sep. 12th –17th, 2022 (2022), pp. 1–3.
- A. Yakovlev, R. G. MacDonald, A. Ventisei, T. Knightley, **W. Aljuaid**, W. Rogers, J. A. Riley, and V. Pacheco-Pena, "From TEM pulse switching to computing with light," in 2022 3rd URSI Atlantic and Asia Pacific Radio Science Meeting, AT-AP-RASC 2022 (2022), (June), pp. 1–3.
- A. Yakovlev, R. G. Macdonand, A. Ventisei, T. Knightley, **W. Aljuaid**, W. Rogers, J. A. Riley, and V. Pacheco-Peña, "Engineering pulse propagation in waveguide crossing to compute decision-making processes," in UK Semiconductor Conference (2022), p. 1.